Ultracold atoms carrying orbital angular momentum

Gerard Pelegrí Andrés

Submitted in fulfillment of
the requirements for the degree of
Doctor of Physics

Thesis supervisors:
Dr. Verònica Ahufinger Breto
Dr. Jordi Mompart Penina

Departament de Física
Universitat Autònoma de Barcelona

Bellaterra, January 2020

A la meva família

Agraïments

En primer lloc, vull donar les gràcies al Jordi i la Verònica per haver-me donat l'oportunitat de fer el doctorat amb ells i per tot el seu suport durant aquests quatre anys. M'heu ensenyat tot el que cal saber per ser un bon científic, m'heu encoratjat constantment a moure'm per expandir els meus horitzons, heu sabut quan estar pendents de mi i quan deixar-me llibertat per seguir el meu propi criteri, i heu estat disposats a ajudar-me i aconsellar-me sempre que ho he necessitat. També vull destacar el vostre optimisme inesgotable i l'orgull que sempre heu mostrat per la meva feina, gràcies als quals he pogut superar els moments de crisi que inevitablement sorgeixen durant un viatge tan llarg com aquest. Aprendre i treballar en companyia d'uns directors de tesi com vosaltres ha estat un privilegi tant a nivell professional com personal.

També vull dedicar unes línies d'agraïment a la resta de professors del grup d'Òptica de la UAB, que fan que s'hi respiri sempre un molt bon ambient: el Francesc, amb qui he gaudit col·laborant en diverses activitats de divulgació, el Gaspar, que irradia passió quan explica qualsevol cosa sobre ciència, el Todor, que sempre té una anècdota a punt, i els clàssics, el Juan, l'Angel i la Marifí, que són uns molt bons veïns sempre disposats a ajudar en el que calgui. Vull dedicar un record especial al Ramón, que va tenir l'amabilitat de preparar-me per donar les classes de problemes de fotònica i de qui tots trobem a faltar el seu permanent bon humor.

Durant tot aquest temps he estat envoltat d'excel·lents companys a qui estic molt agraït per haver fet que aquest camí hagi estat més fàcil i amè. L'Alex em va rebre amb els braços oberts al grup amb la seva alegria habitual i em va ensenyar moltes coses sobre com fer recerca. El Joan, amb qui vaig tenir el gust de col·laborar estretament durant

gairebé un any, em va ajudar molt al principi del doctorat transmetent-me els seus coneixements sobre programació i ensenyant-me a fer servir eines que m'han resultat molt útils. Amb el Josep i el Gerard, els meus camarades més veterans, he compartit una infinitat de dubtes i idees sobre les nostres investigacions, debats interessants sobre física i molts temes més, i rialles i bones estones a la UAB i a les conferències a què hem anat junts. L'Alessio, amb qui és sempre una delícia parlar de física i de la vida, m'ha donat molt bons consells pels meus projectes. El Juanlu, que espero que sigui aviat el següent doctor, ha amenitzat molts àpats amb les seves aventures. Quan ha estat al grup, el Dani ha generat bon ambient constantment amb la seva simpatia i els seus acudits. Amb el sector dels clàssics, format per la Irene, el Haolin i l'Albert, també he passat molt bons moments dinant i preparant activitats de divulgació. Finalment, vull desitjar-li el millor pel doctorat a l'Eulàlia, que s'ha incorporat recentment al grup i em pren el relleu en la recerca.

A wonderful experience that has had a major impact in my PhD is the research stay that I did in Glasgow. I had the pleasure to work there with Andrew Daley, to whom I want to express my most sincere gratitude for giving me the opportunity to learn a lot of interesting physics, for coming up with exciting projects that have ended up being a central part of this thesis, and for making me feel as a member of the group from my first until my last day at the University of Strathclyde. I also want to thank him for his generous offer to continue working with him as a postdoc, about which I am very thrilled. I would also like to give many thanks to the rest of the people from the group for the nice discussions that I had with them, for all the help that they provided during my visit, and, most importantly, for being amazing hosts who made me enjoy my four months in Glasgow to the fullest.

I am deeply indebted to my close collaborators from Portugal, Ricardo Dias and Anselmo Marques, who have done essential contributions to a substantial portion of the work contained in this thesis and who welcomed me warmly when I visited them in Aveiro. It has been my pleasure to learn so much physics with you, and I hope to continue doing so in the future.

I would also like to thank Maciej Lewenstein for giving me the chance to spend a summer in his incredible group at ICFO just before starting my PhD and for his valuable collaboration in the projects that we conducted during the first stage of my doctorate.

Al llarg dels anys he tingut grans mentors que han influit de manera decisiva en la meva formació i que tenen bona part de la culpa que se'm passés pel cap la idea de fer un doctorat en física. A tots ells els he d'agrair el fet d'haver arribat fins aquí, però voldria fer una menció especial a l'Eugenio Salvatierra, a qui vaig tenir la sort de tenir de professor al batxillerat. Gràcies a la seva passió desbordant per la física vaig descobrir per primera vegada la bellesa d'aquesta ciència i em vaig decidir a estudiar-la

en profunditat a la universitat. També vull dedicar un agraïment particular a l'Artur Polls i al Bruno Juliá, que van ser uns excel·lents tutors de treball de màster a la UB gràcies als quals em vaig començar a interessar per tot això dels àtoms freds i que em van obrir generosament la porta per començar una nova etapa a l'Autònoma. I also want to thank Bruno, together with Alexandre Dauphin and Matteo Rizzi, for agreeing to be part of my PhD thesis committee.

Fora de l'àmbit acadèmic, vull donar les gràcies a tots els amics i amigues que durant tots aquests anys m'han donat el seu caliu, han escoltat les meves inquietuds i han compartit amb mi incomptables estones d'esbarjo que m'han ajudat a desconnectar de la feina i a mantenir l'equilibri necessari per afrontar un repte de les dimensions d'un doctorat. Vull donar també les gràcies a l'Adri per haver-se encarregat de dissenyar la portada tan bonica que cobreix aquesta tesi.

Per últim, vull agrair de tot cor a la meva família la seva estima i el seu recolzament incondicional que m'han fet ser qui sóc. Sense vosaltres no estaria escrivint això.

Gerard Pelegrí Andrés
Bellaterra, Gener de 2020.

List of publications

The research contained in this thesis is supported by the following publications:

Chapter 3: Quantum sensing using imbalanced counter-rotating Bose–Einstein condensate modes

1. G. Pelegrí, J. Mompart, and V. Ahufinger, *Quantum sensing using imbalanced counter-rotating Bose–Einstein condensate modes*, New Journal of Physics **20**, 103001 (2018).

Chapter 4: Topological edge states and Aharonov-Bohm caging with ultracold atoms carrying orbital angular momentum in a diamond chain

2. G. Pelegrí, A. M. Marques, R. G. Dias, A. J. Daley, V. Ahufinger, and J. Mompart *Topological edge states with ultracold atoms carrying orbital angular momentum in a diamond chain*, Phys. Rev. A **99**, 023612 (2019).

3. G. Pelegrí, A. M. Marques, R. G. Dias, A. J. Daley, J. Mompart, and V. Ahufinger, *Topological edge states and Aharanov-Bohm caging with ultracold atoms carrying orbital angular momentum*, Phys. Rev. A **99**, 023613 (2019).

Chapter 5: Quantum magnetism with ultracold bosons carrying orbital angular momentum

4. G. Pelegrí, J. Mompart, V. Ahufinger, and A. J. Daley, *Quantum magnetism with ultracold bosons carrying orbital angular momentum*, Phys. Rev. A **100**, 023615 (2019).

Chapter 7: Second-order topological corner states with ultracold atoms carrying orbital angular momentum in optical lattices

5. G. Pelegrí, A. M. Marques, V. Ahufinger, J. Mompart, and R. Dias *Second-order topological corner states with ultracold atoms carrying orbital angular momentum in optical lattices*, Phys. Rev. B **100**, 205109 (2019).

Other publications by Gerard Pelegrí not included in this thesis:

6. G. Pelegrí, J. Polo, A. Turpin, M. Lewenstein, J. Mompart, and V. Ahufinger, *Single-atom edgelike states via quantum interference*, Phys. Rev. A **95**, 013614 (2017).

7. A. Turpin, G. Pelegrí, J. Polo, J. Mompart, and V. Ahufinger, *Engineering of orbital angular momentum supermodes in coupled optical waveguides*, Scientific Reports **7**, 44057 (2017).

Contents

CHAPTER 1

Introduction

In the 1920's, Bose [1] and Einstein [2, 3] formulated the statistical law that governs the distribution of identical quantum particles with integer spin, known since then as bosons. An immediate consequence of their finding was the prediction that, at very low temperatures, bosonic systems experience a quantum phase transition into an exotic state of matter known as Bose–Einstein condensate (BEC), in which all the particles occupy a single quantum state and behave as a macroscopic coherent object. In atomic systems, the critical temperature of the BEC transition can be estimated by comparing the mean interatomic distance d with the de Broglie thermal wavelength λ_{dB}, which for free particles is given by $\lambda_{dB} = h/\sqrt{2\pi m k_B T}$, where m is the mass of the atoms, T the temperature, k_B the Boltzmann constant, and h the Planck constant. When T is low enough that $\lambda_{dB} \sim d$, the wave functions of the different atoms start to overlap, setting in coherence effects in the system and thus enabling the formation of a BEC. Bose–Einstein condensation was observed for the first time in 1937, when Kapitza [4] and Allen and Misener [5] managed to cool liquid ^{4}He until reaching its superfluid phase. However, due to the strong interactions caused by the large density of this system, only a small fraction of the particles were in the BEC phase. It became thus apparent that total condensation was more likely to occur in very dilute systems with weak interactions, for which the critical temperature of the BEC transition is several orders of magnitude lower than the ~ 2.17 K at which ^{4}He becomes superfluid. After decades of improvements in laser cooling techniques [6] (for which the 1997 Nobel prize in Physics was awarded to Steven Chu, Claude Cohen-Tannoudji and William D. Phillips) and the additional development of evaporative cooling protocols [7], almost full condensation was finally

reached in 1995, first with a gas of ^{87}Rb [8] and shortly after with ^{7}Li [9] and ^{23}Na [10]. This milestone achievement was worth a second Nobel Prize, awarded in 2001 to Eric Cornell, Carl Wieman and Wolfgang Ketterle. In order to operate in a regime where interactions would not destroy the condensate, these alkali-atom BECs were realized with extremely dilute gases (with densities on the order of $\sim 10^{12} - 10^{14}$cm^{-3}), for which the critical temperature of the transition is ~ 100nK. A few years later, extended cooling techniques were developed to reach the quantum degenerate regime in ultracold fermionic gases [11–13]. Nowadays, BECs and degenerate Fermi gases are routinely produced with a wide range of atomic species in laboratories all over the world, and temperatures as low as 1 nK are within the experimental capabilities [14].

In spite of the extreme conditions under which they are produced, ultracold atom systems offer a great degree of controllability through external electromagnetic fields. An example of this is the possibility to tune with very high precision the strength of the interatomic interactions (which, in general, can be considered to depend only on the $s-$ wave scattering length) by means of optical [15–17] or magnetic [18–20] Feshbach resonances, enabling to explore in a single experiment the attractive, repulsive or even non-interacting regime [21]. An impressive demonstration of the power of Feshbach resonances is the realization in Fermi gases of the crossover between the Bardeen-Cooper-Schrieffer state of Cooper pairs, which are characterized by a large pairing distance, to a BEC formed by diatomic molecules of bosonic nature [22–24]. We also point out that, besides having an unquestionable fundamental interest, BECs and cold atoms are very well suited for a number of applications in sensing and metrology, ranging from the measurement of magnetic fields [25], rotations [26], and gravitational forces [27], to the fabrication of the most precise atomic clocks [28].

A very remarkable feature of ultracold atoms is that they can realize almost on-demand quantum many-body systems when they are placed in the sine of optical lattices, which are standing electromagnetic waves resulting from the interference between counter-propagating laser beams. As a result of their far detuned interaction with the atomic dipolar moment [29], optical lattices create effective periodic potentials for the atoms, opening the door to the emulation of a vast amount of Hamiltonians of interest in condensed matter physics in a very clean and versatile environment [30, 31]. The first important demonstration of this possibility was the observation in 2002 of the phase transition between the superfluid and Mott insulator regimes in a system of cold bosons loaded in a three-dimensional optical lattice [32], which had been theoretically predicted more than a decade earlier [33]. This system is well-described by the Bose-Hubbard model [34], which is a simple but very rich model that accounts for the atom hopping between the different sites of the lattice and the on-site interaction between atom pairs. The transition was probed by changing the lattice depth, in such a way that different ratios between the hopping rate and the interaction strength could be

realized. In subsequent experiments, fermionic species were also trapped in optical lattices [35–38] and the use of Feshbach resonances to tune the strength of the atom-atom interactions was also demonstrated in these systems [16, 36, 37, 39, 40]. In recent years, there have been many substantial advances that have pushed the degree of control over ultracold atoms in optical lattices to an extraordinary level. To cite a few examples, it is nowadays possible to create lattices with many different geometries [41–44] and quasicrystals [45], to engineer artificial gauge fields [46–48] and spin-orbit coupling [49] for neutral atoms, to probe the samples with single-site resolution using quantum gas microscopes [50–55], to excite atoms beyond the first Bloch band [56–58] or to realize models with different types of long-range interactions [59–61]. All these achievements have consolidated ultracold atoms in optical lattices as an excellent platform to perform quantum simulations [62], i.e., to mimic in a very well-controlled manner other quantum systems of interest that are difficult to study, as originally suggested by Feynman as early as in the 1980's [63].

The study of topological phases is a prominent topic in condensed matter physics. In the standard Landau-Ginzburg paradigm, phase transitions occur through the breaking of some symmetry, which can be characterized by a local order parameter that takes different values in the distinct phases [64]. This theory has proven to be very successful in describing not only classical phase transitions like the ones experienced by water, but also quantum critical phenomena such as, e.g., Bose–Einstein condensation [65]. Topological phases of matter, however, exhibit surprising properties that can not be explained within this approach. The pioneering development of a theoretical framework capable of describing these exotic states was worth the 2016 Nobel Prize in Physics, awarded to David J. Thouless, F. Duncan M. Haldane and J. Michael Kosterlitz.

The essential ideas behind the description of these phases have been borrowed from the mathematical discipline of topology, which studies the properties of geometric objects that remain unaltered under continuous deformations. From a topological perspective, a doughnut and a cup are equivalent because it is possible to continuously transform one into the other, but they are different from a trophy because it would be necessary to break them in order to open up another hole. Thus, the topologically invariant quantity that distinguishes these objects is the genus, i.e., the number of holes that can be used as a handle, which is $g = 1$ for the doughnut and the cup and $g = 2$ for the trophy. According to the Gauss-Bonnet theorem [66], the genus can be computed as an integral of the curvature of the surface, and can only be equal to a positive integer or zero. It is, therefore, a global property of the object that does not depend on the details of its surface. Analogously, topological phases of matter are characterized by global order parameters, also called topological invariants, that are insensitive to local pertur-

bations. In discrete systems, these invariants are usually defined as integrals over the different bands that form the energy spectrum, and their values can only be changed by deformations capable of closing the band gaps and opening them again. Thus, smooth deformations can be regarded in this context as those that do not close any band gap and, therefore, can not induce a topological phase transition, i.e., a change of the values of the topological invariants [67].

One of the most remarkable examples of topological states of matter is the Integer Quantum Hall Effect (IQHE), which was observed experimentally for the first time in 1980 in a two-dimensional semiconductor at very low temperature pierced by a magnetic field [68]. The IQHE consists on a very robust quantization of the transeverse electric (or Hall) conductance in units of e^2/h, where e is the elementary charge, that does not depend on the microscopic details of the material [69, 70]. Two years after its discovery, it was shown that the IQHE is originated by the direct correspondence between the Hall conductance and the Chern number, a two-dimensional topological invariant which is computed as a closed integral over the Brillouin zone and can only take integer values [70]. The currents that give rise to the quantized conductivity are transported by chiral edge states, which are protected by the topology of the bulk and are therefore robust against local defects and perturbations. This mechanism, often called the bulk-boundary correspondence, is common to a broader family of systems known as topological insulators, which are materials that exhibit insulating properties in their bulk but have conducting states at the edges [67].

Since the successful theoretical explanation of the IQHE, there have been many advances in the comprehension of topological insulators. In an early stage, it was commonly accepted that topological states could only appear in the presence of a magnetic field that breaks time-reversal symmetry. However, in 1988 Haldane proved this belief to be wrong by proposing a simple model of non-interacting spinless electrons in a honeycomb lattice without a magnetic field that has non-trivial topological properties [71]. The key element of his proposal was the introduction of next-nearest-neighbour complex hopping terms, which are responsible for the breaking of time-reversal symmetry. Almost two decades later, Kane and Mele [72] demonstrated that the spin-orbit coupling can also give rise to topological insulators with a global time-reversal symmetry, in what is known as the quantum spin Hall effect. Shortly after its discovery, this effect was predicted [73] and observed [74] in HgTe quantum wells and generalized to three-dimensional systems [75–78]. Topological insulators have been systematically classified in terms of their dimensionality and protecting symmetries in a celebrated "periodic table" [79]. Far from experiencing a decay in scientific activity after this remarkable achievement, the study of topological effects in condensed matter systems remains an active field of research, as exemplified by the recent discovery of novel topological phases such as Weyl semimetals [80], topological Anderson insulators [81], or higher-order topological systems [82].

Ultracold atoms in optical lattices constitute a very flexible and controllable environment to implement and probe a variety of models of topological quantum matter [83]. The simulation of two-dimensional topological systems typically requires the presence of spin-orbit coupling or strong magnetic fields, to which the atoms are insensitive due to their charge neutrality. However, there exist strategies to engineer artificial gauge fields for neutral atoms [84–86] which allow to produce effective magnetic fields that would indeed be very difficult to reach in other systems [87, 88]. These approaches rely on the imprinting of phase factors on the hopping amplitudes, which, according to the Peierls substitution, encode the effect of a vector potential [89]. The two methods that are most commonly employed to obtain these complex couplings consist on the use of laser-assisted tunneling [84] and Floquet engineering [85, 90], which is based on applying periodical modulations to the lattice with a period much smaller than any characteristic time scale of the system and yields indeed topological states with singular properties [91, 92]. Using these techniques, the Hofstadter [46, 47, 93] and Haldane [94] models have been realized with ultracold atoms. Spin-orbit coupling can also be implemented in cold atoms [49], allowing for the observation of the spin Hall effect [95]. Another interesting possibility to simulate topological systems that can be exploited with ultracold atoms is to take profit of synthetic dimensions [96, 97], i.e., mapping an internal or motional atomic degree of freedom into an extra spatial direction. This approach has been used, for instance, to obtain quantum Hall stripes from one-dimensional lattices filled with bosons [98] and fermions [99] by associating hyperfine states with an effective transverse direction, or to realize tailored one-dimensional topological models by mapping the momenta states of a BEC into spatial sites [100]. In addition to a vast toolbox for designing topological models, ultracold atoms in optical lattices offer the possibility to prepare topological states with high fidelity through dissipative engineering [101, 102], to image them with high resolution by means of quantum gas microscopes [50–55], and to directly probe topological invariants [93, 103–105]. We also note that ultracold atoms offer a natural playground for the realization of strongly correlated topological phases [106], which have been recently obtained with arrays of Rydberg atoms manipulated with optical tweezers [107].

The focus of this thesis is on ultracold atoms carrying Orbital Angular Momentum (OAM) and their potential use for quantum sensing, quantum simulation, and the realization of topological phases of matter. The interest in these specific states is motivated by the important role that they play in the emergent field of atomtronics [108], which aims at building neutral-atom analogues of electric circuits and to create novel

devices that take profit of the unique properties of ultracold atoms. The basic building blocks of these circuits are ring-shaped traps [109–116], which constitute closed loops for matter waves that naturally support OAM states and their associated persistent currents [117–121]. In these trapping geometries, OAM can be transferred to the atoms using light beams [120, 122], by means of quenches [123] or by rotating a weak link [121, 124], an approach which has been successfully employed to obtain the matter-wave version of Superconducting Quantum Interference Devices (SQUIDs) [125–129]. Furthermore, matter waves in toroidal traps offer potential uses in the sensing of rotations [130–133]. In this thesis, we will explore the sensing applications of a device based on a BEC trapped in a ring potential and prepared in an imbalanced superposition of counter-rotating OAM states [134]. Alternatively, OAM states can be considered in the context of optical lattices, where they are in a sense equivalent to the p_x and p_y orbitals of the first excited Bloch band [58]. In these systems, OAM states could also be created in the Mott insulator regime through shaking protocols [135, 136]. An interesting property of ultracold atoms in OAM states is that their tunneling dynamics (which can be studied either in arrays of ring potentials or in conventional optical lattices) is governed by complex amplitudes, the phases of which can be modulated by tuning the geometrical arrangement of the traps [137]. As we will show in this thesis, these tunable complex hoppings provide an alternative way to engineer topological models with ultracold atoms [138–140] and allow to perform flexible quantum simulations of spin$-1/2$ magnetic Hamiltonians related to the XYZ Heisenberg model [141].

Outline of the thesis

Before starting to describe the results of our research, in Chapter 2 we introduce the main models and theoretical tools that we will use to investigate the different systems under consideration. We start by reviewing two different approaches to the description of ultracold gases that are valid for different regimes: the Gross–Pitaevskii equation (GPE), which is a mean-field equation adequate for weakly interacting BECs at zero temperature, and the Hubbard model, which provides a full quantum treatment of ultracold atoms in optical lattices. Then, we introduce basic concepts that we will employ in the characterization of topological phases. Specifically, we discuss the Berry phase and its relation with one- and two-dimensional topological invariants, we outline how these invariants are related to edge states and macroscopic observables, and we illustrate the discussion with the Su-Schrieffer-Heeger model, which is the simplest example of a one-dimensional topological insulator. Finally, we make extensive considerations about the single-trap physics and tunneling dynamics of ultracold atoms in OAM states, which constitute the common element to all the systems considered in the next Chapters.

In Chapter 3, we study in the context of the GPE a device consisting of a BEC

trapped in a ring potential and prepared in an imbalanced superposition of counter-rotating OAM modes. By computing numerically the time evolution of the system, we show that the density profile of the BEC exhibits a minimal line that rotates due to the non-linear interaction between the atoms. We analyse the equations of motion of the probability amplitudes of the different OAM modes and we derive a model which provides a simple relation between the frequency of rotation of the nodal line and the strength of the atom-atom interactions. This relation opens the door to the use of the device as a sensor of interactions, magnetic fields and rotations, for which we propose a detailed experimental protocol to perform the corresponding measurements. Furthermore, we provide a method to prepare the imbalanced superposition of OAM states that forms the initial state of the system and we carry out numerical simulations to examine its validity.

In Chapter 4, we introduce a system consisting of an array of side-coupled cyllindrically symmetric traps, where the tunneling dynamics of OAM states is governed by complex hopping amplitudes. In particular, we consider a quasi one-dimensional lattice with a diamond-chain geometry filled with non-interacting ultracold atoms loaded in OAM states. We show that the phases that some of the tunneling amplitudes of the tight-binding model that describes the system acquire due to the OAM degree of freedom give rise to the equivalent of a net magnetic flux through the plaquettes of the chain. This yields a topologically nontrivial band structure signalled by robust edge-localized states which persist after the gap closing points, indicating the absence of a topological phase transition in the system. We also demonstrate by means of successive analytical mappings that this system constitutes a realization of a square-root topological insulator. In addition, we discuss how a proper tuning of the tunneling parameters involved in the dynamics may lead to the simultaneous flattening of all the bands. In this situation, the system exhibits Aharonov-Bohm caging, a single-particle localization phenomenon caused by destructive interference effects in periodic structures.

The effect of interactions in systems where ultracold atoms in OAM states experience tunneling dynamics is addressed for the first time in Chapter 5. In particular, we study a strongly correlated gas of ultracold bosons carrying OAM in arrays of side-coupled cylindrically symmetric potentials. By means of second-order perturbation theory calculations, we show how these systems can be used to simulate a wide family of spin$-1/2$ models of quantum magnetism. By tuning the geometry of the system, the effective spin couplings can be adjusted to realize several spin Hamiltonians of interest related to a general XYZ Heisenberg model with external field. We also discuss how the relative strength of the effective couplings depends on the parameters of the lattice and we analyse some of the phases that can be explored in realistic setups by tuning these parameters. Finally, we make some considerations concerning the readout of spin states and the stability of the system under ellastic collisions.

After having introduced in the preceding Chapter the effect of interactions in lattices filled with ultracold atoms in OAM states, in Chapter 6 we turn our attention back to the diamond-chain lattice considered in Chapter 4 to examine a new scenario. Specifically, we focus on the limit where all the bands are flat and we study the properties of two-boson states in the presence of a weak attractive interaction. In this situation, the kinetic energy is frozen and the interactions between single-particle states localized in overlapping Aharonov-Bohm cages determine the shape of the two-body eigenstates. We analyse the lowest-energy sector of the spectrum, which is composed of states in which the two bosons occupy single-particle states belonging to the lowest flat bands. We show that this sector can be divided in subspaces which are described by effective models that can be rendered topologically non-trivial by tuning separately the strength of the interactions in the different sites of the diamond chain. Thus, in the topological phase, this system exhibits two-boson edge states that are in turn composed of compactly localized single-particle modes. In the last part of the Chapter, we perform numerical calculations to check our analytical predictions and to analyse the effect of deviations from the flat-band and weakly interacting limits.

In contrast with the previous Chapters, where we mainly study quasi one-dimensional arrays of traps, in Chapter 7 we consider a fully two-dimensional lattice. In particular, we study the topological properties of a system consisting of a square lattice with unequal intra- and inter-cell spacings filled with ultracold atoms loaded into OAM states. We find that the band structure of the corresponding Hubbard model is topologically non-trivial at first order, a fact signalled by the presence of edge states in the spectrum. More interestingly, we show that this system also has second-order topological properties, as indicated by the apparition of robust zero-energy states with a strong localization at the corners of the lattice. Furthermore, we perform realistic numerical calculations which demonstrate that these second-order topological effects can be observed in a wide range of experimentally feasible parameters.

Finally, in Chapter 8 we summarize the main conclusions of this thesis and we provide a brief outlook on further perspectives open by this work.

Physical models and theoretical tools

In this Chapter, we provide a general overview of the main models and theoretical tools that we will use throughout the thesis to investigate the different physical systems under consideration. The first two sections are devoted to introducing the descriptions of bosonic gases in two distinct regimes. In particular, in Sec. 2.1 we focus on the mean-field modelling of Bose–Einstein Condensates through the Gross-Pitaevskii Equation, which is adequate for bosonic gases formed by a large number of weakly-interacting particles at zero temperature. In Sec. 2.2, we discuss the full quantum treatment with the Bose-Hubbard model of systems formed by ultracold bosons trapped in optical lattices. In Sec. 2.3, we change gears to review general concepts and techniques related to the characterization of topological phases in discrete systems. We illustrate the discussion with the specific example of the Su-Schrieffer-Heeger model, which is the simplest one-dimensional model of a topological insulator. Finally, in Sec. 2.4 we analyse the physics of ultracold atoms carrying orbital angular momentum in two-dimensional cylindrically symmetric potentials, which constitute the common thread that relates all the systems studied in this thesis, considering first a single atom in a single trap and then describing the tunneling dynamics in side-coupled traps.

2.1   Mean-field description of Bose–Einstein Condensates

In this section, we review a few aspects of the mean-field description of weakly-interacting Bose–Einstein Condensates (BECs) at zero temperature, which is usually done with the Gross–Pitaevskii Equation (GPE). First, we analyse in which situation a three-dimensional bosonic gas can be considered to be in the mean field regime and we outline the derivation of the GPE. After this, we comment briefly on the insights about the superfluid properties of the BEC that can be gained by making a simple analysis of the GPE and we introduce the main characteristics of persistent currents in cylindrically symmetric geometries. Finally, we discuss under which conditions a two-dimensional Bose gas can be described within the mean field approach and how the GPE is modified in this case.

2.1.1   Gross–Pitaevskii equation

We consider a gas formed by N identical bosonic atoms of mass m and subjected to an external potential $V_{\text{ext}}(\vec{r})$. The atoms occupy a total volume V such that the diluteness condition is fulfilled

$$r_0 \ll d, \tag{2.1}$$

where r_0 is the range of the atom-atom interactions and $d = (N/V)^{-1/3}$ is the mean distance between the atoms. In this situation, one can safely neglect interaction processes involving three or more particles and consider only elastic collisions between pairs of atoms caused by the two-body interatomic potential $V(\vec{r'} - \vec{r})$. Thus, the many-body Hamiltonian of the system reads [65]

$$\hat{H} = \int d^3r \hat{\Psi}^\dagger(\vec{r}) \left[-\frac{\hbar^2 \nabla^2}{2m} + V_{\text{ext}}(\vec{r}) \right] \hat{\Psi}(\vec{r}) + \frac{1}{2} \int \int d^3r d^3r' \hat{\Psi}^\dagger(\vec{r}) \hat{\Psi}^\dagger(\vec{r'}) V(\vec{r'} - \vec{r}) \hat{\Psi}(\vec{r}) \hat{\Psi}(\vec{r'}), \tag{2.2}$$

where $\hat{\Psi}(\vec{r})$ and $\hat{\Psi}^\dagger(\vec{r})$ are respectively the bosonic annihilation and creation field operators, which satisfy the commutation relations

$$\left[\hat{\Psi}(\vec{r}), \hat{\Psi}^\dagger(\vec{r'}) \right] = \delta(\vec{r} - \vec{r'}), \tag{2.3a}$$

$$\left[\hat{\Psi}^\dagger(\vec{r}), \hat{\Psi}^\dagger(\vec{r'}) \right] = \left[\hat{\Psi}(\vec{r}), \hat{\Psi}(\vec{r'}) \right] = 0. \tag{2.3b}$$

Making use of the Heisenberg picture, one obtains the following equation of motion for the bosonic field operator

$$
\begin{aligned}
i\hbar \frac{\partial \hat{\Psi}(\vec{r},t)}{\partial t} &= \left[\hat{\Psi}(\vec{r},t), \hat{H} \right] \\
&= \left[-\frac{\hbar^2 \nabla^2}{2m} + V_{\text{ext}}(\vec{r}) + \int d^3 r' \hat{\Psi}^\dagger(\vec{r'},t) V(\vec{r'}-\vec{r}) \hat{\Psi}(\vec{r'},t) \right] \hat{\Psi}(\vec{r},t).
\end{aligned} \tag{2.4}
$$

The GPE can be derived from this general equation of motion by making assumptions that are justified for dilute systems at very low temperatures. In order for the bosons to form a BEC, the temperature T must be low enough that the thermal de Broglie wavelengths of the atoms start to overlap, a situation that occurs when they become of the order of the mean interatomic distance

$$
d \lesssim \lambda_{dB} = \frac{h}{p} = \frac{h}{\sqrt{2\pi m k_b T}}, \tag{2.5}
$$

where p is the momentum of the atom and k_B the Boltzmann's constant. Combining Eq. (2.5) and the diluteness condition (2.1), we see that the relevant values of the momenta of the atoms satisfy the condition $p r_0 / h \ll 1$. According to standard scattering theory [142], for such low momenta the scattering amplitude is isotropic and independent of the energy, and the two-body interactions are described by a single parameter: the $s-$wave scattering length a_S. Therefore, we can substitute the real interaction potential $V(\vec{r'}-\vec{r})$ by a contact pseudo-potential which has the same low-energy scattering properties as the original one

$$
V_{\text{eff}}(\vec{r'}-\vec{r}) = \frac{4\pi \hbar^2 a_S}{m} \delta(\vec{r'}-\vec{r}) \equiv g_{3D} \delta(\vec{r'}-\vec{r}). \tag{2.6}
$$

We note that a_S can be either positive or negative (yielding repulsive or attractive interactions, respectively) and can be tuned in a wide range of values using Feshbach resonances [20]. Furthermore, assuming a large number of particles in the condensate and considering the zero-temperature limit, we can neglect thermal and quantum fluctuations in the bosonic field operator and substitute it by its mean value

$$
\hat{\Psi}(\vec{r},t) = \langle \hat{\Psi}(\vec{r},t) \rangle + \delta \hat{\Psi}(\vec{r},t) \approx \langle \hat{\Psi}(\vec{r},t) \rangle \equiv \Psi(\vec{r},t). \tag{2.7}
$$

The mean value of the field operator $\Psi(\vec{r},t) = |\Psi(\vec{r},t)| e^{iS(\vec{r},t)}$, which is usually called the condensate wave function, is a classical order parameter that can be interpreted as the wave function of each of the bosons in the situation in which there is complete condensation. Inserting Eqs. (2.6) and (2.7) into Eq. (2.4) and assuming that $\Psi(\vec{r},t)$ varies slowly in the range of the interatomic interactions, we obtain a non-linear mean-field equation that governs the dynamics of the condensate wave function, the celebrated

GPE [143, 144]

$$i\hbar\frac{\partial\Psi(\vec{r},t)}{\partial t} = \left[-\frac{\hbar^2\nabla^2}{2m} + V_{\text{ext}}(\vec{r}) + g_{3D}|\Psi(\vec{r},t)|^2\right]\Psi(\vec{r},t), \qquad (2.8)$$

where the condensate wave function is normalized to the total number of particles, $\int d^3r|\Psi(\vec{r},t)|^2 = N$. It can be easily checked that N is a conserved quantity under a time evolution governed by the GPE [65]. The total energy, which is also a conserved quantity of the system, is given by the functional

$$E = \int d^3r \left[\frac{\hbar^2}{2}|\nabla\Psi(\vec{r},t)|^2 + V_{\text{ext}}(\vec{r}) + \frac{g_{3D}}{2}|\Psi(\vec{r},t)|^4\right]. \qquad (2.9)$$

An additional condition of applicability of the mean-field approach is that the relation $d \ll \xi$ is fulfilled, where

$$\xi = \frac{\hbar}{\sqrt{2mng_{3D}}} = \frac{1}{\sqrt{8\pi na_S}} \qquad (2.10)$$

is the healing length, which corresponds to the distance at which the interaction and kinetic energy terms of Eq. (2.9) balance.

By considering a stationary solution $\Psi(\vec{r},t) = \Psi(\vec{r})e^{-i\mu t/\hbar}$, we obtain the time-independent version of the GPE

$$\left[-\frac{\hbar^2\nabla^2}{2m} + V_{\text{ext}}(\vec{r}) + g_{3D}|\Psi(\vec{r})|^2\right]\Psi(\vec{r}) = \mu\Psi(\vec{r}), \qquad (2.11)$$

where μ is the chemical potential of the system, i.e., the necessary energy to remove one particle from the BEC.

2.1.2 Superfluidity and persistent currents

Bose–Einstein condensation is closely related to superfluidity, a macroscopic quantum phenomenon by which substances can flow without dissipating energy. A simple analysis of the GPE can provide an initial insight into this connection. By multiplying Eq. (2.8) by $\Psi^*(\vec{r},t)$ and subtracting the complex conjugate, we obtain a continuity equation for the condensate wave function $\Psi(\vec{r},t) = |\Psi(\vec{r},t)|e^{iS(\vec{r},t)}$

$$\frac{\partial|\Psi(\vec{r},t)|^2}{\partial t} + \nabla\cdot\vec{j}(\vec{r},t) = 0, \qquad (2.12)$$

where we have introduced the current density

$$\vec{j}(\vec{r},t) = -\frac{i\hbar}{2m}\left(\Psi^*\nabla\Psi - \Psi\nabla\Psi^*\right) = \frac{\hbar}{m}|\Psi(\vec{r},t)|^2\nabla S(\vec{r},t). \qquad (2.13)$$

By direct analogy with classical hydrodynamic theory [65], we can define the velocity field of the condensate as

$$\vec{v}(\vec{r}, t) = \frac{1}{|\Psi|^2}\vec{j}(\vec{r}, t) = \frac{\hbar}{m}\nabla S(\vec{r}, t), \qquad (2.14)$$

which fulfills the irrotationality condition $\nabla \times \vec{j}(\vec{r}, t) = 0$, a characteristic feature of superfluids.

An interesting example of superfluidity in BECs are persistent circular currents [109, 117–121, 123, 126, 129, 145], which have been reported to flow without dissipation for several seconds [119]. These currents are possible whenever the trapping potential has cylindrical symmetry, in which case the GPE (2.8) admits solutions of the form

$$\Psi(\vec{r}) = |\Psi(r)|e^{i\nu\varphi}. \qquad (2.15)$$

Due to the single-valuedness of the wave function, ν must be an integer. Therefore, the wave function (2.15) represents a state in which each of the N atoms forming the BEC is in an eigenstate of the angular momentum operator $\hat{L}_z = -i\hbar\frac{\partial}{\partial\varphi}$ with eigenvalue $\hbar\nu$, yielding a total angular momentum $\left\langle \hat{L}_z \right\rangle = N\hbar\nu$. According to Eq. (2.14), the velocity field associated with the condensate wave function (2.15) is

$$\vec{v} = \frac{\hbar}{m}\frac{\nu}{r}\hat{e}_\varphi, \qquad (2.16)$$

where $\hat{e}_\varphi$ is the azimuthal unit vector. Note that this law is quite different from the solid rigid rotation, where the linear velocity is given by $\vec{v} = \vec{\omega} \times \vec{r}$, with $\vec{\omega}$ being a constant angular velocity. The velocity distribution (2.16) is instead associated with a vortex, which is characterized by a vanishing density at its center. The circulation around a closed contour centred about the z axis is quantized in units of h/m:

$$\oint \vec{v} \cdot d\vec{l} = \int_0^{2\pi} \frac{\hbar}{m}\frac{\nu}{r}r d\varphi = \nu\frac{h}{m}. \qquad (2.17)$$

The quantization of the circulation around the center of the vortex has been measured both in systems where the vortices are induced by a rotating weak link [126] or emerge stochastically through the Kibble-Zurek mechanism [123], and is a general feature of BECs with more complicated density distributions including multiple vortices [146].

2.1.3   The two-dimensional Gross–Pitaevskii equation

A fundamental requirement for the existence of a BEC is that the one-body density matrix $\langle \hat{\Psi}(\vec{r})\hat{\Psi}(\vec{r}) \rangle$ has long-range order. While in three-dimensional systems true condensation always exists below a critical temperature T_c [65], at finite temperatures phase

fluctuations in the field operator may destroy the long-range order in one-dimensional [147] and two-dimensional [148] Bose gases, giving rise to quasicondensate phases. However, at $T = 0$ the fluctuations can be neglected and true condensation is also possible in weakly-interacting low-dimensional systems [65]. When this occurs, under certain conditions it is possible to obtain lower-dimensional versions of the three-dimensional GPE (2.8). Here, we discuss the derivation of the two-dimensional GPE, which is the main theoretical tool that we will use in Chapter 3.

We consider a Bose gas at $T = 0$ with a uniform density in the $x - y$ plane and confined in the z direction by a harmonic potential $V(z) = m\omega_z^2 z^2/2$, which has an associated length scale $a_z = \sqrt{\hbar/m\omega_z}$. The condensate wave function can be written as

$$\Psi(z) = \frac{\sqrt{n_2} f(z')}{\sqrt{a_z}}, \tag{2.18}$$

where $z' = z/a_z$ and $n_2 = \int dz |\Psi(z)|^2 = N/S$, with N and S being respectively the total number of atoms and the surface that the gas occupies in the $x - y$ plane. Introducing the Ansatz (2.18) into the time-independent GPE (2.11), we obtain an equation for $f(z')$

$$\left(-\frac{1}{2}\frac{\partial^2}{\partial z'^2} + \frac{1}{2}z'^2 + 4\pi a_z a_S n_2 f(z')^2 \right) f(z') = \frac{\mu}{\hbar\omega_z} f(z'). \tag{2.19}$$

In the $a_z a_S n_2 \ll 1$ limit, we can neglect the interaction term and approximate the solution of Eq. (2.19) by the ground state of the axial harmonic potential, $f(z') = (1/\pi^{1/4})e^{-z^2/2a_z^2}$, which fulfills the normalization condition $\int dz' |f(z')| = 1$. Since the BEC is tightly confined along the z direction, the mean interatomic distance becomes $d = 1/\sqrt{n_2}$. As a consequence of this, the ξ/d ratio turns out to be $\xi/d \propto \sqrt{a_z/a_S}$. In contrast with the three dimensional case, where this ratio scales as $\xi/d \propto (na_S)^{-1/6}$, in this two-dimensional scenario the quantity ξ/d is independent of the density. Thus, the mean-field approach is justified as long as the condition $a_S \ll a_z$ is fulfilled.

By treating the interaction term in Eq. (2.19) as a perturbation, we find that the chemical potential of the system is given by

$$\mu = \frac{\hbar\omega_z}{2} + g_{2D}n_2, \tag{2.20}$$

where we have defined the two-dimensional interaction parameter

$$g_{2D} = \sqrt{8\pi}\frac{\hbar^2}{2m}\frac{a_S}{a_z}. \tag{2.21}$$

If we now introduce a shallow potential $V(x, y)$ such that the trapping frequencies along the x and y directions are much lower than along z and the conditions $a_S a_z n_2 \ll 1$ and

$a_S \ll a_z$ are satisfied, we can factorize the condensate wave function as

$$\Psi(\vec{r}) = \frac{f(z')}{\sqrt{a_z}}\psi(x,y) = \frac{e^{-z^2/2a_z^2}}{\pi^{1/4}\sqrt{a_z}}\psi(x,y). \tag{2.22}$$

By inserting Eq. (2.22) into Eq. (2.11) and integrating over the z coordinate, we obtain the time-independent two-dimensional GPE

$$\left[-\frac{\hbar^2\nabla^2}{2m} + V(x,y) + g_{2D}|\psi(x,y)|^2\right]\psi(x,y) = \mu'\psi(x,y), \tag{2.23}$$

where we have defined the two-dimensional chemical potential $\mu' \equiv \mu - \hbar\omega_z/2$.

2.2 Ultracold atoms in optical lattices

In this section, we describe some of the basic aspects of the physics of ultracold atoms in optical lattices and their treatment with the Bose–Hubbard (BH) model. First, we review the physics of a single particle in a one-dimensional periodic potential, as the one created by two counter-propagating laser beams to form an optical lattice. Then, we derive the single-band BH model, which describes a system of many interacting cold bosons in an optical lattice, and we discuss its main phases. Finally, we briefly explain how to address two practical examples of calculations using the BH model: the exact diagonalization of the Hamiltonian and the calculation of the single-particle energy bands in the tight-binding regime.

2.2.1 Single-particle properties

We start by considering the problem of a single particle of mass m in a periodic potential. For simplicity, we assume that the lattice is one-dimensional, but the generalization to higher dimensions can be done in a straightforward manner. This system is described by the Hamiltonian

$$H_0 = -\frac{\hbar}{2m}\frac{\partial}{\partial x} + V(x), \tag{2.24}$$

where the potential has the form $V(x) = V(x+d)$ with d being the periodicity of the lattice. As it is well known from solid state physics [149], Bloch's theorem states that the eigenstates of the Hamiltonian (2.24) are of the form

$$\Psi_k^n(x) = e^{ikx}u_k^n(x); \tag{2.25}$$
$$H_0\Psi_k^n(x) = E_k^n\Psi_k^n(x), \tag{2.26}$$

where $u_k^n(x) = u_k^n(x+d)$ is a function with the same periodicity as the lattice, k is a quantum number known as the quasimomentum and n is an integer labelling the energy levels. The Bloch waves (2.26) are spatially delocalized eigenstates that can be interpreted as plane waves modulated by the potential of the lattice through the function $u_k^n(x)$. These states fulfill the orthonormality relation

$$\int \Psi_{k'}^{n'*}(x)\Psi_k^n(x)dx = \delta_{n'n}\delta_{k'k}. \tag{2.27}$$

As a consequence of Bloch's theorem, the Bloch waves $\Psi_k^n(x)$ also have the periodicity of the lattice, $\Psi_k^n(x) = \Psi_k^n(x+d)$, and the relevant values of the quasimomentum are restricted to the first Brillouin zone, $k \in (-\pi/d, \pi/d]$. Therefore, for each value of n the energies form a band as a function of the quasimomentum k, the values of which are restricted to the first Brillouin zone. Typically, these bands are separated by energy gaps.

Bloch waves do not constitute the only possible basis for addressing the physics of periodic potentials. A particularly useful alternative is provided by the Wannier functions, which can be constructed by superposing Bloch waves according to the relation

$$w_n(x - x_i) = \frac{1}{\sqrt{M}} \sum_k e^{-ikx_i}\Psi_k^n(x), \tag{2.28}$$

where the sum runs over the first Brillouin zone and M is the number of minima of the potential, i.e., of lattice sites. These functions are exponentially localized around the minima of the potential x_i and fulfill the orthonormality relation

$$\int w_{n'}^*(x - x_{i'})w_n(x - x_i)dx = \delta_{n'n}\delta_{i'i}. \tag{2.29}$$

The general formalism presented so far can be applied to optical lattices, which are periodic distributions of light created by the interference of counter-propagating laser beams that can be used to trap cold atoms through the dipole force of light [29, 30]. In one dimension, the effective potential that the atom sees has the form

$$V(x) = V_0 \sin^2(k_L x), \tag{2.30}$$

where V_0 is the lattice depth and $k_L = 2\pi/\lambda$ is the wave vector of the laser, which defines a natural energy scale $E_R = \hbar^2 k_L^2/2m$. In Fig. 2.1 we show the band structure associated with the potential (2.30) for different values of the ratio V_0/E_R. In the free particle limit, $V_0 = 0$, the band structure is gapless and corresponds to a quadratic dispersion folded into the first Brillouin zone. Increasing the lattice depth V_0 has the effect of flattening the bands and widening the gaps between them. This behaviour, which is more pronounced for the lower part of the spectrum, can be understood by

considering the deep lattice limit $V_0 \gg E_R$. In this regime, the potential (2.30) can be locally approximated by a harmonic trap

$$V_0 \sin^2(k_L(x - x_i)) \approx V_0 k_L^2 (x - x_i)^2 = \frac{m\omega_{\text{o.l.}}^2 (x - x_i)^2}{2}, \qquad (2.31)$$

where we have defined the optical lattice trapping frequency

$$\omega_{\text{o.l.}} \equiv \sqrt{\frac{2 V_0 k_L^2}{m}} = \frac{2\sqrt{V_0 E_R}}{\hbar}. \qquad (2.32)$$

Therefore, in this limit the Wannier functions are harmonic oscillator eigenstates localized at the minima of the potential and the energy spectrum is composed of flat bands of energy $E^n = (1/2 + n)\,\hbar\omega_{\text{o.l.}}$.
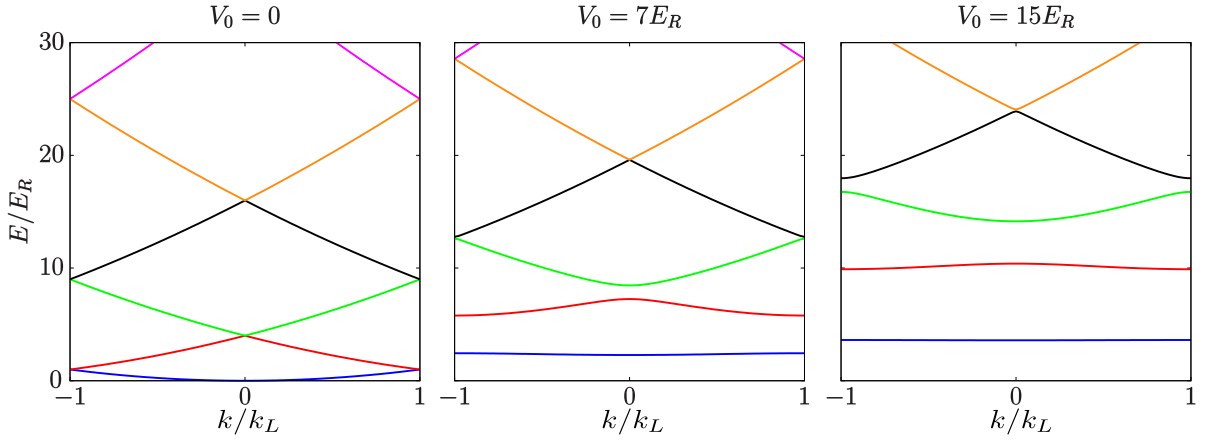
Figure 2.1: Band structure of a one-dimensional optical lattice, described by the potential (2.30), for different values of the lattice depth V_0.

2.2.2 Bose-Hubbard model

After describing the physics of a single ultracold atom in an optical lattice, we are now in a position to consider the many-body scenario. As we discussed in Sec. 2.1, if the atomic gas is sufficiently cold and dilute we can assume that the only relevant interactions are two-body $s-$wave collisions, in such a way that the many-body Hamiltonian of the system can be written as

$$\hat{H} = \int d\vec{r}\, \hat{\Psi}^\dagger(\vec{r}) \left[-\frac{\hbar^2 \nabla^2}{2m} + V(\vec{r}) \right] \hat{\Psi}(\vec{r}) + \frac{g}{2} \int d\vec{r}\, \hat{\Psi}^\dagger(\vec{r}) \hat{\Psi}^\dagger(\vec{r}) \hat{\Psi}(\vec{r}) \hat{\Psi}(\vec{r}), \qquad (2.33)$$

where $V(\vec{r})$ is the generalization to any number of dimensions of the optical lattice potential Eq. (2.30) and g is a parameter proportional to the $s-$wave scattering length

whose exact expression depends on the dimensionality of the problem. The bosonic field operator can be expanded in terms of the Wannier functions as

$$\hat{\Psi} = \sum_n \sum_i w_n(\vec{r} - \vec{r}_i)\hat{a}_i^n, \tag{2.34}$$

where $\hat{a}_i^n$ ($\hat{a}_i^{n\dagger}$) is a bosonic operator associated with the annihilation (creation) of a particle localized at site i and belonging to the nth band. These operators satisfy the commutation relations

$$\left[\hat{a}_{i'}^{n'}, \hat{a}_i^{n\dagger}\right] = \delta_{i'i}\delta_{n'n}, \tag{2.35a}$$

$$\left[\hat{a}_{i'}^{n'}, \hat{a}_i^{n}\right] = \left[\hat{a}_{i'}^{n'\dagger}, \hat{a}_i^{n\dagger}\right] = 0. \tag{2.35b}$$

Assuming that the lattice is sufficiently deep and that the temperature is low enough that interband transitions are suppressed, the operator (2.34) can be restricted to a single energy band. For illustrative purposes, we discuss here the standard BH model, which is obtained by considering that the gas is confined to the lowest band and that the tight-binding approximation is applicable, i.e., that the Wannier functions are localized over a smaller distance than the separation between the lattice sites. Retaining only the terms of the interaction part of the Hamiltonian (2.33) that describe collisions between bosons occupying the same site, one arrives at the BH Hamiltonian

$$\hat{H}_{\mathrm{BH}} = -\sum_{i,i'} J_{i,i'}\left(\hat{a}_{i'}^{\dagger}\hat{a}_i + \hat{a}_i^{\dagger}\hat{a}_{i'}\right) + \frac{1}{2}\sum_i U_i \hat{n}_i(\hat{n}_i - 1) - \sum_i \mu_i \hat{n}_i, \tag{2.36}$$

where we have dropped for simplicity the band index from the lowest-band bosonic operators at site i and we have defined the bosonic number operator $\hat{n}_i = \hat{a}_i^{\dagger}\hat{a}_i$. For fermionic atoms, an equivalent Hubbard model could be formulated [30] by taking into account that the corresponding creation and annihilation operators fulfill anti-commutation relations instead of the commutation relations (2.35). In this case, many-body configurations with more than one atom in the same internal state and in the same site are forbidden due to the Pauli principle.

The first term of Eq. (2.36) describes the single particle hopping between sites i and i'. The second one accounts for the on-site interactions between bosons occupying the same site, yielding an energy U_i for each pair of bosons on every site i. Finally, the third term accounts for the chemical potential, which is the necessary energy to remove one boson from the lattice. The amplitudes of these terms appearing in Eq. (2.36) can be

computed in terms of the lowest-band Wannier functions $w(\vec{r} - \vec{r}_i)$ as

$$J_{i,i'} = \int w^*(\vec{r} - \vec{r}_i) \left[-\frac{\hbar^2 \nabla^2}{2m} + V(\vec{r}) \right] w(\vec{r} - \vec{r}_{i'}) d\vec{r}, \tag{2.37}$$

$$\mu_i = \int w^*(\vec{r} - \vec{r}_i) \left[-\frac{\hbar^2 \nabla^2}{2m} + V(\vec{r}) \right] w(\vec{r} - \vec{r}_i) d\vec{r}, \tag{2.38}$$

$$U_i = g \int |w(\vec{r} - \vec{r}_i)|^4 \, d\vec{r}. \tag{2.39}$$

Considering that all sites are equivalent and that, due to the exponential decay of the Wannier functions, the tunneling processes are restricted to nearest neighbours, the BH model is reduced to the simpler form

$$\hat{H}_{\mathrm{BH}} = -J \sum_{\langle i,i' \rangle} \left(\hat{a}_{i'}^\dagger \hat{a}_i + \hat{a}_i^\dagger \hat{a}_{i'} \right) + \frac{U}{2} \sum_i \hat{n}_i(\hat{n}_i - 1) - \mu \sum_i \hat{n}_i, \tag{2.40}$$

where the notation $\langle i, i' \rangle$ indicates that the sum runs over nearest-neighbouring sites. We note that the total number of particles is conserved under the action of the BH Hamiltonian, as can be checked by computing the commutator with the sum of the particle number operators

$$[\hat{H}_{\mathrm{BH}}, \sum_i \hat{n}_i] = 0. \tag{2.41}$$

2.2.3   Superfluid and Mott Insulator phases

A cold bosonic gas in an optical lattice described by the BH model (2.40) can be in two distinct phases depending on the ratio between the interaction strength U and the tunneling rate J [33, 34]. These phases can be intuitively understood by considering the extreme limits $U/J = 0, \infty$ in a one-dimensional lattice with M sites and filled with N bosons, in such a way that $r = N/M$ is an integer number. On the one hand, in the non-interacting limit, $U/J = 0$, the bosons can hop freely and are thus delocalized over the entire lattice. Therefore, the ground state of the system consists of a superfluid many-body coherent state in which all the bosons occupy a single particle state equally distributed through all sites

$$|\Psi\rangle_{SF} = \left(\frac{1}{\sqrt{M!}} \sum_{i=1}^{M} \hat{a}_i^\dagger \right)^N |0\rangle, \tag{2.42}$$

where $|0\rangle$ stands for the vacuum state. In the superfluid state, the occupation numbers of the different sites follow a Poissonian distribution. On the other hand, in the strongly interacting limit, $U/J = \infty$, the tunneling processes are completely suppressed. Since each pair of bosons on every site of the lattice yields an interaction energy U, the energy

of the system is minimized by reducing as much as possible the number of bosons on every site. Therefore, the many-body ground state, which is known as the Mott insulator state, consists of all sites being equally occupied by r bosons

$$|\Psi\rangle_{MI} = \prod_{i=1}^{M} \frac{1}{\sqrt{r!}} (\hat{a}_i^\dagger)^r |0\rangle . \tag{2.43}$$

In this phase, the coherence is completely lost and the occupation number becomes a precisely defined quantity. Thus, the Mott insulator state can be regarded as a localized state in real space, whereas the superfluid state is composed of a single Bloch function and is therefore completely localized in momentum space.

The phase diagram of the BH model for a fixed value of U as a function of J and μ has a characteristic form of Mott lobes which have higher mean occupation numbers as μ is increased [30]. The phase transition between the Mott insulator and superfluid phases was probed by varying the lattice depth [32], in such a way that the regimes $U \ll J$ and $U \gg J$ could be realized by implementing a shallow and a deep lattice, respectively.

2.2.4   Fock basis and matrix representation

In order to deal with practical calculations of eigenstates and eigenenergies in the context of the BH model, it is necessary to fix a basis that describes all the possible many-body configurations of bosons in the different modes of the optical lattice (here, we adopt a broad definition of mode that does not necessarily refer to physical sites of the lattice, but can also include internal or external degrees of freedom that yield generalized BH models). A convenient choice is to work in the Fock representation, which is defined as the basis of eigenstates of the number operators associated with each mode. Thus, the Fock states are labelled by the occupation of each of the single-particle modes in the total many-body configuration of the optical lattice, $|n_1, n_2, ..., n_i, ..., n_M\rangle$, and can be constructed by operating over the vacuum state as

$$|n_1, n_2, ..., n_i, ..., n_M\rangle = \prod_{j=1}^{M} \frac{(a_j^\dagger)^{n_j}}{\sqrt{n_j!}} |0\rangle , \tag{2.44}$$

where M is the total number of modes of the lattice. The sum of the populations of all the modes is the total number of bosons, $\sum_{i=1}^{M} n_i = N$. The total number of Fock states is given by the size of the Hilbert space

$$D(N, M) = \binom{M + N - 1}{N} = \frac{(N + M - 1)!}{N!(M - 1)!}. \tag{2.45}$$

By associating a label l to each Fock state, $|l\rangle \equiv |n_1, ..., n_M\rangle$, we can construct a general many-body state as a weighted sum of all the Fock states

$$|\Psi\rangle = \sum_{l=1}^{D} c_l |l\rangle. \tag{2.46}$$

Taking into account that the bosonic creation and destruction operators associated with each mode act over the Fock states as

$$\hat{a}_i^\dagger |n_1, ..., n_i, ..., n_M\rangle = \sqrt{n_i + 1} |n_1, ..., n_i + 1, ..., n_M\rangle, \tag{2.47a}$$

$$\hat{a}_i |n_1, ..., n_i, ..., n_M\rangle = \sqrt{n_i} |n_1, ..., n_i - 1, ..., n_M\rangle, \tag{2.47b}$$

and that the Fock states fulfill the orthonormality condition

$$\langle n_1', ..., n_M' |n_1, ..., n_M\rangle = \prod_{j=1}^{M} \delta_{n_j' n_j} \Rightarrow \langle l' |l\rangle = \delta_{ll'}, \tag{2.48}$$

we can use the Fock basis to compute the matrix elements of the BH Hamiltonian,

$$H_{\text{BH}}^{ll'} = \left\langle l' \left| \hat{H}_{\text{BH}} \right| l \right\rangle = \left\langle n_1', ..., n_M' \left| \hat{H}_{\text{BH}} \right| n_1, ..., n_M \right\rangle. \tag{2.49}$$

In this thesis, we will find the eigenstates and energies of the different BH models that we will consider by diagonalizing exactly their associated matrices [150]. This approach gives access to all the properties of the system, but it is limited by the rapid growth of the Hilbert space size (2.45) with the total number of particles and modes. If we would be interested in dealing with systems of large sizes, it would be more convenient to use reduced Hilbert space methods based on matrix product state representations of the many-body states [151].

2.2.5   Band structure in the tight-binding approximation

The BH model can be used to compute the single-particle spectrum by considering a lattice with periodic boundary conditions. In this situation, it is possible to express the bosonic creation and annihilation operators in terms of their Fourier components

$$\hat{a}_j^\dagger = \frac{1}{\sqrt{N_c}} \sqrt{\frac{d}{2\pi}} \int_{BZ} \hat{a}_k^\dagger e^{ikx_j} dk, \tag{2.50}$$

$$\hat{a}_j = \frac{1}{\sqrt{N_c}} \sqrt{\frac{d}{2\pi}} \int_{BZ} \hat{a}_k e^{-ikx_j} dk, \tag{2.51}$$

where $N_c \to \infty$ is the number of unit cells, d is the lattice spacing, $x_j = jd$ is the position on the lattice of the jth site, and the BZ subindex indicates that the integrals are

restricted to the first Brillouin zone, $k \in (-\pi/d, \pi/d]$. For simplicity, we have considered a one-dimensional system, but Eqs. (2.50) and (2.51) can be readily generalized to higher dimensions. Inserting these expansions into the BH Hamiltonian, one can obtain the energy spectrum in quasimomentum space, which forms the tight-binding equivalent of the band structure.

To illustrate the procedure, we consider the non-interacting BH Hamiltonian describing a uniform one-dimensional lattice, which is given by Eq. (2.36) for $U, \mu = 0$. In this case, the number of unit cells N_c coincides with the number of lattices sites M, so using the expansions (2.50) and (2.51) we can write

$$
\begin{aligned}
\hat{H}_{\mathrm{BH}} &= -J \sum_{j=1}^{M} \hat{a}_j^\dagger \hat{a}_{j+1} + \hat{a}_j^\dagger \hat{a}_{j+1} \\
&= -J \sum_{j=1}^{M} \frac{d}{2\pi M} \int_{\mathrm{BZ}} \int_{\mathrm{BZ}} dk\,dk'\, \hat{a}_k^\dagger \hat{a}_{k'} \left(e^{ikx_j} e^{-ik'(x_j+d)} + e^{-ikx_j} e^{ik'(x_j+d)} \right) \\
&= -\sum_{j=1}^{M} \frac{J}{M} \int_{\mathrm{BZ}} \hat{a}_k^\dagger dk \frac{d}{2\pi} \int_{\mathrm{BZ}} dk' \hat{a}_{k'} \left(e^{ix_j(k-k')} e^{-ik'd} + e^{-ix_j(k-k')} e^{ik'd} \right) \\
&= -\sum_{j=1}^{M} \frac{J}{M} \int_{\mathrm{BZ}} dk \hat{a}_k^\dagger \int_{\mathrm{BZ}} dk' \hat{a}_{k'} \delta(k-k') \left(e^{-ik'd} + e^{ik'd} \right) \\
&= -\sum_{j=1}^{M} \frac{J}{M} \int_{\mathrm{BZ}} dk \hat{a}_k^\dagger \hat{a}_k \left(e^{-ikd} + e^{ikd} \right) = -2J \int_{\mathrm{BZ}} dk \hat{a}_k^\dagger \hat{a}_k \cos(kd) dk. \quad (2.52)
\end{aligned}
$$

Therefore, in the tight-binding approximation the single-particle spectrum is composed of a single energy band $E(k) = -2J\cos(kd)$. Although we have assumed periodic boundary conditions in order to carry out the calculation, this dispersion relation also fits the bulk spectrum of a system with open boundaries. In more sophisticated lattices, such as the one- and two-dimensional ones that we will consider in Chapter 4 and Chapters 6 and 7 respectively, there are as many energy bands in the spectrum as modes per unit cell. In those cases, the Hamiltonian in quasimomentum space can be written in terms of a $k-$ dependent matrix, the eigenvalues of which are the energy bands.

2.3 Topology in discrete systems

In this section, we introduce the general formalism used for the description of topological insulators. We start by discussing the Berry phase, which is a geometrical phase acquired in the adiabatic motion of a particle in a closed circuit in parameter space.

Then, we show how this phase can be used to define topological invariants in lattice models with gapped spectra. As a first specific example of this connection, we define the Chern number and we show how it can be used to explain the integer quantum Hall effect. Finally, we introduce the Zak's phase, which is the one-dimensional version of the Berry phase, and we illustrate its use with the topological characterization of the Su-Schrieffer-Heeger (SSH) model.

2.3.1   Geometrical phase in the adiabatic motion of a particle

Quantum states are always defined up to a global phase. In most cases, this factor has no effect in the computation of observables and therefore plays no physical role. However, as shown by Berry in a seminal paper [152], when the Hamiltonian depends on some adiabatically varying parameters its eigenstates might acquire a geometrical phase, the so-called Berry phase, which has a deep physical meaning. In particular, as we show in this section, the Berry phase has a direct connection with the topological properties of the system [153].

Let us consider a Hamiltonian $H(\mathbf{R})$ that depends on a set of parameters $\mathbf{R} = (R_1, ..., R_n)$ that vary with time, $\mathbf{R} = \mathbf{R}(t)$. We denote by $|n(\mathbf{R})\rangle$ the eigenstates of $H(\mathbf{R})$ at a given time t

$$H(\mathbf{R}) |n(\mathbf{R})\rangle = E_n(\mathbf{R}) |n(\mathbf{R})\rangle . \tag{2.53}$$

Now we consider the time evolution of the state $|n(\mathbf{R})\rangle$ in the interval $t \in (0, T]$. The adiabatic theorem states that if the energy spectrum of the Hamiltonian remains gapped around $E_n(\mathbf{R})$ along the time evolution, i.e., if

$$|E_n(\mathbf{R}) - E_{n\pm1}(\mathbf{R})| > 0 \quad \forall \mathbf{R}(t), \tag{2.54}$$

and the variation of the parameters is slow compared to the frequencies associated with the energy gaps, then the time-evolved state remains an instantaneous eigenstate of $\hat{H}(\mathbf{R})$, picking only a phase factor

$$|\psi(t)\rangle = e^{-i\hbar \int_0^t dt' E_n(\mathbf{R}(t'))} e^{i\varphi_n(t)} |n(\mathbf{R}(t))\rangle . \tag{2.55}$$

The first exponential in Eq. (2.55) is the usual dynamical phase factor that appears in the time evolution of any eigenstate. Inserting Eq. (2.55) into the Schrödinger equation, projecting it into the eigenstate $|n(\mathbf{R})\rangle$ and using the chain-rule relation $\frac{d}{dt} |n(\mathbf{R}(t))\rangle = \frac{d\mathbf{R}(t)}{dt} \frac{\partial}{\partial R} |n(\mathbf{R})\rangle$, we find the following expression for the phase appearing in the second exponential

$$\varphi_n = \int_C \mathcal{A}_n(\mathbf{R}) \cdot d\mathbf{R}, \tag{2.56}$$

where C denotes the contour that $\mathbf{R}(t)$ follows in parameter space and we have defined the Berry connection as

$$\mathcal{A}_n(\mathbf{R}) = i \left\langle n(\mathbf{R}) \left| \frac{\partial}{\partial R} \right| n(\mathbf{R}) \right\rangle. \tag{2.57}$$

The Berry connection is not a gauge-invariant quantity, as can be seen by applying the gauge transformation

$$|n(\mathbf{R})\rangle \rightarrow e^{if(\mathbf{R})} |n(\mathbf{R})\rangle$$

$$\mathcal{A}_n(\mathbf{R}) \rightarrow \mathcal{A}_n(\mathbf{R}) - \frac{\partial}{\partial \mathbf{R}} f(\mathbf{R}). \tag{2.58}$$

Thus, one can always find a gauge transformation that cancels the phase φ_n for an arbitrary contour with open ends. However, if one considers a contour consisting of a closed loop in parameter space, i.e., such that $\mathbf{R}(0) = \mathbf{R}(T)$, then the fact that the eigenstate $|n(\mathbf{R})\rangle$ must be single-valued imposes the following condition on the gauge transformation

$$f(\mathbf{R}(0)) - f(\mathbf{R}(T)) = 2\pi q, \tag{2.59}$$

where q is an integer. Therefore, in this situation φ_n becomes a gauge-invariant quantity known as the Berry phase or geometrical phase

$$\gamma_n = \oint_C \mathcal{A}_n(\mathbf{R}) \cdot d\mathbf{R}. \tag{2.60}$$

Applying Stokes' theorem in Eq. (2.60), we can also compute the Berry phase as

$$\gamma_n = \oiint_C \Omega_n \cdot d\mathbf{S}, \tag{2.61}$$

where the integral is performed over any surface enclosed by the closed loop C and we have defined the Berry curvature

$$\Omega_n = \nabla_{\mathbf{R}} \times \mathcal{A}_n, \tag{2.62}$$

which is a gauge-invariant quantity.

The above defined quantities can be understood intuitively by making an analogy with classical electrodynamics. According to Eqs. (2.57)-(2.62), the Berry connection and Berry curvature can be regarded respectively as a 'magnetic field' and 'vector potential' in $\mathbf{R}$−space, and both of them can be used to compute a parameter-space 'magnetic flux', which corresponds to the Berry phase. In fact, the Berry phase can be directly related to the Aharonov-Bohm effect [154], which consists in the acquisition of a phase by a charged particle after completing a closed loop around a region in space threaded by a magnetic flux.

2.3.2   Berry phase and topological invariants

We now consider the Berry phase associated with the motion of a single particle in a lattice. According to Bloch's theorem, the eigenstates of a periodic Hamiltonian can be written as

$$\Psi_{\vec{k}}^n(\vec{r}) = e^{i\vec{k}\cdot\vec{r}} u_{\vec{k}}^n(\vec{r}), \tag{2.63}$$

where the quasimomentum $\vec{k}$ is defined in the first Brillouin zone and the Bloch function $u_{\vec{k}}^n(\vec{r})$ has the same periodicity as the lattice, $u_{\vec{k}}^n(\vec{r}) = u_{\vec{k}}^n(\vec{r} + \vec{d})$, with $\vec{d}$ being the Bravais lattice vector. Inserting the Ansatz (2.63) into the time-independent Schrödinger equation, it can be readily seen that $u_{\vec{k}}^n(\vec{r})$ fulfills the eigenvalue equation

$$H(\vec{k})u_{\vec{k}}^n(\vec{r}) = \left[\frac{(\vec{p} + \vec{k})^2}{2m} + V(\vec{r})\right] u_{\vec{k}}^n(\vec{r}) = E_n(\vec{k})u_{\vec{k}}^n(\vec{r}) \tag{2.64}$$

where $V(\vec{r}) = V(\vec{r} + \vec{d})$ is the lattice potential and we have used the real-space expression of the momentum operator $\vec{p} = -i\hbar\nabla$. Thus, in the context of the Berry phase formalism, we can identify the components of the quasimomentum as the set of adiabatic parameters $\mathbf{R}$ controlling the Hamiltonian $H(\vec{k})$ that describes the system. The basis eigenstates of $H(\vec{k})$, which we denote as $u_{\vec{k}}^n(\vec{r})$ in position representation and as $\left|u_n(\vec{k})\right\rangle$ in ket notation, form energy bands $E_n(\vec{k})$ which have associated Berry phases

$$\gamma_n = i \int_{BZ} \left\langle u_n(\vec{k}) \left|\nabla_{\vec{k}}\right| u_n(\vec{k}) \right\rangle \cdot d\vec{k}, \tag{2.65}$$

where the subindex BZ indicates that the integral is evaluated over a closed loop in the first Brillouin zone. We note that, in order for the expression (2.65) to be applicable, $E_n(\vec{k})$ must be gapped for each value of $\vec{k}$.

Chern number and integer quantum Hall effect

In two-dimensional lattice models, the Berry phase is proportional to the Chern number. This quantity, which is defined as

$$C_n \equiv \frac{1}{2\pi i} \oiint_{BZ} \Omega_n(\vec{k}) \cdot d\vec{k} = \frac{1}{2\pi i} \int_{BZ} d^2k \left[\left\langle \frac{\partial u_{\vec{k}}^n}{\partial k_x} \middle| \frac{\partial u_{\vec{k}}^n}{\partial k_y} \right\rangle - \left\langle \frac{\partial u_{\vec{k}}^n}{\partial k_y} \middle| \frac{\partial u_{\vec{k}}^n}{\partial k_x} \right\rangle\right], \tag{2.66}$$

with $\Omega_n(\vec{k})$ given in Eq. (2.62), is an integer topological invariant of the band n, i.e., it preserves its value under continuous deformations of the band as long as the gap is kept open [152]. In the celebrated TKNN paper [70], Thouless, Kohmoto, Nightingale and den Nijs used the Kubo formula to show that, when a two-dimensional system is at

zero temperature and the Fermi energy lies in an energy gap, the Hall conductance σ_{xy} is related to the Chern number according to the expression

$$\sigma_{xy} = \frac{e^2}{h} \sum_{n \in \text{occ.}} C_n, \tag{2.67}$$

where e is the elementary charge and the sum runs over the occupied bands. In the TKNN paper, this general expression was applied to a tight-binding model describing spinless fermions in a square lattice in the presence of a magnetic field known as the Harper-Hofstadter model [155, 156]. By doing so, the authors obtained a successful explanation of the Integer Quantum Hall Effect (IQHE). This effect, which consists in the quantization in units of e^2/h of the Hall conductivity, was first observed in a two-dimensional electron gas at low temperatures pierced by a magnetic field [68]. According to Eq. (2.67), every time that the Fermi energy crosses an energy band, the Hall conductivity varies in quantized jumps that can be evaluated by computing the Chern number of each band. Since the Chern number is a topological invariant, this quantization of the Hall conductivity is robust against any perturbation that does not close the band gaps. In a finite system, the Hall current is transported through chiral edge states protected by the non-trivial topology of the bulk bands. This is a manifestation of a phenomenon ubiquitous to topological insulators known as the bulk-boundary correspondence [152], which consists in the apparition of gapless states protected by some symmetry of the system at the interface between a topological and a trivial insulator (notice that a topological insulator with open boundaries can be regarded as being in contact with the vaccuum, which is a trivial insulator).

Zak's phase

The Berry phase in one-dimensional lattices, also called Zak's phase after the author of the paper where it was first considered [157], is given by

$$\gamma_n = i \int_{-\frac{\pi}{d}}^{\frac{\pi}{d}} dk \left\langle u_n(k) \left| \frac{d}{dk} \right| u_n(k) \right\rangle, \tag{2.68}$$

where d is the lattice spacing. In his seminal work [157], Zak showed that, in systems with inversion symmetry, the Zak's phase of a given band is restricted to the values $\gamma_n = 0, \pi \pmod{2\pi}$, and it can only be changed by a variation of the parameters governing the Hamiltonian capable of closing the energy gap surrounding the band and opening it again. Therefore, the Zak's phase (2.68) can be used to characterize the topology of the bands of inversion-symmetric one-dimensional lattice models. The total Zak's phase of a model describing a one-dimensional insulator is given by the sum of

the phases of the occupied bands,

$$\gamma = \sum_{n \in \text{occ.}} \gamma_n, \tag{2.69}$$

and it is said to be trivial (non-trivial) if it takes the value $\gamma = 0(\pi)$. According to the bulk-boundary correspondence, a non-trivial value of the Zak's phase in a periodic (or infinite) system predicts the apparition of topologically protected edge states for a system described by the same Hamiltonian but with open boundaries. Furthermore, the Zak's phase is related to macroscopic properties of the system such as, for instance, the bulk polarization [158, 159]. In order to explain this connection, we consider the Bloch eigenstates of the different bands of an insulator

$$|\Psi_n(k)\rangle = |k\rangle \otimes |u_n(k)\rangle = e^{-i\alpha(k)} \frac{1}{\sqrt{M}} \sum_{j=1}^{M} e^{ix_j k} |j\rangle \otimes |u_n(k)\rangle, \tag{2.70}$$

where M is the total number of sites, $x_j = jd$ is the position of the site j and $\alpha(k)$ is an arbitrary phase. With them, we can construct Wannier states localized at the different sites of the lattice [160]

$$|w_n(j)\rangle = \sqrt{\frac{d}{2\pi}} \int_{-\frac{\pi}{d}}^{\frac{\pi}{d}} dk\, e^{i\alpha(k)} e^{-ix_j k} |\Psi_n(k)\rangle, \tag{2.71}$$

where the phase $\alpha(k)$ is chosen such that the wave functions are maximally localized. In an electronic system, the center of the Wannier states $\langle w_n(j) | \hat{x} | w_n(j) \rangle$ determines the mean position of the electrons in each unit cell, which is in turn directly related to the polarization. We can compute this quantity using the momentum-space expression for the position operator $\hat{x} = i \frac{\partial}{\partial k}$

$$\langle w_n(j) | \hat{x} | w_n(j) \rangle = d \frac{i}{2\pi} \int_{-\frac{\pi}{d}}^{\frac{\pi}{d}} \left\langle u_n(k) \left| \frac{d}{dk} \right| u_n(k) \right\rangle + dj = d \left(\frac{\gamma_n}{2\pi} + j \right). \tag{2.72}$$

The total bulk polarization P of the system, which is defined as the sum of all the displacements of the Wannier centers from the center of their respective unit cell (i.e. $\langle w_n(j) | \hat{x} | w_n(j) \rangle - dj$), multiplied by the elementary charge e and normalized by the total number of sites N and the cell size d, is proportional to the sum of the Zak's phases of the occupied bands,

$$P = \frac{e}{2\pi} \sum_{n \in \text{occ.}} \gamma_n = \frac{e}{2\pi} \gamma, \tag{2.73}$$

and is therefore quantized to the values $P = 0, e/2$.

An alternative way to Eq. (2.68) for computing the Zak's phase is provided by the Wilson loop [160], which is defined as

$$\mathcal{W}_n = \prod_{j=0}^{M-1} \langle u_n(-\pi + j\Delta k) \,|\, u_n(-\pi + (j+1)\Delta k) \rangle \,, \tag{2.74}$$

where we have set the lattice spacing $d = 1$ and we have defined the momentum-space increment $\Delta k = 2\pi/M$. In the limit of a large number of sites, $M \to \infty$ and $\Delta k \to 0$, each element of the Wilson loop becomes $\langle u_n(-\pi + j\Delta k) \,|\, u_n(-\pi + (j+1)\Delta k) \rangle = e^{i\phi_j}$, with ϕ_j being an infinitesimal phase. The Zak's phase can then be computed as the argument of the Wilson loop

$$\gamma_n = \mathrm{Arg} \left(\lim_{M \to \infty} \mathcal{W}_n \right) = \lim_{M \to \infty} \sum_{j=0}^{N} \phi_j. \tag{2.75}$$

Since $\mathcal{W}_n$ is a gauge-independent quantity (i.e., it is invariant under gauge transformations $|u_n(k)\rangle \to e^{if(k)} |u_n(k)\rangle$), Eq. (2.75) provides an efficient way for computing numerically the Zak's phase of a given band. In contrast, Eq. (2.68) involves the gauge-dependent Berry connection $i \langle u_n(k) \,\big|\, \frac{d}{dk} \,\big|\, u_n(k)\rangle$, and is therefore less useful for practical calculations.

2.3.3 The Su-Schrieffer-Heeger model

In order to illustrate some of the concepts previously introduced in this section, we consider the simplest 1D model of a topological insulator, which is the one introduced by Su, Schrieffer and Heeger (SSH) [161] to explain the formation of solitons in the polyacetilene molecule. It is a tight-binding model describing spinless fermions in a chain formed by unit cells with two sites, A and B, that are coupled by intra- and inter-cell hoppings t_1 and t_2, as illustrated in the left part of Fig. 2.2 (a). The Hamiltonian of this model reads

$$\hat{H}_{\mathrm{SSH}} = \sum_{i=1}^{N_c} t_1 \hat{a}_i^\dagger \hat{b}_i + t_2 \hat{b}_i^\dagger \hat{a}_{i+1} + \mathrm{h.c.}, \tag{2.76}$$

where N_c is the total number of unit cells of the chain, and $\hat{a}_i^\dagger$ and $\hat{b}_i^\dagger$ are the operators associated with the creation of a particle at the site A and B of the ith unit cell, respectively. In addition to inversion symmetry, this model possesses also chiral symmetry, i.e., it can be formulated in terms of two chains, formed respectively by the A and B sites, that do not have any internal coupling. This symmetry ensures that the spectrum is symmetric around zero-energy and is responsible for the topological protection of the edge states [160]. These states can be understood intuitively by considering the fully

dimerized limits, shown in the right part of Fig. 2.2 (a). For $t_1 \neq 0, t_2 = 0$, the chain is composed of N_c isolated dimers, which have two eigenstates of energies $\pm t_1$. However, for $t_1 = 0, t_2 \neq 0$, the chain is instead composed of $N_c - 1$ dimers with eigenenergies $\pm t_2$ in the bulk and two isolated zero-energy states at the edges. As we show here below, these states are indeed topologically protected, and for general values of the couplings fulfilling $t_2/t_1 > 1$, they show up in the spectrum as zero-energy states that are exponentially localized.
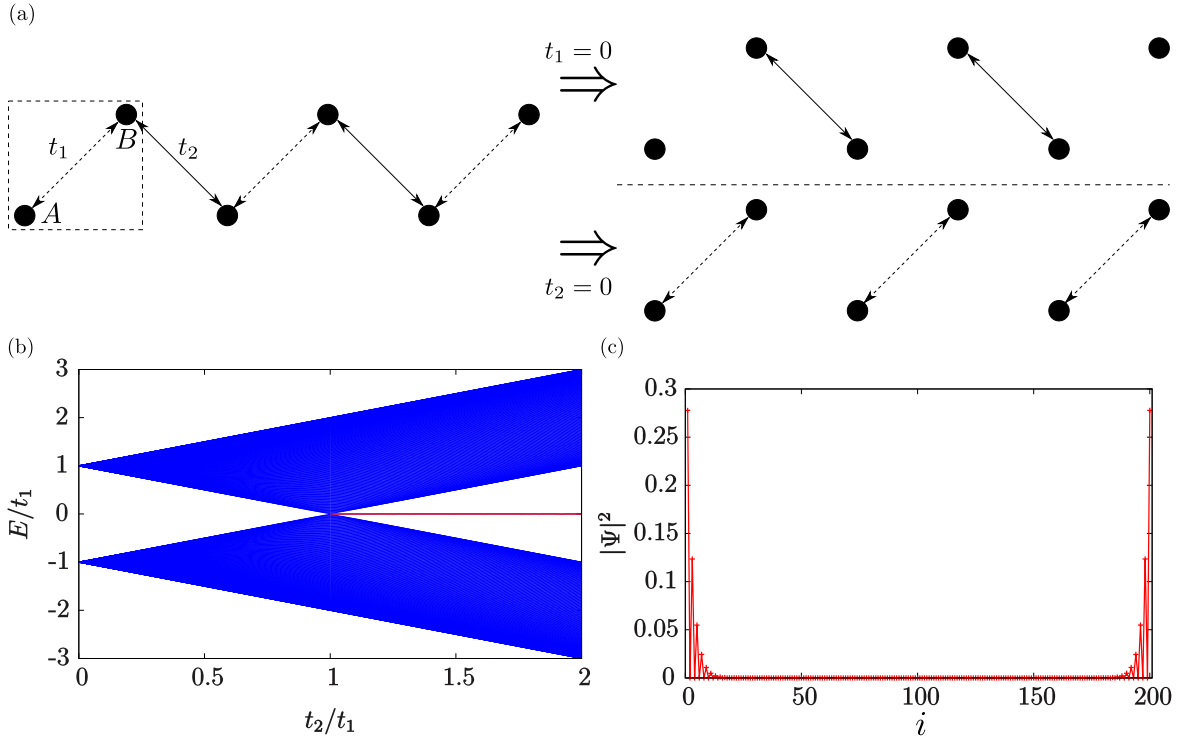
Figure 2.2: (a) Sketch of the SSH model described by Eq. (2.76), with the unit cell marked with a dashed box. The fully dimerized limits $t_1 = 0$, $t_2 = 0$, which correspond respectively to the topological and trivial phase, are also illustrated. (b) Spectrum of an open SSH chain formed by $N_c = 200$ unit cells as a function of the ratio t_2/t_1. The topological edge states, which appear for $t_2 > t_1$ after the gap closing point $t_1 = t_2$, are marked with red lines. (c) Density distribution of a zero-energy edge state corresponding to a chain with $N_c = 100$ unit cells and couplings $t_2/t_1 = 1.5$.

In order to perform the topological characterization of the model, we write the momentum-space version of the Hamiltonian (2.76) by Fourier-transforming the creation and annihilation operators

$$\hat{H}_{\text{SSH}} = \oint_{BZ} \hat{\boldsymbol{\Psi}}_k^\dagger H_k \hat{\boldsymbol{\Psi}}_k dk, \tag{2.77}$$

where we have defined $\hat{\mathbf{\Psi}}^\dagger = (\hat{a}_k^\dagger, \hat{b}_k^\dagger)$ and the k-space Hamiltonian

$$H_k = \begin{pmatrix} 0 & t_1 + t_2 e^{-ik} \\ t_1 + t_2 e^{ik} & 0 \end{pmatrix}. \tag{2.78}$$

The chiral symmetry of the system is manifested in momentum space by the fact that the $k-$space Hamiltonian fulfills the condition $\Gamma H_k \Gamma = -H_k$, with $\Gamma = \mathrm{diag}\{1, -1\}$. Diagonalizing the matrix (2.78) we obtain the basis eigenstates and their corresponding energy bands, which read

$$|u_1(k)\rangle = \frac{1}{\sqrt{2}} \left(\frac{\sqrt{t_1^2 + t_2^2 + 2t_1 t_2 \cos k}}{t_1 + t_2 e^{ik}} |a(k)\rangle - |b(k)\rangle \right); \quad E_1(k) = -\sqrt{t_1^2 + t_2^2 + 2t_1 t_2 \cos k}$$
$$\tag{2.79}$$

$$|u_2(k)\rangle = \frac{1}{\sqrt{2}} \left(\frac{\sqrt{t_1^2 + t_2^2 + 2t_1 t_2 \cos k}}{t_1 + t_2 e^{ik}} |a(k)\rangle + |b(k)\rangle \right); \quad E_2(k) = \sqrt{t_1^2 + t_2^2 + 2t_1 t_2 \cos k}.$$
$$\tag{2.80}$$

The Zak's phases associated with these bands are $\gamma_1, \gamma_2 = \pi$ for $t_1 < t_2$ and $\gamma_1, \gamma_2 = 0$ for $t_1 > t_2$. Therefore, as shown in Fig. 2.2 (b), the spectrum has no zero-energy edge states for $t_2/t_1 < 1$. However, at the gap closing at $t_2/t_1 = 1$ there is a topological phase transition and for $t_2/t_1 > 1$ edge states (signalled with red lines) appear in the gap between the two bands. In Fig. 2.2 (c) we plot the density profile of one of these edge states for a chain with $N_c = 100$ unit cells and $t_1/t_2 = 1.5$, showing its strong localization at the edges of the chain. In an electronic system, if one would fill the available states in the topological phase until $E = 0$ (i.e., the Fermi energy at $T = 0$), due to the edge states the total charge distribution would have an associated polarization $P = e/2$.

2.4 Ultracold atoms in orbital angular momentum states

In this section, we review the single-particle physics of ultracold atoms carrying Orbital Angular Momentum (OAM) in two-dimensional cylindrically symmetric potentials. We start by addressing the problem of a single atom in a harmonic trap, for which the wave functions of the OAM states can be derived analytically. We then generalize the OAM states to trapping potentials with a ring shape, a geometry that is of great importance for the emerging field of atomtronics [108] and will appear repeatedly throughout the next Chapters. Finally, we analyse the tunneling dynamics of ultracold atoms carrying OAM in systems of side-coupled cylindrically symmetric potentials. We show that this dynamics is characterized by complex hopping amplitudes with phases that can be tuned by modifying the geometry of the system.

2.4.1 Two-dimensional harmonic oscillator

Let us start by considering a single ultracold atom of mass m trapped in a two-dimensional isotropic harmonic potential of radial frequency ω. The time-independent Schrödinger equation for this system reads

$$\hat{H}\ket{\phi} = \left[\frac{\hat{p}_x^2 + \hat{p}_y^2}{2m} + \frac{m\omega^2(\hat{x}^2 + \hat{y}^2)}{2}\right]\ket{\phi} = E\ket{\phi}. \tag{2.81}$$

Noting that the Hamiltonian $\hat{H}$ is separable in the x and y variables, we can solve Eq. (2.81) by defining the usual harmonic oscillator ladder operators [142] in x and y,

$$\hat{a}_x \equiv \frac{1}{\sqrt{2}}\left(\frac{\hat{x}}{\sigma} + \frac{i\sigma\hat{p}_x}{\hbar}\right); \quad \hat{a}_x^\dagger \equiv \frac{1}{\sqrt{2}}\left(\frac{\hat{x}}{\sigma} - \frac{i\sigma\hat{p}_x}{\hbar}\right); \quad [\hat{a}_x, \hat{a}_x^\dagger] = 1, \tag{2.82}$$

and

$$\hat{a}_y \equiv \frac{1}{\sqrt{2}}\left(\frac{\hat{y}}{\sigma} + \frac{i\sigma\hat{p}_y}{\hbar}\right); \quad \hat{a}_y^\dagger \equiv \frac{1}{\sqrt{2}}\left(\frac{\hat{y}}{\sigma} - \frac{i\sigma\hat{p}_y}{\hbar}\right); \quad [\hat{a}_y, \hat{a}_y^\dagger] = 1, \tag{2.83}$$

where we have defined the harmonic oscillator length $\sigma \equiv \sqrt{\hbar/m\omega}$. Since they act over different spaces, all the commutators amongst x and y operators vanish. From Eqs. (2.82) and (2.83), we define a new set of "+" and "−" operators

$$\hat{a}_+ \equiv \frac{1}{\sqrt{2}}\left(\hat{a}_x - i\hat{a}_y\right); \quad \hat{a}_+^\dagger \equiv \frac{1}{\sqrt{2}}\left(\hat{a}_x^\dagger + i\hat{a}_y^\dagger\right); \quad [\hat{a}_+, \hat{a}_+^\dagger] = 1, \tag{2.84}$$

$$\hat{a}_- \equiv \frac{1}{\sqrt{2}}\left(\hat{a}_x + i\hat{a}_y\right); \quad \hat{a}_-^\dagger \equiv \frac{1}{\sqrt{2}}\left(\hat{a}_x^\dagger - i\hat{a}_y^\dagger\right); \quad [\hat{a}_-, \hat{a}_-^\dagger] = 1, \tag{2.85}$$

and their corresponding number operators and associated eigenstates

$$\hat{N}_+ \equiv \hat{a}_+^\dagger\hat{a}_+; \quad \hat{N}_+\ket{n_+} = n_+\ket{n_+}, \tag{2.86}$$
$$\text{since } \hat{a}_+^\dagger\ket{n_+} = \sqrt{n_+ + 1}\ket{n_+ + 1}, \hat{a}_+\ket{n_+} = \sqrt{n_+}\ket{n_+ - 1},$$
$$\hat{N}_- \equiv \hat{a}_-^\dagger\hat{a}_-; \quad \hat{N}_-\ket{n_-} = n_-\ket{n_-}, \tag{2.87}$$
$$\text{since } \hat{a}_-^\dagger\ket{n_-} = \sqrt{n_- + 1}\ket{n_- + 1}, \hat{a}_-\ket{n_-} = \sqrt{n_-}\ket{n_- - 1},$$

where n_+ and n_- are integer numbers [142]. In terms of these operators, the Hamiltonian takes the simple form

$$\hat{H} = \hbar\omega(\hat{a}_+^\dagger\hat{a}_+ + \hat{a}_-^\dagger\hat{a}_- + 1) = \hbar\omega(\hat{N}_+ + \hat{N}_- + 1) \tag{2.88}$$

Thus, the eigenstates of the two-dimensional harmonic oscillator are products of the eigenstates of $\hat{N}_+$ and $\hat{N}_-$

$$\ket{\phi} = \ket{n_+} \otimes \ket{n_-} \equiv \ket{n_+, n_-}; \quad \hat{H}\ket{n_+, n_-} = \hbar\omega(n_+ + n_- + 1)\ket{n_+, n_-}. \tag{2.89}$$

Therefore, the energies associated with the different eigenstates are given by $E = \hbar\omega(n_+ + n_- + 1)$.

In the basis of $+$ and $-$ states, the operator associated with the z component of the angular momentum is also diagonal

$$\hat{L}_z = \hat{x}\hat{p}_y - \hat{y}\hat{p}_x = \hbar(\hat{a}_+^\dagger \hat{a}_+ - \hat{a}_-^\dagger \hat{a}_-) = \hbar(\hat{N}_+ - \hat{N}_-) \tag{2.90}$$

From Eq. (2.90), it is clear that the action of the $\hat{a}_+^\dagger$ operator is to create an excitation with an associated angular momentum $\hbar$, whereas the $\hat{a}_-^\dagger$ operator creates a $-\hbar$ excitation. Therefore, these operators generate states with a well-defined OAM. Such states are characterized by two quantum numbers, namely the total number of excitations $n \equiv n_x + n_y$, which determines the energy of the state, and the difference between the number of $+$ and $-$ excitations $\nu \equiv n_+ - n_-$, which determines the value of the z component of the angular momentum. From these definitions, we see that for a given value of n the possible values of ν are

$$\nu = n, n - 2, n - 4, ..., -n + 4, -n + 2, -n.$$

The ground state wave function can be found by solving in position representation the equations $\hat{a}_+ |0, 0\rangle = 0$, $\hat{a}_- |0, 0\rangle = 0$. By applying to it the $\hat{a}_+^\dagger$ and $\hat{a}_-^\dagger$ operators as many times as needed, the wave function of an eigenstate with a certain value of n and ν can be generated. The wave functions of the three lowest energetic states are given by

$$n = 0, \nu = 0: \quad \langle\vec{r}|n_+ = 0, n_- = 0\rangle = \phi_0^0(r, \varphi) = \frac{1}{\sigma\sqrt{\pi}}e^{-(r^2/2\sigma^2)},$$

$$n = 1, \nu = 1: \quad \langle\vec{r}|n_+ = 1, n_- = 0\rangle = \phi_1^1(r, \varphi) = \frac{r}{\sigma^2\sqrt{\pi}}e^{-(r^2/2\sigma^2)}e^{i\varphi},$$

$$n = 1, \nu = -1: \quad \langle\vec{r}|n_+ = 0, n_- = 1\rangle = \phi_1^{-1}(r, \varphi) = \frac{r}{\sigma^2\sqrt{\pi}}e^{-(r^2/2\sigma^2)}e^{-i\varphi}.$$

These wave functions are eigenstates with eigenvalue $\hbar\nu$ of the $\hat{L}_z$ operator, which in the the polar coordinates (r, φ) is given by $\hat{L}_z = -i\hbar\frac{\partial}{\partial\varphi}$. We point out that the OAM states with $n = 1$ are equivalent to the Wannier states of the $p-$band of an optical lattice in the harmonic approximation [162].

2.4.2   Ring potentials

In general, any cylindrically symmetric potential can support eigenstates with a well-defined OAM. In this thesis, we will consider many physical systems composed of ring potentials, which can be experimentally realized by means a variety of techniques, such

as optically plugged magnetic traps [109], static Laguerre-Gauss Beams [110], painting [111, 112] and time-averaged potentials [113–115, 131, 163] or conical refraction [116].

The time-independent Schrödinger equation for the wave function $\phi(r, \varphi)$ of a single atom of mass m in a ring potential of radius r_0 and radial frequency ω reads

$$\left[-\frac{\hbar \nabla^2}{2m} + \frac{m\omega^2(r - r_0)^2}{2} \right] \phi = E\phi. \tag{2.91}$$

Due to the cylindrical symmetry of the potential $V(r) = \frac{m\omega^2}{2}(r - r_0)^2$, Eq. (2.91) admits solutions which are eigenstates of the $\hat{L}_z$ operator, which take the general form

$$\phi_n^\nu(r, \varphi) = \psi_n^l(r)e^{i\nu\varphi}, \tag{2.92}$$

where $n \in \mathbb{N}^0$ is an index that indicates the number of radial excitations and $\nu = \pm l$ is the winding number. Since the wave function is single-valued, l must be a natural number. Plugging the Ansatz (2.92) into Eq. (2.91), we obtain an equation for the radial part of the wave function $\psi_n^l(r)$

$$-\frac{\hbar}{2m}\left[\frac{d^2\psi_n^l}{dr^2} + \frac{1}{r}\frac{d\psi_n^l}{dr} + \frac{l^2}{r^2}\psi_n^l \right] + \frac{m\omega^2(r - r_0)^2}{2}\psi_n^l = E\psi_n^l \tag{2.93}$$

In this thesis, we will be interested in solutions with no radial excitations and low values of the OAM (typically, we will consider $l = 1$). Since the trapping potential has a harmonic profile around the ring radius r_0, the radial ground state is given in a good approximation by a Gaussian with a maximum around r_0,

$$\phi_0^0(r, \varphi) = \psi_0^0(r) = Ce^{-\alpha(r - r_0\beta)^2}, \tag{2.94}$$

where C is a normalization constant, and $\alpha \sim 1/2\sigma^2$ and $\beta \sim 1$ are parameters that can be precisely determined by means of a variational calculation [164]. Since the probability density is concentrated at the vicinity of the minimum of the potential, in rings with a radius r_0 of the order of a few times σ or bigger we can assume that, for $n = 0$ and low values of l, the centrifugal term $\frac{l^2}{r^2}\psi_n^l$ of Eq. (2.93) does not modify significantly the radial profile of the wave function with respect to the one corresponding to the ground state. In other words, we can make the approximation $\psi_0^l(r) \approx \psi_0^0(r)$, in such a way that the total wave function of the angular momentum eigenstates reads

$$\phi_0^\nu(r, \varphi) = \psi_0^0(r)e^{i\nu\varphi}. \tag{2.95}$$

The energy of these states is given by

$$\begin{aligned} E(l) &= \int d^2r \left[V(r)\left|\phi_0^\nu(r, \varphi)\right|^2 + \frac{\hbar^2}{2m}\left|\nabla\phi_0^\nu(r, \varphi)\right|^2 \right] \\ &= \int d^2r \left[V(r)\left|\psi_0^0\right|^2 + \frac{\hbar^2}{2m}\left|\frac{d\psi_0^0}{dr}\right|^2 \right] + l^2\frac{\hbar^2}{2m}\int d^2r \left|\frac{\psi_0^0}{r}\right|^2 = E_0 + E_c l^2. \end{aligned} \tag{2.96}$$

Thus, the total energy of the OAM eigenstates of a ring potential is the sum of the ground state contribution, E_0, and a centrifugal term, proportional to $E_c = \frac{\hbar^2}{2m} \int d^2r \left| \frac{\psi_0^0}{r} \right|^2$, which grows quadratically with l. Since ψ_0^0 follows approximately a Gaussian distribution with its maximum at r_0, E_c decreases for increasing values of the ring radius.

2.4.3 Tunneling dynamics of OAM states

After introducing the OAM eigenstates of two-dimensional harmonic and ring traps, we now move on to characterize the dynamics of a single atom carrying OAM in arrays of tunnel-coupled cylindrically symmetric potentials. Specifically, we review the study of the cases of two side-coupled rings and three rings forming a triangle presented in [137]. As we show below, the dynamics of such systems are well-described by few-state models that contain all the necessary ingredients to formulate a general description of arbitrary configurations of ring potentials. A key feature of these few-state models is that they contain complex tunneling amplitudes whose phases can be modulated by tuning the orientation between the traps.

Two side-coupled traps

We start by considering a single atom of mass m trapped in the system illustrated in Fig. 2.3, which consists of two 2D ring potentials, named L and R from left and right, of equal radial frequency ω and radius r_0. The perimeters of the two rings are separated by a distance d, which we assume to be large enough that the isolated eigenstates of L and R are quasi-orthogonal.
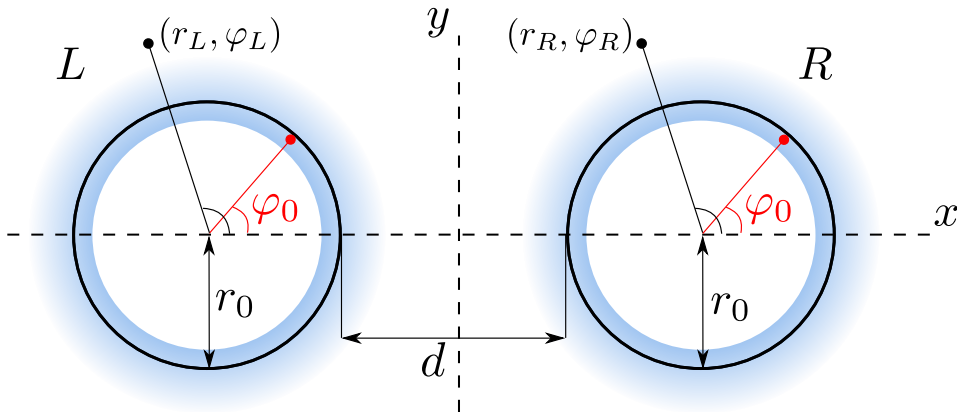

Figure 2.3: Schematic representation of two side-coupled rings traps, named L and R, of radius r_0 with their perimeters separated a distance d. We denote as (r_j, φ_j) the polar coordinates with origin at the center of the ring $j = L, R$. φ_0 is the origin of phases of the wave functions of the OAM eigenstates of each ring, given by Eq. (2.97).

Since the states with different OAM quantum number l are separated in energy, we can study independently the dynamics of each manifold of eigenstates of the isolated traps with a given value of l. Each of these manifolds is formed by four states, corresponding to the angular momentum eigenstates of each ring with winding numbers $\pm l$, the wave functions of which are given by

$$\phi_{\pm l}^{j}(r_j, \varphi_j) = \langle \vec{r} | j, \pm l \rangle \, \psi_l(r_j) e^{\pm il(\varphi_j - \varphi_0)}, \tag{2.97}$$

where (r_j, φ_j) are the polar coordinates with origin at the center of the ring $j = L, R$ [see Fig. 2.3] and φ_0 is a phase origin that can be chosen arbitrarily. Note that the $l = 1$ manifold of a system formed by two harmonic traps (i.e., two rings of $r_0 = 0$) also has four states with the generic form given by Eq. (2.97). Therefore, the arguments that we will present for ring potentials also apply to harmonic traps for this particular case.

Within a given manifold of eigenstates of the two rings with a total OAM l, we can write the total state of the atom as

$$\left| \Psi^l(t) \right\rangle = a_{+l}^{L}(t) \left| L, +l \right\rangle + a_{-l}^{L}(t) \left| L, -l \right\rangle + a_{+l}^{R}(t) \left| R, +l \right\rangle + a_{-l}^{R}(t) \left| R, -l \right\rangle, \tag{2.98}$$

where, due to the normalization condition $\left\langle \Psi^l(t) \middle| \Psi^l(t) \right\rangle = 1$, the coefficients satisfy the relation

$$\sum_{j=L,R} \sum_{\nu=\pm l} |a_\nu^j|^2 = 1. \tag{2.99}$$

The dynamics within this restricted set of states is governed by a Four-State Model (FSM) described by the Hamiltonian

$$\hat{H}_{\text{FSM}}^{l} = \sum_{j,j'=L,R} \sum_{\nu,\nu'=\pm l} J_{j,\nu}^{j',\nu'} \left| j, \nu \right\rangle \left\langle j', \nu' \right|. \tag{2.100}$$

By introducing the expansion (2.98) into the Schrödinger equation, we can derive a set of coupled equations that determine the time evolution of the probability amplitudes of the different eigenstates of the manifold

$$i\hbar \frac{da_\nu^j}{dt} = \sum_{j,j'=L,R} \sum_{\nu,\nu'=\pm l} J_{j,\nu}^{j',\nu'} a_{j'}^{\nu'}, \tag{2.101}$$

where the coupling parameters of the FSM are given by the following overlap integrals

$$J_{j,\nu}^{j',\nu'} = \int d^2 r \, \phi_\nu^{j*} \left[-\frac{\hbar^2 \nabla^2}{2m} + V(\vec{r}) \right] \phi_{\nu'}^{j'}, \tag{2.102}$$

where $V(\vec{r})$ is the total trapping potential of the system, which we consider to be the truncated combination of the two potentials created by each ring

$$V(\vec{r}) = \frac{m\omega^2}{2} \min\{(\sqrt{(x - r_0 - d/2)^2 + y^2} - r_0)^2, \sqrt{(x + r_0 + d/2)^2 + y^2} - r_0)^2\}. \tag{2.103}$$

By analysing the global symmetries of the problem, we can gain analytical insight into the properties of the parameters that govern the tunneling dynamics. In particular, the system formed by the two rings presents x and y inversion symmetries, which act over the OAM eigenstates (2.97) as

$$M_x : (x, y) \rightarrow (x, -y) \quad \Rightarrow \quad M_x(\phi_{\pm l}^j) = e^{\mp 2il\varphi_0}\phi_{\mp l}^j, \tag{2.104a}$$

$$M_y : (x, y) \rightarrow (-x, y) \quad \Rightarrow \quad M_y(\phi_{\pm l}^j) = e^{\mp 2il\varphi_0}e^{\pm il\pi}\phi_{\mp l}^k, \quad k \neq j. \tag{2.104b}$$

Since M_x and M_y are global symmetries of the system, the Hamiltonian of the FSM (2.100) must be invariant under their action. Using the symmetry transformations of the OAM states, Eqs. (2.104), and the expressions for the couplings Eq. (2.102), it can be shown that this invariance condition leaves only four independent parameters in the Hamiltonian [137], which are:

- $J_{j,\pm l}^{j,\pm l} \equiv E^l \in \mathbb{R}$, which is the common energy of the four OAM states of the manifold.

- $J_{L,\pm l}^{L,\mp l} \equiv J_1^l e^{\pm 2il\varphi_0}$, with $J_1^l \in \mathbb{R}$, which is the self-coupling between two states located in the same ring but with opposite winding numbers. This coupling is induced by the global breaking of cylindrical symmetry in the system.

- $J_{L,\pm l}^{R,\pm L} \equiv J_2^l \in \mathbb{R}$, which is the cross-coupling between states localized in different rings and with the same value of the winding number.

- $J_{L,\pm l}^{R,\mp l} \equiv J_3^l e^{\pm 2il\varphi_0}$, with $J_3^l \in \mathbb{R}$, which is the cross-coupling between states localized in different rings and with a different value of the winding number.

Thus, we see that the tunneling amplitudes involving an exchange of the winding number acquire phases that are related to the parameter φ_0. However, in a system formed by two rings these phases do not play any role because we can set the origin of phases to any desired value. In particular, for $\varphi_0 = 0$ all the couplings are real and Eq. (2.101) can be written in a matricial form as

$$i\hbar\frac{d}{dt}\begin{pmatrix} a_{+l}^L \\ a_{-l}^L \\ a_{+l}^R \\ a_{-l}^R \end{pmatrix} = \begin{pmatrix} E^l & J_1^l & J_2^l & J_3^l \\ J_1^l & E^l & J_3^l & J_2^l \\ J_2^l & J_3^l & E^l & J_1^l \\ J_3^l & J_2^l & J_1^l & E^l \end{pmatrix}\begin{pmatrix} a_{+l}^L \\ a_{-l}^L \\ a_{+l}^R \\ a_{-l}^R \end{pmatrix} \equiv H_{FSM}^l \begin{pmatrix} a_{+l}^L \\ a_{-l}^L \\ a_{+l}^R \\ a_{-l}^R \end{pmatrix}. \tag{2.105}$$

Although Eq. (2.102) provides a qualitatively correct description of the tunneling parameters, it is strictly valid for numerical computations only in the limit when all the states are orthogonal. In the two-ring system that we have analysed, there is a small but finite overlap between the wave functions, and therefore it is necessary to perform

some orthogonalization procedure in order to obtain values of the coupling parameters for which Eq. (2.105) reproduces accurately the dynamics observed with a full numerical integration of the 2D Schrödinger equation. By analysing the eigenstates and eigenvalues of H_{FSM}^l, we can derive a precise method for computing the tunneling amplitudes. This matrix can be readily diagonalized, yielding the stationary states

$$\left|E_1^l\right\rangle = \frac{1}{2}(-\left|L,+l\right\rangle - \left|L,-l\right\rangle + \left|R,+l\right\rangle + \left|R,-l\right\rangle), \tag{2.106a}$$

$$\left|E_2^l\right\rangle = \frac{1}{2}(-\left|L,+l\right\rangle + \left|L,-l\right\rangle - \left|R,+l\right\rangle + \left|R,-l\right\rangle), \tag{2.106b}$$

$$\left|E_3^l\right\rangle = \frac{1}{2}(\left|L,+l\right\rangle - \left|L,-l\right\rangle - \left|R,+l\right\rangle + \left|R,-l\right\rangle), \tag{2.106c}$$

$$\left|E_4^l\right\rangle = \frac{1}{2}(\left|L,+l\right\rangle + \left|L,-l\right\rangle + \left|R,+l\right\rangle + \left|R,-l\right\rangle), \tag{2.106d}$$

with their corresponding energies

$$E_1^l = E^l + J_1^l - J_2^l - J_3^l, \tag{2.107a}$$
$$E_2^l = E^l - J_1^l + J_2^l - J_3^l, \tag{2.107b}$$
$$E_3^l = E^l - J_1^l - J_2^l + J_3^l, \tag{2.107c}$$
$$E_4^l = E^l + J_1^l + J_2^l + J_3^l. \tag{2.107d}$$

Our procedure starts by applying the imaginary time evolution algorithm to the analytical stationary states (2.106) to find the exact eigenstates $\left\{|\tilde{E}_1^l\rangle, |\tilde{E}_2^l\rangle, |\tilde{E}_3^l\rangle, |\tilde{E}_4^l\rangle\right\}$ of the two-ring system belonging to the OAM manifold that we are interested in. Since we are dealing with excited states, this requires finding all the states with lower energies and subtracting at each time step the corresponding projections. Once we have the eigenstates and their corresponding energies $\left\{\tilde{E}_1^l, \tilde{E}_2^l, \tilde{E}_3^l, \tilde{E}_4^l\right\}$, by inverting the relations (2.107) we can compute the common energy and the tunneling parameters as

$$E^l = \frac{1}{4}\left(\tilde{E}_1^l + \tilde{E}_2^l + \tilde{E}_3^l + \tilde{E}_4^l\right), \tag{2.108a}$$

$$J_1^l = \frac{1}{4}\left(\tilde{E}_1^l - \tilde{E}_2^l - \tilde{E}_3^l + \tilde{E}_4^l\right), \tag{2.108b}$$

$$J_2^l = \frac{1}{4}\left(-\tilde{E}_1^l + \tilde{E}_2^l - \tilde{E}_3^l + \tilde{E}_4^l\right), \tag{2.108c}$$

$$J_3^l = \frac{1}{4}\left(-\tilde{E}_1^l - \tilde{E}_2^l + \tilde{E}_3^l + \tilde{E}_4^l\right). \tag{2.108d}$$

The absolute and relative values of the tunneling amplitudes depend on the separation between the rings, d, and their radius, r_0. To illustrate this fact, in Fig. 2.4 we plot the couplings of the OAM $l = 1$ manifold, which we have computed with the procedure described above, as a function of d for rings of radius (a) $r_0 = 0$, (b) $r_0 = 2.5\sigma$ and (c)

$r_0 = 5\sigma$, with $\sigma = \sqrt{\hbar/m\omega}$. In all three plots, we observe that for short d the cross-coupling that involves an exchange of the winding number, J_3^1, is appreciably larger than the one that does not, J_2^1.

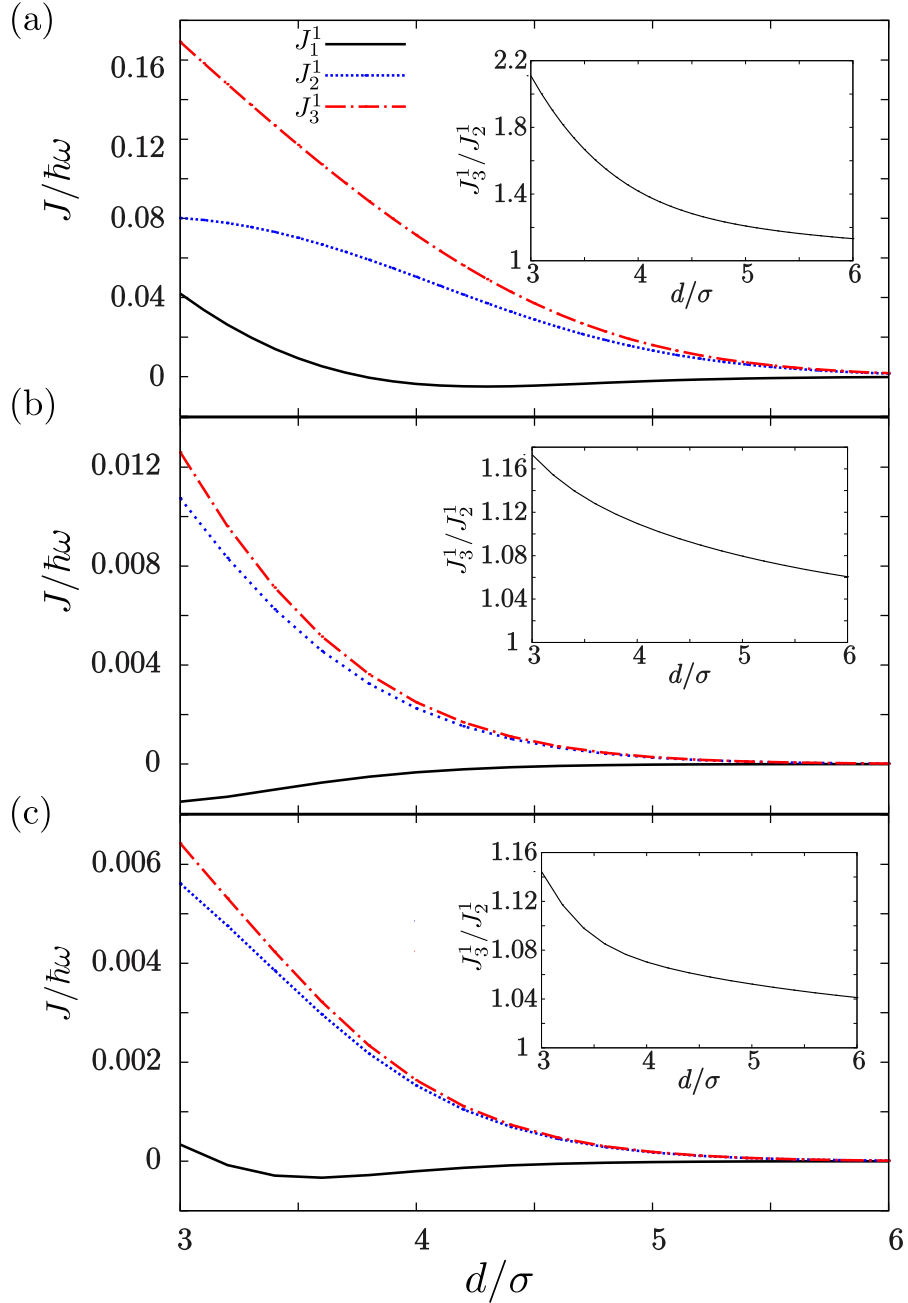
Figure 2.4: Dependence of the J_1^1, J_2^1 and J_3^1 tunneling amplitudes on the trap separation d for two ring potentials of radius (a) $r_0 = 0$ (harmonic traps), (b) $r_0 = 2.5\sigma$ and (c) $r_0 = 5.0\sigma$. The insets show the values of the ratio J_3^1/J_2^1 for the range of values of d considered in the main plots.

However, as the distance between rings is increased, they become closer until they take approximately the same value, as shown in the insets of Fig. 2.4. Regardless of the value of the inter-trap distance, the absolute value of the self-coupling J_1^1 remains approximately one order of magnitude lower than that of J_2^1 and J_3^1.

Three traps in a triangular configuration

After analysing the case of two side-coupled ring potentials, we now consider the system depicted in Fig. 2.5. It consists of three ring potentials, which we denote as L, C, R (from left, central and right), of equal radius r_0 and radial frequency ω that form a triangle with a central angle $\Theta > \pi/3$ and distances between the perimeters of the rings $d_{LC} = d_{RC} \equiv d$ and $d_{LR} = 2d \sin(\Theta/2)$.
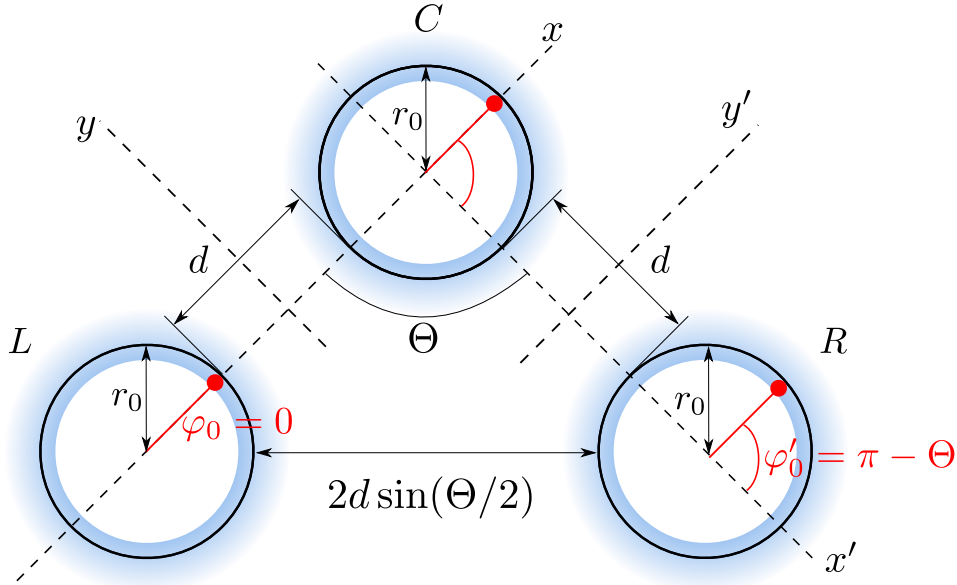
Figure 2.5: Schematic representation of three rings traps of radius r_0, named L, C and R, forming an isosceles triangle with central angle Θ. The perimeters of the L and C and R and C rings are separated by a distance d. The origin of phases φ_0 is set along the line that unites the L and C rings.

Within a manifold of eigenstates of the isolated rings with a well-defined OAM l, the state of the system at any time can be written in the form

$$\left|\Psi^l(t)\right\rangle = a_{+l}^L(t)\left|L, +l\right\rangle + a_{-l}^L(t)\left|L, -l\right\rangle + a_{+l}^C(t)\left|C, +l\right\rangle$$
$$+ a_{-l}^C(t)\left|C, -l\right\rangle + a_{+l}^R(t)\left|R, +l\right\rangle + a_{-l}^R(t)\left|R, -l\right\rangle. \tag{2.109}$$

Since the tunneling amplitudes decay fast with the inter-ring separation [see Fig. 2.4], we can consider that the L and R rings are decoupled, allowing us to describe the system

as two sets of two side-coupled rings, $L - C$ and $R - C$. As shown in Fig. 2.5, if we set the origin of phases along the x axis, i.e., along the line that unites the L and C traps, then in the (x', y') Cartesian coordinates of the $R - C$ system the measured phase origin is $\varphi'_0 = \pi - \Theta$. In this situation, the $L - C$ couplings are real, whereas the $R - C$ couplings are complex numbers with phases $e^{\pm 2il\varphi_0} = e^{\mp 2il\Theta}$. For any other choice of the phase origin φ_0, the relative phases between the complex couplings of the $L - C$ and $R - C$ subsystems would also be $e^{\pm 2il\Theta}$, yielding an equivalent description of the total three-ring system. Since the breaking of cylindrical symmetry in the C ring is due to the presence of both the L and R rings, we can consider that its self-coupling is the sum of the contributions of the two rings, $J_{C,\pm l}^{C,\mp l} = J_{L,\pm l}^{L,\mp l} + J_{R,\pm l}^{R,\mp l} = J_1^l(1 + e^{\mp 2il\Theta})$ [137]. Following the same procedure as in the case of the two side-coupled rings, we can describe the population dynamics of the states of the manifold in terms of a Six-State Model (SSM)

$$
\begin{pmatrix} a_{+l}^L \\ a_{-l}^L \\ a_{+l}^C \\ a_{-l}^C \\ a_{+l}^R \\ a_{-l}^R \end{pmatrix} \equiv H_{SSM}^l \begin{pmatrix} a_{+l}^L \\ a_{-l}^L \\ a_{+l}^C \\ a_{-l}^C \\ a_{+l}^R \\ a_{-l}^R \end{pmatrix}, \tag{2.110}
$$

where the Hamiltonian of the SSM reads

$$
H_{SSM}^l = \begin{pmatrix}
E^l & J_1^l & J_2^l & J_3^l & 0 & 0 \\
J_1^l & E^l & J_3^l & J_2^l & 0 & 0 \\
J_2^l & J_3^l & E^l & J_1^l(1 + e^{-2il\Theta}) & J_2^l & J_3^l e^{-2il\Theta} \\
J_3^l & J_2^l & J_1^l(1 + e^{2il\Theta}) & E^l & J_3^l e^{2il\Theta} & J_2^l \\
0 & 0 & J_2^l & J_3^l e^{-2il\Theta} & E^l & J_1^l e^{-2il\Theta} \\
0 & 0 & J_3^l e^{2il\Theta} & J_2^l & J_1^l e^{2il\Theta} & E^l
\end{pmatrix}. \tag{2.111}
$$

Thus, by manipulating the geometry of the system through the central angle Θ, one can tune the value of the phases of the complex tunneling parameters. For the particular case $\Theta = \pi/2l$, there is a relative π phase between the tunneling parameters of the $L - C$ and $R - C$ subsystems, causing the cancellation of the self-coupling at the central ring $J_{C,+l}^{C,-l}$ due to destructive interference.

In this thesis, we will consider physical systems consisting of arrays of 2D side-coupled ring potentials with different geometrical arrangements. Such arrays of rings could be experimentally implemented by means of several different techniques. Since they were first proposed a few years ago [112, 163], time-averaged adiabatic potentials have proven to be a powerful tool to trap ultracold atoms in on-demand potential landscapes [113, 115, 131]. Recently, it has also been shown that digital micro-mirror devices allow to create trapping potentials with arbitrary shapes [165], and in particular a double ring

trap has been realized [129]. Both of these already demonstrated approaches could be adapted to create lattices of ring potentials. Conical refraction, which is a phenomenon that occurs when a focused light beam passes along one of the optical axes of a biaxial crystal, has also been used to trap ultracold atoms in ring geometries [116]. With this technique, arrays of ring potentials could be generated by reproducing with microlenses the intensity pattern of a laser beam traversing a single crystal. Alternatively, the combination of split lenses and spatial light modulators [166] could also be used to implement arrays of light rings with any desired geometry. Using the OAM eigenstates of each ring potential as the single-particle basis, we can formulate multi-orbital BH models for lattices of rings analogous to the ones used to describe ultracold atoms in excited energy bands of optical lattices [58, 162] with tunneling parameters that follow the same rules as the ones of the three-ring system described in this section.

Quantum sensing using imbalanced counter-rotating Bose–Einstein condensate modes

In this Chapter, we study the implementation of a device capable of measuring two-body interactions, scalar magnetic fields and rotations. The apparatus consists of a Bose–Einstein Condensate (BEC) trapped in a cylindrically symmetric potential and prepared in an imbalanced superposition of Orbital Angular Momentum (OAM) $l = 1$ modes with opposite circulations. Quantum interference between the counter-propagating modes gives rise to a rotating minimal line in the BEC density profile. Harnessing the fact that, in the weakly-interacting regime, the angular frequency of the rotation of this nodal line is related through a simple expression to the strength of the two-body s-wave interactions, we propose an experimental protocol to use the system for sensing purposes.

The Chapter is organized as follows. We start by briefly reviewing in Sec. 3.1 the different ways in which ultracold atoms are employed for applications in sensing of magnetic fields and rotations. In the first part of Sec. 3.2 we describe in detail the physical system that we consider and we derive the general equations of motion for the amplitudes of the OAM modes in the context of the two-dimensional (2D) Gross–Pitaevskii Equation (GPE). We then focus on the weakly-interacting regime, where we derive an analytical model that yields a simple expression that relates the angular rotation frequency of the minimal density line to the strength of the non-linear atom-atom interactions. In Sec. 3.3 we take profit of this expression to propose a full experimental protocol to measure the interaction strength, which is proportional to the s-wave scattering length. The

relation between the scattering length and the applied magnetic field given by Feshbach resonances could be exploited to use the system as a novel type of scalar magnetometer far from the resonant field or with a dilute enough BEC. We also outline the possibility of using the system as a rotation sensor. In Sec. 3.4 we discuss and simulate the preparation of the initial state consisting of an imbalanced superposition of counter-propagating OAM modes. Finally, in Sec. 3.5 we summarize the main conclusions of the Chapter.

3.1   Introduction

Pushing the limits of sensing technologies is one of the main challenges in modern physics, opening the door to high-precision measurements of fundamental constants as well as applications in many different areas of science. Specifically, the development of highly-sensitive compact magnetic field sensors enables from detecting extremely weak biologically relevant signals to localize geological structures or archaeological sites [167]. In this context, superconducting quantum interference devices (SQUIDs) [168, 169] and atomic [25, 170–176] and nitrogen-vacancy diamond [177, 178] magnetometers are the three main approaches that allow achieving, in a non-invasive way, unprecedented sensitivity to extremely small magnetic fields.

In particular, the extraordinary degree of control of ultracold atomic systems [30, 31] makes them ideal platforms for precision measurements [179]. There are basically two types of ultracold atomic magnetometers depending on whether the magnetic field drives the internal or the external degrees of freedom of the atoms. The former are typically based on the detection of the Larmor spin precession of optically pumped atoms, while the latter encode the magnetic field information in the spatial density profile of the matter wave. Atomic magnetometers with BECs have been investigated, for instance, by using stimulated Raman transitions [180], probing separately the different internal states of a spinor BEC after free fall [181], or measuring the Larmor precession in a spinor BEC [182–186]. In the latter case, sensitivity can be increased by probing spin-squeezed states [187]. In [188], the possibility of taking profit of Feshbach resonances to use a two-component BEC as a magnetometer has been outlined. Ultracold atomic magnetometers based on detecting density fluctuations in a BEC due to the deformation of the trapping potential have also been demonstrated [189–191].

Ring-shaped potentials for ultracold atoms are a particularly interesting trapping geometry for quantum sensing [132] and atomtronics [108, 192, 193]. Ring potentials are currently implemented by means of a variety of techniques [109–116, 131, 163]. In fact, persistent currents have been observed in BECs confined in annular traps [119, 123] and it has also been shown that their physical behavior is in close analogy to that of SQUIDs [121, 124–129, 145, 194, 195]. It has also been suggested [113, 127] that BECs

in this trapping geometry could be used as rotation sensors, which have already been realized with superfluid ^{3}He [196] and have been proposed for matter waves based on the Sagnac effect [130, 131, 197, 198].

In this Chapter, we propose to use a BEC trapped in a 2D ring potential for measuring non-linear interactions, scalar magnetic fields and rotations. We consider an imbalanced superposition of counter-rotating OAM modes, whose spatial density distribution presents a minimal line. A weak two-body interaction between the atoms of the BEC leads to a rotation of the minimal atomic density line whose angular frequency is directly related to the strength of such interactions. This phenomenon is somehow reminiscent of the propagation of gray solitons, which originate in repulsively interacting BECs due to a compensation between the kinetic and mean field interaction energies. In this case, however, the minimal density line appears for attractive, repulsive or even non-interacting BECs, and is a consequence of the interference between the counter-propagating modes that takes place due to the circular geometry of the system.

3.2   Quantum sensing device

In this section we show how the system under study can act as a quantum sensing device. In Sec. 3.2.1 we describe the physical system and we derive the equations of motion of the amplitudes of the OAM modes in the context of the 2D GPE. Then, in Sec. 3.2.2 we particularize these general equations of motion to an imbalanced superposition of counter-propagating OAM $l = 1$ modes in the weakly-interacting regime. By doing so, we are able to obtain a simple relation between the rotation frequency of the minimal density line and the strength of the atom-atom interactions that constitutes the basis to harness the system for sensing applications.

3.2.1   Physical system

We consider a BEC formed by N atoms of mass m confined in the z direction by a harmonic potential of frequency ω_z and in the perpendicular plane by an annular trap of radial frequency ω and radius R. We study the system in the limit of strong confinement along the z direction; $\omega_z \gg \omega$. As we discussed in Sec. 2.1 of Chapter 2, in the limit $a_z a_s n_2 \ll 1$, where a_s is the s-wave scattering length, n_2 the two-dimensional density of the BEC and $a_z = \sqrt{\hbar/(m\omega_z)}$ the harmonic oscillator length along the z direction, the 3D GPE can be restricted to the $x - y$ plane by considering the profile for the BEC order parameter along the z direction as a Gaussian of width a_z [65]. In doing so, the 3D two-body interaction parameter $g_{3D} = (N4\pi\hbar^2 a_s)/m$ is transformed to its 2D form $g_{2D} = (N\sqrt{8\pi}\hbar^2 a_s)/(ma_z)$ (note that in these expressions we have taken the BEC wave
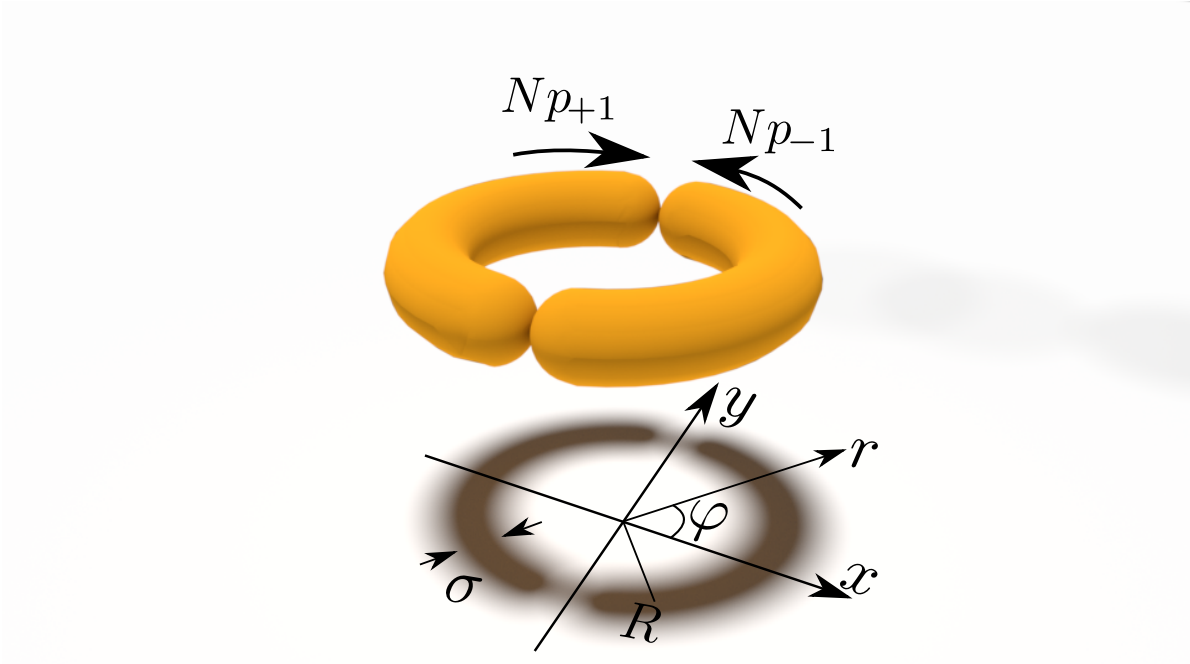
Figure 3.1: Sketch of the physical system under consideration. A BEC formed by N atoms is loaded in an annular trap, with a p_{+1} population of the state $|+1\rangle$ and p_{-1} population of $|-1\rangle$. The interference between these two counter-rotating modes yields a minimum line in the probability density. R is the radius of the annulus and σ is the width of the radial harmonic potential.

function to be normalized to 1). Thus, the 2D GPE that we will use to describe the system reads

$$i\hbar\frac{\partial\Psi}{\partial t} = \left[-\frac{\nabla^2}{2m} + V(r) + g_{2D}|\Psi|^2\right]\Psi, \tag{3.1}$$

where

$$V(r) = \frac{1}{2}m\omega^2(r-R)^2 \tag{3.2}$$

is the potential created by the ring and r is the polar radial coordinate, as shown in Fig. 3.1. Furthermore, by expressing the distances in units of $\sigma = \sqrt{\hbar/m\omega}$, the energies in units of $\hbar\omega$ and time in units of $1/\omega$, we arrive at the following dimensionless form of the 2D GPE, which is the one that we will use throughout the Chapter

$$i\frac{\partial\Psi}{\partial t} = H\Psi = \left[-\frac{\nabla^2}{2} + \frac{1}{2}(r-R)^2 + g_{2d}|\Psi|^2\right]\Psi, \tag{3.3}$$

where all quantities are now expressed in terms of the above defined units and the dimensionless non-linear interaction parameter is given by

$$g_{2d} = N a_s \sqrt{\frac{8\pi m \omega_z}{\hbar}}. \tag{3.4}$$

The system supports stationary states with a well-defined total OAM l and positive or negative circulation, which we denote as $|\pm l\rangle$. The wave functions of the OAM eigenstates are given by

$$\langle \vec{r} | \pm l \rangle = \phi_{\pm l}(\vec{r}) = \phi_{\pm l}(r, \varphi) = \psi_l(r) e^{\pm i l \varphi}, \tag{3.5}$$

where $\psi_l(r)$ is the corresponding radial part of the wave function. Their chemical potential μ_l is independent of the sign of the circulation and is given by the eigenvalue of the time-independent 2D GPE

$$H\phi_{\pm l} = \left[-\frac{\nabla^2}{2} + \frac{1}{2}(r - R)^2 + g_{2d}|\phi_{\pm l}|^2 \right] \phi_{\pm l} = \mu_l \phi_{\pm l}. \tag{3.6}$$

If the radius of the ring is large compared to the characteristic length of the potential, $R \gg \sigma$, the radial wave functions of the OAM modes (3.5) are given in a very good approximation by the ground state of the ring potential, $\psi_l(r) \approx \psi_0(r)$. In this situation, a general state of the BEC can be expressed in terms of the OAM modes as

$$\Psi(\vec{r}, t) = \sum_{m=-l_{\max}}^{l_{\max}} a_m(t)\phi_m(r, \varphi) = \sum_{m=-\infty}^{\infty} a_m(t) \left[\psi_0(r)e^{mi\varphi} \right], \tag{3.7}$$

where $l_{\max}$ is the maximum value of the OAM quantum number that we consider in the expansion. Since the OAM wave functions are normalized to unity, $\int \phi_m^* \phi_n d^2r = \delta_{mn}$, the amplitudes in the expansion (3.7) fulfill the constraint $\sum_m |a_m(t)|^2 = 1$. Substitution of the wave function (3.7) into the 2D GPE (3.3) yields (we drop the explicit dependences on t and $\vec{r}$)

$$
\begin{aligned}
\sum_p i\frac{da_p}{dt}\phi_p &= \left[-\frac{\nabla^2}{2} + V(r) + g_{2d}\sum_{m,m'} a_m a_{m'}^* \phi_m \phi_{m'}^* \right] \sum_k a_k \phi_k \\
&= \left[-\frac{\nabla^2}{2} + V(r) + g_{2d}\sum_m |a_m|^2 |\phi_m|^2 + g_{2d}\sum_{m\neq m'} a_m a_{m'}^* \phi_m \phi_{m'}^* \right] \sum_k a_k \phi_k \\
&= \left[-\frac{\nabla^2}{2} + V(r) + g_{2d}|\psi_0|^2 \right] \sum_k a_k \phi_k + g_{2d}\sum_k \sum_{m\neq m'} a_m a_{m'}^* a_k \phi_m \phi_{m'}^* \phi_k.
\end{aligned}
\tag{3.8}
$$

From the expression (3.8), an equation of motion for each of the amplitudes can be found by multiplying both sides by ϕ_l^* and integrating over the whole 2D space

$$i\frac{da_p}{dt} =$$

$$\sum_k a_k \left\{ \int d^2r\phi_p^* \left[-\frac{\nabla^2}{2} + V(r) + g_{2d}|\psi_0|^2 \right] \phi_k + \sum_{m\neq m'} g_{2d}a_m a_{m'}^* \int d^2r\phi_p^*\phi_m\phi_{m'}^*\phi_k \right\} =$$

$$\sum_k a_k \left\{ \int d^2r\phi_p^* \left[-\frac{\nabla^2}{2} + V(r) + g_{2d}|\phi_k|^2 \right] \phi_k + \sum_{m\neq m'} g_{2d}a_m a_{m'}^* \int d^2r|\psi_0|^4 e^{i\varphi(m+k-m'-p)} \right\}.$$

$$(3.9)$$

Defining $U \equiv g_{2d}\int rdrd\varphi|\psi_0(r)|^4$ and using $\left[-\frac{\nabla^2}{2} + V(r) + g_{2d}|\phi_k|^2 \right]\phi_k = \mu_k\phi_k$, we finally arrive at the more compact expression

$$i\frac{da_p}{dt} = \mu_p a_p + U \sum_{m\neq m'} a_m a_{m'}^* a_{(p+m'-m)}. \tag{3.10}$$

The term $U\sum_{m\neq m'} a_m a_{m'}^* a_{(p+m'-m)}$, which appears due to the presence of the interaction term in the GPE, represents a non-linear coupling between different OAM modes. As we will show in Sec. 3.2.2, this coupling between OAM states yields very rich dynamics and is at the basis of the use of the system as a sensing device.

3.2.2 Dynamics of an imbalanced superposition of counter-propagating OAM $l = 1$ modes in the weakly-interacting regime

We now consider as the initial state of the BEC an imbalanced superposition of the OAM $l = 1$ states with opposite circulations, $|\pm 1\rangle$, i.e., a state of the form given by Eq. (3.7) with weights $|a_{\pm 1}(t = 0)| \equiv \sqrt{p_{\pm 1}}$ fulfilling $p_{+1} + p_{-1} = 1$ and $a_m(t = 0) = 0$ for $|m| \neq 1$. Such a state could be realized, for instance, by directly transferring OAM with a laser beam to the BEC [120, 122] or, as we will discuss in detail in Sec. 3.4, by preparing the BEC in the ground state of the ring, imprinting a 2π round phase and momentarily breaking the cylindrical symmetry of the potential to induce a coupling between the degenerate states of positive and negative circulation [137, 199]. The wave function of this initial state is given by

$$\Psi(t = 0) = \sqrt{p_{+1}}\phi_{+1}(r,\varphi) + e^{i\alpha}\sqrt{p_{-1}}\phi_{-1}(r,\varphi) = \psi_0(r)(\sqrt{p_{+1}}e^{i\varphi} + \sqrt{p_{-1}}e^{i\alpha}e^{-i\varphi}), \tag{3.11}$$

and its density profile reads

$$|\Psi(t = 0)|^2 = |\psi_0(r)|^2(1 + 2\sqrt{p_{+1}p_{-1}}\cos(2\varphi - \alpha)). \tag{3.12}$$

Due to quantum interference between the counter-propagating OAM modes, the angular atomic density distribution has a minimal line at $\varphi_{\min} = (\pi + \alpha)/2, (3\pi + \alpha)/2$, as sketched in Figure 3.1.

As we discussed in Sec. 3.2.1, in the presence of atom-atom interactions the different OAM modes are connected through a non-linear coupling described by the second term on the right hand side of Eq. (3.10). Since for the initial state considered here $a_l(0) = 0 \ \forall l \neq \pm 1$, the only higher order OAM states that are directly coupled to the initial state are those in which the non-linear part of (3.10) has terms such as $a_{+1}a_{-1}^*a_{+1}$ or any other combination of amplitudes of OAM $l = 1$ modes. The only modes that have terms of this type are the OAM $l = 3$ states. Higher odd OAM modes, $l = 5, 7, ...$, are subsequently populated through coupling terms that contain combinations of amplitudes of lower odd OAM modes. However, for this particular form of the initial state, the even OAM modes, $l = 0, 2, ...$, cannot be excited because in their dynamical equations the terms in $\sum_{m \neq m'} a_m a_{m'}^* a_{(l+m'-m)}$ always contain at least one even OAM amplitude and, since the lowest even modes $l = 0, \pm 2$ are not directly coupled to the $l = \pm 1$ modes, none of the even modes will be populated during the time evolution.

We now focus on the weakly interacting regime, in which the energy difference between the OAM $l = 1$ and $l = 3$ states is much bigger than the non-linear interaction strength, $(\mu_3 - \mu_1) \equiv \Delta \gg U$, allowing us to set $l_{\max} = 3$ in the expansion (3.7). This condition is typically fulfilled for values of the interaction parameter of the 2D GPE (3.3) $g_{2d} \sim 1$. In this situation, the dynamics is described in terms of a four-state model (FSM) that is obtained by truncating Eq. (3.10) to the OAM $l = 3$ modes. The equations governing the time evolution of the probability amplitudes that are present in the truncated model, namely $a_{\pm 1}, a_{\pm 3}$, can be written in a matrix form as

$$i\frac{d}{dt}\begin{pmatrix} a_{+1} \\ a_{-1} \\ a_{+3} \\ a_{-3} \end{pmatrix} = H_{\text{FSM}} \begin{pmatrix} a_{+1} \\ a_{-1} \\ a_{+3} \\ a_{-3} \end{pmatrix}, \tag{3.13}$$

where the four-state model (FSM) Hamiltonian reads

$H_{\text{FSM}}/U =$

$$\begin{pmatrix} \mu_1/U & \rho_{+1-1} + \rho_{+1+3}^* + \rho_{-1-3} & \rho_{+1-1}^* + \rho_{+1+3} + \rho_{-1-3}^* & \rho_{+1-3} + \rho_{-1+3}^* \\ \rho_{+1-1}^* + \rho_{+1+3} + \rho_{-1-3}^* & \mu_1/U & \rho_{+1-3}^* + \rho_{-1+3} & \rho_{+1-1} + \rho_{+1+3}^* + \rho_{-1-3} \\ \rho_{+1-1} + \rho_{+1+3}^* + \rho_{-1-3} & \rho_{+1-3} + \rho_{-1+3}^* & \mu_3/U & \rho_{3+3-} \\ \rho_{+1-3}^* + \rho_{-1+3} & \rho_{+1-1}^* + \rho_{+1+3} + \rho_{-1-3}^* & \rho_{+3-3}^* & \mu_3/U \end{pmatrix},$$

$$\tag{3.14}$$

where $\rho_{\pm i \pm j} \equiv a_{\pm i} a_{\pm j}^*$, with $i, j = 1, 3$, are the density matrix elements.

Fig. 3.2(a) shows a typical temporal evolution of the populations of all the OAM states involved in the dynamics considering as initial state an imbalanced superposition of the $|+1\rangle$ and $|-1\rangle$ states in the weakly-interacting regime. The continuous lines have been obtained by solving with a high-order Runge–Kutta method the FSM, Eq. (3.13), and the insets show the comparison with the results obtained by a full numerical integration of the 2D GPE (points). We have performed this integration using a standard Crank-Nicolson algorithm in a space-splitting scheme [200], i.e., we have introduced the Trotter decomposition $e^{iH(x,y)\Delta t} \approx e^{iH(x)\Delta t}e^{iH(y)\Delta t}$, where Δt is the discrete time step, that we have taken to be $\Delta t = 10^{-3}$. The grid used for the simulations has a spatial discretization width $\Delta x = 2.4 \times 10^{-3}$ and a total of 1000 points in each dimension. For all the populations, we find an excellent agreement between the results obtained with the two different methods, with relative discrepancies typically on the order of 10^{-2}. Despite the fact that the populations of the different OAM states present only very small fluctuations, the initial state is not in general a stationary state of the system because the minimum appearing in the density profile rotates at a constant speed. This fact can be appreciated in Fig. 3.2(b), where the density profile is shown for different times. At $t = 0$, the density profile has a minimum density line at $x = 0$, and as time marches on this line rotates in the $x - y$ plane. The fact that the minimum density line rotates means that there is a time-dependent relative phase $\alpha(t)$ between the $a_{+1}(t)$ and $a_{-1}(t)$ coefficients, so that the state of the system evolves in time as

$$\Psi(\vec{r}, t) \approx a_{+1}(0)\phi_{+1}(\vec{r}) + a_{-1}(0)e^{i\alpha(t)}\phi_{-1}(\vec{r}). \qquad (3.15)$$

The phase difference $\alpha(t)$ is due to the non-linear interaction, and can be understood as a consequence of the presence of off-diagonal terms in the FSM Hamiltonian (3.14). In Fig. 3.2(c) we plot the temporal evolution of the normalized real part of the ρ_{+1-1} coherence, which is related to the phase difference $\alpha(t)$ as

$$\frac{\mathrm{Re}[\rho_{+1-1}]}{|\rho_{+1-1}|} = \frac{\mathrm{Re}[a_{+1}(0)a_{-1}(0)e^{-i\alpha(t)}]}{|a_{+1}(0)a_{-1}(0)|} = \cos\alpha(t). \qquad (3.16)$$

We observe that the real part of the coherence oscillates harmonically, which means that α evolves linearly with time. The angular rotation frequency of the line of minimum density can be calculated from the phase difference between the counter-propagating OAM $l = 1$ modes as

$$\Omega = \frac{d\varphi_{\min}}{d\alpha}\frac{d\alpha}{dt} = \frac{1}{2}\frac{d\alpha}{dt} \qquad (3.17)$$

(a)

(b)

(c)
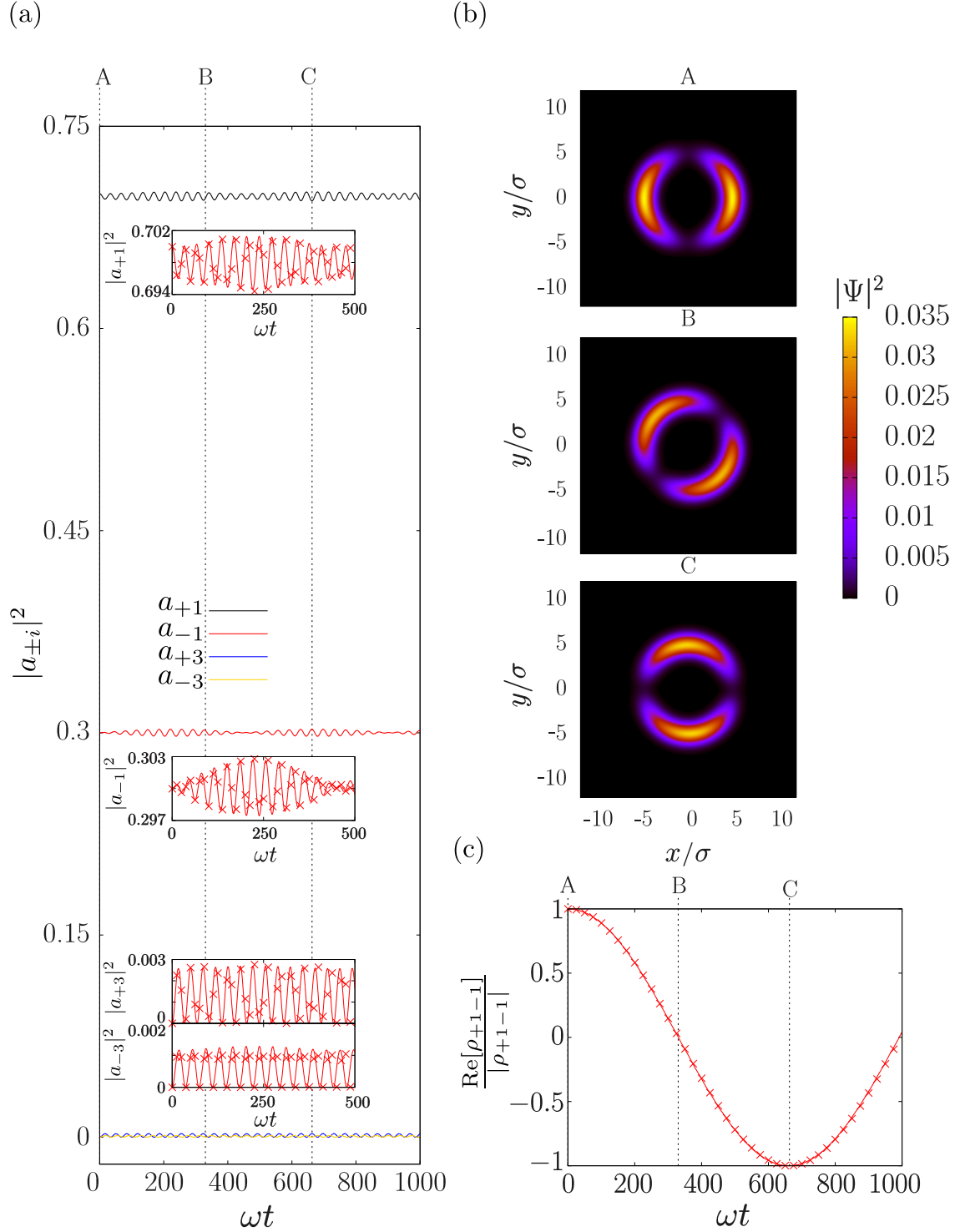
Figure 3.2: (a) Time evolution of the population of the states involved in the dynamics. (b) Snapshots of the density profile for different instants of the dynamical evolution. (c) Time evolution of the real part of the coherence between the $|{+}1\rangle$ and $|{-}1\rangle$ states. In (a) and (c), the points correspond to the numerical simulation of the GPE, while the continuous lines have been obtained by solving the FSM equations. The considered parameter values are $R = 5$ and $g_{2d} = 1$, for which $U = 0.0128$, $\mu_1 = 0.529$ and $\mu_3 = 0.699$, $a_{+1}(0) = \sqrt{p_{+1}} = \sqrt{0.7}$ and $a_{-1}(0) = \sqrt{p_{-1}(0)} = \sqrt{0.3}$.

From the FSM, we can obtain an expression for the oscillation frequency of ρ_{+1-1} by solving the von Neumann equation $i\dot{\rho} = [H_{\text{FSM}}, \rho]$. After assuming $\rho_{+1+1} = p_{+1}$ and $\rho_{-1-1} = p_{-1}$ to be constant and neglecting all terms $\mathcal{O}(a_{\pm 3}^2(t))$, we arrive at a linear system of three coupled differential equations

$$\begin{pmatrix} \dot{\rho}_{+1-1} \\ \dot{\rho}_{+1+3}^* \\ \dot{\rho}_{-1-3} \end{pmatrix} = -i \begin{pmatrix} U(p_{-1}-p_{+1}) & U(2p_{-1}-p_{+1}) & U(p_{-1}-2p_{+1}) \\ Up_{+1} & \Delta + Up_{+1} & 2Up_{+1} \\ -Up_{-1} & -2Up_{-1} & -\Delta - Up_{-1} \end{pmatrix} \begin{pmatrix} \rho_{+1-1} \\ \rho_{+1+3}^* \\ \rho_{-1-3} \end{pmatrix} = M \begin{pmatrix} \rho_{+1-1} \\ \rho_{+1+3}^* \\ \rho_{-1-3} \end{pmatrix}.$$

(3.18)

The characteristic frequencies k of the system of equations (3.18) are obtained by solving the eigenvalue equation

$$\det[M - \mathbb{1}k] = 0 \Rightarrow ik^3 + ik(U\Delta + \Delta^2 - p_{+1}p_{-1}U^2) + U\Delta^2(p_{+1} - p_{-1}) = 0. \quad (3.19)$$

Since $U \ll \Delta$ in the weakly interacting regime, the term proportional to $p_{+1}p_{-1}U^2$ can be neglected in front of the others. The three eigenvalues that are obtained after solving Eq. (3.19) are imaginary. In the weakly-interacting regime, the eigenmode associated with the eigenvalue $k_0 = i|k_0|$ of lowest modulus has a very predominant component of $\rho_{+1-1}(t)$, allowing us to write $\rho_{+1-1}(t) \approx \rho_{+1-1}(0)e^{i|k_0|t}$. Thus, according to Eq. (3.17), the rotation frequency of the nodal line is $\Omega_{\text{FSM}} = \frac{1}{2}|k_0|$, where the subscript indicates that the rotation frequency has been obtained in the context of the FSM. In the limit $\Delta \gg \Omega_{\text{FSM}}$, we can neglect the ik^3 term in Eq. (3.19) and the rotation frequency of the nodal line is given by

$$\Omega_{\text{FSM}} = \frac{Un_{\pm 1}}{2(1 + \frac{U}{\Delta})}, \quad (3.20)$$

where we have defined the population imbalance $n_{\pm 1} \equiv (p_{+1} - p_{-1}) \in [-1, 1]$. Note that, although the $l = 3$ states are nearly not populated during the dynamical evolution, the parameter Δ, which contains the chemical potential μ_3, plays a significant role in the expression of the rotation frequency (3.20). Thus, these states must be taken into account for an accurate description of the dynamics of the system.

In order to test the validity of the expression provided by the FSM, we have computed the rotation frequency of the minimal density line using the 2D GPE for several values of the parameters and compared the results with Eq. (3.20). In Fig. 3.3(a) we plot, for different values of g_{2d} and $n_{\pm 1}$, Ω computed using Eq. (3.20) (continuous lines) and the full numerical integration of the 2D GPE (points). We observe an excellent agreement between the two methods for low non-linearities and population imbalances. Fig. 3.3(b) shows the relative error $\frac{\delta\Omega}{\Omega_{\text{GPE}}}$, where Ω_{GPE} is the rotation frequency of the nodal line obtained from the GPE and $\delta\Omega = |\Omega_{\text{FSM}} - \Omega_{\text{GPE}}|$, as a function of the values of $n_{\pm 1}$ and g_{2d} used in the numerical simulation of the GPE. In the parameter region explored in Fig. 3.3(b), which corresponds to values of the interaction strength $g_{2d} < 4$, we find a maximum relative error of 10^{-2}.

(a)

(b)
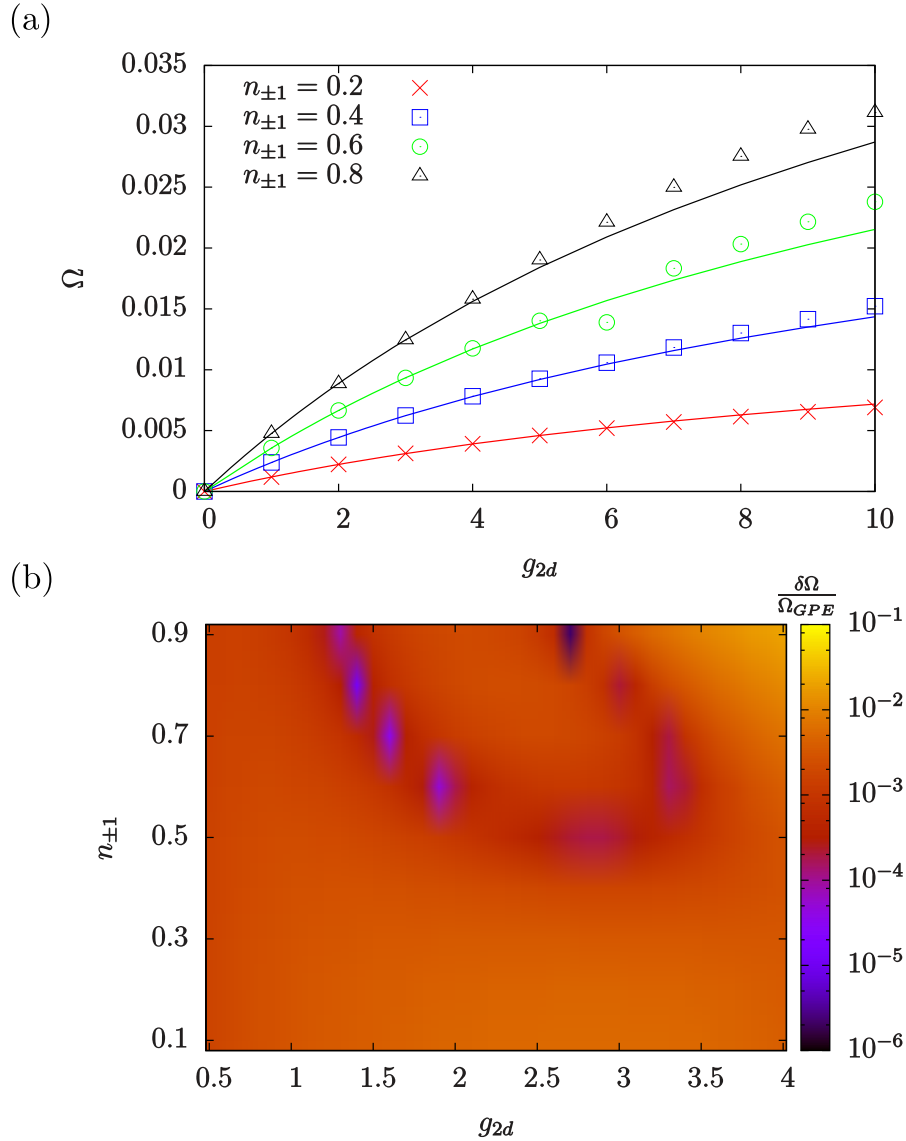
Figure 3.3: (a) Rotation frequency of the nodal line Ω as a function of g_{2d} for different values of $n_{\pm1}$ obtained with the FSM (continuous lines) and full integration of the GPE (points) (b) Relative error committed in the determination of Ω using Eq. (3.20) as a function of the values of g_{2d} and $n_{1\pm}$ used in the GPE simulation.

3.3   Quantum sensing protocol

In this section, we describe how the expression for the rotation frequency of the nodal line provided by the FSM, Eq. (3.20), can be exploited to use the system as a sensor of two-body interactions, magnetic fields and external rotations.

3.3.1   Sensing of two-body interactions

Recalling that the parameter U of the FSM Hamiltonian (3.14) is given by $U = g_{2d} \int d^2r |\psi_0(r)|^4 \equiv g_{2d} I$ and assuming that we are in the regime of validity of the FSM, Eq. (3.20) allows us to express the interaction parameter g_{2d} as

$$g_{2d} = \frac{1}{I} \frac{2\Omega}{n_{\pm 1} - 2\frac{\Omega}{\Delta}}, \qquad (3.21)$$

where Ω is the observed frequency of rotation of the nodal line. The relation (3.21) constitutes the basis to use the physical system under consideration as a quantum sensing device. By determining the parameters appearing on the right hand side of Eq. (3.21), one can infer the value of g_{2d} and thus, from Eq. (3.4), the s-wave scattering. Next, we describe how each of these quantities could be experimentally measured from fluorescence images of the BEC.

Rotation frequency of the minimum density line

The rotation frequency of the minimum density line, Ω, can be measured by direct imaging in real time of the density distribution of the BEC [129]. If the coherence time of the BEC is τ, in order for this measurement to be possible the condition $\Omega\omega \gtrsim 1/\tau$ must be fulfilled, since otherwise the rotation would be so slow that it could not be appreciated during the time that the experiment lasts. The conditions of validity of the model impose an upper limit on the values of Ω that allow to measure g_{2d}. As we discussed in Sec. 3.2.2, if the interaction is too large, the assumptions of the FSM model are no longer valid and it is thus not possible to relate the rotation frequency of the nodal line to the non-linear interaction parameter using Eq. (3.21). However, as can be seen in Fig. 3.3, for $g_{2d} < 4$ the FSM predicts with high accuracy the value of Ω.

Population imbalance

The population imbalance between the two OAM $l = 1$ states, $n_{\pm 1}$, can be directly determined by analysing the density profile of the BEC at any instant of the time evolution. According to Eq. (3.12), the angular atom density distribution has two minima and maxima with a separation of $\pi/2$ rad. Let us now consider the two integration regions A_1 and A_2 shown in Fig. 3.4, which are arcs of radius ρ and angle 2θ centred around a maximum and a minimum of intensity, respectively. The integrals of the atom density (given by Eq. (3.12)) over A_1 and A_2 can be performed numerically and, for

sufficiently small θ, they approximately yield

$$I_1 = \int_{A_1} d^2 r |\Psi|^2 = \int_0^\rho \int_{\varphi_{\max}-\theta}^{\varphi_{\max}+\theta} r d\varphi dr |\Psi|^2 \approx 2\theta(1 + 2\sqrt{p_{1+}p_{1-}}) \int_0^\rho r \psi_0^2(r) dr \quad (3.22\text{a})$$

$$I_2 = \int_{A_2} d^2 r |\Psi|^2 = \int_0^\rho \int_{\varphi_{\min}-\theta}^{\varphi_{\min}+\theta} r d\varphi dr |\Psi|^2 \approx 2\theta(1 - 2\sqrt{p_{1+}p_{1-}}) \int_0^\rho r \psi_0^2(r) dr \quad (3.22\text{b})$$

Thus, combining (3.22a) and (3.22b) one can determine the product of populations as

$$p_{+1}p_{-1} = \left(\frac{I_1 - I_2}{2(I_1 + I_2)} \right)^2 , \quad (3.23)$$

which, together with the constraint $p_{+1} + p_{-1} = 1$, allows to determine the population imbalance from a fluorescence image.
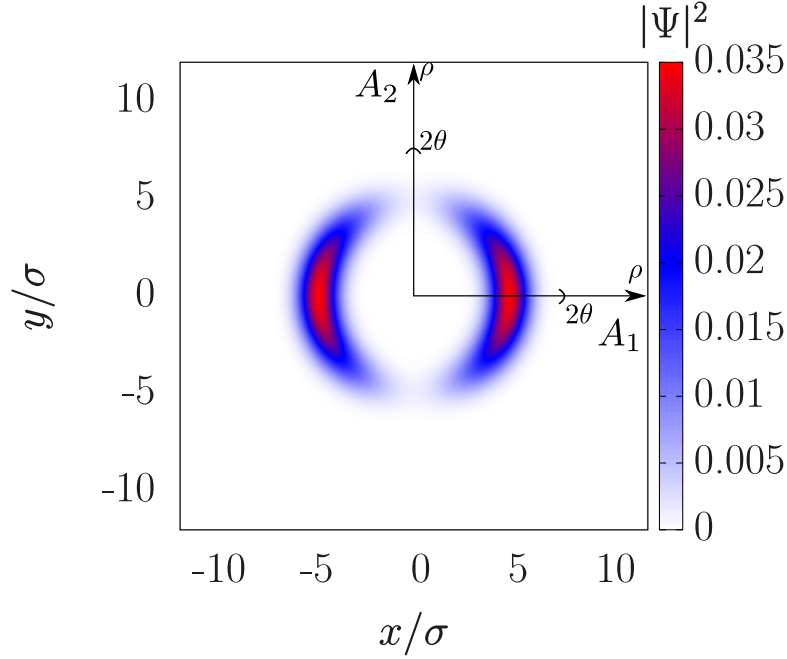
Figure 3.4: Example of A_1 and A_2 integration areas to experimentally determine the population imbalance.

Integral of the radial wave function

A fluorescence image of the BEC also allows to compute the integral $I = \int d^2 r |\psi_0(r)|^4$ that appears on the right hand side of Eq. (3.21). From equation (3.12), we can write

$$|\Psi|^4 = |\psi_0(r)|^4 \left(1 + 4\sqrt{p_{+1}p_{-1}} \cos(2\varphi - \alpha) + 4p_{+1}p_{-1} \cos^2(2\varphi - \alpha) \right). \quad (3.24)$$

From a fluorescence image, one can numerically perform the integral $\int d^2r|\Psi|^4$ over the whole space, which yields

$$\int |\Psi|^4 r dr d\varphi = (2\pi + 4\pi p_{+1}p_{-1}) \int |\psi_0(r)|^4 r dr = (1 + 2p_{+1}p_{-1}) \int d^2r|\psi_0(r)|^4. \quad (3.25)$$

Therefore, the desired quantity can be calculated as

$$I = \int d^2r|\psi_0(r)|^4 = \frac{\int d^2r|\Psi|^4}{1 + 2p_{+1}p_{-1}}. \quad (3.26)$$

The product $p_{+1}p_{-1}$ appearing on the right hand side of Eq. (3.26) can be determined using the previously described procedure to measure the population imbalance, see Eq. (3.23).

Chemical potential difference

The chemical potential of the angular momentum states can be decomposed into its kinetic, potential and interaction contributions. Since one can assume that the wave functions take the form $\phi_{\pm l}(\vec{r}) = \psi_0(r)e^{\pm il\varphi}$, the potential and interaction contributions will be the same regardless of l, while the kinetic contribution is given by

$$E_l^{\text{kin}} = \frac{1}{2} \int d^2r|\nabla\phi_{\pm l}(\vec{r})|^2 = \frac{1}{2} \int d^2r \left[\left|\frac{d\psi_0}{dr}\right|^2 + l^2 \left|\frac{\psi_0}{r}\right|^2 \right] = \mu_0 + l^2 E_c. \quad (3.27)$$

Thus, the chemical potential difference is only due to the difference in the centrifugal terms of the kinetic energy

$$\Delta = \mu_3 - \mu_1 = E_3^{\text{kin}} - E_1^{\text{kin}} = 8E_c = 4 \int d^2r \left|\frac{\psi_0(r)}{r}\right|^2. \quad (3.28)$$

From Eq. (3.12), one can see that the integral (3.28) can be numerically performed after determining $|\psi_0(r)|^2$ from a fluorescence image as $|\psi_0(r)|^2 = \frac{|\Psi(r,\varphi_{min})|^2}{1 - 2\sqrt{p_{+1}p_{-1}}}$.

In order to check the accuracy of the proposed experimental protocol, we have computed g_{2d} using Eq. (3.21) and determining all the parameters on the right hand side following the above described numerical procedures using images of the integration of the 2D GPE. Then, we have compared the obtained results with the *ab initio* values of g_{2d} used in the simulations. In Fig. 3.5 we plot the relative error $\delta g_{2d}/g_{2d}$ committed as a function of the *ab initio* values of g_{2d} and $n_{\pm 1}$. In the region $g_{2d} \approx 1$ and $n_{\pm 1} \approx 0.6$, the relative error is minimal and it reaches very low values, on the order of 10^{-5}. The maximum value of the relative error is about 10%, and is found for low values of $n_{\pm 1}$. In our simulations, we have used a grid of dimensions $24\sigma \times 24\sigma$ and 1000 points in

each spatial direction. With higher grid precision, the relative error committed with the proposed protocol could prove to be even lower.
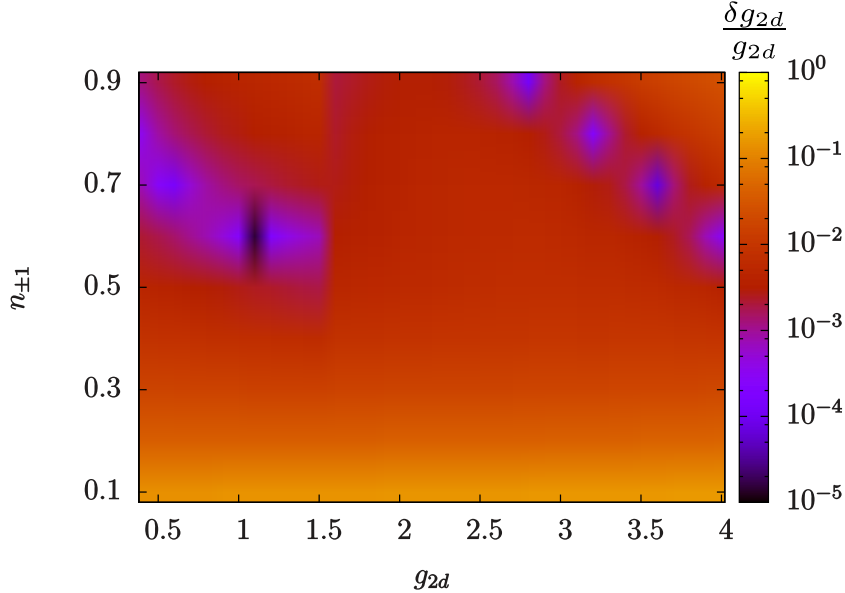

Figure 3.5: Relative error committed in the determination of g_{2d} using the full experimental protocol described in the text as a function of the *ab initio* values of g_{2d} and $n_{\pm 1}$ in the simulation.

Currently, there are different approaches to measure the *s*-wave scattering length of ultracold atoms [201] such as those based on photoassociation spectroscopy, ballistic expansion, and collective excitations. Our proposal constitutes an alternative to these approaches where all the unknowns can be directly inferred from fluorescence images of the BEC. However, the limit $g_{2d} < 4$ obtained for the configuration discussed in Fig. 3.3 implies that for a BEC of, e.g., $N = 10^4$ atoms of ^{23}Na, with a trapping frequency ω_z of a few hundreds of Hz, the maximum *s*-wave scattering length that could be measured with high precision, e.g., with a relative error of 10^{-2}, would be a few times the Bohr radius.

3.3.2   Sensing of magnetic fields

Assuming that the total number of atoms N of the BEC and the trapping frequency in the z direction ω_z are precisely known quantities, Eqs. (3.21) and (3.4) together with the protocols to measure $n_{\pm 1}$, I and Δ allow to determine the scattering length a_S. If the scattering length depends somehow on the modulus B of an external magnetic field, a change in B will be translated into a variation of Ω. Thus, the system could be used as a scalar magnetometer by relating changes on the frequency of rotation of the minimal

density line to variations of the modulus of the magnetic field. Taking into account that I and Δ are almost independent of g_{2d} and thus of B in the regime of interaction strengths for which the model is valid, combining Eqs. (3.4) and (3.20) we can evaluate the sensitivity that this magnetometer would have as

$$\frac{d\Omega_{\text{FSM}}}{dB} = \frac{n_{\pm 1}IN\sqrt{\frac{8\pi m\omega_z}{\hbar}}}{2(1 + \frac{U(B)}{\Delta})^2}\frac{da_S}{dB}. \tag{3.29}$$

Since we must have $U \ll \Delta$ in order for the model to be valid, we can define a threshold limit for the sensitivity by taking $U/\Delta = 1$ in (3.29). Defining the aspect ratio $\Lambda \equiv \omega_z/\omega$ and changing the differentials in (3.29) by finite increments, we find the following upper threshold for the sensitivity in magnetic field variations ΔB_{th} as a function of the change in the rotation frequency of the nodal line $\Delta\Omega$

$$\Delta B_{\text{th}} = \frac{8\sigma}{n_{\pm 1}IN\sqrt{8\pi\Lambda}}\frac{1}{\frac{da_S}{dB}}\Delta\Omega. \tag{3.30}$$

From Eq. (3.30), we observe that the sensitivity is improved by having a large number of condensed particles and a strong dependence of the scattering length on the magnetic field modulus. However, since the parameter $g_{2d} \propto Na_s$ needs to be small in order for the model to be valid, it is also required that the scattering length takes small values.

In the presence of a Feshbach resonance, the scattering length depends of the magnetic field modulus as

$$a_S(B) = \tilde{a}_S\left(1 - \frac{\delta}{B - B_0}\right), \tag{3.31}$$

where $\tilde{a}_S$ is the background scattering length, B_0 is the value of B at resonance and δ is the width of the resonance. Thus, by placing the magnetic field close to the resonant value B_0, one could in principle meet both the requirement that the scattering length is small and that it depends strongly on the magnetic field modulus. Combining Eqs. (3.30) and (3.31) and assuming that close to the resonant field $(B - B_0) \approx \delta$, we arrive at the following expression for the magnetic field sensitivity

$$\Delta B_{\text{th}} = \frac{8\sigma}{n_{\pm 1}IN\sqrt{8\pi\Lambda}}\frac{\delta}{\tilde{a}_S}\Delta\Omega. \tag{3.32}$$

However, for most atomic species this procedure would have the inconvenience that close to a Feshbach resonance the three-body losses are greatly enhanced, limiting the lifetime of the BEC and hindering the measurement procedure. Nevertheless, some atomic species such as ^{85}Rb [18], ^{133}Cs [21], ^{39}K [202] or ^{7}Li [19] have been reported to form BECs that are stable across Feshbach resonances, so they could be potential candidates for using the system as a magnetometer. Additionally, the BECs formed by

these species have lifetimes on the order of a few seconds. Taking into account that the trapping frequency ω, in units of which Ω is expressed, is typically of the order of a few hundreds of Hz for ring-shaped traps, and considering typical values of Ω as the ones in Fig. 3.3(a), in International System units $\Omega/2\pi \sim 1$Hz. This means that in the typical time that an experiment would last, $\tau \sim 1$s, the minimum density line would perform a few complete laps. Under the reasonable assumption that the fluorescence imaging system could resolve angular differences on the order of ~ 0.1 rad, incrementals in the rotation frequency on the order of 10^{-2}Hz could be measured. Thus, in the dimensionless units of Eq. (3.30), sensitivites on the order of $\Delta\Omega \sim 10^{-4}$ could be achieved. These atomic species have, however, the drawback that they typically form BECs with a low number of particles, which limits the sensitivity to magnetic fields. Although it is outside of the scope of this Chapter to give accurate values of the sensitivities that could be achieved with this apparatus, making use of Eq. (3.32) and considering the experimental parameters reported in [194], we have estimated that, in principle, this magnetometer would allow to measure changes in the magnetic field on the order of a few pT at a bandwidth of 1 Hz.

3.3.3 Sensing of rotations

Let us consider the case when the BEC is placed in a reference frame rotating at an angular frequency Ω_{ext}, which is positive (negative) if the rotation is clockwise (counter-clockwise). Now the dynamics is governed by the modified GPE [146]

$$i\frac{\partial\Psi}{\partial t} = \left[-\frac{\nabla^2}{2} + V(r) + g_{2d}|\Psi|^2 + i\Omega_{\mathrm{ext}}\frac{\partial}{\partial\varphi}\right]\Psi. \tag{3.33}$$

The extra term $i\Omega_{\mathrm{ext}}\frac{\partial}{\partial\varphi}$ introduces an energy splitting $\Delta E = 2\Omega_{\mathrm{ext}}l$ between two counter-propagating states with total OAM l. The ideal instance for using the system under study as a sensor of rotations is the non-interacting limit $g_{2d} = 0$. In that case, the effect of the external rotation is to make the line of minimal density rotate at an angular speed Ω_{ext}, which can be directly measured in experiments.

In the weakly interacting regime, the system under study can still be used as a sensor of external rotations. In that case, the only difference in the dynamics with respect to the case when there is no external rotation is that the rotation frequency of the nodal line is shifted precisely by a quantity Ω_{ext}. Thus, if g_{2d} is known and I, $n_{\pm 1}$ and Δ are measured using the protocol provided in Sec. 3.3.1, the system under consideration can be used as a sensing device for external rotations by computing the external rotation as $\Omega_{\mathrm{ext}} = \Omega - \Omega_{\mathrm{FSM}}$, where Ω is the rotation frequency of the nodal line observed in the experiment and Ω_{FSM} is given by (3.20).

The proposed setup constitutes an alternative to the two main lines of development

of rotation sensors using ultracold atoms: the atomic-gas analogues of superconducting quantum interference devices (SQUIDs) [121, 124–127, 129] and Sagnac interferometers, see [197] for a review. Gyroscopes based on the Sagnac effect measure a rotation rate relative to an inertial reference frame, based on a rotationally induced phase shift between two paths of an interferometer and the low available atomic fluxes and low effective areas are the main limiting factors of their sensitivity.

3.4   Initial state preparation

As a complement of the study of a quantum sensing device based on a BEC carrying OAM in a ring potential presented in this Chapter, in this section we discuss some possible strategies to prepare the initial state consisting of an imbalanced superposition of counter-propagating OAM $l = 1$ states. As we outlined in Sec. 3.2.1, there are two main possibilities to prepare such a state, namely:

i) Directly imprint to a BEC trapped in a ring potential the phase and density profiles associated with the state given by Eq. (3.11).

ii) Prepare the BEC in one of the OAM modes, e.g. in state $|+1\rangle$ state, then deform adiabatically the ring in order to induce a coupling with the $|-1\rangle$ state and finally return adiabatically the ring potential to its original shape.

Next, we discuss separately the implementation of these two strategies.

3.4.1   Direct imprinting of the phase and density profiles

The most direct strategy to generate an imbalanced superposition of the OAM $l = 1$ counter-rotating modes is to imprint the corresponding density and phase profiles onto the BEC by manipulating the trapping potential. The wave function of such a superposition, which is given by Eq. (3.11), can be written as $\Psi(r, \varphi) = |\Psi(r, \varphi)|e^{i\beta(\varphi)}$. The modulus $|\Psi(r, \varphi)|$ is given by Eq. (3.12), and the phase profile reads (we assume a relative phase between the counter-propagating modes $\alpha = 0$ for simplicity)

$$\beta(\varphi) = \arctan\left(\frac{\text{Im}[\Psi(r, \varphi)]}{\text{Re}[\Psi(r, \varphi)]}\right) = \arctan\left(\frac{\sqrt{p_{+1}} - \sqrt{p_{-1}}}{\sqrt{p_{+1}} + \sqrt{p_{-1}}}\tan\varphi\right) \qquad (3.34)$$

This density and phase patterning could be done, for instance, by using highly programmable digital micromirror devices [165].

3.4.2 Adiabatic deformation of the ring trap

The method described in the previous section might be difficult to implement experimentally due to the high degree of precision required in the phase and density imprinting. An alternative approach which does not demand such a fine control of the system is to adiabatically deform the ring trap to induce a coupling between the counter-rotating OAM modes. In order to do so one could, for instance, implement the following protocol

1. Load the OAM $l = 1$ state with clock-wise circulation, $|+1\rangle$, in a ring potential of radius R. This could be done by preparing the BEC in the ground state of the ring and then imprinting a 2π round phase with a Laguerre-Gaussian beam [120, 122].

2. Adiabatically deform the ring potential into an ellipse with the same area as the original ring,

$$V(r, \varphi) = \frac{1}{2}(r - \tilde{R}(\varphi)), \qquad (3.35)$$

   with

$$\tilde{R}(\varphi) = \frac{R}{\sqrt{\frac{\cos^2 \varphi}{a^2} + \frac{\sin^2 \varphi}{b^2}}}, \qquad (3.36)$$

   such that $ab = R^2$. The a and b semiaxes of the ellipse are varied in time according to the relations

$$a(t) = R\left(1 + k\frac{t}{t_r^{(1)}}\right); \quad b(t) = \frac{R}{1 + k\frac{t}{t_r^{(1)}}} \qquad (3.37)$$

   where $t_r^{(1)}$ is the total time of the adiabatic ramp and k is a factor that sets the maximum eccentricity of the ellipse.

3. Keep the elliptic potential with semiaxes $a = R(1+k)$ and $b = R/(1+k)$ during a hold time t_h in order to populate the counter-propagating OAM mode $|-1\rangle$ due to the coupling induced by the breaking of the cylindrical symmetry of the potential [137].

4. Adiabatically deform the semiaxes of the ellipse into their original form according to the relations

$$a(t) = R\left(1 + k\left(1 - \frac{t}{t_r^{(2)}}\right)\right); \quad b(t) = \frac{R}{1 + k\left(1 - \frac{t}{t_r^{(2)}}\right)}, \qquad (3.38)$$

   where $t_r^{(2)}$ is the total time of the second adiabatic ramp.

We have performed numerical simulations of this protocol with the parameters $k = 0.2$, $\omega t_r^{(1)} = \omega t_r^{(2)} = 100$ and $\omega t_h = 250$ for different values of the ring radius R and g_{2d}. For rings of small radius, $R \lesssim 5\sigma$, we observe that the final state is an imbalanced superposition of $|1, \pm\rangle$ OAM modes with very small populations of higher odd OAM modes. In Fig. 3.6 (a) we plot, for a ring of $R = 5\sigma$, the time evolution of the populations of the OAM $l = 1, 3$ states during the protocol for $g_{2d} = 0.5$ and 1; and in Fig. 3.6 (b) we show several snapshots of the density distribution for $g_{2d} = 0.5$. For rings of larger radius, the final state contains significant populations of higher odd OAM modes. An example of this is shown in Fig. 3.7, which contains the same information as Fig. 3.6 but for a ring of $R = 15\sigma$. As can be seen in Fig. 3.7 (a), in this case the final state contains a significant population of the $|-3\rangle$ state, and therefore, as shown Fig. 3.7 (b), its density profile has two minimal density lines. In both Fig. 3.6 (a) and Fig. 3.7 (a), it can be seen that the final population of the $|-1\rangle$ state is bigger for smaller values of g_{2d}.

The reason why higher OAM states are populated in bigger rings is that the energy separation between OAM states decreases as the ring radius increases, as illustrated in table 3.1. As we discussed in Sec. 3.3.1, the only difference in energy between the OAM states comes from the centrifugal term of the kinetic energy. According to Eqs. (3.27), (3.28), this term is smaller for bigger values of R because the amplitude of the ground state wave function $\psi_0(r)$ is maximal around the radial position $r = R$. During the process of adiabatic deformation of the potential, the total energy of the BEC is slightly increased. When this slight increment is of the order of the energy separation between the OAM modes, states with higher values of l become significantly populated. Although a more detailed study of this effect is outside of the scope of this Chapter, the adiabatic trap deformation protocol could in principle be optimized to selectively populate a desired OAM state. Alternatively, one could design a faster scheme to obtain the desired state based on shortcuts to adiabaticity [203].

R/σ	$E_c/\hbar\omega$
5	2.13×10^{-2}
7.5	9.13×10^{-3}
10	5.07×10^{-3}
15	2.23×10^{-3}
20	1.25×10^{-3}

Table 3.1: Energy separation between the $l = 1$ and $l = 0$ OAM states for different values of the ring radius.

(a)

(b)

Figure 3.6: (a) Time evolution of the populations of the $|\pm 1\rangle$ and $|\pm 3\rangle$ OAM states during the trap deformation protocol described in the main text. The instants A, B, C, D correspond to $\omega t = 0, \omega t_r^{(1)}, \omega(t_r^{(1)} + t_h), \omega(t_r^{(1)} + t_h + t_r^{(2)})$, respectively. (b) Snapshots of the BEC density profile at the instants A, B, C, D for $g_{2d} = 0.5$. The parameters of the simulation are $R = 5\sigma$, $\omega t_r^{(1)} = \omega t_r^{(2)} = 100$, $\omega t_h = 250$.
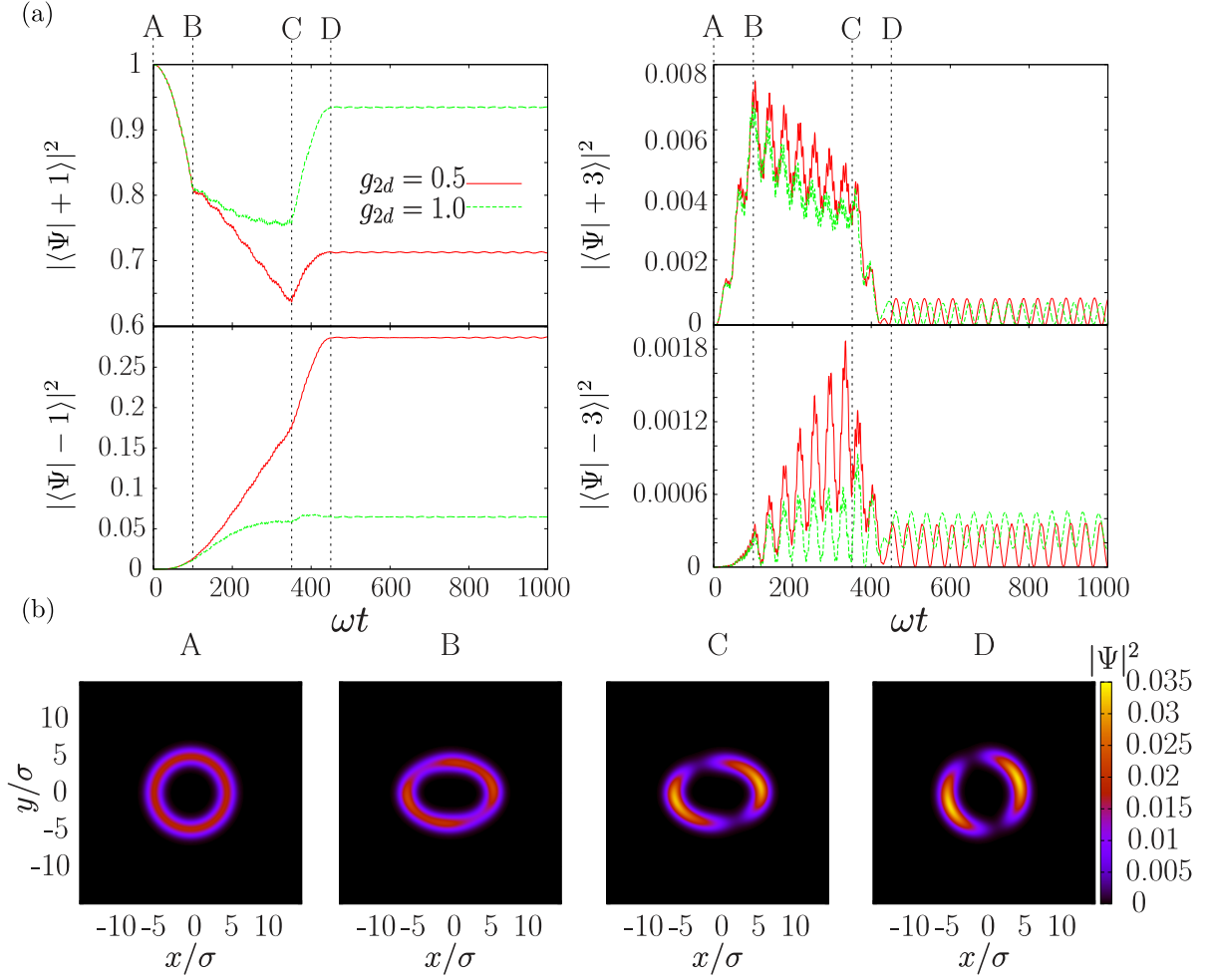
(a)

(b)
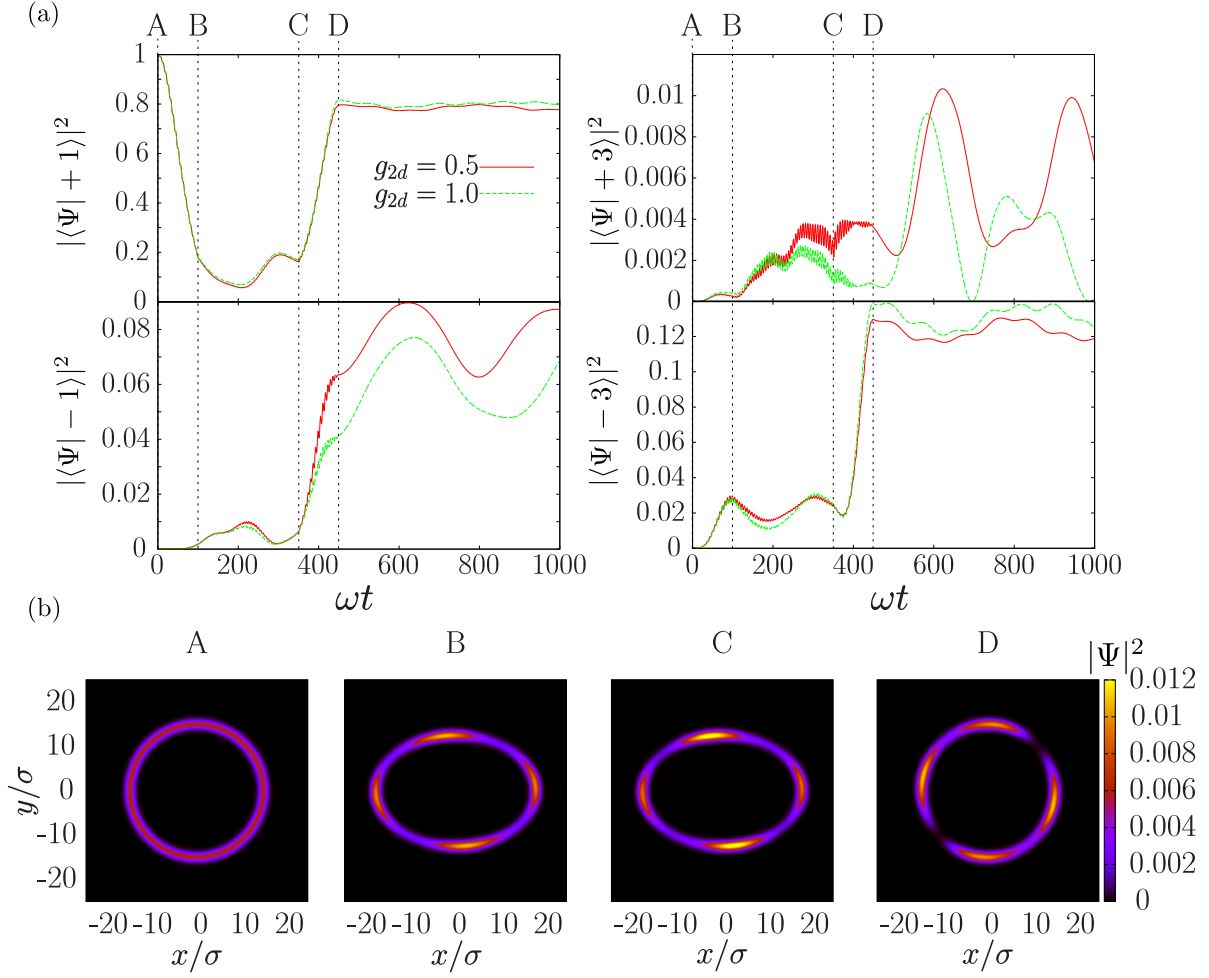
Figure 3.7: (a) Time evolution of the populations of the $|\pm1\rangle$ and $|\pm3\rangle$ OAM states during the trap deformation protocol described in the main text. The instants A, B, C, D correspond to $\omega t = 0, \omega t_r^{(1)}, \omega(t_r^{(1)} + t_h), \omega(t_r^{(1)} + t_h + t_r^{(2)})$, respectively. (b) Snapshots of the BEC density profile at the instants A, B, C, D for $g_{2d} = 0.5$. The parameters of the simulation are $R = 15\sigma$, $\omega t_r^{(1)} = \omega t_r^{(2)} = 100$, $\omega t_h = 250$.

3.5   Conclusions

In this Chapter we have studied the implementation of a quantum sensing device based on a weakly interacting BEC trapped in a 2D ring potential. We have started by deriving, in the context of the GPE description of the BEC, the general set of coupled non-linear equations that govern the time evolution of the amplitudes of the OAM modes. Then, we have focused on an initial state consisting of an imbalanced superposi-

tion of the two counter-propagating OAM $l = 1$ modes in the weakly interacting regime. The density profile of this state has a minimal line that rotates due to a time-dependent relative phase between the counter-propagating modes induced by the non-linear couplings. By comparison with a direct integration of the full 2D GPE, we have shown that it is enough to restrict the general equations of motion to the OAM $l = 1$ and $l = 3$ modes to obtain a very good description of the dynamics of the BEC. Within this truncated model, we have obtained a simple analytical expression that relates the atom-atom interaction strength to the rotation frequency of the minimal density line

Harnessing the latter analytical relation, we have proposed a protocol to use the system as a sensor of two-body interactions in dilute BECs. The experimental determination of all the quantities involved in the measurement could be done by analysing fluorescence images of the BEC density profile. We have tested the protocol by comparing the numerical results of the analysis of the BEC density profiles with the *ab initio* known values of the interaction strength used in the simulations. In the weakly interacting regime, the protocol provides accurate estimations of the interaction strength. In the presence of a Feshbach resonance, the system could also be used as a magnetic field sensor by measuring the change in the rotation frequency of the nodal line induced by variations of the s-wave scattering length caused by magnetic field fluctuations. For atomic species with low three-body losses close to the resonant value of the magnetic field, the sensitivity would be enhanced around this region. We have also discussed the use of the device as a sensor of external rotations, which could be measured as the difference between the experimentally observed rotation frequency of the minimal density line and the one predicted by the model.

Finally, we have discussed two possible ways to prepare the initial state consisting of an imbalanced superposition of counter-propagating OAM $l = 1$ modes. The most straightforward -although experimentally challenging- approach would be to directly imprint the phase and density profiles corresponding to this state onto a BEC loaded in the ground state of the 2D ring potential. Alternatively, one could initially load only one of the OAM modes and induce a coupling with the mode with opposite circulation by momentarily breaking the cylindrical symmetry of the potential. We have performed full GPE numerical simulations which confirm the feasibility of this latter approach.

Topological edge states and Aharonov-Bohm caging with ultracold atoms carrying orbital angular momentum in a diamond chain

In this Chapter, we study the single-particle properties of a system formed by ultracold atoms loaded into the manifold of $l = 1$ Orbital Angular Momentum (OAM) states of an optical lattice with a diamond chain geometry. We find that this system has a topologically non-trivial band structure and exhibits robust edge states that persist across the gap closing points, indicating the absence of a topological transition. We discuss how to perform the topological characterization of the model with a generalization of the Zak's phase and we show that this system constitutes a realization of a square-root topological insulator. In addition, we demonstrate that quantum interference between the different tunneling processes involved in the dynamics may lead to Aharonov-Bohm caging in the system.

The Chapter is organized as follows. In Sec. 4.1 we give a brief overview on recent progress on the study of topological systems with ultracold atoms and photonic platforms. In Sec. 4.2 we describe in detail the physical system that we consider and we derive the tight-binding model that we use to describe its single-particle properties. We also compute the band structure and discuss the differences with the model of a diamond chain without the OAM degree of freedom. Next, we introduce three successive analytical mappings that allow to unravel the main features of the model. In particular, the basis rotation introduced in Sec. 4.3 decouples the original chain with two states per site into two independent chains with one orbital per site and a net π flux through the plaquettes. Then, in Sec. 4.4 we map each of these independent chains into a modi-

fied Su-Schrieffer-Heeger (SSH) model. This mapping allows to understand the different types of eigenstates of the system and the occurrence of Aharonov-Bohm caging in the limit when all the bands are flat. To complete the analytical analysis of the model, in Sec. 4.5 we perform a third mapping that allows to characterize the topology of the system. In Sec. 4.6 we support the analytical findings discussed in the previous sections with numerical results. Finally, in Sec. 4.7 we summarize our conclusions and outline some further perspectives for this work.

4.1   Introduction

Since the observation of the quantum Hall effect in two-dimensional electron gases [68, 106] and the discovery of its relation with topology [70], the study of systems with non-trivial topological properties has become a central topic in condensed matter physics. A very interesting example of such exotic phases of matter are topological insulators [67], which are materials that exhibit insulating properties on their bulk but possess a bulk-boundary correspondence that correlates non-trivial topological indices of the bulk energy bands, such as, e.g., the Berry phase [152], with the existence of conducting edge states under open boundary conditions. There are many different types of topological insulators, which can be systematically classified in terms of their symmetries and dimensionality [79].

In recent years, many efforts have been devoted to implementing topologically non-trivial models in clean and highly controllable systems. Topological states have been observed and characterized in light-based platforms [204] such as photonic crystals [205–209] and photonic quantum walks [210, 211]. Ultracold atoms in optical lattices are also a well-suited environment to implement topological phases of matter [83]. Remarkable achievements in this platform include the realisation of the Haldane [94] and Hofstadter [46, 47] models, the demonstration of a link between topology and out-of-equilibrium dynamics [104], the observation of a many-body topological phase with Rydberg atoms [107], the experimental measurement [103] of the Zak's phase [157], the detection of topological states [100, 212] or the observation of a topological Anderson insulator [81]. There are a wide range of further theoretical proposals for the observation of topological phenomena in cold atoms [213–219], most of which are based around the realisation of artificial gauge fields by laser dressing [46, 47, 220], or periodically driving the lattice system [85, 89]. In both photonic and ultracold atom systems, the possibility to use synthetic dimensions provides a powerful way to explore topological matter [96, 97].

In this Chapter, we explore topologically non-trivial multi-level models that arise naturally for ultracold atoms in excited OAM states of a one-dimensional (1D) chain. We study a concrete example of a diamond chain to demonstrate how this model is rendered

topologically non-trivial due to relative phases in the tunneling amplitudes between OAM $l = 1$ states with opposite circulations. Such a system could be experimentally realized, for instance, by exciting the atoms to the p-band of a conventional optical lattice [58, 135, 221, 222] or by optically transferring OAM [109, 122] to atoms confined to an arrangement of ring-shaped potentials, which can be created by a variety of techniques [109–114, 116]. Remarkably, we find that topological states exist regardless of the values of the parameters of the model, with no topological transition across the gap closing points. This system constitutes an unusual example of a topological insulator with non-quantized values of the Zak's phase due to the inversion axes not crossing the center of any choice of unit cell [157]. In order to circumvent this difficulty, we make use of a recently developed technique [223] to perform the topological characterization. Furthermore, the model belongs to a new class of square-root topological insulators [224, 225], in which the quantized values of the Zak's phases are recovered after taking the square of the bulk Hamiltonian. Fundamentally, this behaviour arises because the OAM $l = 1$ states are equivalent to the p_x and p_y orbitals in optical lattices [58, 135, 221], which have been shown to naturally display non-trivial topological properties in one-[222] and two-[226, 227] dimensional systems due to the parity of their wave functions. In the OAM $l = 1$ basis, the mechanism that yields topological properties is the appearance of relative phases in the tunnelling amplitudes, which are controllable by tuning the geometry of the lattice [137].

Additionally, a proper tuning of the inter-site separation and the central angle can lead to Aharonov-Bohm caging, which consists in the confinement of wave packets due to quantum interference [225, 228–231]. A distinctive advantage regarding the realization of Aharonov-Bohm caging in this model is that, at variance with other proposals [225, 230–232], one does not need to rely on creating synthetic gauge fields [84–86, 233] to produce the magnetic flux required for Aharonov-Bohm caging. Instead, in our OAM $l = 1$ model complex phases with values controlled by the central angle appear naturally in some of the tunneling parameters [137, 234], giving rise to an effective magnetic flux.

4.2 Physical system

The physical system that we consider is depicted in Fig. 4.1. It consists of a gas of ultracold atoms of mass m trapped in a quasi-1D optical lattice with the shape of a diamond chain. The chain is formed by an integer number N_c of unit cells, each of which has a central site A and two sites, B and C, equally separated from A and with the lines connecting them to it forming a relative angle Θ. Each of the sites is the center of a cylindrically symmetric potential with trapping frequency ω such as, for instance, a ring-shaped trap of radius R that generates a potential $V(r) = \frac{1}{2}m\omega^2(r - R)^2$, where
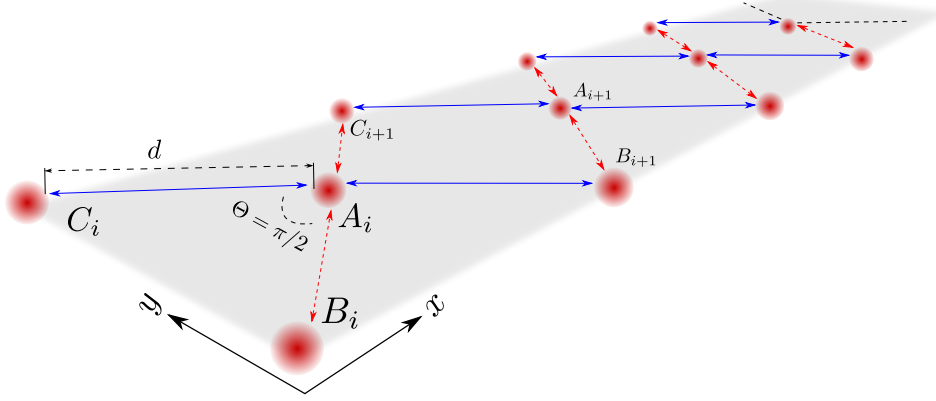
Figure 4.1: Schematic representation of the diamond chain optical lattice loaded with ultracold atoms in the OAM $l = 1$ states considered in this Chapter. The directions along which all the couplings are real are signalled with blue straight arrows, whereas the red dashed arrows are drawn in the directions along which the tunneling couplings involving a change in the circulation, i.e., those whose amplitude is J_1 or J_3 in Eq. (4.4), acquire a π phase.

r is the radial coordinate about the centre of the trap. In the case $R = 0$, the ring trap reduces to a harmonic potential. These potentials define a characteristic length scale $\sigma = \sqrt{\hbar/(m\omega)}$. As shown in Fig. 4.1, we denote the distance between the perimeters of nearest-neighbour rings as d, so that the unit cells are separated by a distance $s = \sqrt{2}d$. The atoms may occupy the two states of total OAM $l = 1$ of each site, $|j_i, \pm\rangle$, where i is an index labelling the unit cell and $j = A, B, C$. Thus, the total field operator of the system reads

$$\hat{\Psi} = \sum_{i=1;\,\alpha=\pm}^{N_c} \phi_\alpha^{A_i}(r_{A_i}, \varphi_{A_i})\hat{a}_\alpha^i + \phi_\alpha^{B_i}(r_{B_i}, \varphi_{B_i})\hat{b}_\alpha^i + \phi_\alpha^{C_i}(r_{C_i}, \varphi_{C_i})\hat{c}_\alpha^i, \tag{4.1}$$

where

$$\phi_\alpha^{j_i}(r_{j_i}, \varphi_{j_i}) = \langle\vec{r}|j_i, \alpha\rangle = \psi(r_{j_i})e^{\alpha i(\varphi_{j_i} - \varphi_0)} \tag{4.2}$$

are the wave functions of the OAM $l = 1$ states with positive/negative circulation ($\alpha = \pm$) with respect to the center of each site j_i, and $\hat{a}_\alpha^i, \hat{b}_\alpha^i, \hat{c}_\alpha^i$ are the annihilation operators of these states at the sites A_i, B_i and C_i, respectively. In the expression of the wave functions (4.2), (r_{j_i}, φ_{j_i}) are polar coordinates with origin at the site j_i and φ_0 is an absolute phase origin, which can be chosen arbitrarily. We will analyze the non-interacting case, for which the Hamiltonian is

$$\hat{H} = \int d\vec{r}\,\hat{\Psi}^\dagger \left[-\frac{\hbar^2\nabla^2}{2m} + V(\vec{r}) \right] \hat{\Psi}, \tag{4.3}$$

where the total potential of the lattice $V(\vec{r})$ can be taken in a good approximation as the truncated combination of all the cylindrically symmetric potentials centered at each of the sites forming the diamond chain. The Hamiltonian (4.3) describes the tunneling dynamics of ultracold atoms between the different coupled traps of the diamond chain restricted to the manifold of $l = 1$ OAM states of each site. In Sec. 2.4 of Chapter 2, we have derived few-state models governing this type of dynamics in systems formed by two and three side-coupled traps which are readily generalizable to larger arrays of cylindrically symmetric traps. In the specific case of the diamond chain geometry studied here, since the strength of the tunneling amplitudes decays rapidly with d [see Fig. 2.4], it is a good approximation to consider coupling terms only between nearest-neighbour sites [234]. Setting the origin of phases φ_0 along the direction of the lines connecting the sites $C_i \leftrightarrow A_i \leftrightarrow B_{i+1}$, so that complex factors $e^{\pm 2i\Theta}$ appear in the tunneling amplitudes along the $B_i \leftrightarrow A_i \leftrightarrow C_{i+1}$ line that involve an exchange of the OAM circulation. Therefore, the Hamiltonian (4.3) can be written in a second-quantized form as

$$
\begin{aligned}
\hat{H} = {}& J_1 \sum_{\alpha=\pm} e^{-2\alpha i\Theta} \hat{b}_\alpha^{1\dagger} \hat{b}_{-\alpha}^1 + \hat{c}_\alpha^{1\dagger} \hat{c}_{-\alpha}^1 \\
& + J_2 \sum_{i=1}^{N_c} \sum_{\alpha=\pm} \left[\hat{a}_\alpha^{i\dagger}(\hat{b}_\alpha^i + \hat{b}_\alpha^{i+1} + \hat{c}_\alpha^i + \hat{c}_\alpha^{i+1}) \right] + \text{h.c.} \\
& + J_3 \sum_{i=1}^{N_c} \sum_{\alpha=\pm} \left[\hat{a}_\alpha^{i\dagger}(e^{-2\alpha i\Theta}\hat{b}_{-\alpha}^i + \hat{b}_{-\alpha}^{i+1} + \hat{c}_{-\alpha}^i + e^{-2\alpha i\Theta}\hat{c}_{-\alpha}^{i+1}) \right] + \text{h.c.},
\end{aligned}
\tag{4.4}
$$

where for simplicity we have dropped the OAM manifold index $l = 1$ from the tunneling amplitudes. Note that for $\Theta \lesssim \pi/3$, the B_i and C_i sites become sufficiently close to each other that their coupling is no longer negligible in a nearest-neighbor approximation. In what follows we set $\Theta = \pi/2$, which translates into a π phase in the tunneling processes involving a change in the circulation along the lines connecting the B_i, A_i and C_{i+1} sites (indicated by red dashed arrows in Fig. 4.1). We point out that the Hamiltonian (4.4) possesses inversion symmetry, so that the Zak's phase associated with each of the energy bands can only take the values 0 and π [157]. Nevertheless, due to the two-fold degeneracy of its energy bands, which will be discussed below, a direct topological characterization would overlook several new features of our model, which can only be revealed and explained after lifting the degeneracies using the exact mappings detailed in Secs. 4.3, 4.4 and 4.5. The time-reversal symmetry operation exchanges the circulation of the states, thus acting on the operators as $\{\hat{a}_\pm^{i(\dagger)}, \hat{b}_\pm^{i(\dagger)}, \hat{c}_\pm^{i(\dagger)}\} \rightarrow \{\hat{a}_\mp^{i(\dagger)}, \hat{b}_\mp^{i(\dagger)}, \hat{c}_\mp^{i(\dagger)}\}$, and reverses the sign of the effective flux, $e^{\pm 2i\Theta} \rightarrow e^{\mp 2i\Theta}$. Therefore, the Hamiltonian (4.4) describing our system is also time-reversal symmetric.

Note that the self-coupling amplitude J_1 is only present at the left corners of the

chain. This is due to the fact that these are the only sites of the chain that are connected to only one site, whereas the rest of sites are connected to an even number of sites and, for the central angle $\Theta = \pi/2$, the contributions to the self-coupling amplitude coming from the different sites interfere destructively [137]. Since the self-coupling at the left edge of the chain is a small effect, for simplicity we will initially take $J_1 = 0$ in the following sections, and then return to the case of a non-zero value for J_1 in Sec. 4.6.

As a starting point of our analysis of the system, we consider a diamond chain of $N_c \to \infty$ unit cells described by the Hamiltonian (4.3) and compute its band structure. To do this calculation, we employ the usual method of Fourier-expanding the annihilation operators as (we consider an inter-cell separation $s \equiv 1$)

$$\hat{o}_\alpha^i = \frac{1}{\sqrt{N_c}}\sqrt{\frac{1}{2\pi}}\int_{-\pi}^{\pi} dk\, e^{-ikx_i}\hat{o}_\alpha^k, \tag{4.5}$$

where x_i is the position of the ith cell along the direction of the diamond chain, k is the quasi-momentum, $o = \{a, b, c\}$ and $\alpha = \pm$. Since there are six states per unit cell (two for each of the three sites), the spectrum has six energy bands. By plugging the expansion (4.5) into the Hamiltonian (4.4), we can re-express it in k-space as

$$\hat{H}^k = \int dk\,\hat{\mathbf{\Psi}}_k^\dagger H_k \hat{\mathbf{\Psi}}_k, \tag{4.6}$$

with $\hat{\mathbf{\Psi}}_k^\dagger = (\hat{a}_+^{k\dagger}, \hat{a}_-^{k\dagger}, \hat{b}_+^{k\dagger}, \hat{b}_-^{k\dagger}, \hat{c}_+^{k\dagger}, \hat{c}_-^{k\dagger})$ and

$$H_k = \begin{pmatrix} 0 & 0 & J_2(1+e^{-ik}) & J_3(-1+e^{-ik}) & J_2(1+e^{-ik}) & J_3(1-e^{-ik}) \\ 0 & 0 & J_3(-1+e^{-ik}) & J_2(1+e^{-ik}) & J_3(1-e^{-ik}) & J_2(1+e^{-ik}) \\ J_2(1+e^{ik}) & J_3(-1+e^{ik}) & 0 & 0 & 0 & 0 \\ J_3(-1+e^{ik}) & J_2(1+e^{ik}) & 0 & 0 & 0 & 0 \\ J_2(1+e^{ik}) & J_3(1-e^{ik}) & 0 & 0 & 0 & 0 \\ J_3(1-e^{ik}) & J_2(1+e^{ik}) & 0 & 0 & 0 & 0 \end{pmatrix}. \tag{4.7}$$

The model possesses also chiral symmetry, as can be seen by the fact that the matrix $\Gamma = \mathrm{diag}\{-1, -1, 1, 1, 1, 1\}$ makes the k-space Hamiltonian fulfill the relation $\Gamma H_k \Gamma = -H_k$. The energy bands, which are given by the eigenvalues of H_k, appear in three degenerate pairs

$$E_1(k) = E_2(k) = 0 \tag{4.8a}$$

$$E_3(k) = E_4(k) = -2\sqrt{(J_2^2 + J_3^2) + \cos k(J_2^2 - J_3^2)} \tag{4.8b}$$

$$E_5(k) = E_6(k) = 2\sqrt{(J_2^2 + J_3^2) + \cos k(J_2^2 - J_3^2)}. \tag{4.8c}$$

The band structure (4.8) always presents an energy gap of size $2\sqrt{2}J_2$ (for $J_2 < J_3$) or $2\sqrt{2}J_3$ (for $J_3 < J_2$). Two of the bands are flat regardless of the values of J_2 and J_3,

and, in the $J_2 = J_3$ limit, which can be realized by setting a large value of d, all of the six bands become flat. These facts are illustrated in Fig. 4.2, where the energy bands (4.8) are plotted using realistic values of J_2 and J_3 computed for different values of d and considering harmonic traps.

The band structure of the diamond chain in the $l = 1$ manifold presents some differences with the one that would be obtained in the manifold of ground states ($l = 0$) of each of the sites. In this manifold, there is only one state per site and one tunneling amplitude J, which does not acquire any phases. The three energy bands that one obtains in this system are $E(k) = 0, \pm 2\sqrt{2}J\cos(k/2)$. Although there is a zero-energy flat band like in the OAM $l = 1$ manifold, the other two bands touch at the points $k = \pm\pi$. However, if a flux through the plaquettes of the diamond chain is introduced, a gap opening occurs [235]. As we will show in Sec. 4.3, the addition of the OAM degree of freedom can be interpreted as the introduction of a net flux through the plaquettes that causes the gap opening in the band structure, see Eqs. (4.8).
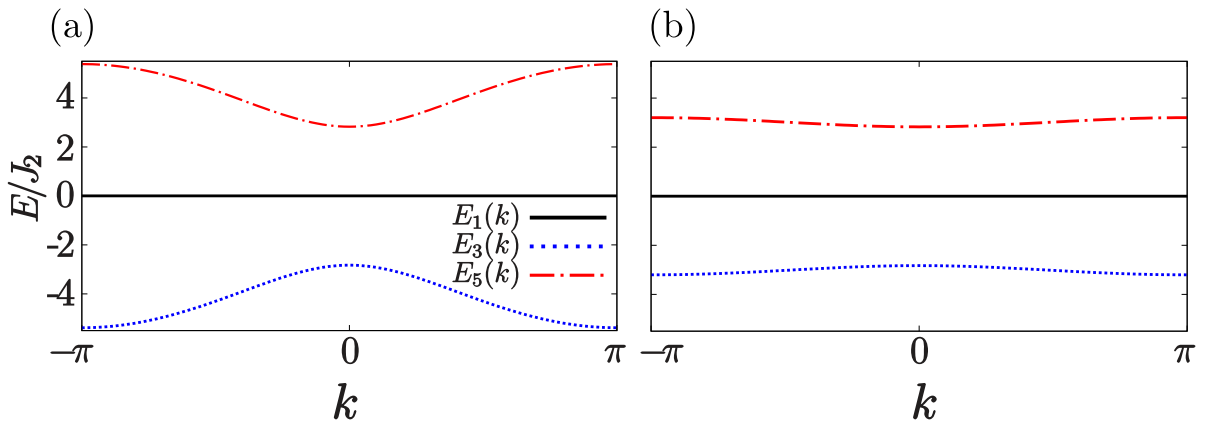
Figure 4.2: Energy bands of the diamond chain in the OAM $l = 1$ manifold computed using the values of J_2 and J_3 that are obtained for harmonic potentials separated by distances (a) $d = 3.5\sigma$, for which $J_3/J_2 = 1.67$, and (b) $d = 6\sigma$, for which $J_3/J_2 = 1.13$ [see Fig. 2.4 (a)].

4.3 Mapping into two decoupled diamond chains

Many features of the band structure can be understood by performing exact mappings of the diamond chain in the OAM $l = 1$ manifold into other models. We start by

considering the following basis rotation

$$|D_i, \pm\rangle = \frac{1}{\sqrt{2}}(|C_i, +\rangle \pm |B_i, +\rangle) \tag{4.9a}$$

$$|F_i, \pm\rangle = \frac{1}{\sqrt{2}}(|C_i, -\rangle \pm |B_i, -\rangle). \tag{4.9b}$$

In this rotated basis, the only non-vanishing matrix elements of the Hamiltonian (4.4) are

$$\left\langle A_i, + \left| \hat{H} \right| D_i, + \right\rangle = \left\langle A_i, + \left| \hat{H} \right| D_{i+1}, + \right\rangle = \sqrt{2} J_2 \tag{4.10a}$$

$$\left\langle A_i, - \left| \hat{H} \right| F_i, + \right\rangle = \left\langle A_i, - \left| \hat{H} \right| F_{i+1}, + \right\rangle = \sqrt{2} J_2 \tag{4.10b}$$

$$\left\langle A_i, + \left| \hat{H} \right| F_i, - \right\rangle = \left\langle A_i, - \left| \hat{H} \right| D_i, - \right\rangle = \sqrt{2} J_3 \tag{4.10c}$$

$$\left\langle A_i, + \left| \hat{H} \right| F_{i+1}, - \right\rangle = \left\langle A_i, - \left| \hat{H} \right| D_{i+1}, - \right\rangle = -\sqrt{2} J_3. \tag{4.10d}$$

The fact that only these couplings survive after the basis rotation (4.9) can be interpreted as a splitting of the original diamond chain with two states per site into two identical and decoupled diamond chains, one in which the $|D_i, +\rangle$ and $|F_i, -\rangle$ states are coupled to the $|A_i, +\rangle$ states and another one in which the $|F_i, +\rangle$ and $|D_i, -\rangle$ states are coupled to the $|A_i, -\rangle$ states. These two chains, which we denote as H^1 and H^2 respectively, are depicted in Fig. 4.3 and are described by the Hamiltonians

$$H^1 = \sum_{i=1}^{N_c} \hat{a}_+^{i\dagger} [\sqrt{2} J_2 (\hat{d}_+^i + \hat{d}_+^{i+1}) + \sqrt{2} J_3 (\hat{f}_-^i - \hat{f}_-^{i+1})] + \text{h.c.} \tag{4.11a}$$

$$H^2 = \sum_{i=1}^{N_c} \hat{a}_-^{i\dagger} [\sqrt{2} J_2 (\hat{f}_+^i + \hat{f}_+^{i+1}) + \sqrt{2} J_3 (\hat{d}_-^i - \hat{d}_-^{i+1})] + \text{h.c.}, \tag{4.11b}$$

where $\hat{d}_\pm^i$ and $\hat{f}_\pm^i$ are the annihilation operators associated with the states $|D_i, \pm\rangle$ and $|F_i, \pm\rangle$, respectively.
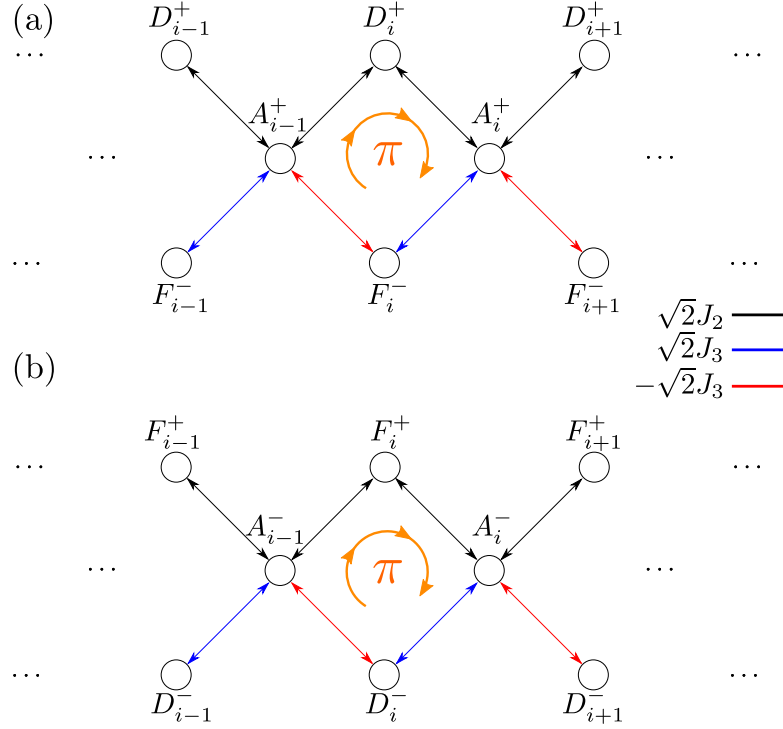
Figure 4.3: Sketch of the decoupled diamond chains H^1 (a) and H^2 (b) that are obtained after performing the basis rotation (4.9).

Each of these two identical Hamiltonians has the same band structure (4.8) as the original one, but with three bands instead of six because there is only one state per site. This makes it possible to understand the degeneracy of the spectrum in the original model, which is a consequence of the symmetry between the two OAM states with different circulations. As shown in Fig. 4.3, the fact that in each chain one of the couplings has an alternating sign can be regarded as a net π flux through the plaquettes of each of the decoupled diamond chains. As we discussed in the previous section, this effective net flux through the plaquettes explains the gap opening in the band structure.

4.4 Mapping into a modified SSH chain

We can gain further insight into the features of the band structure by performing a second basis rotation, given for the H^1 chain by

$$|G_i, +\rangle = \frac{1}{\sqrt{J_2^2 + J_3^2}} (J_2 |D_i, +\rangle + J_3 |F_i, -\rangle) \tag{4.12a}$$

$$|G_i, -\rangle = \frac{1}{\sqrt{J_2^2 + J_3^2}} (J_3 |D_i, +\rangle - J_2 |F_i, -\rangle). \tag{4.12b}$$

For the H^2 chain, an equivalent mapping can be defined by substituting F by D everywhere in eqs. (4.12). Since the two chains are identical, from now on we will base the discussion on the H^1 chain and indicate the results that are obtained for the H^2 chain.

The basis rotation (4.12) reduces even further the number of non-vanishing matrix elements, which now are

$$\left\langle A_i, + \left| H^1 \right| G_i, + \right\rangle = \sqrt{2}\sqrt{J_2^2 + J_3^2} \equiv \Omega_1 \tag{4.13a}$$

$$\left\langle A_i, + \left| H^1 \right| G_{i+1}, - \right\rangle = \frac{2\sqrt{2}J_2 J_3}{\sqrt{J_2^2 + J_3^2}} \equiv \Omega_2 \tag{4.13b}$$

$$\left\langle A_i, + \left| H^1 \right| G_{i+1}, + \right\rangle = \frac{\sqrt{2}(J_2^2 - J_3^2)}{\sqrt{J_2^2 + J_3^2}} \equiv \Omega_3 \tag{4.13c}$$

As shown in Fig. 4.4 (a), the couplings (4.13) between the states (4.12) can be represented in a graphical way as a modified SSH model, consisting of the usual SSH chain [161] with alternating strong (Ω_1) and weak (Ω_3) couplings and extra dangling sites coupled to the chain with a strength Ω_2.
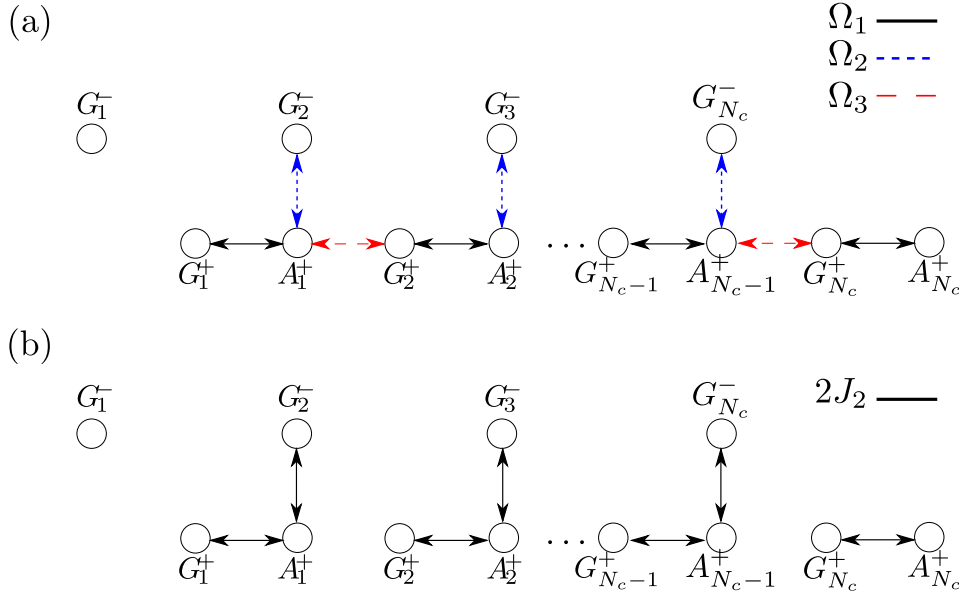

Figure 4.4: (a) Sketch of the modified SSH chain that is obtained after performing the basis rotation (4.12) on the H^1 diamond chain that was obtained after the first basis rotation (4.9). (b) Modified SSH chain in the $\Omega_3 = 0$ ($J_2 = J_3$) limit, where the bulk sites become decoupled in trimers and an isolated dimer appears at the right edge.

Thus, the Hamiltonian of this modified SSH chain reads

$$H^1_{SSH} = \sum_{i=1}^{N_c} \hat{a}^{i\dagger}_+ (\Omega_1 \hat{g}^i_+ + \Omega_2 \hat{g}^{i+1}_- + \Omega_3 \hat{g}^{i+1}_+) + \text{h.c.}, \tag{4.14}$$

where $\hat{g}^i_\pm$ are the annihilation operators associated with the states $|G_i, \pm\rangle$. This modified SSH model allows us to clarify the origin of the flat bands and the in-gap edge states. Next, we discuss separately these two features of the model.

4.4.1 Flat-band states

Zero-energy states

First, let us consider the general case $J_2 \neq J_3$ and therefore $\Omega_3 \neq 0$, as shown in Fig. 4.4 (a). In this case, two of the three energy bands of H^1 are dispersive, but there is always a zero-energy flat band. This band also appears in a diamond chain in which the atoms occupy the ground state ($l = 0$) manifold, so its presence is insensitive to the existence of a net flux through the plaquettes [235]. In order to understand better the flat-band states of the OAM $l = 1$ manifold, let us first examine the simpler case of the ground state manifold. In that manifold, there is only one tunneling amplitude J which does not acquire any phase. Hence, by imposing in each cell i of the chain the condition that the site A_i is not populated due to destructive interference, one finds a zero-energy eigenstate localized in ith unit cell, given by $\frac{1}{\sqrt{2}}(|B_i\rangle - |C_i\rangle)$. Similarly, in the OAM $l = 1$ manifold we can find zero-energy states by imposing the destructive interference condition on the A sites. In the modified SSH chain picture, this is achieved by populating appropriately in every two unit cells the states $|G_i, +\rangle$, $|G_i, -\rangle$ and $|G_{i+1}, -\rangle$ in such a way that there is destructive interference and neither the $|A_i, +\rangle$ nor the $|A_{i-1}, +\rangle$ states are populated. The states that fulfil this condition in every pair of consecutive unit cells are

$$\left|W^1_{0,i}\right\rangle = \frac{1}{\sqrt{C}} \left(\frac{\Omega_3}{\Omega_2} |G_i, -\rangle - |G_i, +\rangle + \frac{\Omega_1}{\Omega_2} |G_{i+1}, -\rangle \right), \tag{4.15}$$

where C is a normalization constant. It can be readily checked that this is a zero-energy eigenstate of the Hamiltonian (4.14). Additionally, at the left edge of the chain the state $|G_1, -\rangle$ is decoupled from the rest of states and therefore it is a zero-energy state too. Similarly, in the H^2 chain one can find a state $\left|W^2_{0,i}\right\rangle$ such that $H^2_{SSH} \left|W^2_{0,i}\right\rangle = 0$. By reverting the basis rotations (4.12) and (4.9), one can find expressions for the states

$\left|W_{0,i}^1\right\rangle$ and $\left|W_{0,i}^2\right\rangle$ in the original basis of OAM $l = 1$ states

$$\left|W_{0,i}^1\right\rangle = \frac{1}{\sqrt{2}\Omega_1} \left[J_3(|C_{i+1}, +\rangle + |B_{i+1}, +\rangle - |C_i, +\rangle - |B_i, +\rangle) \right.$$
$$\left. + J_2(|B_i, -\rangle + |B_{i+1}, -\rangle - |C_i, -\rangle - |C_{i+1}, -\rangle) \right] \qquad (4.16\text{a})$$
$$\left|W_{0,i}^2\right\rangle = \frac{1}{\sqrt{2}\Omega_1} \left[J_3(|C_{i+1}, -\rangle + |B_{i+1}, -\rangle - |C_i, -\rangle - |B_i, -\rangle) \right.$$
$$\left. + J_2(|B_i, +\rangle + |B_{i+1}, +\rangle - |C_i, +\rangle - |C_{i+1}, +\rangle) \right]. \qquad (4.16\text{b})$$

From the expressions (4.16), we observe that the most compact form of the localized states doubles in size with respect to the ground state ($l = 0$) manifold, occupying four sites instead of the two in the latter case and spanning two unit cells instead of one. In Fig. 4.5 we show examples of numerical density plots of (a) zero-energy flat-band states and (b) dispersive states in a diamond chain of $N_c = 10$ unit cells. The chain is formed by harmonic traps with a separation between nearest-neighbour sites $d = 6\sigma$, for which $J_3/J_2 = 1.13$. The two states of Fig. 4.5 (a) have no population at the central (A) sites of the chain, and are expanded across all the unit cells of the lattice because they contain components of many maximally localized states, given by Eqs. (4.16). The state of the right panel of Fig. 4.5 (a) also contains a component of the zero-energy decoupled mode localized at the left edge $|G_1, -\rangle$ [see Fig. 4.4 (b)]. Fig. 4.5 (b) shows the two degenerate ground states of the system, which belong to the dispersive bands of lowest energy. Differently from the flat-band states of Fig. 4.5 (a), these states span all the sites of the chain.
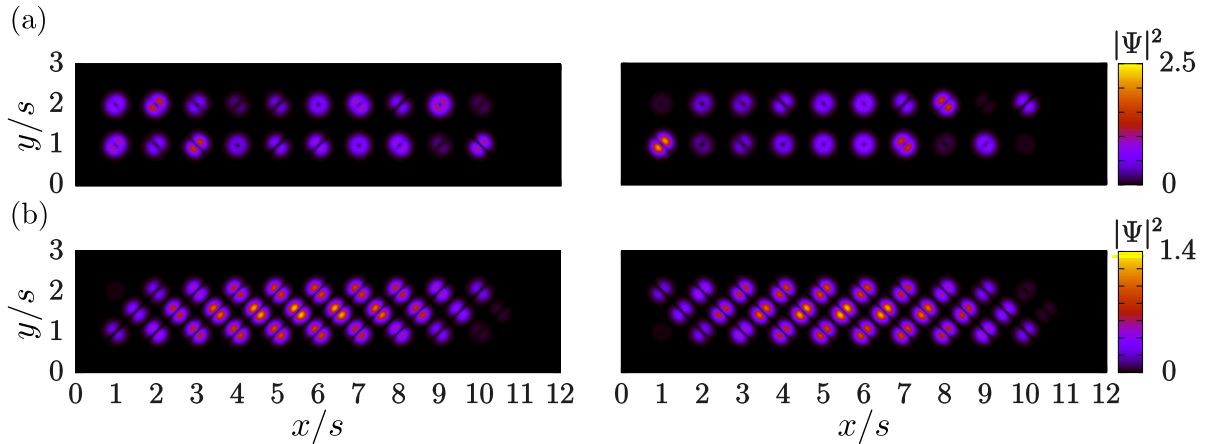

Figure 4.5: Numerical density profiles of (a) two states of the zero-energy flat band and (b) the two degenerate ground states in a diamond chain of $N_c = 10$ units cells composed of harmonic traps with an inter-site separation $d = 6\sigma$, for which $J_3/J_2 = 1.13$.

Flat bands in the $J_2 = J_3$ limit

As we discussed when we computed the band structure, in the $J_2 = J_3$ limit (which physically corresponds to having a large inter-trap separation d), the two energy bands that are generally dispersive become flat with energies $E = \pm 2\sqrt{2}J_2$. The corresponding eigenstates can also be analytically derived in the modified SSH chain picture. In this particular limit, we have $\Omega_3 = 0$ and $\Omega_1 = \Omega_2 = 2J_2$. Thus, as shown in Fig. 4.4 (b), each trio of states in two consecutive unit cells $|G_i, +\rangle$, $|A_i, +\rangle$ and $|G_{i+1}, -\rangle$ becomes decoupled from the rest of the chain and forms a three-site system that can be readily diagonalized. When doing so, apart from the zero-energy state that we have already discussed one finds the two eigenstates

$$\left| W^1_{\pm,i} \right\rangle = \frac{1}{2} \left(|G_i, +\rangle \pm \sqrt{2} |A_i, +\rangle + |G_{i+1}, -\rangle \right), \tag{4.17}$$

such that

$$H^1_{SSH}(\Omega_3 = 0) \left| W^1_{\pm,i} \right\rangle = \pm 2\sqrt{2}J_2 \left| W^1_{\pm,i} \right\rangle. \tag{4.18}$$

Similarly, in the H^2 chain there are two states $\left| W^2_{\pm,i} \right\rangle$ in every pair of consecutive unit cells such that $H^2_{SSH}(\Omega_3 = 0) \left| W^2_{\pm,i} \right\rangle = \pm 2\sqrt{2}J_2 \left| W^2_{\pm,i} \right\rangle$. By reverting again the basis rotations (4.9) and (4.12), we find the following expressions for these states in the original basis of OAM $l = 1$ states

$$\left| W^1_{\pm,i} \right\rangle = \frac{1}{4} \left[|C_i, +\rangle + |B_i, +\rangle + |C_{i+1}, +\rangle + |B_{i+1}, +\rangle \right.$$
$$\left. + |C_i, -\rangle - |B_i, -\rangle - |C_{i+1}, -\rangle + |B_{i+1}, -\rangle \right] \pm \frac{1}{\sqrt{2}} |A_i, +\rangle \tag{4.19a}$$

$$\left| W^2_{\pm,i} \right\rangle = \frac{1}{4} \left[|C_i, -\rangle + |B_i, -\rangle + |C_{i+1}, -\rangle + |B_{i+1}, -\rangle \right.$$
$$\left. + |C_i, +\rangle - |B_i, +\rangle - |C_{i+1}, +\rangle + |B_{i+1}, +\rangle \right] \pm \frac{1}{\sqrt{2}} |A_i, -\rangle. \tag{4.19b}$$

Like the zero-energy states, all these states are localized in two consecutive unit cells of the original diamond chain, but now with the difference that they do not form destructive interferences on the A sites and have thus non-zero energy values.

4.4.2   Aharonov-Bohm caging

Aharonov-Bohm caging is a phenomenon of localization of wave packets in a periodic structure that occurs due to quantum interference. Although it was originally studied in the context of tight-binding electrons in two-dimensional lattices threaded by a magnetic flux [228], its occurrence has been predicted in other physical platforms. In particular, it has been suggested and experimentally shown that Aharonov-Bohm cages can be

realized in photonic lattices with a diamond-chain shape in the presence of artificial gauge fields [225, 230, 231].

In the $J_2 = J_3$ limit (i.e., for large values of the inter-trap separation d), the system studied here also presents Aharonov-Bohm caging. In this situation, the eigenstates (4.19) are localized in the unit cells i and $i + 1$, forming two two-fold degenerate flat bands of energies $\pm 2\sqrt{2}J_2$ in the spectrum of the full diamond chain. The states localized at the central site of the ith cell, $|A_i, \pm\rangle$, can be expressed in terms of these flat-band states as

$$|A_i, +\rangle = \frac{1}{\sqrt{2}} \left(\left|W^1_{+,i}\right\rangle - \left|W^1_{-,i}\right\rangle \right) \tag{4.20a}$$

$$|A_i, -\rangle = \frac{1}{\sqrt{2}} \left(\left|W^2_{+,i}\right\rangle - \left|W^2_{-,i}\right\rangle \right). \tag{4.20b}$$

Let us now consider explicitly the time evolution of an initial state of the form $|\Psi(t = 0)\rangle^{\pm} = |A_i, \pm\rangle$ in the $J_2 = J_3$ limit:

$$
\begin{aligned}
|\Psi(t)\rangle^{\pm} &= \frac{1}{\sqrt{2}} \left(e^{i2\sqrt{2}J_2 t} \left|W^{1/2}_{+,i}\right\rangle - e^{-i2\sqrt{2}J_2 t} \left|W^{1/2}_{-,i}\right\rangle \right) \\
&= \frac{1}{\sqrt{2}} \left[\left(e^{i2\sqrt{2}J_2 t} - e^{-i2\sqrt{2}J_2 t} \right) \frac{1}{4} \left(|C_i, \pm\rangle + |B_i, \pm\rangle + |C_{i+1}, \pm\rangle + |B_{i+1}, \pm\rangle \right. \right. \\
&\quad + |C_i, \mp\rangle - |B_i, \mp\rangle - |C_{i+1}, \mp\rangle + |B_{i+1}, \mp\rangle \Big) + \left(e^{i2\sqrt{2}J_2 t} + e^{-i2\sqrt{2}J_2 t} \right) \frac{1}{\sqrt{2}} |A_i, \pm\rangle \Big] \\
&= \frac{i \sin 2\sqrt{2}J_2 t}{2\sqrt{2}} \left(|C_i, \pm\rangle + |B_i, \pm\rangle + |C_{i+1}, \pm\rangle + |B_{i+1}, \pm\rangle \right. \\
&\quad + |C_i, \mp\rangle - |B_i, \mp\rangle - |C_{i+1}, \mp\rangle + |B_{i+1}, \mp\rangle \Big) + \cos 2\sqrt{2}J_2 t \, |A_i, \pm\rangle. \tag{4.21}
\end{aligned}
$$

From Eq. (4.21), we observe that the population oscillates coherently from the initial state $|A_i, \pm\rangle$ to a combination of states belonging to the cells i and $i + 1$ with an angular frequency $2\sqrt{2}J_2$, given by the absolute value of the energies of the flat-band states. This coherent oscillation is illustrated in Fig. 4.6 (a), where we show different snapshots of the density profile of a wave packet prepared initially in the state $|A_3, +\rangle$ of a diamond chain of $N_c = 5$ unit cells in the $J_2 = J_3$ limit. More generally, since the $|A_i, +\rangle$ and $|A_i, -\rangle$ states belong respectively to the decoupled chains H^1 and H^2, any initial state consisting of a linear combination of them evolves in time by oscillating coherently to the states $|B_i, \pm\rangle$, $|C_i, \pm\rangle$, $|B_{i+1}, \pm\rangle$ and $|C_{i+1}, \pm\rangle$, that is, it remains confined in the Aharonov-Bohm cages of the diamond chain. This effect is illustrated in Fig. 4.6 (b), which shows, for a chain of $N_c = 5$ unit cells in the $J_3/J_2 = 1$ limit, the numerically computed time evolution of the population of the states $|A_3, +\rangle$ (black solid lines) and $|A_3, -\rangle$ (blue dotted lines) and of the total sum of the populations of the states $|B_3, \pm\rangle, |C_3, \pm\rangle, |A_3, \pm\rangle, |B_4, \pm\rangle, |C_4, \pm\rangle$ (red dash-dotted lines) after taking

(a)

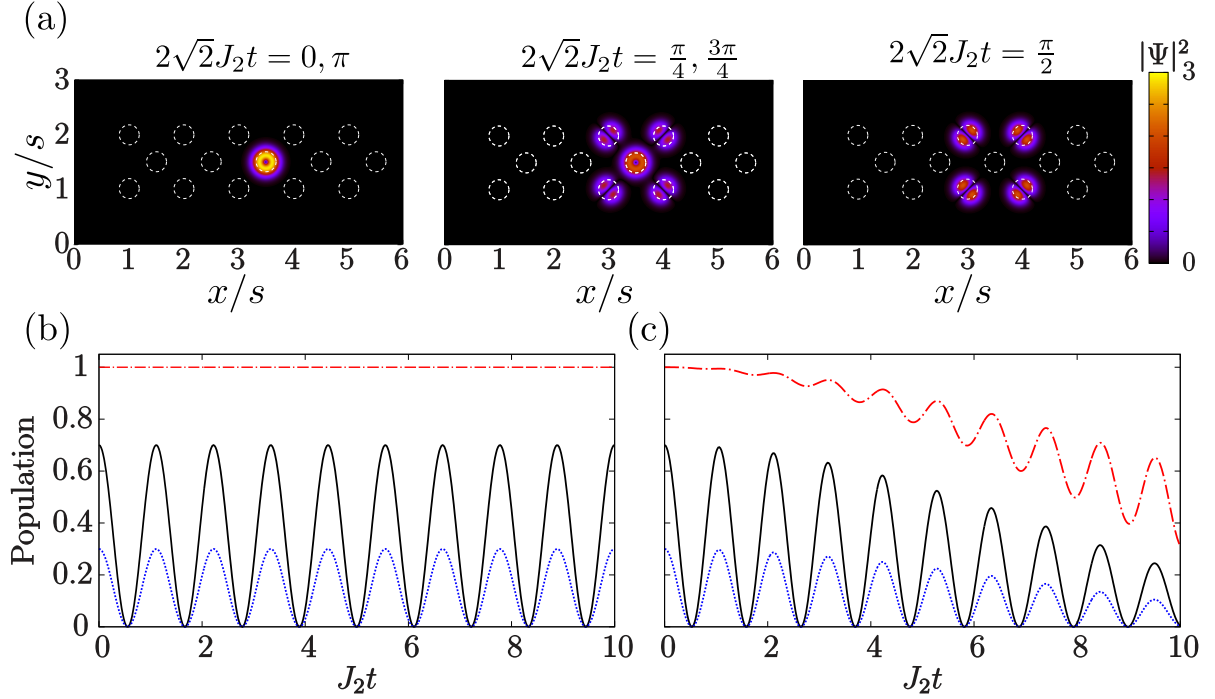(b)   (c)

Figure 4.6: Aharonov-Bohm caging in a diamond chain of $N_c = 5$ unit cells. (a) Snap-shots at different times of the density profiles corresponding to the time evolution of a wave packet initially prepared in the state $|A_3, +\rangle$ in the perfect caging limit, $J_2/J_3 = 1$. (b),(c) Numerically computed time evolution of the population of the states $|A_3, +\rangle$ (black solid lines) and $|A_i, -\rangle$ (blue dotted lines) and of the total sum of the popula-tions of the states $|B_3, \pm\rangle , |C_3, \pm\rangle , |A_3, \pm\rangle , |B_4, \pm\rangle , |C_4, \pm\rangle$ (red dash-dotted lines) after taking the initial state $|\Psi\rangle = \sqrt{0.7}\,|A_3, +\rangle + \sqrt{0.3}\,|A_3, -\rangle$. The tunneling parameters fulfill the relations (b) $J_3/J_2 = 1$ and (c) $J_3/J_2 = 1.1$.

the initial state $|\Psi\rangle = \sqrt{0.7}\,|A_3, +\rangle + \sqrt{0.3}\,|A_3, -\rangle$. Although the caging effect is only perfect in the $J_3/J_2 = 1$ limit, we still expect it to prevail during the initial stage of the time evolution for values of the J_3/J_2 ratio sufficiently close to 1. In Fig. 4.6 (c) we plot the time evolution of the same quantites as in Fig. 4.6 (b) considering the same system and initial state, but taking now a ratio between the tunneling rates $J_3/J_2 = 1.1$. In this situation, we observe that for times $J_2 t \lesssim 2$ almost all of the population remains inside the cage. Then, the damping of the coherent oscillations of the populations of the $|A_3, \pm\rangle$ states starts to be more significant, and at the final time $J_2 t = 10$ the population inside the cage represents about 40% of the total.

4.4.3   In-gap edge states in the $\Omega_3 = 0$ limit

If one considers a chain of finite size, in the $\Omega_3 = 0$ (i.e., $J_2 = J_3$) limit there are two states at the right edge of the chain, $|G_{N_c}, +\rangle$ and $|A_{N_c}, +\rangle$, forming a dimer which is decoupled from the rest of the chain, as can be seen in Fig. 4.4 (b). Thus, at the right edge of the chain there are two additional eigenstates

$$\left|E_\pm^1\right\rangle = \frac{1}{\sqrt{2}}(|G_{N_c}, +\rangle \pm |A_{N_c}, +\rangle), \tag{4.22}$$

such that

$$H_{SSH}^1(\Omega_3 = 0)\left|E_\pm^1\right\rangle = \pm 2J_2\left|E_\pm^1\right\rangle \tag{4.23}$$

Similarly, in the H^2 chain there are two edge eigenstates, $H_{SSH}^2(\Omega_3 = 0)\left|E_\pm^2\right\rangle = \pm 2J_2\left|E_\pm^2\right\rangle$. By reverting the basis rotations (4.9) and (4.12), we find the following expressions for these edge states in the original basis of OAM $l = 1$ states

$$\left|E_\pm^1\right\rangle = \frac{1}{2\sqrt{2}}\left(|C_{N_c}, +\rangle + |B_{N_c}, +\rangle + |C_{N_c}, -\rangle - |B_{N_c}, -\rangle \pm 2\left|A_{N_c}, +\rangle\right) \tag{4.24a}$$

$$\left|E_\pm^2\right\rangle = \frac{1}{2\sqrt{2}}\left(|C_{N_c}, -\rangle + |B_{N_c}, -\rangle + |C_{N_c}, +\rangle - |B_{N_c}, +\rangle \pm 2\left|A_{N_c}, -\rangle\right) \tag{4.24b}$$

Since the energies of the flat band states are $\pm 2\sqrt{2}J_2$, these edge states appear as in-gap states in the energy spectrum, which is suggestive of a possible topological origin. Furthermore, edge-localized states also appear for $J_2 \neq J_3$, as illustrated in the numerical profiles of Fig. 4.7, which correspond to a chain of $N_c = 10$ unit cells formed by harmonic traps with a separation $d = 6\sigma$, for which $J_3/J_2 = 1.13$.
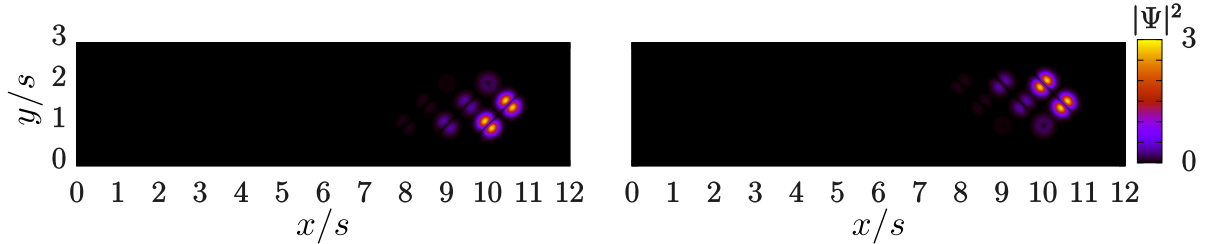
Figure 4.7: Numerical density profiles of two edge states in a diamond chain of $N_c = 10$ units cells composed of harmonic traps with an inter-site separation $d = 6\sigma$, for which $J_3/J_2 = 1.13$.

In order to see if the model is indeed topologically non-trivial, we should compute the Zak's phases of the different bands [157]. However, this is not possible in the original model (4.4) due to the degeneracy of the bands (4.8). In the mapped models (4.11) and

(4.14) the bands are no longer degenerate, but there is no inversion symmetry and thus the Zak's phase is not quantized. It is therefore necessary to perform a third mapping into an inversion-symmetric model in order to recover quantized Zak's phases for the bands, therefore allowing for a topological characterization of the model.

4.5   Mapping into a modified diamond chain and topological characterization

In order to map the modified SSH chain H^1 into a model that allows to compute meaningful Zak's phases, we take two consecutive unit cells, i and $i+1$, of this relabelled chain and define a basis rotation into 6 new states, which we shall denote as $|i, j\rangle$ ($j = 1, ..., 6$), in the following way

$$|i, 1\rangle = \frac{1}{\sqrt{t_1^2 + t_2^2}} (t_2 |G_{i+1}, +\rangle - t_1 |G_{i+1}, -\rangle) \tag{4.25a}$$

$$|i, 2\rangle = \frac{1}{\sqrt{t_1^2 + t_2^2}} (t_1 |G_{i+1}, +\rangle + t_2 |G_{i+1}, -\rangle) \tag{4.25b}$$

$$|i, 3\rangle = |A_{i+1}, +\rangle \tag{4.25c}$$

$$|i, 4\rangle = \frac{1}{\sqrt{t_1^2 + t_2^2}} (t_2 |G_i, +\rangle - t_1 |G_i, -\rangle) \tag{4.25d}$$

$$|i, 5\rangle = \frac{1}{\sqrt{t_1^2 + t_2^2}} (t_1 |G_i, +\rangle + t_2 |G_i, -\rangle) \tag{4.25e}$$

$$|i, 6\rangle = |A_i, +\rangle , \tag{4.25f}$$

where the parameters t_1 and t_2 fulfill the relations $2t_1 t_2 = \Omega_1 \Omega_2$ and $t_1^2 - t_2^2 = \Omega_1 \Omega_3$. After applying this rotation, a modified SSH chain of N_c unit cells gets mapped into a modified diamond chain of $N_c/2$ unit cells with 6 states per unit cell and alternate t_1 and t_2 hopping constants. The resulting chain has an integer or half-integer number of unit cells depending on the parity of N_c. However, since there is no qualitative difference between the two cases, from now on we restrict ourselves to the case when N_c is even. The mapping process and the resulting modified diamond chain are illustrated in Fig. 4.8. Note also that, under this mapping, the number of bands gets doubled (6 instead of 3) but the Brillouin zone is folded in half, such that one has the same number of allowed energy states before and after the mapping, as expected. The Hamiltonian

describing this modified diamond chain reads

$$\hat{H}^1_{t_1 t_2} = \sum_{i=1}^{N_c/2} \hat{a}_i^{2\dagger}(t_1 \hat{a}_i^1 + t_2 \hat{a}_i^4) + \hat{a}_i^{3\dagger}(t_2 \hat{a}_i^1 + t_4 \hat{a}_i^4) + \text{h.c.}$$

$$+ \sum_{i=1}^{N_c/2} \hat{a}_i^{5\dagger}(t_2 \hat{a}_i^4 + t_1 \hat{a}_{i+1}^1) + \hat{a}_i^{6\dagger}(t_1 \hat{a}_i^4 + t_2 \hat{a}_{i+1}^1) + \text{h.c.}, \qquad (4.26)$$

where $\hat{a}_i^j$ are the annihilation operators associated with the states $|i,j\rangle$ ($j=1,...,6$). The modified diamond chain (4.26) has inversion symmetry, and thus the Zak's phases of its bands are quantized.
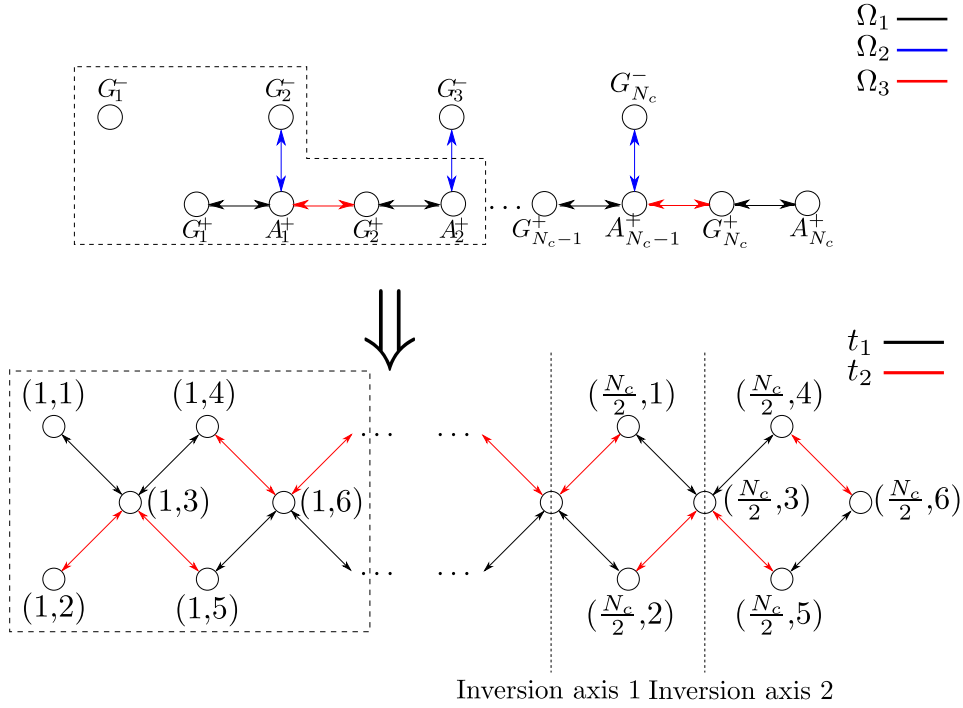

Figure 4.8: Schematic representation of the mapping from the modified SSH H^1 chain into a diamond chain with alternate hoppings. The two possible choices for the inversion symmetry axis within a given unit cell, under periodic boundary conditions, are also shown. Note that neither of them are localized at the central axis of the unit cell.

The topological characterization of this model was addressed in [236]. As shown in Fig. 4.8, the inversion symmetry axes are not in the center of the unit cells, and it is thus necessary to use a generalized formula to compute the Zak's phases of the bands [223]. Taking this issue into account, in [236] it was shown that the model of the modified diamond chain with alternate hoppings hosts topologically protected edge states. Thus, by reverting the mapping we can conclude that the edge states of the original diamond

chain in the OAM $l = 1$ manifold (4.4) are topologically protected, so we expect them to be robust against changes in the condition $J_2 = J_3$, and to disappear completely only on the gap closing points $J_2 = 0, J_3 \neq 0$ and $J_3 = 0, J_2 \neq 0$. As we will discuss in more detail in Sec. 4.6, after crossing these points the edge states also survive, implying the absence of a topological transition in the model.

4.5.1 Square-root topological insulator

Alternatively, the topological characterization of the model obtained after the basis rotation (4.25) can be performed by regarding it as a square-root topological insulator, as described for a photonic system in [224, 225]. The k-space Hamiltonian of the model of the modified diamond chain (4.26) reads (we take the inter-cell spacing $s \equiv 1$):

$$\hat{H}^1_{t_1 t_2} = \sum_k \hat{\mathbf{b}}^\dagger_k \hat{H}^1_{t_1 t_2}(k) \hat{\mathbf{b}}_k,$$

$$\hat{H}^1_{t_1 t_2}(k) = \begin{pmatrix} 0 & 0 & t_1 & 0 & 0 & t_2 e^{-ik} \\ 0 & 0 & t_2 & 0 & 0 & t_1 e^{-ik} \\ t_1 & t_2 & 0 & t_1 & t_2 & 0 \\ 0 & 0 & t_1 & 0 & 0 & t_2 \\ 0 & 0 & t_2 & 0 & 0 & t_1 \\ t_2 e^{ik} & t_1 e^{ik} & 0 & t_2 & t_1 & 0 \end{pmatrix}, \tag{4.27}$$

where $\hat{\mathbf{b}}^\dagger_k = (\hat{b}^\dagger_{k,1}, \hat{b}^\dagger_{k,2}, \hat{b}^\dagger_{k,3}, \hat{b}^\dagger_{k,4}, \hat{b}^\dagger_{k,5}, \hat{b}^\dagger_{k,6})$ and $\hat{b}^\dagger_{k,i}$ is the bosonic creation operator acting at the ith component of the momentum state k. Then, the model resulting from squaring the bulk Hamiltonian (4.27) reads

$$\left[\hat{H}^1_{t_1 t_2}(k)\right]^2 =$$
$$\begin{pmatrix} t_1^2 + t_2^2 & 2t_1 t_2 & 0 & t_1^2 + t_2^2 e^{-ik} & t_1 t_2(1 + e^{-ik}) & 0 \\ 2t_1 t_2 & t_1^2 + t_2^2 & 0 & t_1 t_2(1 + e^{-ik}) & t_2^2 + t_1^2 e^{-ik} & 0 \\ 0 & 0 & 2(t_1^2 + t_2^2) & 0 & 0 & 2t_1 t_2(1 + e^{-ik}) \\ t_1^2 + t_2^2 e^{ik} & t_1 t_2(1 + e^{ik}) & 0 & t_1^2 + t_2^2 & 2t_1 t_2 & 2t_1 t_2 \\ t_1 t_2(1 + e^{ik}) & t_2^2 + t_1^2 e^{ik} & 0 & 2t_1 t_2 & t_1^2 + t_2^2 & 0 \\ 0 & 0 & 2t_1 t_2(1 + e^{ik}) & 0 & 0 & 2(t_1^2 + t_2^2) \end{pmatrix}.$$
$$\tag{4.28}$$

By inverse Fourier-transforming the $k-$space squared Hamiltonian (4.28), one arrives at the following real-space squared Hamiltonian, which is composed of two independent

terms

$$\left[\hat{H}_{t_1 t_2}^1\right]^2 = \hat{H}_{LC} + \hat{H}_{2LL}, \tag{4.29}$$

$$\hat{H}_{LC} = \sum_{j=1}^{N_c/2} \sum_{i=3,6} 2(t_1^2 + t_2^2)\hat{b}_{i,j}^\dagger \hat{b}_{i,j} + \sum_{j=1}^{N_c/2} 2t_1 t_2 \left(\hat{b}_{3,j}^\dagger \hat{b}_{6,j} + \hat{b}_{6,j}^\dagger \hat{b}_{3,j+1} + \text{h.c.}\right), \tag{4.30}$$

$$\hat{H}_{2LL} = \sum_{j=1}^{N_c/2} \sum_{i=1,2,4,5} (t_1^2 + t_2^2)\hat{b}_{i,j}^\dagger \hat{b}_{i,j} + \sum_{j=1}^{N_c/2} \left[t_1^2\left(\hat{b}_{1,j}^\dagger \hat{b}_{4,j} + \hat{b}_{5,j}^\dagger \hat{b}_{2,j+1}\right) + t_2^2\left(\hat{b}_{2,j}^\dagger \hat{b}_{5,j} + \hat{b}_{4,j}^\dagger \hat{b}_{1,j+1}\right) + \text{h.c.} \right.$$

$$+ \sum_{j=1}^{N_c/2} t_1 t_2 \left(2\hat{b}_{1,j}^\dagger \hat{b}_{2,j} + 2\hat{b}_{4,j}^\dagger \hat{b}_{5,j} + \hat{b}_{1,j}^\dagger \hat{b}_{5,j} + \hat{b}_{2,j}^\dagger \hat{b}_{4,j} + \hat{b}_{4,j}^\dagger \hat{b}_{2,j+1} + \hat{b}_{5,j}^\dagger \hat{b}_{1,j+1} + \text{h.c.}\right) \Bigg]. \tag{4.31}$$

The first term, described by $\hat{H}_{LC}$, is a linear chain with inter-site coupling $2t_1 t_2$ and a constant on-site potential $2(t_1^2 + t_2^2)$, as shown in the bottom of Fig. 4.9. This linear chain is topologically trivial, meaning that one does not need to consider it in order to account for the topological properties of the squared model as a whole. The other subsystem, described by $\hat{H}_{2LL}$, is a two-leg ladder which has intra-leg couplings t_1^2 and t_2^2 and inter-leg crossed and vertical couplings $t_1 t_2$ and $2t_1 t_2$, respectively, as depicted at the top of Fig. 4.9. The second inter-leg term couples sites within the same sublattice, therefore chiral symmetry is lost under this squaring operation. As shown in Fig. 4.9, it is possible to choose for this two-leg ladder inversion axes that cross the center of the unit cell. Therefore, by applying the squaring operation we recover quantized values of the Zak's phases associated with the different bands, and we can compute them in the usual way. The squared Hamiltonian (4.28) has the following squared energy band structure

$$E_1^2(k) = E_2^2(k) = 0 \tag{4.32a}$$

$$E_3^2(k) = E_4^2(k) = 2(t_1^2 + t_2^2 - t_1 t_2 \sqrt{2(1 + \cos k)}) \tag{4.32b}$$

$$E_5^2(k) = E_6^2(k) = 2(t_1^2 + t_2^2 + t_1 t_2 \sqrt{2(1 + \cos k)}). \tag{4.32c}$$

The dispersive squared energy bands $E_3^2(k)$ and $E_4^2(k)$ are due to the contribution of the linear chain. In Fig. 4.10, the band structure (4.32) is shown for the choice of parameters $t_2 = 0.2t_1$. Due to the degeneracy of the flat band, in order to perform the topological characterization of the squared model we have to consider the cumulative Zak's phases through the Wilczek-Zee formulation [225, 237],

$$\gamma_{1,2} = \int_{-\pi}^{\pi} dk \, \text{Tr}\Big(A(k)\Big), \tag{4.33}$$

$$A(k)^{ij} = -i\left\langle u_i(k) \left| \frac{d}{dk} \right| u_j(k) \right\rangle, \tag{4.34}$$

where the $i, j = 1, 2$ indices in the Berry connection element $A(k)^{ij}$ are restricted to the flat band subspace with eigenstates $\{|u_1(k)\rangle, |u_2(k)\rangle\}$. We find a non-trivial Zak's phase $\gamma_{1,2} = \pi$ for all finite sets of (t_1, t_2), reflecting the topological nature of the edge states. By taking the square-root operation, the topological properties of this squared model are directly reflected in the original one.

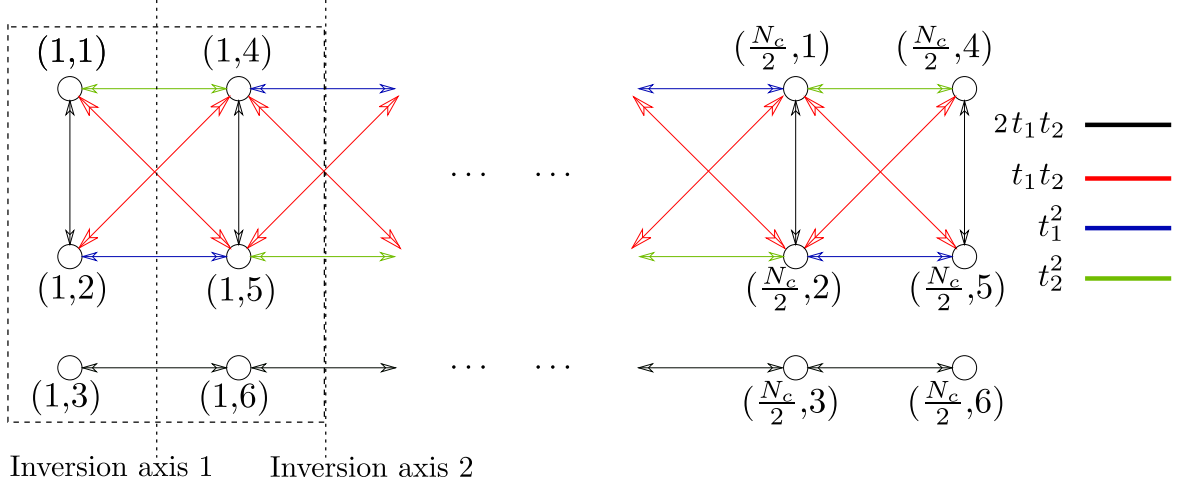Figure 4.9: Sketch of the tight-binding model obtained after squaring the bulk Hamiltonian of the modified diamond chain model (4.27). The upper and lower plots represent respectively the two-leg ladder described by the squared Hamiltonian (4.31) and the linear chain described by the squared Hamiltonian (4.30).
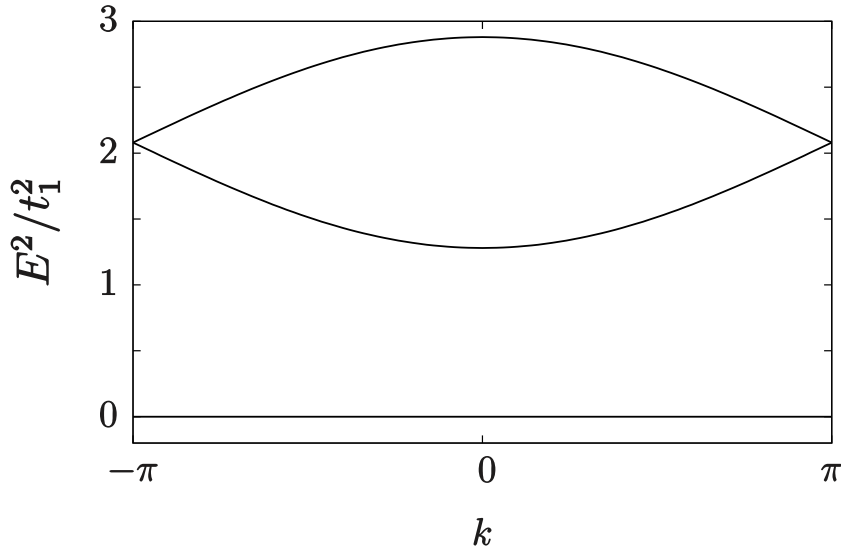

Figure 4.10: Band structure of the squared model (4.28). The relation between the parameters is $t_2 = 0.2t_1$.

4.6   Exact diagonalization results

In this section, we present numerical results that support the analytical predictions that we have made through the band structure calculations and the three consecutive mappings. Specifically, we have performed exact diagonalization of the single-particle Hamiltonian of the diamond chain in the original basis of OAM $l = 1$ states, given by Eq. (4.4). This technique provides access to both the energy spectrum and the corresponding eigenstates of the system. We have considered chains formed by a few tens of unit cells, a size which is enough to capture all the relevant features of the model. Since there are two states per site, the dimension of the Hilbert space of a diamond chain with N_c unit cells is $\dim \mathcal{H} = 2N = 6N_c$, where $N = 3N_c$ is the total number of sites.

4.6.1   Energy spectrum of a diamond chain with open boundaries
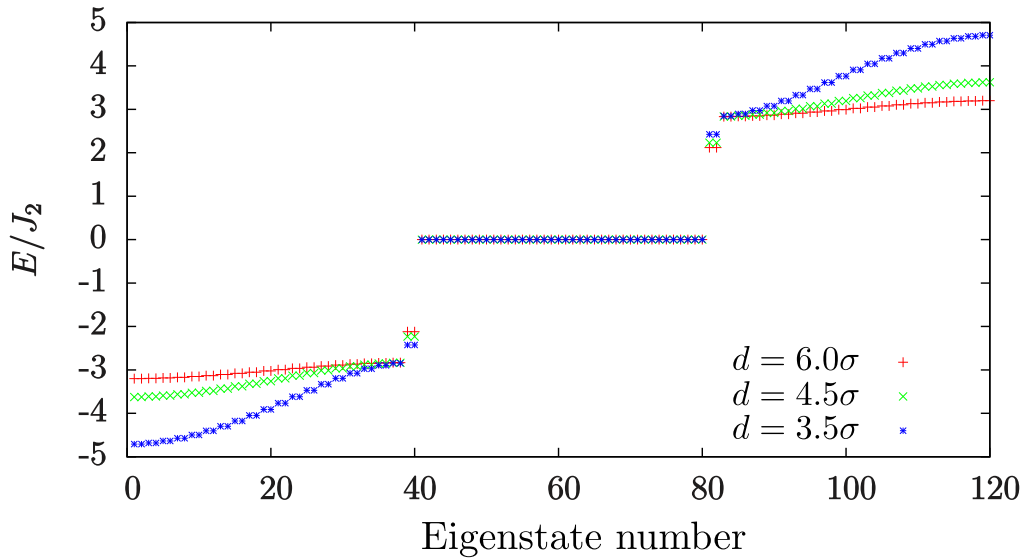
Figure 4.11: Single-particle energy spectra of a diamond chain formed by $N_c = 20$ unit cells [described by the Hamiltonian (4.4)] computed for harmonic traps separated by distances $d = 3.5\sigma$ (blue points), for which $J_3/J_2 = 1.67$, $d = 4.5\sigma$ (green points), for which $J_3/J_2 = 1.28$, and $d = 6\sigma$ (red points), for which $J_3/J_2 = 1.13$ [see Fig. 2.4 (a)].

In Fig. 4.11 we show the energy spectra that one obtains by considering values of J_2 and J_3 corresponding to realistic calculations done with harmonic traps separated by distances $d/\sigma = 3.5, 4.5$ and 6. We observe that, independently of the value of d, all the energies appear in degenerate pairs. This is a consequence of the existence of two

decoupled identical chains, demonstrated by the first mapping Eqs. (4.9). As predicted by the band structure Eqs. (4.8), for all the relative values of of J_2 and J_3 there is a set of states with zero energy. We also observe that as d is increased and therefore the $J_3/J_2 = 1$ limit is approached [see Fig. 2.4], a progressive flattening of the dispersive part of the spectrum occurs. This is in accordance with Eqs. (4.8), which predict that all the bands become flat in the $J_2 = J_3$ limit.

Even though the coupling parameters always fulfill the relation $J_3 > J_2$ in a real physical system of tunnel-coupled traps [see Fig. 2.4], all the spectra plotted in Fig. 4.11 display 4 in-gap states, which have a correspondence with the edge states (4.24) that appear naturally for each of the H^1 and H^2 modified SSH chains in the $J_2 = J_3$ limit. For an inter-trap separation $d = 6.0\sigma$, for which $J_3/J_2 = 1.13$, the energies of these in-gap states are very close to $\pm 2J_2$, as predicted by the analysis of the modified SSH chain. Moreover, one should note that the in-gap edge states of Fig. 4.11 can be exactly mapped into the topological states of the squared model [225]. In Fig. 4.12 we show the squared energy spectrum of an open chain with $N_c = 40$ unit cells in the original OAM $l = 1$ model (which correspond to 20 unit cells and thus 60 sites in the modified diamond chain model) for the same choice of parameters as in Fig. 4.10, with the appearance of two edge states within the band gap. The other two edge states of the original OAM $l = 1$ model correspond to those of the squared model that is obtained for the H^2 chain.
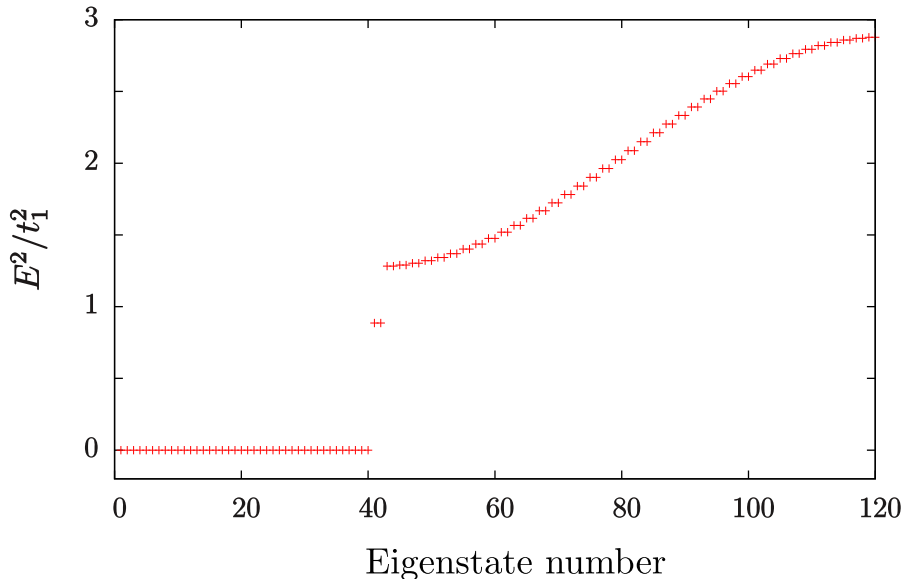

Figure 4.12: Squared energy spectrum of an open chain with 40 unit cells ($N_c = 20$ unit cells in the original OAM $l = 1$ model). The relation between the parameters is $t_2 = 0.2t_1$.

As the relative difference between J_2 and J_3 is increased (i.e., as d is decreased), the

absolute value of the energies of these states increases. As we mentioned in Sec. 4.5, these edge states only disappear at the gap closing points, which occur for the non-physical values of the couplings $J_2 = 0, J_3 \neq 0$ and $J_3 = 0, J_2 \neq 0$. After crossing these points, the edge states emerge again, indicating the absence of a topological transition in the system. These facts are illustrated in Fig. 4.13, where we plot the energy spectrum of a diamond chain of $N_c = 80$ unit cells keeping J_2 fixed and varying the J_3/J_2 ratio in the $[-1.5, 1.5]$ range. The lines corresponding to the bulk and edge states are colored in blue and red, respectively. We observe that the edge states are insensitive to the sign of J_3/J_2 and only merge completely into the bulk in the gapless point $J_3/J_2 = 0$. If one fixes J_3 and varies the J_2/J_3 ratio, analogous results are obtained.
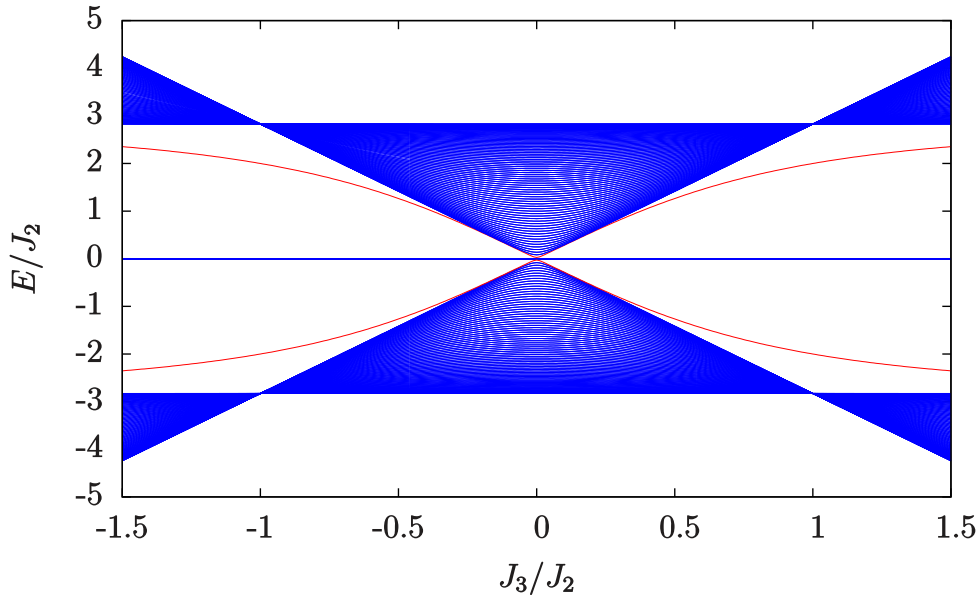
Figure 4.13: Energy spectrum of a diamond chain formed by $N_c = 80$ unit cells [described by the Hamiltonian (4.4)] as a function of the J_3/J_2 ratio for a fixed value of J_2. The bulk and edge states are indicated by blue and red lines, respectively.

4.6.2   Spatial distribution of the edge states for $J_2 \neq J_3$

In order to verify that the topological edge states remain localized at the right edge of the chain for $J_2 \neq J_3$, we have computed their density profiles for different relative values of J_2 and J_3 in a diamond chain of $N_c = 20$ unit cells. The results are shown in Fig. 4.14. The sites have been assigned a number j according to the correspondences $C_i = 3i - 2$, $B_i = 3i - 1$, $A_i = 3i$, i.e., the site $j = 1$ is the C site of the cell $i = 1$ and the site $j = 60$ is the A site of the cell $i = 20$.
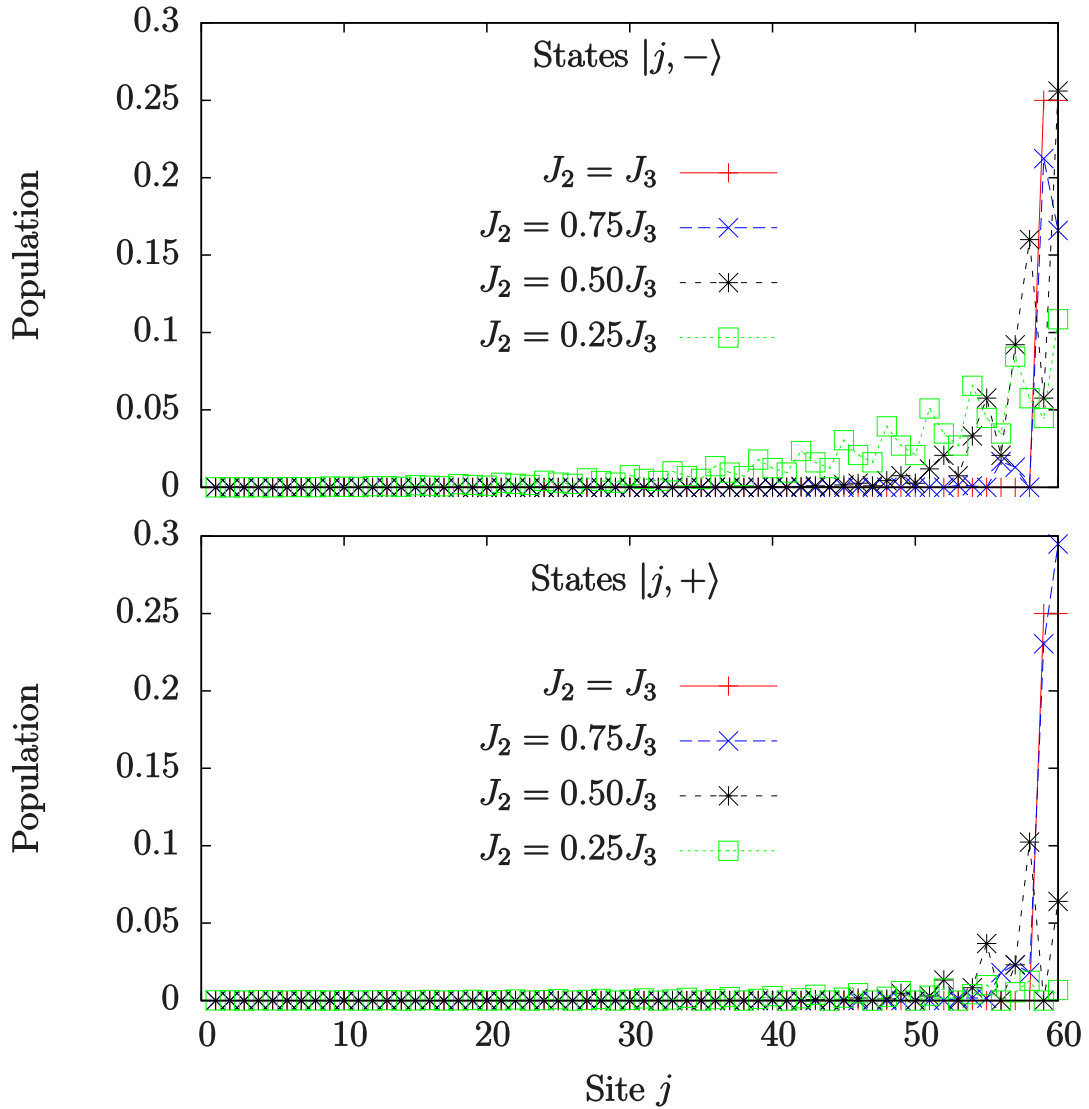
Figure 4.14: Density profiles of one of the in-gap states (eigenstate number 39) of a diamond chain with a total number of unit cells $N_c = 20$ computed for different relative values of J_2 and J_3. The upper plot corresponds to the density distribution of the states with negative circulation and the lower plot to the states with positive circulation.

We observe that in all cases the population of both the states with negative and positive circulation is exponentially localized at the right edge of the chain. As expected, as the ratio J_2/J_3 deviates from 1 the edge states grow longer tails into the bulk. However, as can be seen in Fig. 4.14, even in the case $J_2 = 0.25J_3$ the distribution shows a sharp decay into the bulk. In realistic implementations, the case that deviates most from $J_2 = J_3$ would correspond to harmonic traps very close to each other, as can be seen in Fig. 2.4 (a). But even in that case, one would have an approximate relation between

the couplings $J_2 \approx 0.5 J_3$, so one would observe narrowly localized edge states.

4.6.3   Effect of J_1 at the edges

Finally, we discuss the effect of the self-coupling J_1 at the left edge of the chain, which we have neglected so far. This approximation is justified since typically $|J_1| \ll |J_2|, |J_3|$ and the self-coupling term is only present at the two leftmost sites of the chain. However, this term can be readily incorporated in the exact diagonalization scheme.
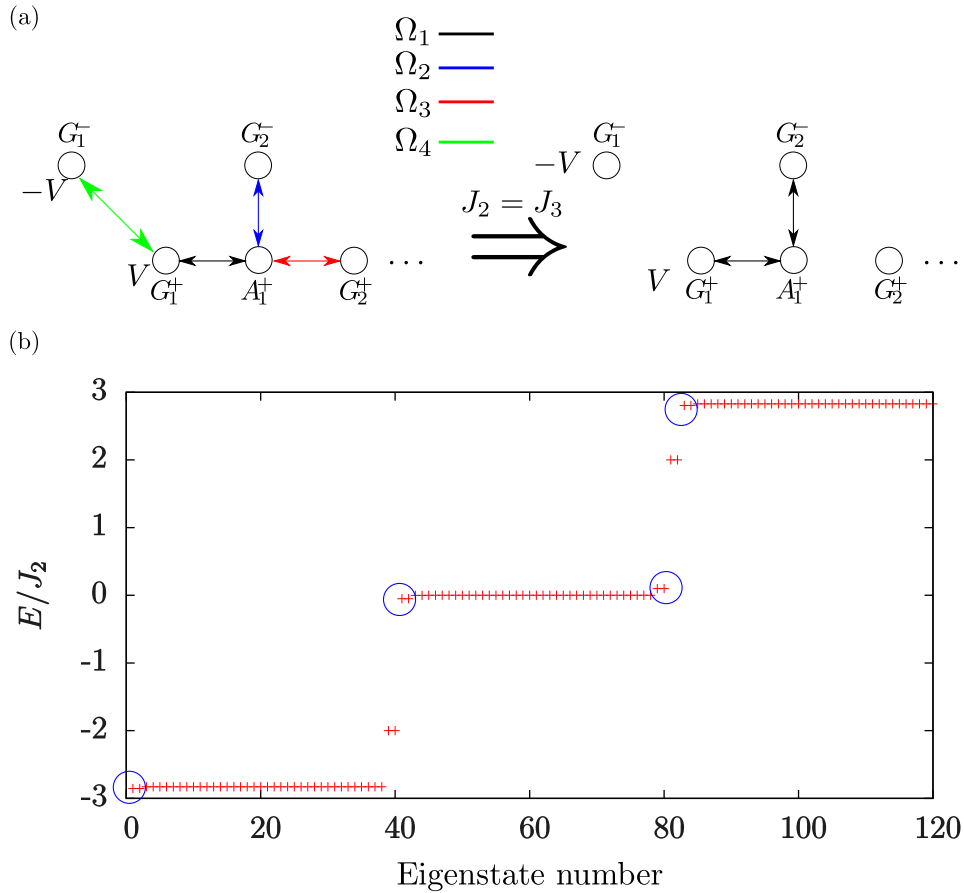
Figure 4.15: (a) Schematic representation of the left end of the modified SSH chain in the presence of a non-zero value of J_1 for $J_2 \neq J_3$ (left), for which $\Omega_3, \Omega_4 \neq 0$, and for $J_2 = J_3$ (right), for which $\Omega_3, \Omega_4 = 0$. The on-site potential $V = \frac{2 J_1 J_2 J_3}{J_2^2 + J_3^2}$ shifts the energies of 4 states with respect to the case $J_1 = 0$. (b) Energy spectrum of a diamond lattice with 20 unit cells and tunneling parameters $J_2 = J_3 = -10 J_1$. A total of 8 states, which are indicated on the plot by blue circles, have small shifts with respect to the case $J_1 = 0$.

Before presenting the numerical results, let us retrieve the effect of the self-coupling

term on the analytical mappings (4.9) and (4.12). Due to this term, the left edges of the H^1 and H^2 chains are coupled because of the matrix elements $\left\langle D_1,+\left|\hat{H}\right|F_1,-\right\rangle = \left\langle D_1,-\left|\hat{H}\right|F_1,+\right\rangle = J_1$. In the modified SSH chain H^1 obtained with the basis rotation (4.12), this extra term translates into a coupling at the left end of the chain,

$$\Omega_4 = \left\langle G_1,-\left|\hat{H}\right|G_1,+\right\rangle = \frac{J_1(J_2^2 - J_3^2)}{J_2^2 + J_3^2}, \tag{4.35}$$

and an on-site potential also in the two sites at the left end of the chain

$$V = \left\langle G_1,+\left|\hat{H}\right|G_1,+\right\rangle = -\left\langle G_1,-\left|\hat{H}\right|G_1,-\right\rangle = \frac{2J_1J_2J_3}{J_2^2 + J_3^2} \approx J_1. \tag{4.36}$$

These two extra terms are illustrated in Fig. 4.15 (a). In the $J_2 = J_3$ limit, the state $|G_1,-\rangle$ is an eigenstate of energy $-V$, and, if $|J_1| \ll |J_2|, |J_3|$, due to the on-site potential the energies of the isolated trimer formed by the states $|G_1,+\rangle, |A_1,+\rangle, |G_2,-\rangle$ are approximately $\pm 2\sqrt{2}J_2 \mp V/4$ and $V/2$. In Fig. 4.15 (b) we show the spectrum corresponding to the tunneling amplitudes $J_2 = J_3 = -10J_1$, with $J_1, V < 0$. Due to the contributions from the H^1 and H^2 chains, we observe that two states have energy $-V$, another two have energy $V/2$ and two states from each of the flat bands are shifted by a quantity $\approx V/4$. In summary, since the self-coupling is only present in two of the sites of the chain and its amplitude is typically much lower than the one of the cross-couplings, its effect is only to shift the energy of a few states by a small quantity and can thus be safely neglected in a diamond chain with a large number of unit cells.

4.7   Conclusions

In this Chapter, we have explored the consequences of the addition of the OAM degree of freedom in the physics of non-interacting ultracold atoms in an optical lattice with a tunable geometry. Specifically, we have analysed the single-atom properties of a diamond-chain optical lattice filled with a gas of ultracold atoms loaded into the manifold of OAM $l = 1$ states. In this simple geometry, due to the angles between the lines connecting the different sites, relative phases appear naturally in the tunneling amplitudes between OAM states with opposite circulation. The appearance of these phases has deep consequences in the physics of the diamond chain, which we have unraveled by means of three consecutive analytical mappings.

First, we have performed a basis rotation which decouples the original diamond chain with two OAM orbitals per site into two identical chains with only one state per site. Each of these chains is threaded by a net π flux through each plaquette, which explains the gap opening in the band structure. Then, we have introduced a second mapping

that allows to re-interpret each of the decoupled chains in terms of a modified SSH model with an extra dangling site per unit cell. This mapping allows us to explain in an intuitive way the existence of a zero-energy flat band in the system and, for a certain relation between the tunneling parameters, the flattening of the dispersive bands and the occurrence of Aharonov-Bohm caging. Furthermore, we have used this model to predict the appearance of in-gap edge states in the system, which are indicative of non-trivial topology. In order to circumvent the lack of inversion symmetry in the mapped models and therefore be able to perform the topological characterization of the system, we have introduced a third mapping into a modified diamond chain. Making use of a recently developed technique adapted for systems where the inversion axis is not centered around the unit cell, we have computed the Zak's phases of the different bands, finding that the system is topologically non-trivial for any choice of the coupling parameters for which the gap is open. We have also shown that the system can be regarded as a square-root topological insulator.

Finally, we have performed exact diagonalization calculations that support the results derived analytically. In particular, we have demonstrated numerically the existence of in-gap states and we have confirmed that they remain localized at the right edge, as predicted by their topological nature.

This work opens up many interesting perspectives. As a direct extension, in Chapter 6 we study the physics of two interacting bosons loaded in the manifold of OAM $l = 1$ states of the diamond chain. There, we show that in the Aharonov-Bohm cage limit, i.e., when all the bands are flat, the system hosts two-body topological states. In Chapter 7, we study a two-dimensional lattice of ring potentials with unequal intra- and inter-cell separations. We show that in such a system the phases in the tunneling amplitudes may give rise to second-order topological effects, signalled by the presence of zero-energy corner modes. In Chapter 5, we consider a scenario with many strongly interacting bosons loaded in OAM states. By tuning the geometry of the lattice (and thus the phases of the tunneling amplitudes), such a system allows to engineer a variety of effective spin-1/2 that are of interest for quantum magnetism.

Quantum magnetism with ultracold bosons carrying orbital angular momentum

In this Chapter, we study a gas of ultracold bosons loaded in Orbital Angular Momentum (OAM) states of an array of cylindrically symmetric potentials in the strongly correlated limit. By means of perturbation theory calculations, we show how this system can realize a variety of spin-1/2 models of quantum magnetism. We consider explicitly the dependence of the effective couplings on the geometry of the system and demonstrate that different models of interest related to a general XYZ Heisenberg model with external field can be obtained. Furthermore, we discuss how the relative strength of the effective couplings can be tuned and which phases can be explored in realistic setups. Finally, we address questions concerning the experimental readout and implementation.

The Chapter is organized as follows. In Sec. 5.1, we give a brief overview on recent progress on simulation of quantum magnetism with ultracold atoms in optical lattices and we contextualize our work in this field of research. In the first part of Sec. 5.2, we introduce the general Hamiltonian of the physical system that we consider. We then focus on the Mott insulator limit at unit filling, in which we show that the OAM degree of freedom can be encoded in a spin-1/2 variable, and we describe in detail how to compute the couplings that govern the effective spin model. Taking profit of these general calculations, in Sec. 5.3 we make concrete proposals to implement several spin-1/2 models of interest by arranging the ring potentials in different geometries. In Sec. 5.4, we discuss how the strength of the effective couplings can be tuned experimentally by varying the separation between the ring traps and we analyse some of the phases of the effective

models that can be realized by this process. In Sec. 5.5, we consider some aspects of the experimental realization. In particular, we describe the readout of the OAM states and we analyse their stability under collisional processes. Finally, in section Sec. 5.6 we summarize the main conclusions of this work.

5.1   Introduction

Ultracold atoms in optical lattices provide a clean and highly tunable playground to study a plethora of many-body phenomena [30, 31]. Recent years have witnessed important breakthroughs that have pushed the degree of control over these systems to a very precise quantitative level and have opened new routes towards the quantum simulation of previously unexplored systems in a wide range of fields [62]. In particular, ultracold atoms have proven to be a very powerful tool for exploring quantum magnetism in a form originally inspired by solid state systems. Remarkable achievements of quantum simulation of magnetism with ultracold atoms include the implementation of spin-frustrated lattices [41, 238], extensive experimental studies of the magnetic properties of the Hubbard model [239–246], or the realization of high-resolution quantum gas microscopes for bosonic [50, 51] and fermionic [52–55] atoms that have led to the observation of antiferromagnetic order in a one-dimensional (1D) Ising chain [247], bound magnons in the XXZ Heisenberg model [248], and spin-resolved dynamics [249–251]. There are also proposals to realize spin models with strongly interacting ultracold bosons excited to $p-$bands [252], and realizations of magnetic models with bosons in tilted optical lattices [247, 253–256].

In this work, we show that strongly interacting ultracold bosons loaded into OAM states of lattices of side-coupled cylindrically symmetric traps can realize a variety of spin-1/2 models, including the XYZ Heisenberg model with or without external field. In particular, we focus on the Mott insulator regime at unit filling, where each trap is occupied by a single atom and a direct mapping between the OAM and spin-1/2 states can be performed. Recently, a proposal to realize such a state by periodically modulating an optical lattice has been made [136]. Alternatively, this state could be generated by optically transferring OAM [109, 122] to atoms confined to an arrangement of ring-shaped potentials, which can be created by a variety of techniques [109–116, 129, 131, 163] and have proven to support long-lived persistent currents associated to the OAM states [119, 123]. The mechanisms that yield these effective spin-1/2 models are analogous to the ones described in [252], where it was shown that the XYZ Heisenberg model can be realized with ultracold bosons in the p-bands of a two-dimensional optical lattice [58, 221], which are equivalent to the OAM $l = 1$ states. Our proposal, however, extends this to lattices made up of general cylindrically symmetric potentials such as

ring traps, and is valid for higher OAM states. The new degree of control offered by the flexibility in the arrangements of the traps opens up the possibility to engineer a wide variety of spin models beyond the XYZ Heisenberg model and makes it possible to modify the effective coupling parameters at the level of a single site.

5.2 Quasi one-dimensional ladder and effective spin-1/2 model

For the sake of clarity, we start by considering the simplest quasi one-dimensional lattice in which an effective spin-1/2 model of quantum magnetism can be obtained using ultracold atoms carrying OAM, namely an array of equivalent ring-shaped potentials. From the analysis of the second order processes that we will discuss for this system, the generalization of the effective spin model to other quasi one-dimensional geometries and to two-dimensional lattices is straightforward.

5.2.1 Physical system

The quasi one-dimensional system on which we focus consists of a gas of M ultracold bosons of mass m trapped in a ladder of N identical ring-shaped potentials, labelled by the index j. This can be constructed by concatenating $N/2$ two-ring unit cells, labelled by the index i, as depicted in Fig. 5.1. All of the rings have the same radius R and radial trapping frequency ω, which defines the natural length scale $\sigma = \sqrt{\hbar/m\omega}$. The outer parts of two rings belonging to the same unit cell are separated by a distance d, and three consecutive rings form a triangle with a central angle Θ. The bosons may occupy the two degenerate eigenstates of total OAM $l \geq 1$ of each ring with positive or negative circulation, $|j, \pm l\rangle$, the wave functions of which are given by

$$\phi_{\pm l}^{j}(r_j, \varphi_j) = \langle \vec{r}|j, \pm l\rangle = \psi_l(r_j)e^{\pm il(\varphi_j - \varphi_0)}, \tag{5.1}$$

where (r_j, φ_j) are the polar coordinates with origin at the center of the jth ring and φ_0 is an arbitrary origin of phases. The radial part of the wave function, $\psi_l(r_j)$, can be approximated by the ground state of the jth ring potential, $\psi_0(r_j)$. Under this approximation, the energy of the modes of total OAM l is given by

$$E(l) = E_0 + E_{\rm c}l^2, \tag{5.2}$$

where E_0 is the energy of the ground state of the ring and $E_{\rm c} = \frac{\hbar^2}{2m}\int d^2r \left|\frac{\psi_0(r)}{r}\right|^2$ is the centrifugal part of the kinetic energy. We assume that the motion of the bosons is restricted to the manifold of states of total OAM l without coupling to other OAM
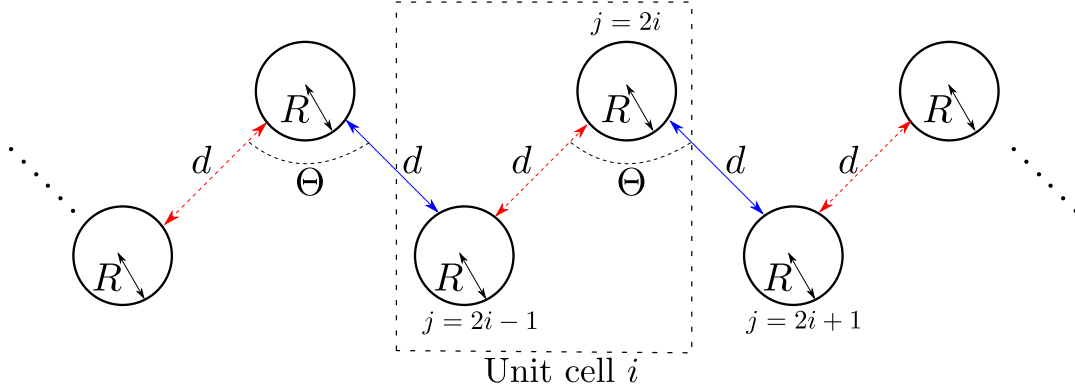
Figure 5.1: Quasi one-dimensional ladder of ring potentials of radius R (labelled by the index j) obtained by concatenating unit cells (labelled by the index i) formed by two rings such that the central angle of the triangles formed by three neighbouring rings is Θ. The origin of phases is taken along the direction $2i \leftrightarrow 2i + 1$ (indicated with blue straight arrows), so that the couplings are real along this direction and all hopping phases appear in the $2i \leftrightarrow 2i - 1$ links (indicated with red dashed arrows). The distance between the closest points of two nearest-neighbour rings is d.

manifolds, an approximation that we will further justify in Sec. 5.5.2. In this situation, the bosonic field operator of the system reads

$$\hat{\Psi}_l = \sum_{j=1}^{N} \phi_{+l}^j(r_j, \varphi_j)\hat{a}_{+l}^j + \phi_{-l}^j(r_j, \varphi_j)\hat{a}_{-l}^j, \qquad (5.3)$$

where $\hat{a}_{\pm l}^j$ are bosonic operators associated with the annihilation of the OAM states at site j that satisfy the commutation relations

$$[\hat{a}_{\alpha}^j, \hat{a}_{\alpha'}^{j'}] = 0 \qquad (5.4a)$$

$$[\hat{a}_{\alpha}^{j\dagger}, \hat{a}_{\alpha'}^{j'\dagger}] = 0 \qquad (5.4b)$$

$$[\hat{a}_{\alpha}^j, \hat{a}_{\alpha'}^{j'\dagger}] = \delta_{jj'}\delta_{\alpha\alpha'}. \qquad (5.4c)$$

The Hamiltonian of the system can be decomposed into its single particle and interacting parts

$$\hat{H}_l = \int d\vec{r}\hat{\Psi}_l^\dagger \left[-\frac{\hbar^2\nabla^2}{2m} + V(\vec{r}) \right] \hat{\Psi}_l + \frac{g}{2} \int d\vec{r}\hat{\Psi}_l^\dagger\hat{\Psi}_l^\dagger\hat{\Psi}_l\hat{\Psi}_l \equiv \hat{H}_l^0 + \hat{H}_l^{\text{int}}, \qquad (5.5)$$

where $V(\vec{r})$ is the total trapping potential of the ladder, which can be approximated by a truncated combination of all the ring potentials $V_j(r) = \frac{1}{2}m\omega^2(R - r_j)^2$, and g is the strength of the $s-$wave atom-atom interactions. The kinetic part of the Hamiltonian, $\hat{H}_l^0$, describes the tunneling dynamics of the states of total OAM l between neighbouring

rings as well as between the two degenerate states within the same ring, which we reviewed in Sec. 2.4 of Chapter 2. Assuming that the central angle takes values $\Theta > \pi/3$, one can consider that only nearest-neighbour sites are coupled. By making this approximation and choosing the origin of phases to be along the line that unites the sites $2i \leftrightarrow 2i + 1$, the single particle term of the Hamiltonian takes the form

$$
\begin{aligned}
\hat{H}_l^0 = {} & J_1^l \sum_{j=1}^{N} \hat{a}_{+l}^{j\dagger} \hat{a}_{-l}^{j} (1 + e^{-i2l\Theta}) + \text{h.c.} \\
& + J_2^l \sum_{i=1}^{N/2} \hat{a}_{+l}^{2i\dagger} (\hat{a}_{+l}^{2i+1} + \hat{a}_{+l}^{2i-1}) + \hat{a}_{-l}^{2i\dagger} (\hat{a}_{-l}^{2i+1} + \hat{a}_{-l}^{2i-1}) + \text{h.c.} \\
& + J_3^l \sum_{i=1}^{N/2} \hat{a}_{+l}^{2i\dagger} (\hat{a}_{-l}^{2i+1} + e^{-i2l\Theta} \hat{a}_{-l}^{2i-1}) + \hat{a}_{-l}^{2i\dagger} (\hat{a}_{+l}^{2i+1} + e^{i2l\Theta} \hat{a}_{+l}^{2i-1}) + \text{h.c.} \quad (5.6)
\end{aligned}
$$

Assuming that only on-site interactions take place, the interacting part of the Hamiltonian is given by

$$
\begin{aligned}
\hat{H}_l^{\text{int}} = {} & \frac{g}{2} \int d\vec{r} \, \hat{\Psi}_l^\dagger \hat{\Psi}_l^\dagger \hat{\Psi}_l \hat{\Psi}_l = \frac{g}{2} \int d\vec{r} \sum_{j=1}^{N} \left[\phi_{+l}^{j*}(\vec{r_j}) \hat{a}_{+l}^{j\dagger} + \phi_{-l}^{j*}(\vec{r_j}) \hat{a}_{-l}^{j\dagger} \right]^2 \left[\phi_{+l}^{j}(\vec{r_j}) \hat{a}_{+l}^{j} + \phi_{-l}^{j}(\vec{r_j}) \hat{a}_{-l}^{j} \right]^2 \\
= {} & \frac{g}{2} \sum_{j=1}^{N} \int d\vec{r} |\psi_0(r)|^4 \left[e^{-il\varphi} \hat{a}_{+l}^{j\dagger} + e^{il\varphi} \hat{a}_{-l}^{j\dagger} \right]^2 \left[e^{il\varphi} \hat{a}_{+l}^{j} + e^{-il\varphi} \hat{a}_{-l}^{j} \right]^2 \\
= {} & \frac{g}{2} \sum_{j=1}^{N} \int d\vec{r} |\psi_0(r)|^4 \left[e^{-2il\varphi} (\hat{a}_{+l}^{j\dagger})^2 + e^{2il\varphi} (\hat{a}_{+l}^{j\dagger})^2 + 2\hat{a}_{+l}^{j\dagger} \hat{a}_{-l}^{j\dagger} \right] \left[e^{2il\varphi} (\hat{a}_{+l}^{j})^2 + e^{-2i\varphi} (\hat{a}_{-l}^{j})^2 + 2\hat{a}_{+l}^{j} \hat{a}_{-l}^{j} \right] \\
= {} & \frac{U}{2} \sum_{j=1}^{N} (\hat{a}_{+l}^{j\dagger})^2 (\hat{a}_{+l}^{j})^2 + (\hat{a}_{-l}^{j\dagger})^2 (\hat{a}_{-l}^{j})^2 + 4\hat{a}_{+l}^{j\dagger} \hat{a}_{-l}^{j\dagger} \hat{a}_{+l}^{j} \hat{a}_{-l}^{j} \\
= {} & \frac{U}{2} \sum_{j=1}^{N} \hat{n}_{+l}^{j} (\hat{n}_{+l}^{j} - 1) + \hat{n}_{-l}^{j} (\hat{n}_{-l}^{j} - 1) + 4\hat{n}_{+l}^{j} \hat{n}_{-l}^{j}, \quad (5.7)
\end{aligned}
$$

where we have defined $U \equiv g \int d\vec{r} |\psi_0(r)|^4$ and the usual number operators $\hat{n}_{\pm l}^{j} \equiv \hat{a}_{\pm l}^{j\dagger} \hat{a}_{\pm l}^{j}$.

5.2.2 Mott insulator phase and effective spin model

We now focus on the scenario in which the ladder is at unit filling, $M = N$, and the interaction strength is positive and much larger than the tunneling amplitudes, $U \gg |J_1^l|, |J_2^l|, |J_3^l|$. In this particular situation, the system is in a Mott Insulator phase, in which the most energetically favoured states are those where all rings are occupied by a single boson. Due to the OAM degree of freedom, the ladder has 2^N such states,

which correspond to all possible configurations of many-body states consisting on each ring being occupied by a single boson in a OAM state of positive or negative circulation. We can perform a direct mapping between these states and a spin-1/2 configuration by identifying a spin up (down) for each ring with a boson in the state of positive (negative) OAM circulation, i.e., $|j, +l\rangle \Rightarrow |\uparrow\rangle_j$, $|j, -l\rangle \Rightarrow |\downarrow\rangle_j$.

The physics of the ladder in the Mott Insulator phase can be described by an effective model that incorporates interaction terms between the neighbouring spins induced by the kinetic part of the Hamiltonian, $\hat{H}_l^0$, which we treat as a perturbation. To derive the effective Hamiltonian, we define a projector $\hat{M}$ to the Mott space of singly occupied sites as well as the projector to the space orthogonal to this one, $\hat{O} = 1 - \hat{M}$. In terms of these operators, the Schrödinger equation for a many-body state $|\Psi\rangle$ belonging to the manifold of states with total OAM l, $(\hat{H}_l^0 + \hat{H}_l^{\text{int}})|\Psi\rangle = E|\Psi\rangle$, can be decomposed as [252]

$$(\hat{O}\hat{H}_l^0\hat{O} + \hat{O}\hat{H}_l^0\hat{M} + \hat{O}\hat{H}_l^{\text{int}}\hat{O} + \hat{O}\hat{H}_l^{\text{int}}\hat{M})|\Psi\rangle = E\hat{O}|\Psi\rangle \tag{5.8}$$

$$(\hat{M}\hat{H}_l^0\hat{O} + \hat{M}\hat{H}_l^0\hat{M} + \hat{M}\hat{H}_l^{\text{int}}\hat{O} + \hat{M}\hat{H}_l^{\text{int}}\hat{M})|\Psi\rangle = E\hat{M}|\Psi\rangle. \tag{5.9}$$

The terms $\hat{M}\hat{H}_l^{\text{int}}\hat{M}$, $\hat{O}\hat{H}_l^{\text{int}}\hat{M}$ and $\hat{M}\hat{H}_l^{\text{int}}\hat{O}$ are all identically zero: the first two ones for computing two-body interactions in single-ocupied rings and the last one for computing overlaps between orthogonal spaces. Taking this fact into account, we can combine eqs. (5.8) and (5.9) to write

$$\hat{H}_{\text{eff}}\hat{M}|\Psi\rangle = E\hat{M}|\Psi\rangle, \tag{5.10}$$

where the effective Hamiltonian reads

$$\hat{H}_{\text{eff}}^l = -\hat{M}\hat{H}_l^0\hat{O}\frac{1}{\hat{O}\hat{H}_l^{\text{int}}\hat{O} - E}\hat{O}\hat{H}_l^0\hat{M} + \hat{M}\hat{H}_l^0\hat{M}. \tag{5.11}$$

The physical action of the first term of the effective Hamiltonian is to connect a Mott state to a state of the orthogonal space through the tunneling term of the original Hamiltonian, associate an energy to this state in the orthogonal space according to $(\hat{O}\hat{H}_l^{\text{int}}\hat{O} - E)^{-1}$ and then take the state back to the Mott subspace. All the second order processes induced by this term occur via intermediate states in which all the rings are singly occupied except for one ring, say j, that is empty, and the ring $j \pm 1$, that is doubly occupied. Therefore, we restrict the orthogonal subspace to these states, which can be compactly represented by the three possible two-spin states for the doubly occupied rings, namely $\{|\uparrow\uparrow\rangle_{j\pm1}, |\downarrow\downarrow\rangle_{j\pm1}, |\uparrow\downarrow\rangle_{j\pm1}\}$. Furthermore, since we are in the Mott insulator regime, we can assume that $(\hat{O}\hat{H}_l^{\text{int}}\hat{O} - E)^{-1} \approx (\hat{O}\hat{H}_l^{\text{int}}\hat{O})^{-1}$. In the subspace of states where only a single ring has double occupation, this operator takes the form $(\hat{O}\hat{H}_l^{\text{int}}\hat{O})^{-1} = \text{diag}\{1/U, 1/U, 1/2U\}$. The second term of the effective Hamiltonian, $\hat{M}\hat{H}_l^0\hat{M}$, takes into account the first order processes that occur within the subspace of singly occupied states, which are due to the self-coupling amplitude J_1^l.

The resulting effective Hamiltonian contains four types of processes. On the one hand, there are three different kinds of second order processes induced by the effective interaction: those in which the final states of the rings j and $j \pm 1$ have 0, 1, or 2 spins flipped with respect to the initial state. Furthermore, a single spin flip can also occur via the first order process due to the self-coupling. Next, we compute separately the amplitudes corresponding to each of the processes involving a different number of spin flips. As we will show, the fact that the tunneling phases depend on the central angle of the ladder Θ leads to non-trivial dependence of the effective model on the geometry of the lattice. In order to use a language more natural to spin-1/2 systems, we define the spin-flip operators $\sigma_j^{\pm} = a_{\pm l}^{j\dagger} a_{\mp}^j$, which can be expressed in terms of the x and y Pauli matrices as $\sigma_j^{\pm} = \frac{1}{2}(\sigma_j^x \pm i\sigma_j^y)$. We also define the z Pauli matrix as $\sigma_j^z = a_{+l}^{j\dagger} a_{+l}^j - a_{-l}^{j\dagger} a_{-l}^j$ and the spin up and down projectors $P_j^{\uparrow} = a_{+l}^{j\dagger} a_{+l}^j$, $P_j^{\downarrow} = a_{-l}^{j\dagger} a_{-l}^j$.

Processes involving no spin flips

The first type of interaction processes in the effective model are those in which the initial and final states coincide, i.e., no spins are flipped. In Fig. 5.2 we show two examples of such processes, one in which a boson at ring $j = 2i$ tunnels to $j = 2i + 1$ and back and another one in which it tunnels to $j = 2i - 1$ and back. In spite of the fact that along the direction $2i \leftrightarrow 2i - 1$ there are hopping phases in the tunneling terms that exchange angular momentum, in the total second order processes they cancel out because there have to be two opposite flips in order to come back to the initial state. Thus, the total amplitude of these processes is the same regardless of the direction of the interaction. For each pair of interacting rings, there are in total 16 different second order processes not involving any total spin flip, which correspond to the 4 possible two-ring spin configurations and the 4 possible doubly occupied virtual states that mediate the interaction. Adding up all the amplitudes of these processes, we find that the part of the effective Hamiltonian corresponding to these processes in a given pair of nearest-neighbour rings $j, j \pm 1$ reads

$$\hat{H}_{j \leftrightarrow j \pm 1}^{l, 0 \text{ flip}} = -\frac{3\left[(J_2^l)^2 - (J_3^l)^2\right]}{2U} \sigma_j^z \sigma_{j\pm1}^z - \frac{5\left[(J_2^l)^2 + (J_3^l)^2\right]}{2U} \mathbb{1}. \tag{5.12}$$

We note that these amplitudes do not depend on the position of the ring j inside the unit cell where it belongs.
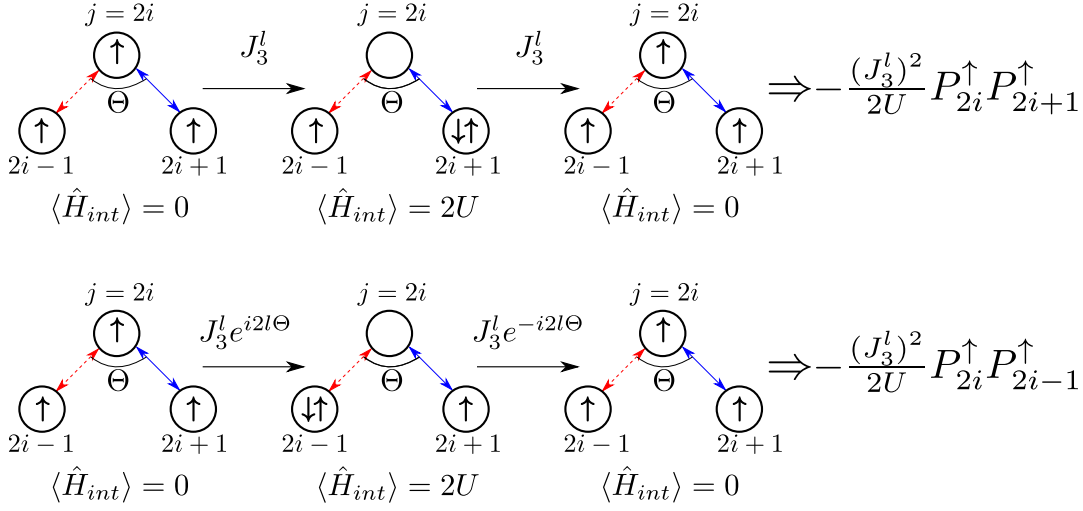
Figure 5.2: Sketches and amplitudes of examples of second order processes not involving any flipping of the spins with respect to the initial state. The processes can be mediated by the site $j+1$ (upper plot) or $j-1$ (lower plot). Each process can also occur with the same amplitude by having the site j doubly occupied in the intermediate state. $\langle \hat{H}_{int} \rangle$ indicates the expectation value of the interacting Hamiltonian (5.7) over each state.

Processes involving one spin flip

The second type of interaction processes in the effective model are those in which a single spin is flipped. The first way in which this can occur is by the action of the self-coupling J_1^l. For each ring j, there are in total two of such processes, which correspond to the flipping of a spin that is initially in the down or up state. Since they are of first order, the total amplitude of these processes can be directly computed with the Hamiltonian (5.6). In spin notation, it is given by $J_1^l \left[\left(1 + e^{i2l\Theta}\right) \sigma_j^- + \left(1 + e^{-i2l\Theta}\right) \sigma_j^+ \right] = J_1^l \left[\sigma_j^x (1 + \cos 2l\Theta) + \sigma_j^y \sin 2l\Theta \right]$.

Additionally, a single spin can be flipped by means of second order processes. In Fig. 5.3 we show two examples of such processes that lead to the flipping of a spin at the ring $j = 2i$, one with a virtual interaction occurring at $j = 2i + 1$ and another one mediated by the ring $j = 2i - 1$. In this case, the amplitudes of the processes depend on the direction of the interaction: when they occur along $j = 2i \leftrightarrow 2i + 1$ they are real, whereas along the line $j = 2i \leftrightarrow 2i - 1$ a net hopping phase $e^{\pm i2l\Theta}$ appears. Adding up the amplitudes of all the different 12 second order processes that lead to the flipping of a single spin and the two first order processes, we find that the part of the effective Hamiltonian describing this type of interactions in the jth ring reads

$$\hat{H}_j^{l,1 \text{ flip}} = \left(J_1^l - \frac{3 J_2^l J_3^l}{U} \right) \left[\sigma_j^x (1 + \cos 2l\Theta) + \sigma_j^y \sin 2l\Theta \right] . \qquad (5.13)$$

Again, the total amplitude does not depend on the position of the ring inside the unit cell because all rings are coupled to a ring along each of the two directions with different hopping phases. Nevertheless, it does depend on the geometry of the ladder through the central angle Θ. For instance, for $l\Theta = \pi/2 \pmod{2\pi}$, the single spin-flip amplitude vanishes, whereas for $l\Theta = 0, \pi \pmod{2\pi}$, it becomes $\hat{H}_j^{1\text{flip}} = \left(2J_1^l - \frac{6J_2^l J_3^l}{U}\right)\sigma_j^x$.
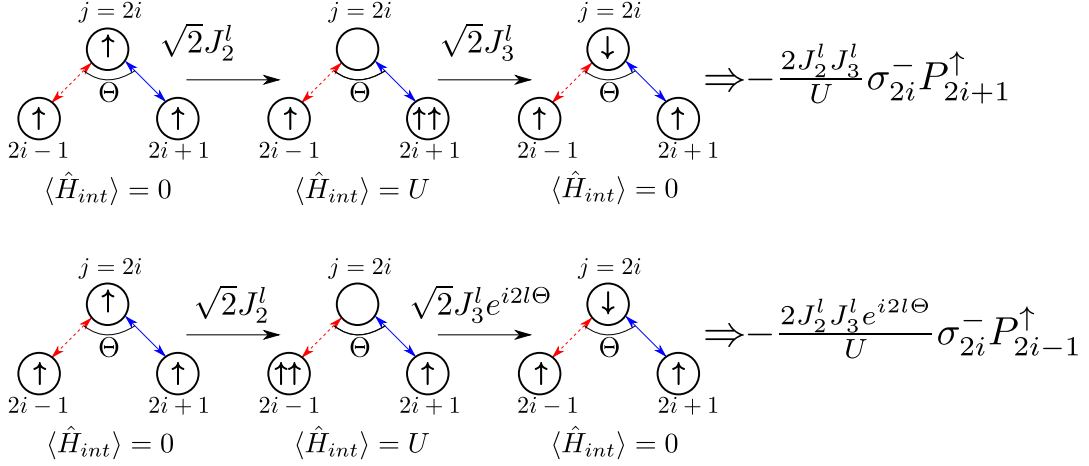

Figure 5.3: Sketches and amplitudes of examples of second order processes involving the flipping of a single spin with respect to the initial state. The processes can be mediated by the site $j+1$ (upper plot) or $j-1$ (lower plot). Each process can also occur with the same amplitude by having the site j doubly occupied in the intermediate state. $\langle\hat{H}_{int}\rangle$ indicates the expectation value of the interacting Hamiltonian (5.7) over each state.

Processes involving two spin flips

The third and last type of interactions in the effective model are those that lead to the simultaneous flipping of two spins. Two examples of such processes are shown in Fig. 5.4. As in the case of single spin-flip processes, along the $j = 2i \leftrightarrow 2i-1$ direction hopping phases appear, whereas in the $j = 2i \leftrightarrow 2i+1$ directions all the tunneling amplitudes are real. In this case, there are no total phase cancellations and the sum of the amplitudes of these processes depends on the direction along which the bosons interact. Adding up the 8 possible processes that lead to the simultaneous flipping of two spins in the final states, we find that the part of the effective Hamiltonian that accounts for these interactions in a given pair of rings reads

$$\hat{H}_{2i\leftrightarrow 2i+1}^{l,2\text{ flip}} = -\frac{(J_2^l)^2 + (J_3^l)^2}{2U}\sigma_{2i}^x\sigma_{2i+1}^x - \frac{(J_2^l)^2 - (J_3^l)^2}{2U}\sigma_{2i}^y\sigma_{2i+1}^y \qquad (5.14)$$

$$\hat{H}^{2\text{flip}}_{2i\leftrightarrow2i-1} = -\frac{(J_2^l)^2 + \cos 4l\Theta(J_3^l)^2}{2U}\sigma_{2i}^x\sigma_{2i-1}^x$$

$$-\frac{(J_2^l)^2 - \cos 4l\Theta(J_3^l)^2}{2U}\sigma_{2i}^y\sigma_{2i-1}^y$$

$$-\frac{\sin 4l\Theta(J_3^l)^2}{2U}\left[\sigma_{2i}^x\sigma_{2i-1}^y + \sigma_{2i}^y\sigma_{2i-1}^x\right]. \tag{5.15}$$

As in the case of the processes leading to a single spin flip, the amplitude of the interactions along the $2i \leftrightarrow 2i - 1$ direction depends on the geometry of the ladder. For central angles such that $l\Theta = 0, \pi/2, \pi \pmod{2\pi}$, the two-spin flip processes have equal amplitude along the $2i \leftrightarrow 2i - 1$ and $2i \leftrightarrow 2i + 1$ directions.
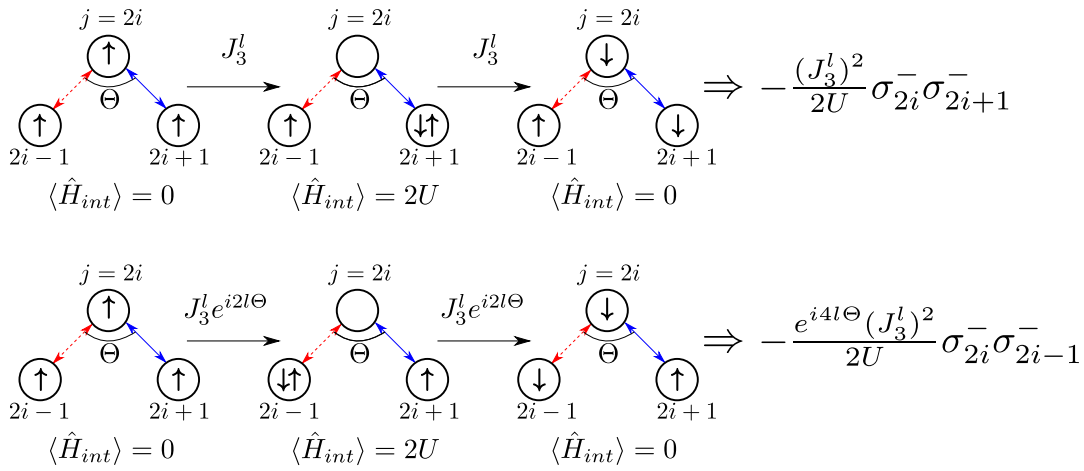
Figure 5.4: Sketches and amplitudes of examples of second order processes leading to the simultaneous flipping of two spins with respect to the initial state. The processes can be mediated by the site $j+1$ (upper plot) or $j-1$ (lower plot). Each process can also occur with the same amplitude by having the site j doubly occupied in the intermediate state. $\langle\hat{H}_{int}\rangle$ indicates the expectation value of the interacting Hamiltonian (5.7) over each state.

Benchmark of the effective model

Taking into account all the processes and summing over all sites, the effective Hamiltonian of a ladder with a central angle Θ reads

$$
\begin{aligned}
H_{\text{eff}}^l =& \sum_{\text{ladder}} \hat{H}_{j\leftrightarrow j\pm1}^{l,0\,\text{flip}} + \hat{H}_j^{l,1\,\text{flip}} + \hat{H}_{2i\leftrightarrow2i+1}^{2\text{flip}} + \hat{H}_{2i\leftrightarrow2i-1}^{2\text{flip}} \\
=& \sum_{j=1}^{N} \left(J_1^l - \frac{3J_2^l J_3^l}{U} \right) \left[\sigma_j^x (1 + \cos 2l\Theta) + \sigma_j^y \sin 2l\Theta \right] \\
& - \sum_{i=1}^{N/2} \frac{(J_2^l)^2 + (J_3^l)^2}{2U} \sigma_{2i}^x \sigma_{2i+1}^x + \frac{(J_2^l)^2 - (J_3^l)^2}{2U} \sigma_{2i}^y \sigma_{2i+1}^y \\
& - \sum_{i=1}^{N/2} \frac{(J_2^l)^2 + (J_3^l)^2 \cos 4l\Theta}{2U} \sigma_{2i}^x \sigma_{2i-1}^x + \frac{(J_2^l)^2 - (J_3^l)^2 \cos 4l\Theta}{2U} \sigma_{2i}^y \sigma_{2i-1}^y \\
& - \sum_{i=1}^{N/2} \frac{(J_3^l)^2 \sin 4l\Theta}{2U} \left[\sigma_{2i}^x \sigma_{2i-1}^y + \sigma_{2i}^y \sigma_{2i-1}^x \right] \\
& - \sum_{i=1}^{N/2} \frac{3 \left[(J_2^l)^2 - (J_3^l)^2 \right]}{2U} \sigma_i^z \left(\sigma_{2i+1}^z + \sigma_{2i-1}^z \right).
\end{aligned}
\tag{5.16}
$$

Since its effect is just to cause a global shift in the energy, we have not included the term in Eq. (5.2) proportional to the identity matrix. Note also that in Eq. (5.16) we have not taken into account the effect of the boundaries, where some second order processes are not possible and therefore the effective amplitudes are modified. Nevertheless, these effects can be neglected by assuming Periodic Boundary Conditions (PBC) or considering a ladder with a large number of sites N.

In order to check that the effective Hamiltonian (5.16) is correct, we have computed the time evolution of an initial state consisting of all spins being in the "up" state with both the spin$-1/2$ effective Hamiltonian, given by Eq. (5.16), and the full Bose–Hubbard model, described by Eqs. (5.5), (5.6) and (5.7). In Fig. 5.5 we plot the expectation value of the z Pauli matrix acting on the site $j = 1$ computed with the two methods. We have considered a ladder formed by $M = 6$ sites with PBC, in such a way that all sites are equivalent, and filled with $N = 6$ bosons in the Mott insulator regime and with a central angle (a) $l\Theta = 0.48\pi$ and (b) $l\Theta = 0.90\pi$. For both values of $l\Theta$, we observe an excellent agreement between the calculations performed with the full Bose-Hubbard Hamiltonian (blue solid lines) and the effective model (red dots). Although in Fig. 5.5 the interaction parameter is $U/100 = J_2^l = J_3^l$, for values of the interaction parameter as low as $U/20 \sim J_2^l, J_3^l$ we still observe a good agreement between the two methods.
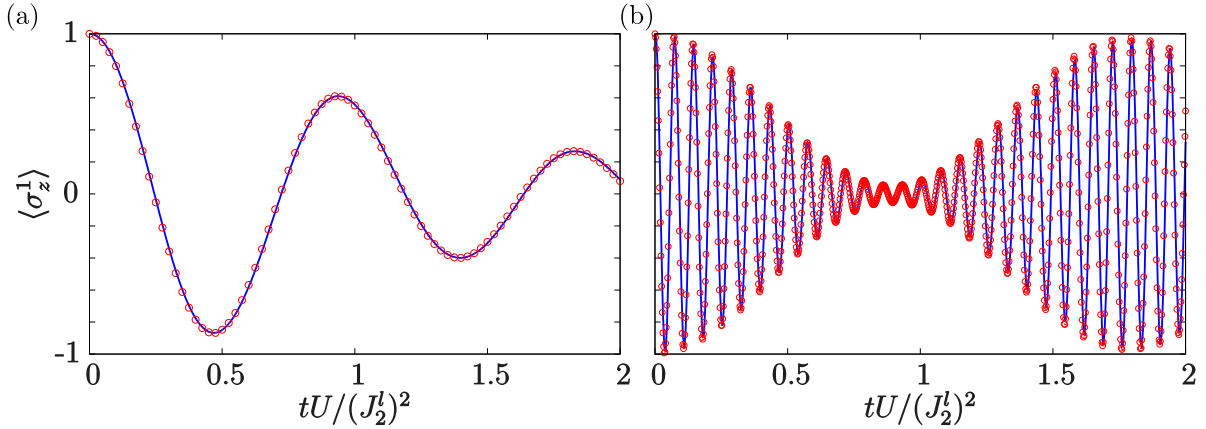
(a)

(b)

Figure 5.5: Time evolution of the expectation value of σ_1^z after setting in a ladder of $M = N = 6$ and with PBC an initial state consisting of all spins being in the "up" state, computed with the full Bose-Hubbard Hamiltonian (blue solid lines) and the effective spin model (red dots). The central angle of the ladder is (a) $l\Theta = 0.48\pi$ and (b) $l\Theta = 0.9\pi$ and the parameters of the model fulfill the relations $J_2^l = J_3^l = -0.2J_1^l$, $U = 100J_2^l$.

5.3 XYZ models

In the previous section, we have shown that by tuning the central angle of the ladder Θ, the amplitudes of the second order processes that govern the effective spin model can be varied. Furthermore, these amplitudes can be modified locally in each ring. Therefore, by modifying the geometry of the lattice of rings a range of quantum magnetic models can be engineered. Next, we give examples of geometric arrangements of the ring potentials that lead to interesting effective spin-1/2 models related to the XYZ Heisenberg model.

5.3.1 XYZ model without external field

For central angles $\Theta_s^l = (2s+1)\pi/2l$, with $s \in \mathbb{N}$, the single-spin flip term Eq. (5.13) vanishes at all rings and the two-spin flip amplitude along the direction where hopping phases appear, Eq. (5.15), becomes equal to that along the direction where all couplings are real, Eq. (5.14). In this situation, the Hamiltonian of the effective spin-1/2 model reads

$$\hat{H}_{\text{eff}}^l(\Theta_s^l) = \sum_{j=1}^{N} J_{xx}^l \sigma_j^x \sigma_{j+1}^x + J_{yy}^l \sigma_j^y \sigma_{j+1}^y + J_{zz}^l \sigma_j^z \sigma_{j+1}^z, \tag{5.17}$$

where the effective couplings are given by

$$J_{xx}^l = -\frac{(J_2^l)^2 + (J_3^l)^2}{2U} \tag{5.18}$$

$$J_{yy}^l = -\frac{(J_2^l)^2 - (J_3^l)^2}{2U} \tag{5.19}$$

$$J_{zz}^l = -\frac{3\left[(J_2^l)^2 - (J_3^l)^2\right]}{2U}. \tag{5.20}$$

The Hamiltonian (5.17) is equivalent to the one of the Heisenberg XYZ model without external field, which is a prominent model of quantum magnetism and it is exactly solvable [257].

5.3.2 XYZ model with external field

For values of the central angle $\Theta = 2\Theta_s^l$, the single-spin flip amplitude contains only σ_x one-body terms and the two-spin flip term remains isotropic. Thus, for these particular values of Θ the effective model of the ladder becomes

$$\hat{H}_{\text{eff}}^l(2\Theta_s^l) = \sum_{j=1}^{N} J_{xx}^l \sigma_j^x \sigma_{j+1}^x + J_{yy}^l \sigma_j^y \sigma_{j+1}^y + J_{zz}^l \sigma_j^z \sigma_{j+1}^z + h^l \sigma_j^x, \tag{5.21}$$

with

$$h^l = 2J_1^l - \frac{6J_2^l J_3^l}{U}. \tag{5.22}$$

The Hamiltonian (5.21) corresponds to a XYZ Heisenberg model with an external field h^l along the x direction. In the system of $p-$ orbital bosons described in [252], the external magnetic field is created by the imbalance between the p_x and p_y interaction strengths and on-site energies, while in the ladder of rings loaded with OAM states that we consider here it arises as a consequence of the geometry of the system.

5.3.3 XYZ model with staggered fields

By tuning the geometry of the ring potential lattice, it is also possible to obtain effective models in which the spin-1/2 Hamiltonian is not uniform across all sites. As an example of a system in which this effect can be engineered, we consider the ladder with four sites per unit cell and a central angle $l\Theta = \pi/2$ depicted in Fig. 5.6. At sites A_i and C_i, the single-spin flip terms cancel. The B_i and D_i sites behave as if they belonged to a ladder of central angle $l\Theta = \pi$, but due to their different orientations there is a relative π phase between the amplitudes of their single-spin flip terms. Choosing the origin of
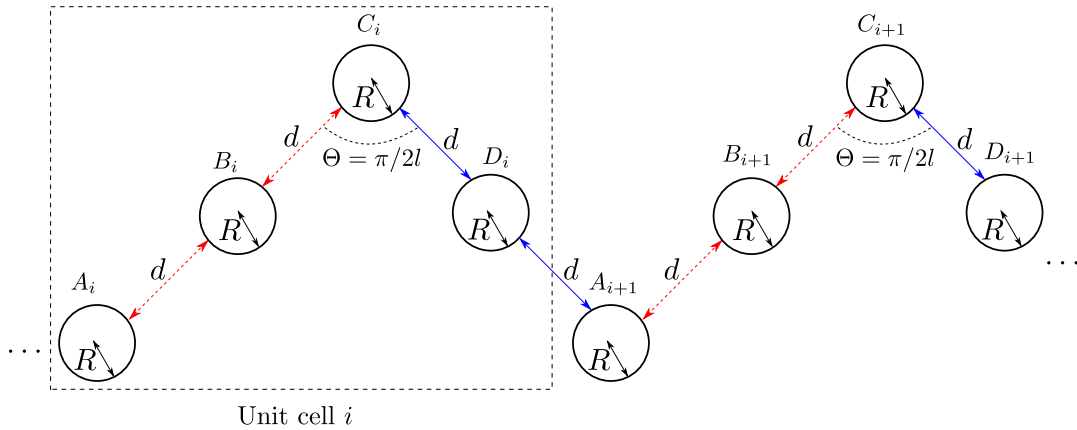
Figure 5.6: Ladder of ring potentials with four sites per unit cell. The origin of phases is taken along the direction $C_i \leftrightarrow D_i \leftrightarrow A_{i+1}$ (indicated with blue straight arrows), so that the couplings are taken real along this direction and all hopping phases appear in the $A_i \leftrightarrow B_i \leftrightarrow C_i$ links (indicated with red dashed arrows). The distance between the closest points of two nearest-neighbour rings is d.

phases along the line $A_i \leftrightarrow B_i \leftrightarrow C_i$, the effective spin Hamiltonian of this system reads

$$H_{\text{eff}}^l(l\Theta = \pi/2) = \sum_j J_{xx}^l \sigma_j^x \sigma_{j+1}^x + J_{yy}^l \sigma_j^y \sigma_{j+1}^y + J_{zz}^l \sigma_j^z \sigma_{j+1}^z + h^l \left(\sigma_{B_i}^x - \sigma_{D_i}^x \right). \quad (5.23)$$

In the model (5.23), the external magnetic fields appear in a staggered pattern only at the B_i and D_i sites.

5.4   Control over parameters and quantum phases through the trap geometry

In this section, we describe how the effective parameters of the spin$-1/2$ models can be tuned by modifying the size of the ring potentials and the separation between them. We also discuss the different phases of the XYZ model without external field [given by Eq. (5.17)] that can be explored with the system and we analyse their robustness against deviations of the central angle of the ladder from the values Θ_s^l that yield the effective model (5.17). Although we focus on the case of $l = 1$ OAM states, our considerations can be generalized to other OAM manifolds in a straightforward manner.

5.4.1   Control of the effective model parameters

In Sec. 2.4 of Chapter 2 we showed that the relative values of the couplings $\{J_1^l, J_2^l, J_3^l\}$ depend on the ring radius R and the separation between rings d. As can be seen in Fig. 2.4, for small values of the inter-ring distance (of the order of a few times σ), J_3^1 is several times larger than J_2^1. As shown in Fig. 5.7 (a), which corresponds to a ring of $R = 5\sigma$, in the most extreme limit of this regime the couplings of the effective model fulfill the relation $J_{xx}^1 \approx -J_{yy}^1 = -J_{zz}^1/3$. For rings of smaller radius, as the ring of $R = 2.5\sigma$ corresponding to Fig. 5.7 (b), J_2^1 and J_3^1 are more similar at small values of d, and therefore the ratio $|J_{zz}^1|/|J_{xx}^1|$ is smaller. However, for both values of R there is a range of inter-ring separations for which the condition $3J_{yy}^1 = J_{zz}^1 > -J_{xx}^1$ holds. In this region, the XYZ model without external field is in an anti-ferromagnetic phase in the z direction [258]. As d is increased, J_3^1 and J_2^1 become more similar, until the critical point $J_{zz} = -J_{xx}$ is reached. This point, which is signalled with dashed vertical lines in Figs. 5.7 (a) and (b), marks the transition to a ferromagnetic phase in the x direction [258]. In the limit of very large d, $J_3^1 = J_2^1$ and therefore $J_{zz}^1 = J_{yy}^1 = 0$.

The behaviour of the J_1^1/J_3^1 ratio as a function of d is shown in Fig. 5.7 (c) for rings of $R = 2.5\sigma$ and $R = 5\sigma$. For small values of d, J_1^1 has the same sign as J_3^1 and is of the same order. As d is increased, J_1^1/J_3^1 decreases until zero, and then it remains small and negative. As shown in the inset of Fig. 5.7 (c), this behaviour of the J_1^1/J_3^1 ratio translates into the effective field h^1 being positive at small values of d, and as d is increased decreasing to a minimum negative value and finally remaining negative and with an approximately constant value. Therefore, by tuning d it is possible to choose the sign of the external magnetic field in the effective model, or even make it vanish.

5.4.2   Properties of the obtainable quantum phases

In order to analyse numerically the phases of ladders with different central angles Θ, we have performed exact diagonalization in systems of up to $N = 16$ spins with PBC. If a quantum critical point exists, we expect that the energy gap Δ between the ground and first excited state scales with the system size as $\Delta \sim \frac{1}{N}$ [253]. Therefore, we have searched for the critical point by plotting, for ladders of different sizes, the quantity ΔN as a function of the inter-ring separation d and looking at the point where all the lines intersect. In order to confirm directly the presence of the transition point between the $z-$antiferromagnetic and the $x-$ferromagnetic phases, we have also computed for a ladder of $N = 16$ spins with PBC the ground state correlations between two fixed spins as a function of d.

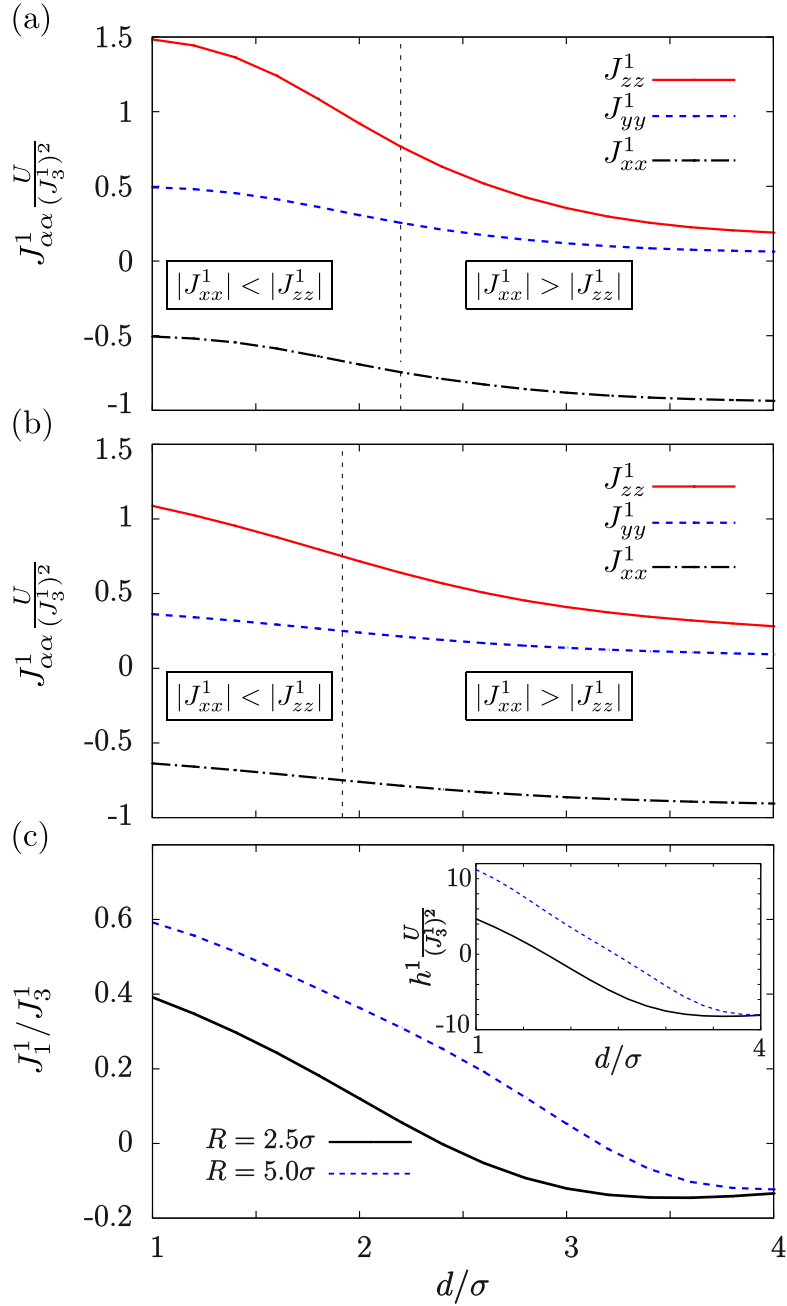Figure 5.7: Dependence of the effective couplings of the XYZ model on the inter-ring separation d for rings of (a) $R = 5\sigma$ and (b) $R = 2.5\sigma$. The dashed vertical lines mark the value of d for which $|J_{xx}^1| = |J_{zz}^1|$. (c) Dependence of the ratio J_1^1/J_3^1 on the inter-ring separation. The inset shows the dependence of h^1 on the inter-ring separation taking $U/J_3^1 = 20$ for all values of d.

(a) $|J_{zz}^1/J_{xx}^1|$

(b) $|J_{zz}^1/J_{xx}^1|$
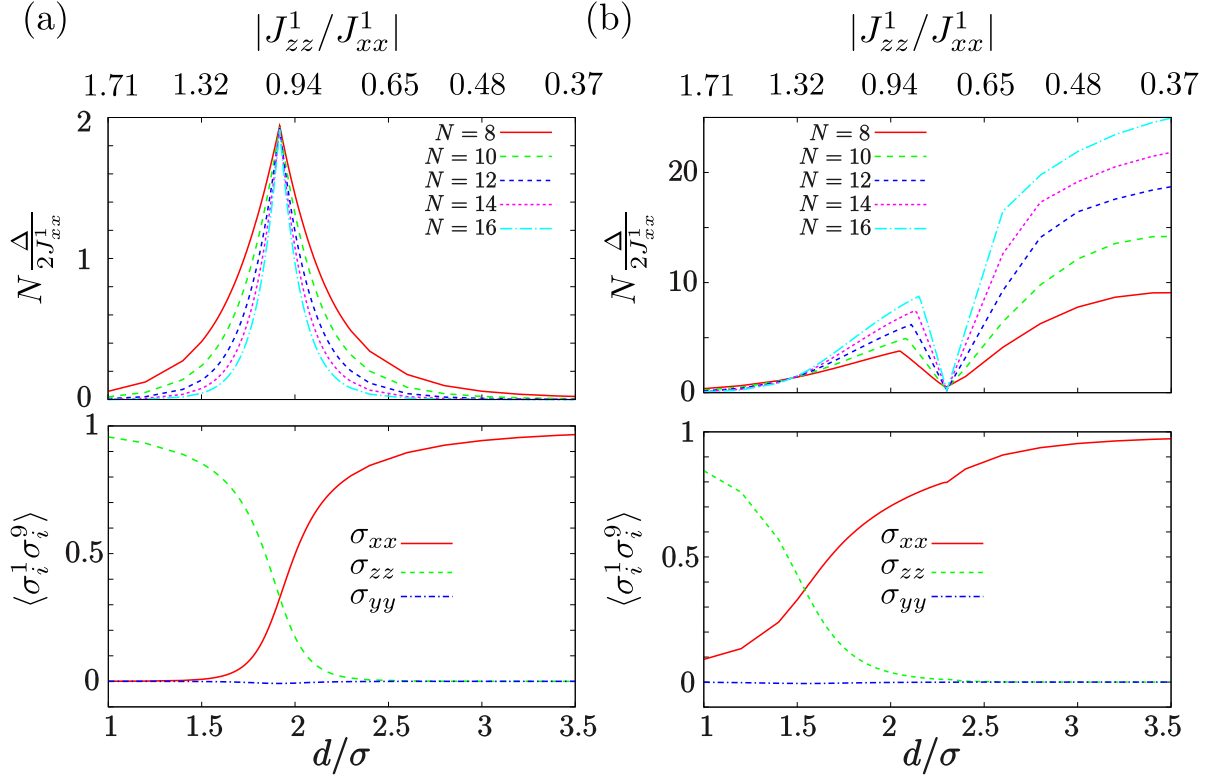
Figure 5.8: Upper plots in (a) and (b): dependence of the energy difference between the ground and first excited states on the inter-ring distance d for ladders of different sizes formed by rings of radius $R = 2.5\sigma$. Lower plots in (a) and (b): correlations between spin 1 and 9 in a ladder of $N = 16$ spins with PBC formed by rings of $R = 2.5\sigma$. In (a) the central angle of the ladder is $\Theta = 0.5\pi$ and in (b) $\Theta = 0.48\pi$. For all values of d, the parameters of the model fulfill the relation $U = 50(J_2^1 + J_3^1)$.

In Fig. 5.8 (a) we show the results of these two analyses for a ladder formed by rings of $R = 2.5\sigma$, filled with bosons in $l = 1$ OAM states and with a central angle $\Theta = 0.5\pi$, which is described by the XYZ model without external field (5.17). The upper plot shows the dependence of ΔN on d for different system sizes. As expected, all the lines intersect at the value of d for which $|J_{zz}^1| = |J_{xx}^1|$, where the phase transition occurs. As shown in the lower plot, in the $z-$antiferromagnetic phase, the zz correlation is higher than the xx one. As d increases, the zz correlation decays and the xx one increases, until they reach the same value at an inter-ring distance that coincides with the corresponding one for the critical point.

In Fig. 5.8 (b), we perform the same analysis for a ladder as in Fig. 5.8 (a) but with a central angle $\Theta = 0.48\pi$. According to Eq. (5.16), for this central angle the effective model incorporates one- and two-spin terms that are not present in the XYZ model

without external field that is realized for $\Theta = 0.5\pi$. Due to this effect, in the upper plot we observe that there are two points where the ΔN lines intersect, which correspond to $|J_{zz}^1|/|J_{xx}^1| \approx 1.34, 0.76$ and $d \approx 1.47\sigma, 2.30\sigma$. The one that occurs for a smaller value of d corresponds to a point where the zz and xx correlations become equal. Therefore, it marks the transition between the $z-$antiferromagnetic and the $x-$ferromagnetic phases. This transition occurs at a smaller value of d than in the ladder with a central angle $\Theta = 0.5\pi$ because of the presence of the magnetic field along the x direction. For values of the central angle more deviated from 0.5π, the presence of the magnetic field destroys the $z-$antiferromagnetic phase and the transition does not occur. The other point where the ΔN curves intersect occurs at a larger value of d, and coincides with the inter-ring distance for which the external magnetic field h^1 vanishes.

5.5   Experimental considerations

In this section, we address several questions concerning the experimental implementation of the system. In particular, we discuss the readout of the states and we analyse the stability of the OAM states under collisional processes.

5.5.1   Experimental readout of the spin states

Making use of a scheme of two-photon stimulated Raman transitions in the Lamb-Dicke regime analogous to the one discussed in [252], the OAM states of a single site could be addressed separately. By tuning the frequencies of the lasers, side-band transitions between the ground state of the ring potential and the $\pm l$ OAM states could be induced. Once the OAM states are encoded in the internal atomic states, a quantum gas microscope [50, 51] could be used to read the spin states of the effective models with single-site resolution.

In order to select a specific OAM mode, two different approaches could be followed. As pointed out in [252], one option would be to choose the laser beams such that their wave vector difference is oriented along the x or y direction. In that manner, the lasers would only interact with states that have nodes along the x or y axes, which can be expressed as symmetric or anti-symmetric superpositions of OAM modes. Alternatively, with the aid of e.g. spatial light modulators, one could also make a small adiabatic deformation of the ring trap in order to break cylindrical symmetry and induce an energy splitting between the dressed OAM states such that they can be independently resolved.

5.5.2   Collisional stability of the OAM states

An important question concerning the feasibility of the experimental realization of the system is whether collisional processes may cause transitions between states with different OAM that invalidate the assumption that all the atoms remain always in the same OAM manifold [259]. These collisional processes are described in the Born approximation by the operator

$$\hat{U} = \frac{g}{2} \int d\vec{r}\, \hat{\Psi}^{\dagger}\hat{\Psi}^{\dagger}\hat{\Psi}\hat{\Psi}, \tag{5.24}$$

where $\hat{\Psi} = \sum_{l=0}^{\infty} \hat{\Psi}_l$ is the full bosonic field operator of the lattice, given by the sum of all the field operators of the different OAM manifolds (5.3). In order to analyse the stability of the OAM states under the most relevant collisional processes, it is enough to restrict ourselves to the examination of two-boson states in a single ring. This is because in the strongly interacting regime that we consider, the role of tunnelling is significantly reduced and the collisional interactions are dominated by on-site processes. In the opposite limit where atoms are delocalised, we would have to consider the full Bloch band widths. To simplify the analysis, we only consider collisions in which the total OAM of each of the atoms changes at most by one unit, which are the most relevant ones. In order to describe these processes, it is enough to expand the bosonic field operator as

$$\hat{\Psi} = \hat{\Psi}^{l-1} + \hat{\Psi}^{l} + \hat{\Psi}^{l+1} = \sum_{m=l-1}^{l+1} \hat{a}_{-m}\phi_{-m}(\vec{r}) + \hat{a}_{m}\phi_{m}(\vec{r}). \tag{5.25}$$

Note that since we are considering a single ring we have dropped the j index that labels the site. Due to the azimuthal part of the wave functions $\phi_{\pm m}(\vec{r})$ [see Eq. (5.1)], the $\hat{U}$ operator Eq. (5.24) only yields non-zero matrix elements between two-boson states in which the sum of the circulations of the two bosons is the same. Using the expansion Eq. (5.25) and neglecting all the terms that yield null matrix elements, we can write the $\hat{U}$ operator as

$$
\begin{aligned}
\hat{U} = {} & \frac{U}{2} \left((\hat{a}_{+l}^{\dagger})^2 + 2\hat{a}_{+(l-1)}^{\dagger}\hat{a}_{+(l+1)}^{\dagger} \right) (\hat{a}_{+l})^2 \\
& + \frac{U}{2} \left(2\hat{a}_{+l}^{\dagger}\hat{a}_{-l}^{\dagger} + 2\hat{a}_{+(l-1)}^{\dagger}\hat{a}_{-(l-1)}^{\dagger} + 2\hat{a}_{+(l+1)}^{\dagger}\hat{a}_{-(l+1)}^{\dagger} \right) (2\hat{a}_{+l}\hat{a}_{-l}) \\
& + \frac{U}{2} \left((\hat{a}_{-l}^{\dagger})^2 + 2\hat{a}_{-(l-1)}^{\dagger}\hat{a}_{-(l+1)}^{\dagger} \right) (\hat{a}_{-l})^2 \\
& + \text{h.c.},
\end{aligned}
\tag{5.26}
$$

where the U parameter is the same as in Eq. (5.7). The operator Eq. (5.26) yields 4 transitions from the 3 possible two-boson initial states $|i\rangle$ to final states $|f\rangle$ in which

the atoms are in different OAM manifolds. In table 5.1 we summarize the values of the matrix elements of the transitions and the total energies of the initial and final states, which are computed as the sum of their interaction energies, given by $\left\langle i \left| \hat{U} \right| i \right\rangle$ and $\left\langle f \left| \hat{U} \right| f \right\rangle$, and the sum of the single-particle energies $E(l)$ of the two bosons, given by Eq. (5.2). Since the separation between the OAM energy levels is anharmonic, the allowed transitions between two-boson states that are not within the same OAM manifold are in general off-resonant, contributing to the stability of the Mott insulator state. From table 5.1, we observe that the lowest energy differences between the initial and final states are of the order of $U \pm E_c$, whereas the transition matrix elements are of the order of U. Thus, in order to minimize the importance of these transitions, the E_c/U ratio should be maximized. This may be done by using rings of radius $R \lesssim 2.5\sigma$ and setting the interaction strength g to a value as small as possible, but still large enough that the system is in the Mott insulator phase. Moreover, since we are assuming that the gas of ultracold atoms is in the Mott insulator phase at unit filling, the ground state has only very small contributions from states with more than one atom per site. Therefore, the occurrence of these collisional processes is suppressed in the first place by the population distribution of the many-body states in the ground state [56].

$\lvert i \rangle$	$\lvert f \rangle$	$\left\langle i \left\lvert \hat{H} \right\rvert i \right\rangle$	$\left\langle f \left\lvert \hat{H} \right\rvert f \right\rangle$	$\left\langle f \left\lvert \hat{U} \right\rvert i \right\rangle$
$\frac{1}{\sqrt{2}}\hat{a}_{+l}^{\dagger}\hat{a}_{+l}^{\dagger}\lvert 0\rangle$	$\hat{a}_{+(l-1)}^{\dagger}\hat{a}_{+(l+1)}^{\dagger}\lvert 0\rangle$	$\frac{U}{2}+2[E_0+E_cl^2]$	$2[U+E_0+E_c(l^2+1)]$	U
$\hat{a}_{+l}^{\dagger}\hat{a}_{-l}^{\dagger}\lvert 0\rangle$	$\hat{a}_{+(l-1)}^{\dagger}\hat{a}_{-(l-1)}^{\dagger}\lvert 0\rangle$	$2[U+E_0+E_cl^2]$	$2[U+E_0+E_c(l-1)^2]$	$2U$
$\hat{a}_{+l}^{\dagger}\hat{a}_{-l}^{\dagger}\lvert 0\rangle$	$\hat{a}_{+(l+1)}^{\dagger}\hat{a}_{-(l+1)}^{\dagger}\lvert 0\rangle$	$2[U+E_0+E_cl^2]$	$2[U+E_0+E_c(l+1)^2]$	$2U$
$\frac{1}{\sqrt{2}}\hat{a}_{-l}^{\dagger}\hat{a}_{-l}^{\dagger}\lvert 0\rangle$	$\hat{a}_{-(l+1)}^{\dagger}\hat{a}_{-(l-1)}^{\dagger}\lvert 0\rangle$	$\frac{U}{2}+2[E_0+E_cl^2]$	$2[U+E_0+E_c(l^2+1)]$	U

Table 5.1: Summary of the possible initial and final states in the collisional processes, their energies and the transition matrix elements.

5.6   Conclusions

In this Chapter, we have studied the physics of ultracold bosons carrying OAM in arrays of cylindrically symmetric potentials in the Mott insulator phase at unit filling. In this regime, the degree of freedom corresponding to the circulation of the OAM states can be mapped to a spin$-1/2$ variable. By tuning the relative phases in the tunneling amplitudes, which depend on the orientation between the traps, the system can be used to simulate a variety of spin$-1/2$ models of quantum magnetism.

First, we have computed by means of second-order perturbation theory the explicit dependence of the effective couplings on the relative angle between the traps. We have

benchmarked the calculation by comparing, in a system of small size, the spin dynamics obtained with the effective model and the full Bose-Hubbard Hamiltonian. Then, we have discussed how, by tuning the geometry of the lattice, different models of interest such as the XYZ model with uniform or staggered external fields can be obtained.

Besides engineering different spin$-1/2$ models by tuning the geometry of the lattice, the system also allows to adjust the relative strength between the effective couplings by changing the radius of the ring traps and their separation. We have shown that this fact can be exploited in realistic experimental set-ups to explore two distinct phases of the XYZ model without external field. Furthermore, we have analysed the effect of small changes of the relative angle between the traps on these phases.

Concerning the experimental implementation of the system, we have introduced single-site addressing techniques that might allow to retrieve the state of each individual spin. We have also analysed the collisional stability of the system and concluded that the anharmonic energy spacing between OAM states introduced by the ring geometry extends the lifetime of the Mott state.

Interaction-induced topological properties of two bosons carrying orbital angular momentum in flat-band systems

In this Chapter, we extend the study of the diamond chain filled with ultracold atoms carrying Orbital Angular Momentum (OAM) performed in Chapter 4 to incorporate the effect of interactions. Specifically, we consider two-boson states in a lattice with weak attractive on-site interactions in the limit where all the bands are flat. In this situation, the effective mass becomes infinite and the properties of the system are solely determined by the interactions between overlapping single-particle localized eigenstates. We focus on the lowest-energy subspaces of the spectrum, which are composed of two-body states in which the two bosons occupy states belonging to the two lowest degenerate flat bands. By projecting the Hamiltonian into these bands, we derive effective models for these subspaces and we show that topologically non-trivial phases with their corresponding two-boson edge states can be obtained.

The Chapter is organized as follows. In Sec. 6.1 we give an overview on recent studies on the topological properties of two-body states, and we briefly discuss the peculiarities of flat-band lattices with geometric frustration such as the one that we consider in this work. In Sec. 6.2 we describe in detail the physical system and we identify the lowest-energy subspaces of two-boson states. In Sec. 6.3, we derive effective models for the two subspaces of lowest energy by restricting the Hamiltonian to the two degenerate lowest flat bands. Each of these two effective models for two-boson states can be reinterpreted as single-particle lattice models with hopping amplitudes that depend on the strength of the on-site interactions of the original Hamiltonian. Making use of this picture, we

analyse the topology of the effective models and we show that it can be rendered non-trivial by tuning independently the interaction strength in the odd and even unit cells of the lattice. In Sec. 6.4 we present exact diagonalization calculations that support the analytical predictions made in Sec. 6.3 and confirm the presence of in-gap two-boson edge states in the topological phase. We also examine numerically the effects of deviations from the weakly interacting and flat-band limits. Finally, in Sec. 6.5 we summarize the main conclusions of this Chapter and we outline further research directions.

6.1   Introduction

Over the last years, there has been an increasing interest in the study of few-body states in periodic potentials. Besides being fascinating by themselves, the properties of these states are relevant for the physics of ultracold atoms in optical lattices [30, 31]. In turn, these systems constitute an ideal platform to explore few-particle phenomena under flexible and well-controlled conditions. The first observation of long-lived bound pairs of repulsively interacting atoms in optical lattices [260], also known as doublons, has been followed by a number of experimental [261–263] and theoretical [264–275] studies of these exotic two-body states, which can also be implemented in photonic systems [276, 277].

In recent years, the study of topological phases of matter has been the focus of much attention. One of the main features of these quantum phases is the existence of a bulk-boundary correspondence, which correlates the non-trivial topological indices of the bulk energy bands with the presence of robust edge modes. The properties of topological materials, which can be explored with cold atoms [83] and photonic systems [204], are well understood at the single-particle level [67, 79]. However, due to the difficulty of defining topological invariants in strongly correlated systems [278], much less is known about the effect of interactions on these quantum phases. Recently, several works have concentrated on the topological properties of two-body states [236, 263, 279–288], with the long-term aim of paving the path to a better comprehension of topological phases in a many-body interacting scenario [289]. A distinctive advantage that these small-sized systems offer is that it is often possible to map the problem of two interacting particles in a lattice into a single-particle model defined in a different lattice, the topological characterization of which can be performed with the usual tools [236, 281, 282, 285].

In this Chapter, we study the topological properties of two-boson states in a system that is topologically non-trivial at the single-particle level. Specifically, we consider the diamond-chain lattice that we studied in detail in Chapter 4 in the limit in which all the bands are flat. In this situation, quantum interference leads to the localization of non-interacting particles in small regions of the lattice, giving rise to the Aharonov-Bohm

caging effect [225, 231] and to a rich variety of quantum phases in the many-body case [290]. This localization effect is a general feature of flat-band systems [291], wherein a strong frustration occurs due to the large degeneracies between localized eigenstates and the role of the kinetic energy becomes irrelevant. This peculiar feature is responsible for the appearance in such systems of a number of quantum states determined solely by the interactions and the geometry of the lattice [292–302], including topologically non-trivial phases [232, 303–306]. In this work, we focus on the limit of weak attractive interactions, in which the low-energy properties of the system can be studied by projecting the Hamiltonian to the lowest flat bands [292–295]. By mapping the subspaces of two-boson states of lowest self-energy into single-particle models, we show that the system has a topologically non-trivial phase. In a diamond chain with open boundaries, this topological phase is benchmarked by the presence of robust in-gap states localized at the edges, which are in turn composed of bound pairs of bosons occupying localized single-particle eigenstates.

6.2   Physical system

The physical system that we consider is the quasi-1D optical lattice with a diamond chain shape formed by ring potentials of radius R with a nearest-neighbour separation d and filled with ultracold bosons loaded into OAM $l = 1$ states that we studied in Chapter 4. The new element here is the introduction of a weak attractive on-site interaction between the bosons, which is generically described by the Hamiltonian Eq. (5.7). For reasons that will become clear in Sec. 6.2.2, we let the interaction strength take the value $U_A < 0$ in the A sites of each cell, and $U_1 < 0$ and $U_2 < 0$ in the B and C sites of odd and even unit cells, respectively. In Chapter 4, we showed that the kinetic part of the Hamiltonian is given by Eq. (4.4). For simplicity, we neglect the self-coupling term J_1, which only appears at singly connected sites. As we argued in Sec. 4.6.3, this approximation does not affect significantly the results. Thus, the total Hamiltonian of the system reads

$$\hat{H} = \hat{H}_{\text{kin}} + \hat{H}_{\text{int}};$$ (6.1)

$$\hat{H}_{\text{kin}} = J_2 \sum_{i=1}^{N_c-1} \sum_{\alpha=\pm} \left[\hat{a}_\alpha^{i\dagger}(\hat{b}_\alpha^i + \hat{b}_\alpha^{i+1} + \hat{c}_\alpha^i + \hat{c}_\alpha^{i+1}) \right] + \text{h.c.}$$

$$+ J_3 \sum_{i=1}^{N_c-1} \sum_{\alpha=\pm} \left[\hat{a}_\alpha^{i\dagger}(\hat{b}_{-\alpha}^{i+1} - \hat{b}_{-\alpha}^i + \hat{c}_{-\alpha}^i - \hat{c}_{-\alpha}^{i+1}) \right] + \text{h.c.},$$ (6.2)

$$\hat{H}_{\text{int}} = \frac{U_A}{2} \sum_{i=1}^{N_c} \hat{n}_+^{a_i}(\hat{n}_+^{a_i} - 1) + \hat{n}_-^{a_i}(\hat{n}_-^{a_i} - 1) + 4\hat{n}_+^{a_i}\hat{n}_-^{a_i}$$

$$+ \frac{U_1}{2} \sum_{i=1}^{[N_c/2]} \sum_{j=b,c} \hat{n}_+^{j_{2i}}(\hat{n}_+^{j_{2i-1}} - 1) + \hat{n}_-^{j_{2i-1}}(\hat{n}_-^{j_{2i-1}} - 1) + 4\hat{n}_+^{j_{2i-1}}\hat{n}_-^{j_{2i-1}}$$

$$+ \frac{U_2}{2} \sum_{i=1}^{[N_c/2]} \sum_{j=b,c} \hat{n}_+^{j_{2i}}(\hat{n}_+^{j_{2i}} - 1) + \hat{n}_-^{j_{2i}}(\hat{n}_-^{j_{2i}} - 1) + 4\hat{n}_+^{j_{2i}}\hat{n}_-^{j_{2i}},$$ (6.3)

where i labels the unit cell, $\hat{a}_\alpha^{i\dagger}$, $\hat{b}_\alpha^{i\dagger}$ and $\hat{c}_\alpha^{i\dagger}$ are the annihilation operators associated with the OAM states of circulation α at the sites A_i, B_i and C_i, respectively, N_c is the total number of unit cells, $[N_c/2]$ denotes the integer part of $N_c/2$, and in Eq. (6.3) we have defined $\hat{n}_\alpha^{j_i} \equiv \hat{j}_\alpha^{i\dagger}\hat{j}_\alpha^i$, with $\alpha = \pm$ and $j = \{a, b, c\}$. The operators $\hat{j}_\alpha^{i\dagger}$ and $\hat{j}_\alpha^i$ satisfy the usual bosonic commutation relations

$$[\hat{j}_\alpha^i, \hat{j'}_{\alpha'}^{i'}] = 0,$$ (6.4a)

$$[\hat{j}_\alpha^{i\dagger}, \hat{j'}_{\alpha'}^{i'\dagger}] = 0,$$ (6.4b)

$$[\hat{j}_\alpha^i, \hat{j'}_{\alpha'}^{i'\dagger}] = \delta_{jj'}\delta_{ii'}\delta_{\alpha\alpha'}.$$ (6.4c)

6.2.1   Flat-band localized eigenstates

Let us start by addressing the kinetic part of the Hamiltonian, Eq. (6.2). We focus on the $J_2 = J_3 \equiv J$ limit, which, as we discussed in Sec. 2.4 of Chapter 2, can be approximately realized by setting a large value of d and using rings with a large radius. As we explained in Sec. 4.2 of Chapter 4, in this limit the band structure Eq. (4.8) is composed of three two-fold degenerate flat bands of energies

$$E_-^1 = E_-^2 = -2\sqrt{2}J,$$ (6.5)

$$E_0^1 = E_0^2 = 0,$$ (6.6)

$$E_+^1 = E_+^2 = 2\sqrt{2}J.$$ (6.7)

In Sec. 4.4 of Chapter 4, we also discussed the presence of in-gap states with energies $E = \pm 2J$ localized at the right edge of the diamond chain. These states, which are given by Eq. (4.24), can be removed from the single-particle spectrum by cutting the A site of the last unit cell, as shown in Fig. 6.1 (a). From now onwards, we will assume that there are no single-particle edge states in the lattice.

The eigenstates belonging to each of the flat bands can be expressed as compact modes that are completely localized in two consecutive unit cells. Retrieving Eqs. (4.16) and (4.19), we can write the following expressions for the bosonic creation operators associated with the modes localized in the i and $i + 1$ unit cells belonging to the lower, zero-energy and upper bands

$$\hat{W}_{-,i}^{1\dagger} = \frac{1}{4}\left(-\frac{4}{\sqrt{2}}\hat{a}_{+}^{i\dagger} + \hat{b}_{+}^{i\dagger} - \hat{b}_{-}^{i\dagger} + \hat{c}_{+}^{i\dagger} + \hat{c}_{-}^{i\dagger} + \hat{b}_{+}^{i+1\dagger} + \hat{b}_{-}^{i+1\dagger} + \hat{c}_{+}^{i+1\dagger} - \hat{c}_{-}^{i+1\dagger}\right),$$

$$\hat{W}_{-,i}^{2\dagger} = \frac{1}{4}\left(-\frac{4}{\sqrt{2}}\hat{a}_{-}^{i\dagger} - \hat{b}_{+}^{i\dagger} + \hat{b}_{-}^{i\dagger} + \hat{c}_{+}^{i\dagger} + \hat{c}_{-}^{i\dagger} + \hat{b}_{+}^{i+1\dagger} + \hat{b}_{-}^{i+1\dagger} - \hat{c}_{+}^{i+1\dagger} + \hat{c}_{-}^{i+1\dagger}\right),$$

$$\hat{H}_{\text{kin}}\left(\hat{W}_{-,i}^{1/2\dagger}|0\rangle\right) = -2\sqrt{2}J\left(\hat{W}_{-,i}^{1/2\dagger}|0\rangle\right). \tag{6.8}$$

$$\hat{W}_{0,i}^{1\dagger} = \frac{1}{2\sqrt{2}}\left(-\hat{b}_{+}^{i\dagger} + \hat{b}_{-}^{i\dagger} + \hat{c}_{+}^{i\dagger} + \hat{c}_{-}^{i\dagger} - \hat{b}_{+}^{i+1\dagger} - \hat{b}_{-}^{i+1\dagger} + \hat{c}_{+}^{i+1\dagger} - \hat{c}_{-}^{i+1\dagger}\right),$$

$$\hat{W}_{0,i}^{2\dagger} = \frac{1}{2\sqrt{2}}\left(\hat{b}_{+}^{i\dagger} - \hat{b}_{-}^{i\dagger} + \hat{c}_{+}^{i\dagger} + \hat{c}_{-}^{i\dagger} - \hat{b}_{+}^{i+1\dagger} - \hat{b}_{-}^{i+1\dagger} - \hat{c}_{+}^{i+1\dagger} + \hat{c}_{-}^{i+1\dagger}\right),$$

$$\hat{H}_{\text{kin}}\left(\hat{W}_{0,i}^{1/2\dagger}|0\rangle\right) = |0\rangle. \tag{6.9}$$

$$\hat{W}_{+,i}^{1\dagger} = \frac{1}{4}\left(\frac{4}{\sqrt{2}}\hat{a}_{+}^{i\dagger} + \hat{b}_{+}^{i\dagger} - \hat{b}_{-}^{i\dagger} + \hat{c}_{+}^{i\dagger} + \hat{c}_{-}^{i\dagger} + \hat{b}_{+}^{i+1\dagger} + \hat{b}_{-}^{i+1\dagger} + \hat{c}_{+}^{i+1\dagger} - \hat{c}_{-}^{i+1\dagger}\right),$$

$$\hat{W}_{+,i}^{2\dagger} = \frac{1}{4}\left(\frac{4}{\sqrt{2}}\hat{a}_{-}^{i\dagger} - \hat{b}_{+}^{i\dagger} + \hat{b}_{-}^{i\dagger} + \hat{c}_{+}^{i\dagger} + \hat{c}_{-}^{i\dagger} + \hat{b}_{+}^{i+1\dagger} + \hat{b}_{-}^{i+1\dagger} - \hat{c}_{+}^{i+1\dagger} + \hat{c}_{-}^{i+1\dagger}\right),$$

$$\hat{H}_{\text{kin}}\left(\hat{W}_{+,i}^{1/2\dagger}|0\rangle\right) = -2\sqrt{2}J\left(\hat{W}_{+,i}^{1/2\dagger}|0\rangle\right). \tag{6.10}$$

In Fig. 6.1 (b) we show graphic representations of the states localized in two consecutive unit cells of the diamond chain created by the operators (6.8), (6.9) and (6.10). Since each of these states spans a plaquette formed by the sites $\{A_i, B_i, C_i, B_{i+1}, C_{i+1}\}$, a diamond chain with N_c unit cells has $N_c - 1$ completely localized modes of each type. Using the linearity of the commutation operation and applying the relations (6.4), it can be readily shown that the only non-zero commutators between flat-band annihilation and creation operators are

$$[\hat{W}_{\pm,i}^{1}, \hat{W}_{\pm,i}^{1\dagger}] = [\hat{W}_{\pm,i}^{2}, \hat{W}_{\pm,i}^{2\dagger}] = [\hat{W}_{0,i}^{1}, \hat{W}_{0,i}^{1\dagger}] = [\hat{W}_{0,i}^{2}, \hat{W}_{0,i}^{2\dagger}] = 1. \tag{6.11}$$

(a)

(b)
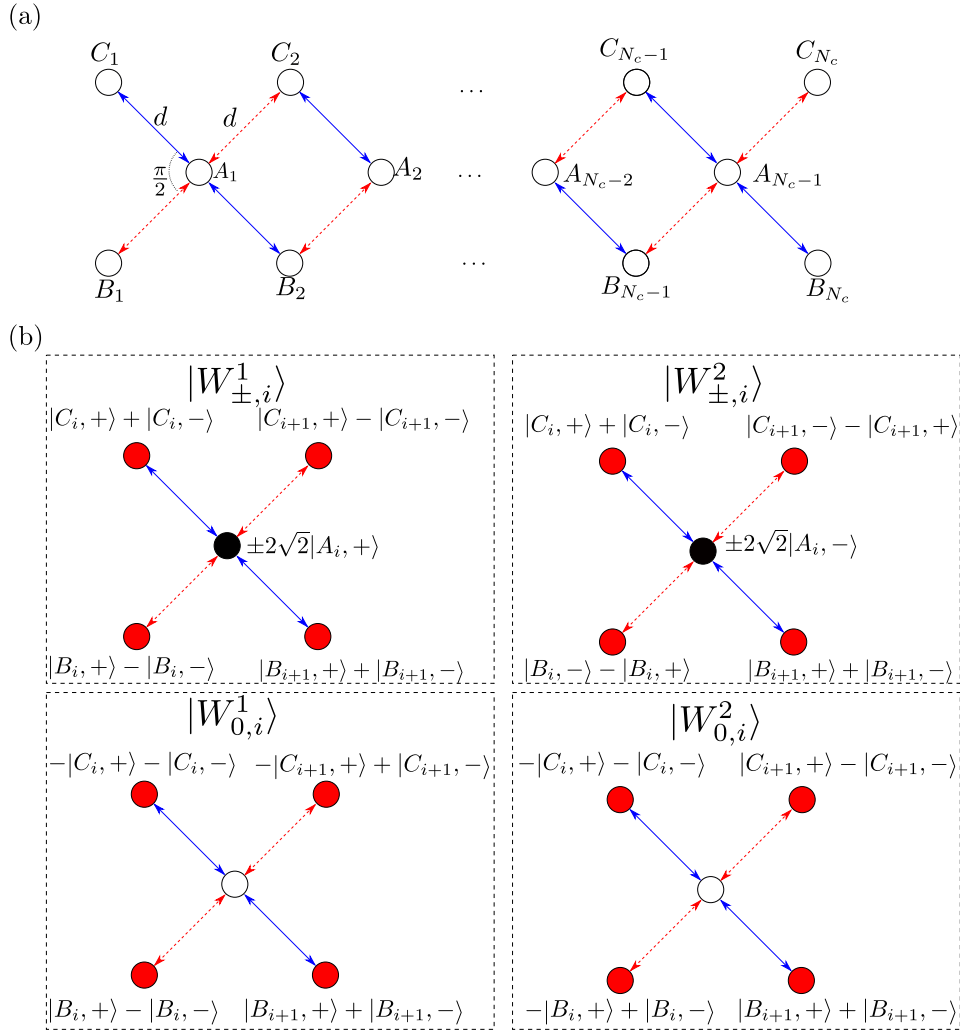
Figure 6.1: (a) Schematic representation of the diamond-chain shaped optical lattice considered in this Chapter. As in Chapter 4, each of the sites corresponds to a ring potential of radius R. The blue and red lines mark respectively the directions along which the couplings are real or acquire a π phase, respectively. We remove the A site from the last unit cell in order to avoid the presence of single-particle edge states in the spectrum. (b) Sketches of the maximally localized flat-band eigenstates (6.8), (6.9) and (6.10) indicating the relative weights of each of the OAM states at the different sites.

In the absence of interactions, many-body eigenstates can be constructed by applying consecutively any of the creation operators (6.8), (6.9), (6.10) to the vacuum state $|0\rangle$. As they will be useful for the forthcoming discussion, we also write explicitly the expressions of the creation operators of the states of the original OAM basis in terms of those of the flat-band localized modes

$$\hat{a}_+^{i\dagger} = \frac{1}{\sqrt{2}} \left(\hat{W}_{+,i}^{1\dagger} - \hat{W}_{-,i}^{1\dagger} \right), \tag{6.12a}$$

$$\hat{a}_-^{i\dagger} = \frac{1}{\sqrt{2}} \left(\hat{W}_{+,i}^{2\dagger} - \hat{W}_{-,i}^{2\dagger} \right), \tag{6.12b}$$

$$\hat{b}_+^{i\dagger} = \frac{1}{4} \left(\hat{W}_{-,i-1}^{1\dagger} + \hat{W}_{-,i-1}^{2\dagger} + \hat{W}_{-,i}^{1\dagger} - \hat{W}_{-,i}^{2\dagger} + \sqrt{2}\hat{W}_{0,i-1}^{1\dagger} + \sqrt{2}\hat{W}_{0,i-1}^{2\dagger} \right.$$
$$\left. -\sqrt{2}\hat{W}_{0,i}^{1\dagger} + \sqrt{2}\hat{W}_{0,i}^{2\dagger} + \hat{W}_{+,i-1}^{1\dagger} + \hat{W}_{+,i-1}^{2\dagger} + \hat{W}_{+,i}^{1\dagger} - \hat{W}_{+,i}^{2\dagger} \right), \tag{6.12c}$$

$$\hat{b}_-^{i\dagger} = \frac{1}{4} \left(\hat{W}_{-,i-1}^{1\dagger} + \hat{W}_{-,i-1}^{2\dagger} - \hat{W}_{-,i}^{1\dagger} + \hat{W}_{-,i}^{2\dagger} + \sqrt{2}\hat{W}_{0,i-1}^{1\dagger} + \sqrt{2}\hat{W}_{0,i-1}^{2\dagger} \right.$$
$$\left. \sqrt{2}\hat{W}_{0,i}^{1\dagger} - \sqrt{2}\hat{W}_{0,i}^{2\dagger} + \hat{W}_{+,i-1}^{1\dagger} + \hat{W}_{+,i-1}^{2\dagger} - \hat{W}_{+,i}^{1\dagger} + \hat{W}_{+,i}^{2\dagger} \right), \tag{6.12d}$$

$$\hat{c}_+^{i\dagger} = \frac{1}{4} \left(\hat{W}_{-,i-1}^{1\dagger} - \hat{W}_{-,i-1}^{2\dagger} + \hat{W}_{-,i}^{1\dagger} + \hat{W}_{-,i}^{2\dagger} + \sqrt{2}\hat{W}_{0,i-1}^{1\dagger} - \sqrt{2}\hat{W}_{0,i-1}^{2\dagger} \right.$$
$$\left. -\sqrt{2}\hat{W}_{0,i}^{1\dagger} - \sqrt{2}\hat{W}_{0,i}^{2\dagger} + \hat{W}_{+,i-1}^{1\dagger} - \hat{W}_{+,i-1}^{2\dagger} + \hat{W}_{+,i}^{1\dagger} + \hat{W}_{+,i}^{2\dagger} \right), \tag{6.12e}$$

$$\hat{c}_-^{i\dagger} = \frac{1}{4} \left(-\hat{W}_{-,i-1}^{1\dagger} + \hat{W}_{-,i-1}^{2\dagger} + \hat{W}_{-,i}^{1\dagger} + \hat{W}_{-,i}^{2\dagger} - \sqrt{2}\hat{W}_{0,i-1}^{1\dagger} + \sqrt{2}\hat{W}_{0,i-1}^{2\dagger} \right.$$
$$\left. -\sqrt{2}\hat{W}_{0,i}^{1\dagger} - \sqrt{2}\hat{W}_{0,i}^{2\dagger} - \hat{W}_{+,i-1}^{1\dagger} + \hat{W}_{+,i-1}^{2\dagger} + \hat{W}_{+,i}^{1\dagger} + \hat{W}_{+,i}^{2\dagger} \right). \tag{6.12f}$$

As we saw in Sec. 4.4 of Chapter 4, a direct consequence of the fact that the OAM states can be expressed as combinations of completely localized eigenmodes is the appearance of Aharonov-Bohm caging, i.e., the confinement of single-atom wavepackets in small regions of the lattice due to quantum interference. In the non-interacting limit, a many-body state will also experience this effect since each atom evolves independently. In recent investigations, it has been shown that Aharonov-Bohm caging can also survive in the presence of small mean-field interactions [307, 308].

6.2.2 Two-boson states with on-site interactions

After reviewing the single-particle properties of the system, we are now in a position to examine the effect of the on-site interactions, described by Eq. (6.3), on the low-energy properties of two-boson states. In the absence of interactions there are many possible ground states, which have an energy $E = -4\sqrt{2}J$ and consist of the two bosons occupying any of the localized modes belonging to the lowest flat bands. However, the introduction of an attractive interaction changes this scenario. From Eq. (6.3), it is clear that whenever two or more bosons occupy the same site an interaction term arises. Therefore, $\hat{H}_{\text{int}}$ yields non-zero matrix elements between two-boson states formed by localized modes which overlap to some extent. We concentrate on the case in which the interaction strength is much smaller than the size of the band gap, $|U_A|, |U_1|, |U_2| \ll$

$2\sqrt{2}J$, in such a way that the bands do not mix and the low-energy properties of the system can be examined by projecting $\hat{H}_{\text{int}}$ into the lowest flat bands. If the lattice would host edge states, the weakly interacting condition would be slightly more stringent and would read $|U_A|, |U_1|, |U_2| \ll 4\sqrt{2}J - 2(1 + \sqrt{2})J \approx 0.8J$. Due to the effect of the on-site interactions, the total space of non-interacting two-boson ground states, which we denote as $\mathcal{H}$, can be divided into the following 4 subspaces according to the values of the self-energies of their states:

1) $\mathcal{H}_1 \equiv \left\{ \hat{W}_{-,i}^{n\dagger} \hat{W}_{-,k}^{m\dagger} |0\rangle \right\}$, with $n, m = 1, 2$; $i = 1, ..., N_c - 1$ and $|k - i| \geq 2$.

This is the subspace of states where the two bosons occupy localized modes separated by two unit cells or more. In these configurations there is no overlap between the two particles, and therefore the interaction energy is zero,

$$\left\langle 0 \left| \hat{W}_{-,i}^{n} \hat{W}_{-,k}^{m} \hat{H}_{\text{int}} \hat{W}_{-,i}^{n\dagger} \hat{W}_{-,k}^{m\dagger} \right| 0 \right\rangle = 0. \tag{6.13}$$

2) $\mathcal{H}_2 \equiv \left\{ \hat{W}_{-,i}^{n\dagger} \hat{W}_{-,i+1}^{m\dagger} |0\rangle \right\}$, with $n, m = 1, 2$ and $i = 1, ..., N_c - 2$.

This is the set of states in which the localized modes of the two atoms are localized in two consecutive unit cells, in such a way that they share the sites B_{i+1} and C_{i+1}. Therefore, in order to compute their self-energy we need to take into account the products of creation operators acting on these sites contained in the expansion of $\hat{W}_{-,i}^{n\dagger} \hat{W}_{-,i+1}^{m\dagger}$. Using the expressions for the modes of the lowest-energy bands (6.8) and retaining only the terms that are relevant for the computation of the self-energy, we can write

$$W_{-,i}^{1\dagger} W_{-,i+1}^{1\dagger} = \frac{1}{16} (\hat{b}_+^{i+1\dagger} \hat{b}_+^{i+1\dagger} - \hat{b}_-^{i+1\dagger} \hat{b}_-^{i+1\dagger} + \hat{c}_+^{i+1\dagger} \hat{c}_+^{i+1\dagger} - \hat{c}_-^{i+1\dagger} \hat{c}_-^{i+1\dagger}), \tag{6.14a}$$

$$W_{-,i}^{2\dagger} W_{-,i+1}^{2\dagger} = \frac{1}{16} (-\hat{b}_+^{i+1\dagger} \hat{b}_+^{i+1\dagger} + \hat{b}_-^{i+1\dagger} \hat{b}_-^{i+1\dagger} - \hat{c}_+^{i+1\dagger} \hat{c}_+^{i+1\dagger} + \hat{c}_-^{i+1\dagger} \hat{c}_-^{i+1\dagger}), \tag{6.14b}$$

$$W_{-,i}^{1\dagger} W_{-,i+1}^{2\dagger} = \frac{1}{16} (-\hat{b}_+^{i+1\dagger} \hat{b}_+^{i+1\dagger} + \hat{b}_-^{i+1\dagger} \hat{b}_-^{i+1\dagger} + \hat{c}_+^{i+1\dagger} \hat{c}_+^{i+1\dagger} - \hat{c}_-^{i+1\dagger} \hat{c}_-^{i+1\dagger}), \tag{6.14c}$$

$$W_{-,i}^{2\dagger} W_{-,i+1}^{1\dagger} = \frac{1}{16} (\hat{b}_+^{i+1\dagger} \hat{b}_+^{i+1\dagger} - \hat{b}_-^{i+1\dagger} \hat{b}_-^{i+1\dagger} - \hat{c}_+^{i+1\dagger} \hat{c}_+^{i+1\dagger} + \hat{c}_-^{i+1\dagger} \hat{c}_-^{i+1\dagger}). \tag{6.14d}$$

Using the expansions (6.14), we find that the self-energy of the states belonging to $\mathcal{H}_2$ is given by

$$\left\langle 0 \left| \hat{W}_{-,i}^{n} \hat{W}_{-,i+1}^{m} \hat{H}_{\text{int}} \hat{W}_{-,i}^{n\dagger} \hat{W}_{-,i+1}^{m\dagger} \right| 0 \right\rangle = \begin{cases} \frac{U_1}{32} & \text{if } i \text{ is even} \\ \frac{U_2}{32} & \text{if } i \text{ is odd} \end{cases} \tag{6.15}$$

3) $\mathcal{H}_3 \equiv \left\{ \frac{1}{\sqrt{2}} \hat{W}_{-,i}^{n\dagger} \hat{W}_{-,i}^{n\dagger} |0\rangle \right\}$, with $n = 1, 2$ and $i = 1, ..., N_c - 2$.

This subspace is formed by the two-boson states in which both atoms occupy the same single-particle state. Since the localized modes overlap completely, there are interaction terms coming from the contributions of the sites A_i, B_i, C_i, B_{i+1} and C_{i+1}. Using again the expansions (6.8) and keeping only the relevant terms for the computation of the self-energy, we find

$$
\begin{aligned}
\frac{W_{-,i}^{1\dagger} W_{-,i}^{1\dagger}}{\sqrt{2}} = {} & \frac{1}{2\sqrt{2}} \hat{a}_{+}^{i\dagger} \hat{a}_{+}^{i\dagger} \\
& + \frac{1}{16\sqrt{2}} \left(\hat{b}_{+}^{i\dagger} \hat{b}_{+}^{i\dagger} + \hat{b}_{-}^{i\dagger} \hat{b}_{-}^{i\dagger} - 2\hat{b}_{+}^{i\dagger} \hat{b}_{-}^{i\dagger} \right) \\
& + \frac{1}{16\sqrt{2}} \left(\hat{b}_{+}^{i+1\dagger} \hat{b}_{+}^{i+1\dagger} + \hat{b}_{-}^{i+1\dagger} \hat{b}_{-}^{i+1\dagger} + 2\hat{b}_{+}^{i+1\dagger} \hat{b}_{-}^{i+1\dagger} \right) \\
& + \frac{1}{16\sqrt{2}} \left(\hat{c}_{+}^{i\dagger} \hat{c}_{+}^{i\dagger} + \hat{c}_{-}^{i\dagger} \hat{c}_{-}^{i\dagger} + 2\hat{c}_{+}^{i\dagger} \hat{c}_{-}^{i\dagger} \right) \\
& + \frac{1}{16\sqrt{2}} \left(\hat{c}_{+}^{i+1\dagger} \hat{c}_{+}^{i+1\dagger} + \hat{c}_{-}^{i+1\dagger} \hat{c}_{-}^{i+1\dagger} - 2\hat{c}_{+}^{i+1\dagger} \hat{c}_{-}^{i+1\dagger} \right),
\end{aligned} \tag{6.16a}
$$

$$
\begin{aligned}
\frac{W_{-,i}^{2\dagger} W_{-,i}^{2\dagger}}{\sqrt{2}} = {} & \frac{1}{2\sqrt{2}} \hat{a}_{-}^{i\dagger} \hat{a}_{-}^{i\dagger} \\
& + \frac{1}{16\sqrt{2}} \left(\hat{b}_{+}^{i\dagger} \hat{b}_{+}^{i\dagger} + \hat{b}_{-}^{i\dagger} \hat{b}_{-}^{i\dagger} - 2\hat{b}_{+}^{i\dagger} \hat{b}_{-}^{i\dagger} \right) \\
& + \frac{1}{16\sqrt{2}} \left(\hat{b}_{+}^{i+1\dagger} \hat{b}_{+}^{i+1\dagger} + \hat{b}_{-}^{i+1\dagger} \hat{b}_{-}^{i+1\dagger} + 2\hat{b}_{+}^{i+1\dagger} \hat{b}_{-}^{i+1\dagger} \right) \\
& + \frac{1}{16\sqrt{2}} \left(\hat{c}_{+}^{i\dagger} \hat{c}_{+}^{i\dagger} + \hat{c}_{-}^{i\dagger} \hat{c}_{-}^{i\dagger} + 2\hat{c}_{+}^{i\dagger} \hat{c}_{-}^{i\dagger} \right) \\
& + \frac{1}{16\sqrt{2}} \left(\hat{c}_{+}^{i+1\dagger} \hat{c}_{+}^{i+1\dagger} + \hat{c}_{-}^{i+1\dagger} \hat{c}_{-}^{i+1\dagger} - 2\hat{c}_{+}^{i+1\dagger} \hat{c}_{-}^{i+1\dagger} \right).
\end{aligned} \tag{6.16b}
$$

Using the expansions (6.16), we find that the self-energy of the states of $\mathcal{H}_3$ is given by

$$
\left\langle 0 \left| \frac{1}{\sqrt{2}} \hat{W}_{-,i}^{n} \hat{W}_{-,i}^{n} \hat{H}_{\text{int}} \frac{1}{\sqrt{2}} \hat{W}_{-,i}^{n\dagger} \hat{W}_{-,i}^{n\dagger} \right| 0 \right\rangle = \frac{U_A}{4} + \frac{3 \left(U_1 + U_2 \right)}{64}. \tag{6.17}
$$

4) $\mathcal{H}_4 \equiv \left\{ \hat{W}_{-,i}^{1\dagger} \hat{W}_{-,i}^{2\dagger} |0\rangle \right\}$, with $i = 1, ..., N_c - 2$.

This subspace is formed by two-boson states in which the two atoms are localized in the same plaquette but occupy orthogonal states, each belonging to one of the two degenerate bands. As in the case of the $\mathcal{H}_3$ subspace, the two particles share 5 different sites. The terms of the expansion of the two-body state relevant for the computation of

the self-energy read

$$
\begin{aligned}
W^{1\dagger}_{-,i}W^{2\dagger}_{-,i} = {} & \frac{1}{2}\hat{a}^{\dagger}_{i,+}\hat{a}^{\dagger}_{i,-} \\
& + \frac{1}{16}\left(-\hat{b}^{\dagger}_{i,+}\hat{b}^{\dagger}_{i,+} - \hat{b}^{\dagger}_{i,-}\hat{b}^{\dagger}_{i,-} + 2\hat{b}^{\dagger}_{i,+}\hat{b}^{\dagger}_{i,-}\right) \\
& + \frac{1}{16}\left(\hat{b}^{\dagger}_{i+1,+}\hat{b}^{\dagger}_{i+1,+} + \hat{b}^{\dagger}_{i+1,-}\hat{b}^{\dagger}_{i+1,-} + 2\hat{b}^{\dagger}_{i+1,+}\hat{b}^{\dagger}_{i+1,-}\right) \\
& + \frac{1}{16}\left(\hat{c}^{\dagger}_{i,+}\hat{c}^{\dagger}_{i,+} + \hat{c}^{\dagger}_{i,-}\hat{c}^{\dagger}_{i,-} + 2\hat{c}^{\dagger}_{i,+}\hat{c}^{\dagger}_{i,-}\right) \\
& + \frac{1}{16}\left(-\hat{c}^{\dagger}_{i+1,+}\hat{c}^{\dagger}_{i+1,+} - \hat{c}^{\dagger}_{i+1,-}\hat{c}^{\dagger}_{i+1,-} + 2\hat{c}^{\dagger}_{i+1,+}\hat{c}^{\dagger}_{i+1,-}\right).
\end{aligned}
\tag{6.18}
$$

Using this expansion, we find that the self-energy of the states belonging to $\mathcal{H}_4$ is

$$
\left\langle 0 \left| \hat{W}^{1}_{-,i}\hat{W}^{2}_{-,i}\hat{H}_{\text{int}}\hat{W}^{1\dagger}_{-,i}\hat{W}^{2\dagger}_{-,i} \right| 0 \right\rangle = \frac{U_A}{2} + \frac{3\left(U_1 + U_2\right)}{32}.
\tag{6.19}
$$

From Eqs. (6.15), (6.17), (6.19), and bearing in mind that $U_A, U_1, U_2 < 0$, we see that the subspace in which the states have a lowest self-energy is $\mathcal{H}_4$, followed by $\mathcal{H}_3$. In the next section, we will derive effective models for these subspaces and we will discuss their topological properties.

6.3   Effective models for the lowest-energy subspaces

We can obtain effective models for the subspaces of two-boson states with lowest self-energy by projecting the Hamiltonian (6.1) into the two lowest flat bands. In order to do so, we remove from the expansions (6.12) all the contributions from higher bands and define a new set of operators

$$
\hat{\tilde{a}}^{i\dagger}_{+} = -\frac{1}{\sqrt{2}}\hat{W}^{1\dagger}_{-,i},
\tag{6.20a}
$$

$$
\hat{\tilde{a}}^{i\dagger}_{-} = -\frac{1}{\sqrt{2}}\hat{W}^{2\dagger}_{-,i},
\tag{6.20b}
$$

$$
\hat{\tilde{b}}^{i\dagger}_{+} = \frac{1}{4}\left(\hat{W}^{1\dagger}_{-,i-1} + \hat{W}^{2\dagger}_{-,i-1} + \hat{W}^{1\dagger}_{-,i} - \hat{W}^{2\dagger}_{-,i}\right),
\tag{6.20c}
$$

$$
\hat{\tilde{b}}^{i\dagger}_{-} = \frac{1}{4}\left(\hat{W}^{1\dagger}_{-,i-1} + \hat{W}^{2\dagger}_{-,i-1} - \hat{W}^{1\dagger}_{-,i} + \hat{W}^{2\dagger}_{-,i}\right),
\tag{6.20d}
$$

$$
\hat{\tilde{c}}^{i\dagger}_{+} = \frac{1}{4}\left(\hat{W}^{1\dagger}_{-,i-1} - \hat{W}^{2\dagger}_{-,i-1} + \hat{W}^{1\dagger}_{-,i} + \hat{W}^{2\dagger}_{-,i}\right),
\tag{6.20e}
$$

$$
\hat{\tilde{c}}^{i\dagger}_{-} = \frac{1}{4}\left(-\hat{W}^{1\dagger}_{-,i-1} + \hat{W}^{2\dagger}_{-,i-1} + \hat{W}^{1\dagger}_{-,i} + \hat{W}^{2\dagger}_{-,i}\right).
\tag{6.20f}
$$

By plugging in Eq. (6.1) the projected OAM operators (6.20) instead of the original ones, we obtain a Hamiltonian expressed in the basis of the single-particle eigenstates

and restricted to the two degenerate flat bands of lowest energy. As expected, the kinetic part of the projected Hamiltonian is diagonal and reads

$$\hat{\bar{H}}_{\mathrm{kin}} = -2\sqrt{2}J \sum_{i=1}^{N_c-1} \hat{W}^{1\dagger}_{-,i}\hat{W}^1_{-,i} + \hat{W}^{2\dagger}_{-,i}\hat{W}^2_{-,i}. \qquad (6.21)$$

The interaction part of the projected Hamiltonian contains products of the type $\hat{\bar{j}}^{i\dagger}_\alpha \hat{\bar{j}}^{i\dagger}_\alpha \hat{\bar{j}}^i_\alpha \hat{\bar{j}}^i_\alpha$ and $\hat{\bar{j}}^{i\dagger}_\alpha \hat{\bar{j}}^{i\dagger}_\alpha \hat{\bar{j}}^i_{-\alpha} \hat{\bar{j}}^i_{-\alpha}$, with $j = \{a, b, c\}$ and $\alpha = \pm$. Therefore, it yields terms that involve products of operators that belong to the $\mathcal{H}_2$, $\mathcal{H}_3$ and $\mathcal{H}_4$ subspaces. However, after a long but straightforward calculation it can be shown that all the coupling terms cancel out and separate projected Hamiltonians can be written for each of these subspaces. In the next subsections, we present the effective models that are obtained for the two lowest-energy subspaces, i.e., $\mathcal{H}_4$ and $\mathcal{H}_3$.

6.3.1 $\mathcal{H}_4$ subspace

Introducing the projected OAM operators (6.20) into Eq. (6.3), we find that the projected interaction Hamiltonian contains the following terms consisting of products of operators associated to the $\mathcal{H}_4$ subspace

$$\begin{aligned} \hat{\bar{H}}^{\mathcal{H}_4}_{\mathrm{int}} = {}&\left(\frac{U_A}{2} + \frac{3\left(U_1 + U_2\right)}{32}\right) \sum_{i=1}^{N_c-1} \hat{W}^{1\dagger}_{-,i}\hat{W}^{2\dagger}_{-,i}\hat{W}^1_{-,i}\hat{W}^2_{-,i} \\ &+ \frac{U_1}{32} \sum_{i=1}^{[N_c/2]-2} \left(\hat{W}^{1\dagger}_{-,2i}\hat{W}^{2\dagger}_{-,2i}\hat{W}^1_{-,2i+1}\hat{W}^2_{-,2i+1} + \mathrm{h.c.}\right) \\ &+ \frac{U_2}{32} \sum_{i=1}^{[N_c/2]-1} \left(\hat{W}^{1\dagger}_{-,2i-1}\hat{W}^{2\dagger}_{-,2i-1}\hat{W}^1_{-,2i}\hat{W}^2_{-,2i} + \mathrm{h.c.}\right). \end{aligned} \qquad (6.22)$$

The first term of Eq. (6.22) is associated with the self-energy of the states of the $\mathcal{H}_4$ subspace, Eq. (6.19), whereas the other two terms correspond to hoppings between two-boson states belonging to neighbouring plaquettes induced by the overlap between the localized modes, as shown in Fig. 6.2 (a). By mapping the two-body states of $\mathcal{H}_4$ into single particle states according to the definition $|i\rangle \equiv \hat{W}^{1\dagger}_{-,i}\hat{W}^{2\dagger}_{-,i}|0\rangle$, we can compute all the matrix elements of Eqs. (6.21) and (6.22) over the two-boson states of $\mathcal{H}_4$ and write an effective single-particle tight-binding model for this subspace

$$H^{\mathcal{H}_4}_{\mathrm{eff}} = V_{\mathcal{H}_4} \sum_{i=1}^{N_c-1} |i\rangle\langle i| + t_1 \sum_{i=1}^{N_c/2-2} \left(|2i\rangle\langle 2i+1| + \mathrm{h.c.}\right) + t_2 \sum_{i=1}^{N_c/2-1} \left(|2i-1\rangle\langle 2i| + \mathrm{h.c.}\right),$$
$$(6.23)$$

where we have defined $V_{\mathcal{H}_4} \equiv \left(-4\sqrt{2}J + \frac{U_A}{2} + \frac{3(U_1+U_2)}{32}\right)$, $t_1 \equiv \frac{U_1}{32}$ and $t_2 \equiv \frac{U_2}{32}$. As illustrated in Fig. 6.2 (b), Eq. (6.23) describes a Su-Schrieffer-Heeger (SSH) chain with

a unit cell formed by two sites that correspond to neighbouring plaquettes of the original diamond chain. The intra- and inter-cell hoppings of this chain are given by t_2 and t_1 respectively, and the energy of all sites is shifted by a uniform potential $V_{\mathcal{H}_4}$.
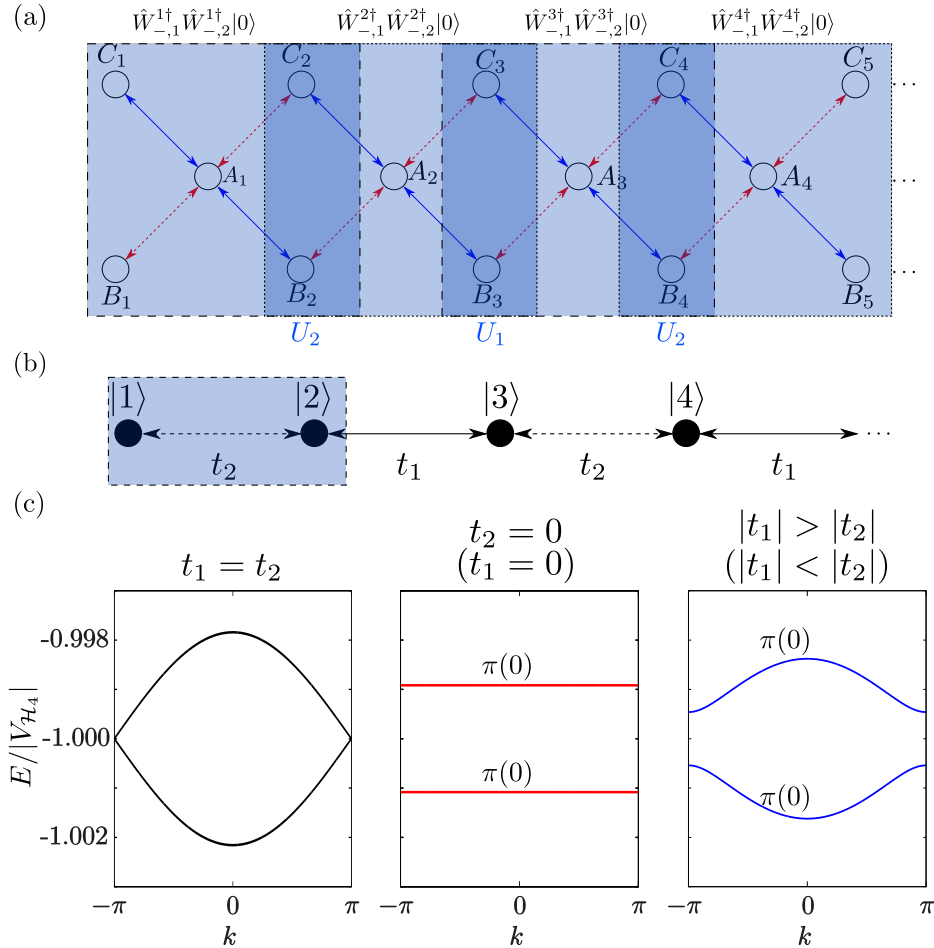

Figure 6.2: Effective model for the $\mathcal{H}_4$ subspace. (a) Original states of $\mathcal{H}_4$ in the diamond chain. The blue squares framed in dashed lines indicate the plaquettes where the states are localized. In the sites with a darker blue shade, neighbouring states overlap and interact with a strength U_1 or U_2. (b) Effective SSH chain describing the $\mathcal{H}_4$ subspace. The blue shaded area indicates the unit cell, which is formed by two neighbouring plaquettes of the original diamond chain. (c) Band structure of the SSH chain for values of the interaction parameters $\{U_A/J = -0.2, U_1/J = -0.2, U_2/J = -0.2\}$ (left plot), $\{U_A/J = -0.2, U_1/J = -0.2(0), U_2/J = 0(-0.2)\}$ (middle plot), and $\{U_A/J = -0.2, U_1/J = -0.2(-0.1), U_2/J = -0.1(-0.2)\}$ (right plot). In the middle and right plots, we also indicate the value of the Zak's phases of the bands for each case.

By Fourier-transforming the Hamiltonian (6.23), we find that the two energy bands

of this model are given by

$$E^1_{\mathcal{H}_4}(k) = V_{\mathcal{H}_4} - \sqrt{t_1^2 + t_2^2 + 2t_1 t_2 \cos k}, \tag{6.24a}$$

$$E^2_{\mathcal{H}_4}(k) = V_{\mathcal{H}_4} + \sqrt{t_1^2 + t_2^2 + 2t_1 t_2 \cos k}. \tag{6.24b}$$

The shape of the band structure (6.24) is shown in Fig. 6.2 (c) for different values of the hopping parameters. As shown in the left plot, for the particular case $t_1 = t_2$ the gap closes at $k = \pm\pi$. As can be seen in the middle plot, for $t_1 = 0$ or $t_2 = 0$ the bands are flat and separated by a gap. In the general case $t_1 \neq t_2$, which is illustrated in the right plot, both bands are dispersive and the gap remains open. In the situations where there is an energy gap, the relative value of the hopping parameters determines the topological properties of the system. If $|t_1| < |t_2|$, the Zak's phases of the bands are $\gamma^1_{\mathcal{H}_4} = \gamma^2_{\mathcal{H}_4} = 0$ and the system is in a topologically trivial phase. On the other hand, if the values of the hoppings are such that $|t_1| > |t_2|$, the Zak's phases are $\gamma^1_{\mathcal{H}_4} = \gamma^2_{\mathcal{H}_4} = \pi$ and the system is in a topological phase. Thus, by introducing the different interaction strengths U_1 and U_2 at B and C sites of odd and even unit cells respectively, we are able to control the shape of the band structure and to render the $\mathcal{H}_4$ subspace topologically non-trivial. According to the bulk-boundary correspondence, in the topological phase we expect a chain with open boundaries to display two edge states of energy $V_{\mathcal{H}_4}$ in its spectrum. Remarkably, these edge states consist of bound pairs of bosons and are induced by the interplay between the strength of different on-site interactions in a system where the kinetic energy plays no role due to the fact that all the bands are flat.

6.3.2 $\mathcal{H}_3$ subspace

Doing the same procedure as in the case of the $\mathcal{H}_4$ subspace, we find that the part of the interaction Hamiltonian projected to the two lowest flat bands containing products of operators associated to the $\mathcal{H}_3$ subspace reads

$$
\begin{aligned}
\bar{\bar{H}}^{\mathcal{H}_3}_{\text{int}} = {} & \left(-4\sqrt{2}J + \frac{U_A}{4} + \frac{3(U_1 + U_2)}{64} \right) \sum_{i=1}^{N_c-1} \frac{\hat{W}^{1\dagger}_{-,i}\hat{W}^{1\dagger}_{-,i}}{\sqrt{2}} \frac{\hat{W}^1_{-,i}\hat{W}^1_{-,i}}{\sqrt{2}} + \frac{\hat{W}^{2\dagger}_{-,i}\hat{W}^{2\dagger}_{-,i}}{\sqrt{2}} \frac{\hat{W}^{1\dagger}_{-,2}\hat{W}^{2\dagger}_{-,i}}{\sqrt{2}} \\
& + \frac{3(U_1 + U_2)}{64} \sum_{i=1}^{N_c} \left(\frac{\hat{W}^{1\dagger}_{-,i}\hat{W}^{1\dagger}_{-,i}}{\sqrt{2}} \frac{\hat{W}^2_{-,i}\hat{W}^2_{-,i}}{\sqrt{2}} + \text{h.c.} \right) \\
& - \frac{U_1}{64} \sum_{i=1}^{[N_c/2]-2} \sum_{n,m=1,2} \left(\frac{\hat{W}^{n\dagger}_{-,2i}\hat{W}^{n\dagger}_{-,2i}}{\sqrt{2}} \frac{\hat{W}^m_{-,2i+1}\hat{W}^m_{-,2i+1}}{\sqrt{2}} + \text{h.c.} \right) \\
& - \frac{U_2}{64} \sum_{i=1}^{[N_c/2]-1} \sum_{n,m=1,2} \left(\frac{\hat{W}^{n\dagger}_{-,2i-1}\hat{W}^{n\dagger}_{-,2i-1}}{\sqrt{2}} \frac{\hat{W}^m_{-,2i}\hat{W}^m_{-,2i}}{\sqrt{2}} + \text{h.c.} \right).
\end{aligned}
\tag{6.25}
$$

The first term of Eq. (6.25) corresponds to the self-energy of the states belonging to $\mathcal{H}_3$, Eq. (6.17), and the other ones can be regarded as pair-tunneling terms induced by the interactions at the sites where the single-particle localized modes interact. More specifically, the second term corresponds to a coupling between two-boson states localized at the same site but belonging to different bands, and the third and fourth terms to hoppings between states localized in neighbouring plaquettes belonging to the same and different bands, respectively. By mapping the two-body states of $\mathcal{H}_3$ into single-particle states according to $|i, 1\rangle \equiv \frac{1}{\sqrt{2}} \hat{W}_{-,i}^{1\dagger} \hat{W}_{-,i}^{1\dagger} |0\rangle$ and $|i, 2\rangle \equiv \frac{1}{\sqrt{2}} \hat{W}_{-,i}^{2\dagger} \hat{W}_{-,i}^{2\dagger} |0\rangle$, we can combine all the non-zero matrix elements of (6.25) and (6.21) over two-boson states of $\mathcal{H}_3$ and write an effective single-particle model for this subspace

$$
\begin{aligned}
\hat{H}_{\text{eff}}^{\mathcal{H}_3} = {} & V_{\mathcal{H}_3} \sum_{i=1}^{N_c} \left(|i, 1\rangle \langle i, 1| + |i, 2\rangle \langle i, 2| \right) + \frac{3\left(t_1 + t_2\right)}{2} \sum_{i=1}^{N_c} \left(|i, 1\rangle \langle i, 2| + \text{h.c.} \right) \\
& - \frac{t_1}{2} \sum_{i=1}^{[N_c/2]-2} \sum_{n,m=1,2} \left(|2i, n\rangle \langle 2i+1, m| + \text{h.c.} \right) \\
& - \frac{t_2}{2} \sum_{i=1}^{[N_c/2]-1} \sum_{n,m=1,2} \left(|2i-1, n\rangle \langle 2i, m| + \text{h.c.} \right),
\end{aligned}
\tag{6.26}
$$

where $V_{\mathcal{H}_3} \equiv \left(-4\sqrt{2} J + \frac{U_A}{4} + \frac{3(U_1 + U_2)}{64} \right)$ and t_1, t_2 are defined in the same way as in Eq. (6.23). As illustrated in Fig. 6.3 (a), Eq. (6.26) describes a Creutz ladder [309] with a unit cell formed by two legs, each of which corresponds to the two states of $\mathcal{H}_3$ localized in each plaquette, $|i, 1\rangle$ and $|i, 2\rangle$. The intra-leg coupling is given by $\frac{3(t_1 + t_2)}{2}$, and the inter-leg hoppings are $-\frac{t_1}{2}$ or $-\frac{t_2}{2}$ depending on the parity of the unit cell. Additionally, the energy of all sites is shifted by a uniform potential $V_{\mathcal{H}_3}$. By Fourier-transforming the Hamiltonian (6.26), we find the following energy bands

$$
E_{\mathcal{H}_3}^1(k) = \frac{3(t_1 + t_2)}{2} + V_{\mathcal{H}_3} - \sqrt{t_1^2 + t_2^2 + 2t_1 t_2 \cos k},
\tag{6.27a}
$$

$$
E_{\mathcal{H}_3}^2(k) = \frac{3(t_1 + t_2)}{2} + V_{\mathcal{H}_3} + \sqrt{t_1^2 + t_2^2 + 2t_1 t_2 \cos k},
\tag{6.27b}
$$

$$
E_{\mathcal{H}_3}^3(k) = E_{\mathcal{H}_3}^4(k) = -\frac{3(t_1 + t_2)}{2} + V_{\mathcal{H}_3}.
\tag{6.27c}
$$

In Fig. 6.3 (c) we plot the band structure (6.27) for different values of the hopping parameters. As long as $t_1 \neq t_2$ there is an energy gap between the dispersive bands $E_{\mathcal{H}_3}^1(k)$ and $E_{\mathcal{H}_3}^2(k)$, which only become flat in the cases $t_1 = 0$ or $t_2 = 0$, as shown in the middle plot of Fig. 6.3 (c). Whenever the gap remains open, if $|t_1| < |t_2|$ the Zak's phases of the bands are $\gamma_{\mathcal{H}_3}^1 = \gamma_{\mathcal{H}_3}^2 = \gamma_{\mathcal{H}_3}^3 = \gamma_{\mathcal{H}_3}^4 = 0$ and the system is in a topologically trivial phase. On the other hand, if the relation between the values of the

hopping parameters is $|t_1| > |t_2|$, the Zak's phases are $\gamma^1_{\mathcal{H}_3} = \gamma^2_{\mathcal{H}_3} = \pi$, $\gamma^3_{\mathcal{H}_3} = \gamma^4_{\mathcal{H}_3} = 0$ and therefore $\mathcal{H}_3$ is in a topologically non-trivial phase.

Thus, the $\mathcal{H}_3$ and $\mathcal{H}_4$ subspaces share the same topological phase diagram as a function of the values of U_1 and U_2. In the non-trivial regime $|U_1| > |U_2|$, we expect that in a lattice with open boundaries the spectrum of $\mathcal{H}_3$ displays two edge states with energy $\frac{3(t_1+t_2)}{2} + V_{\mathcal{H}_3}$, which are of the same nature as those that $\mathcal{H}_4$ exhibits in the same situation.
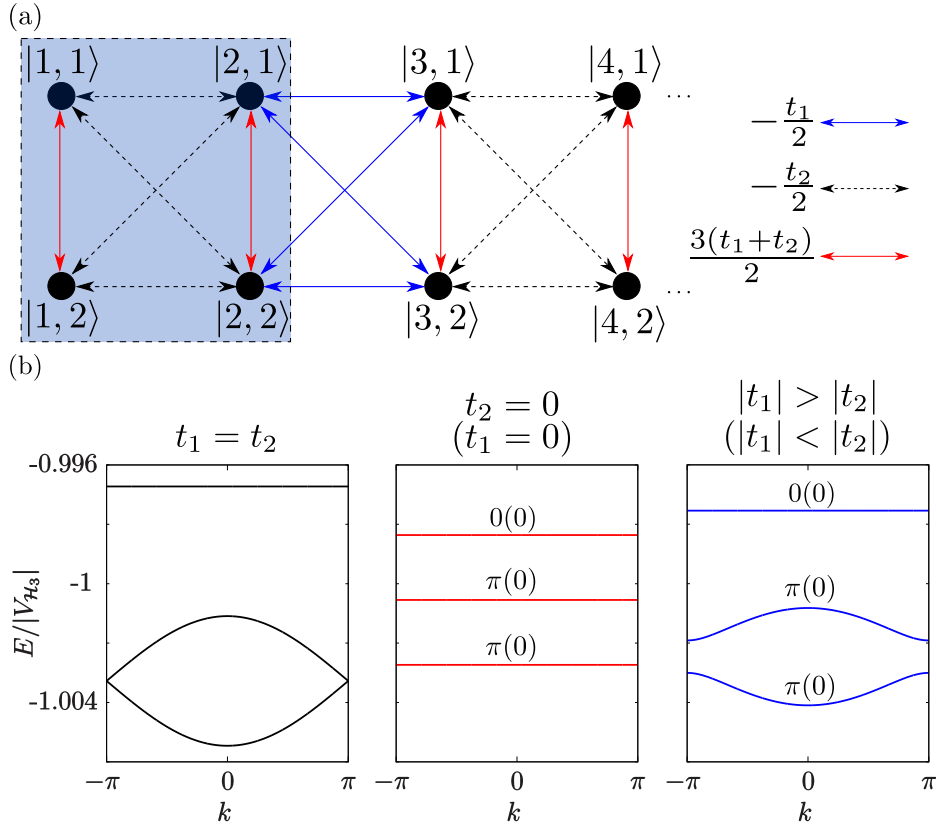

Figure 6.3: (a) Effective Creutz ladder describing the $\mathcal{H}_3$ subspace. The blue shaded area framed in dashed lines indicates the unit cell, which is formed by two neighbouring legs that are in turn composed of the two states of the original diamond chain loacalized in each plaquette. (b) Band structure of the Creutz ladder for values of the interaction parameters $\{U_A/J = -0.2, U_1/J = -0.2, U_2/J = -0.2\}$ (left plot), $\{U_A/J = -0.2, U_1/J = -0.2(0), U_2/J = 0(-0.2)\}$ (middle plot), and $\{U_A/J = -0.2, U_1/J = -0.2(-0.1), U_2/J = -0.1(-0.2)\}$ (right plot). In the middle and right plots, we also indicate the value of the Zak's phases of the bands for each case.

6.4   Exact diagonalization results

In this section, we present exact diagonalization results that support the analysis of the lowest-energy subspaces that we have performed by projecting the Hamiltonian to the two lowest degenerate flat bands. We also explore numerically the effects of deviations from the weakly-interacting and flat-band limits. In our calculations, we consider a full diamond chain formed by N_c unit cells and therefore $3N_c - 1$ sites (for reasons that we explained before, we remove the A site from the last cell), and filled with $N = 2$ bosons. Although the dimension of the Hilbert space corresponding to this system is $\frac{(N+M-1)!}{(M-1)!N!}$, where $M = 2 \times (3N_c - 1)$ is the number of available single-particle states, we focus on the first $3(N_c - 1)$ states of the spectrum. Of these, the $N_c - 1$ states of lowest energy correspond to the $\mathcal{H}_4$ subspace, and the remaining $2(N_c - 1)$ states to the $\mathcal{H}_3$ subspace.

6.4.1   Energy spectra and topological edge states

In Fig. 6.4 we show, for a diamond chain of $N_c = 21$ unit cells with interaction strengths $|U_A|, |U_1|, |U_2| \sim 10^{-2} J$, the energy spectra obtained by exact diagonalization of the full Hamiltonian Eq. (6.1) (red empty dots), the effective Hamiltonian of the $\mathcal{H}_4$ subspace Eq. (6.23) (green dots) and the effective Hamiltonian of the $\mathcal{H}_3$ subspace Eq. (6.26) (blue dots). We observe that both effective models fit very well with the results obtained by tackling the full system. The exact diagonalization results also confirm the predictions about the topological behaviour of the system. When the interaction strengths fulfill the relation $|U_1| < |U_2|$, which is the case shown in Fig. 6.4 (a), the system is in the topologically trivial phase and therefore there are no states inside the gaps. In contrast, in Fig. 6.4 (b), which corresponds to coupling strengths fulfilling $|U_1| > |U_2|$, the system is in the topological phase, as reflected by the presence of two states inside the gaps between the two bands of $\mathcal{H}_4$ and the two lowest bands of $\mathcal{H}_3$. In Fig. 6.5 (a) and Fig. 6.5 (b) we plot respectively the total density profiles (i.e., the sum of the populations of the two OAM states at each site) of the in-gap states of the $\mathcal{H}_4$ and $\mathcal{H}_3$ subspaces that appear in the exact two-boson spectrum of Fig. 6.4 (b). As one expects because of their topological origin, these states are strongly localized at the unit cells of the edge of the diamond chain. In the density profiles of both states, we observe that the population peaks occur at the A sites. This fact can be explained by taking into account that the completely localized modes corresponding to the lowest bands, Eqs. (6.8), have four times more population on the A sites than on the B and C sites. Accordingly, the edge states of Fig. 6.5, which are formed of bound pairs of these modes, also concentrate their population on these sites.
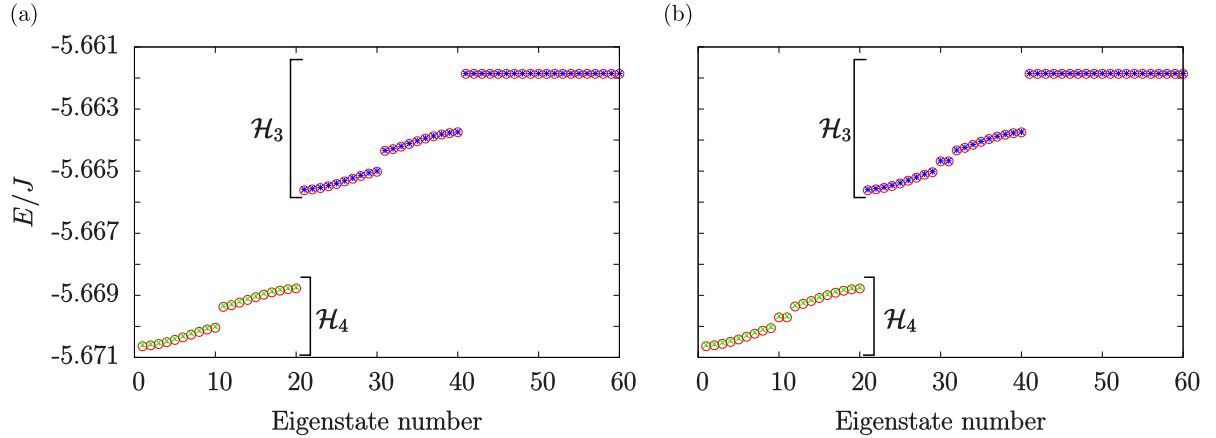
Figure 6.4: Low-energy sector of the spectrum of a diamond chain of $N_c = 21$ unit cells with open boundaries filled with 2 bosons (red empty dots), compared against the spectra of the SSH model describing the $\mathcal{H}_4$ subspace (green dots) and the Creutz ladder describing the $\mathcal{H}_3$ subspace (blue dots). The parameters of the system are (a) $\{U_A/J = -0.02, U_1/J = -0.02, U_2/J = -0.01\}$ and (b) $\{U_A/J = -0.02, U_1/J = -0.01, U_2/J = -0.02\}$.

Figure 6.5: Density profiles of the in-gap states that appear in the spectrum of the full diamond chain plotted with red empty dots in Fig. 6.4 (b). The state plotted in (a) belongs to the $\mathcal{H}_4$ subspace and the one displayed in (b) to the $\mathcal{H}_3$ subspace. The sites have been assigned a number j according to the same correspondences as in Chapter 4, i.e., $C_i = 3_i - 2, B_i = 3_i - 1, A_i = 3_i$, where i labels the unit cell

.

6.4.2 Deviations from the weakly-interacting regime

In the derivation of the effective model for the lowest-energy two-boson states of the diamond chain performed in Sec. 6.3, we have assumed that the interaction strength is much smaller than the gap between the bands, $|U_A|, |U_1|, |U_2| \ll J$, in such a way that the contributions from higher bands can be neglected. In the previous subsection, we have shown that for values of the interaction strength $|U/J| \sim 10^{-2}$ the effective models that are derived from this approximation work very well. By means of exact diagonalization calculations, we can examine to which extent the effective models reproduce the features of the low-energy sector of the full spectrum when the interaction strength is of the order of the band gap. In Fig. 6.6 we show, for a diamond chain of $N_c = 21$ unit cells in which $|U_1| > |U_2|$, a comparison between the exact two-boson spectrum (red empty dots) and the effective models of the $\mathcal{H}_4$ (green dots) and $\mathcal{H}_3$ (blue dots) subspaces. The order of magnitude of the interaction strength is (a) $|U/J| \sim 10^{-1}$ and (b) $|U/J| \sim 1$. Although the quantitative disagreement between the effective models and the exact spectrum increases with the interaction strength, the models provide a good qualitative description of the lowest energetic two-boson states. In particular, in the exact spectra of Fig. 6.6 (a) and (b), the $\mathcal{H}_4$ and $\mathcal{H}_3$ subspaces are well separated in energy, the bands of each subspace maintain the shape predicted by the corresponding effective models, and, since the system is in the topological phase, there are in-gap states.
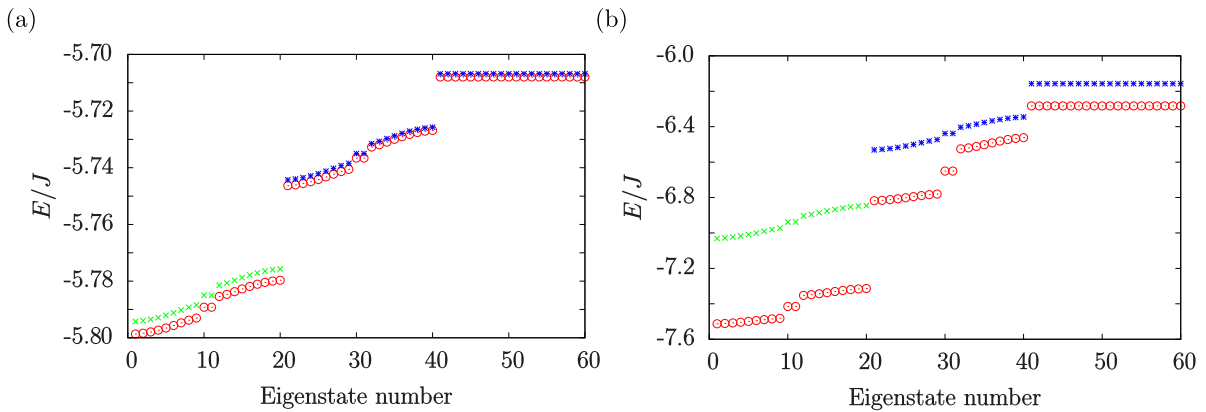
Figure 6.6: Low-energy sector of the spectrum of a diamond chain of $N_c = 21$ unit cells with open boundaries filled with 2 bosons (red empty dots), compared against the spectra of the SSH model describing the $\mathcal{H}_4$ subspace (green dots) and the Creutz ladder describing the $\mathcal{H}_3$ subspace (blue dots). The parameters of the system are (a) $\{U_A/J = -0.2, U_1/J = -0.2, U_2/J = -0.1\}$ and (b) $\{U_A/J = -2, U_1/J = -2, U_2/J = -1\}$.
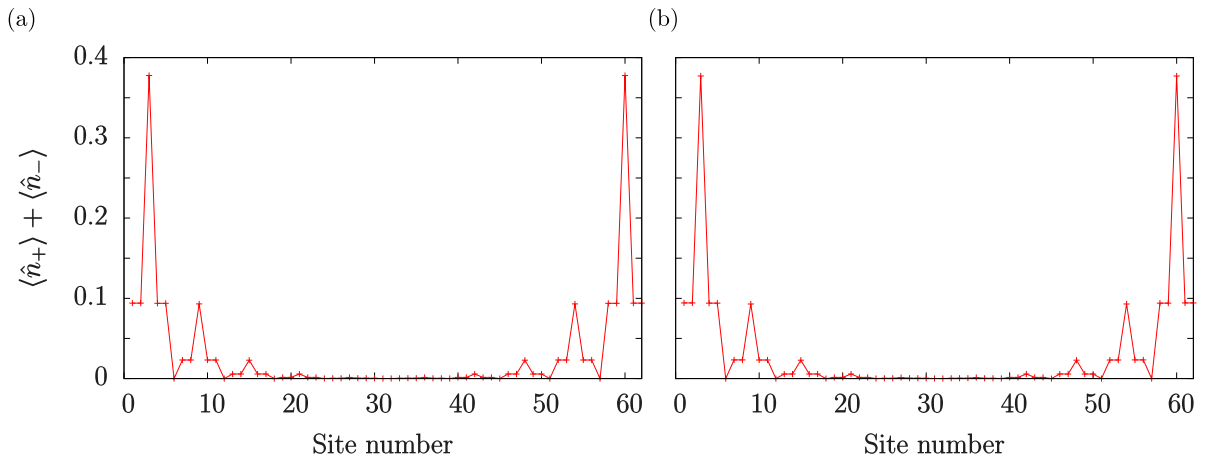
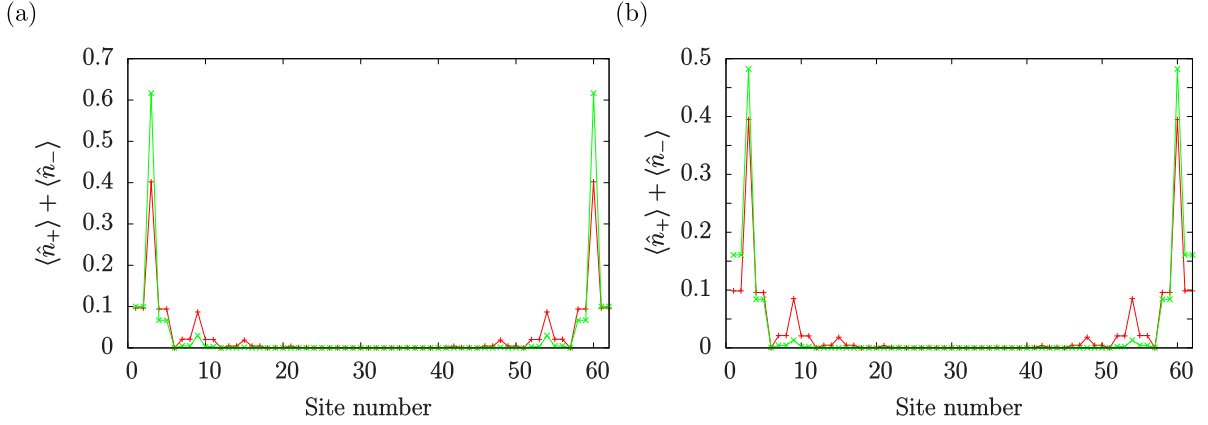(a)   (b)

Figure 6.7: Density profiles of the in-gap states that appear in the the full diamond chain spectra plotted with red empty dots in Fig. 6.6. The states plotted in (a) belong to the $\mathcal{H}_4$ subspace and the ones plotted in (b) to the $\mathcal{H}_3$ subspace. The red lines correspond to the parameters $\{U_A/J = -0.2, U_1/J = -0.2, U_2/J = -0.1\}$ [same as in Fig. 6.6 (a)] and the green ones to $\{U_A/J = -2, U_1/J = -2, U_2/J = -1\}$ [same as in Fig. 6.6 (b)]. The sites have been assigned a number j according to the same correspondences as in Chapter 4, i.e., $C_i = 3_i - 2, B_i = 3_i - 1, A_i = 3_i$, where i labels the unit cell.

In Fig. 6.7 (a) and (b) we plot respectively the density profiles of the in-gap states of $\mathcal{H}_4$ and $\mathcal{H}_3$ that appear in the exact spectra of Fig. 6.6. As in the case of interaction strengths $|U/J| \sim 10^{-2}$ shown in Fig. 6.7, we observe that these states are localized at the unit cells of the edges of the diamond chain. We also notice that the edge localization of the states is more acute for higher values of the interaction strength.

Therefore, introducing interaction strengths of the order of the band gap does not affect the qualitative behaviour of the lowest-energy sector of the spectrum. As a matter of fact, it has the effect of favouring the edge localization of the in-gap states, which is the main signature of the topological phase.

6.4.3 Deviations from the flat-band limit

Throughout this Chapter, we have assumed that the system is in the situation where all the bands of the Hamiltonian (6.2) are flat, which occurs when the two couplings between OAM states J_2 and J_3 are equal. However, as illustrated in Fig. 2.4, in a real system this limit is never actually reached because J_3 is always slightly larger than J_2. Thus, it is relevant to examine the effect of deviations from the $J_2 = J_3$ limit in the low-energy properties of the system that we have analysed in this Chapter. In the situation when $J_2 \neq J_3$, the kinetic part of the Hamiltonian projected to the lowest flat bands

reads

$$\hat{\bar{H}}_{\text{kin}} = -\sqrt{2}(J_2 + J_3) \sum_{i=1}^{N_c-1} \hat{W}_{-,i}^{1\dagger}\hat{W}_{-,i}^{1} + \hat{W}_{-,i}^{2\dagger}\hat{W}_{-,i}^{2}$$

$$+ \frac{(J_3 - J_2)}{\sqrt{2}} \sum_{i=1}^{N_c-1} \left(\hat{W}_{-,i}^{1\dagger}\hat{W}_{-,i+1}^{1} + \hat{W}_{-,i}^{2\dagger}\hat{W}_{-,i+1}^{2} + \text{h.c.} \right). \qquad (6.28)$$

Due to the off-diagonal term of Eq. (6.28), which corresponds to a single-particle hopping between adjacent localized eigenmodes, it is no longer possible to derive effective single-particle models for the different subspaces of two-boson states. However, we can perform exact diagonalization calculations over the full Hamiltonian Eq. (6.1) to examine numerically to which extent the features of the system that we observe in the flat-band limit survive. In Fig. 6.8 we plot, for a diamond chain of $N_c = 21$ in which $|U_1| > |U_2|$, the $3(N_c - 1)$ lowest energetic two-boson states for different values of the J_3/J_2 ratio.
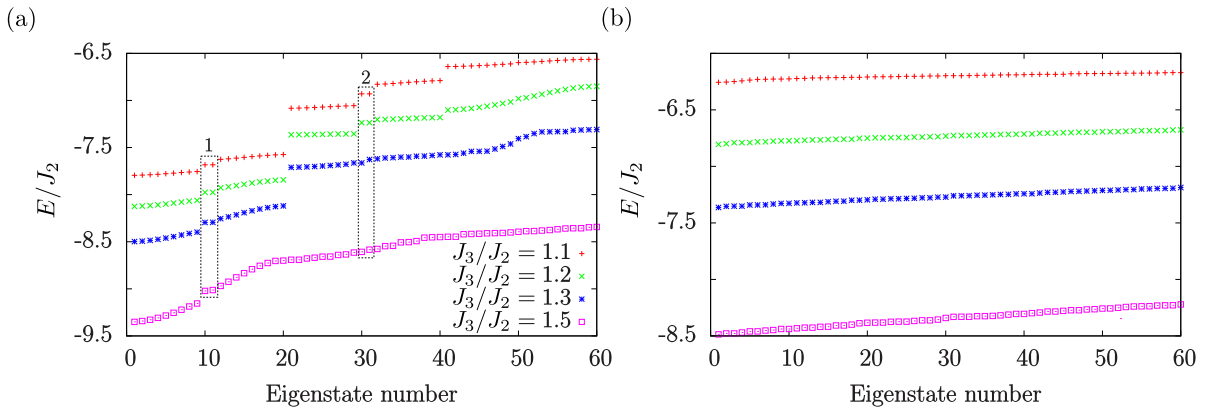
Figure 6.8: Low-energy sector of the spectra of two-boson states of a diamond chain formed by $N_c = 21$ unit cells for different values of the J_3/J_2 ratio. The interaction parameters are (a) $\{U_A/J_2 = -2, U_1/J_2 = -2, U_2/J_2 = -1\}$ and (b) $\{U_A/J_2 = -0.2, U_1/J_2 = -0.2, U_2/J_2 = -0.1\}$. The dashed boxes 1 and 2 in (a) mark respectively the position that the in-gap states of the $\mathcal{H}_4$ and $\mathcal{H}_3$ subspaces would have in the flat-band limit.

Fig. 6.8 (a) corresponds to the $|U| > (J_3 - J_2)$ regime, i.e., when the energy deviations from the flat-band limit are smaller than the interaction strength, whereas in Fig. 6.8 (b) the deviations are of the same order as the interactions, $|U| \sim (J_3 - J_2)$. In Fig. 6.8 (a), the positions in the spectrum that the in-gap states of the $\mathcal{H}_4$ and $\mathcal{H}_3$ subspaces would have in the flat-band are signalled with the dashed boxes 1 and 2, respectively.

In this plot, we observe that for $J_3/J_2 \leq 1.2$ the separation between $\mathcal{H}_4$ and $\mathcal{H}_3$ is still clear and each of the subspaces preserves its in-gap states. For $J_3/J_2 = 1.3$, the two subspaces are still separated in energy, but the in-gap states only persist in $\mathcal{H}_4$. Finally, for the case $J_3/J_2 = 1.5$ of Fig. 6.8 (a), and also for all the values of the J_3/J_2 ratio in Fig. 6.8 (b), the two subspaces merge and all the in-gap states are absorbed into the bulk.
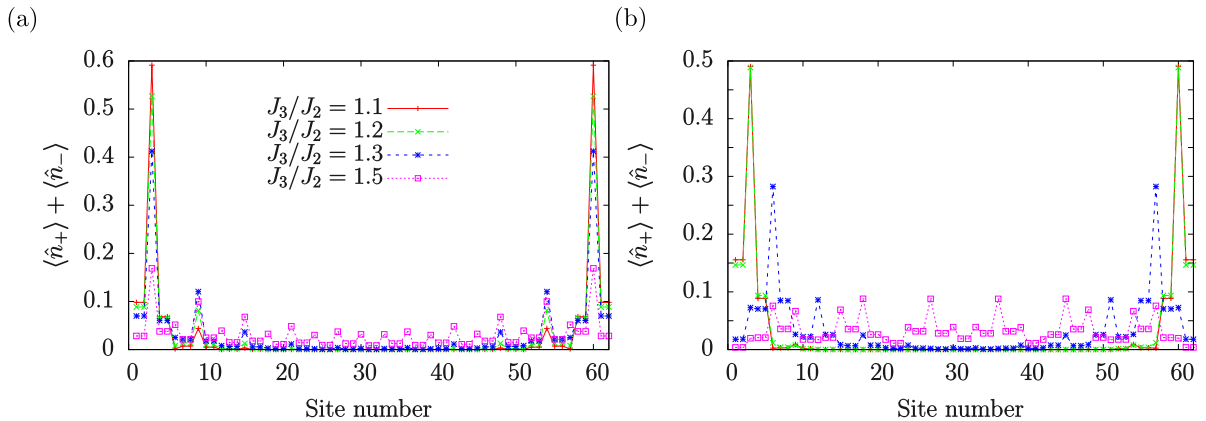

Figure 6.9: Density profiles of the states inside (a) the dashed box 1 of Fig. 6.8 and (b) the dashed box 2 of the same figure. The interaction parameters are $\{U_A/J_2 = -2, U_1/J_2 = -2, U_2/J_2 = -1\}$. The sites have been assigned a number j according to the same correspondences as in Chapter 4, i.e., $C_i = 3_i - 2, B_i = 3_i - 1, A_i = 3_i$, where i labels the unit cell.

In Fig. 6.9 (a) and (b) we plot respectively the total density profiles of the states inside the dashed boxes 1 and 2 of Fig. 6.8 (a). The states that lie inside gaps preserve their localization at the edges, displaying longer decays into the bulk as the J_3/J_2 ratio increases.

From this brief analysis of the effects of deviations from the flat-band limit, we can conclude that for sufficiently low values of the difference between the J_3 and J_2 couplings (compared to the interaction strength $|U|$), the main characteristics of the low-energy sector of the spectrum, i.e., the separation between the $\mathcal{H}_4$ and $\mathcal{H}_3$ subspaces and the presence of topological edge states in the $|U_1| > |U_2|$ regime, are preserved. For instance, in the case examined here in which the parameters of the system are $\{U_A/J_2 = -2, U_1/J_2 = -2, U_2/J_2 = -1\}$, these characteristics are still clearly observed for $J_3/J_2 = 1.2$. As shown in Fig. 2.4, this value of the J_3/J_2 ratio can be realized for realistic values of the radius of the rings and the separation between them.

6.5   Conclusions

In this Chapter, we have extended the analysis of the optical lattice with a diamond-chain shape introduced in Chapter 4 by examining the low-energy properties of two bosons with weak attractive interactions in the Aharonov-Bohm caging regime, that is, in the limit where all the bands are flat and the single-particle eigenstates consist of completely localized modes. As a main result, we have found that this system has a topological phase in which in-gap edge states formed by bound pairs of bosons appear in the spectrum of a chain with open boundaries.

In order to gain analytical insight on the properties of this system, we have first concentrated on the regime in which the interactions are much smaller than the gap between the flat bands. In this situation, the Hamiltonian can be projected into the two lowest degenerate bands. Within the space of two-boson states restricted to the lowest bands, we have identified the two subspaces of lowest self-energy, which are composed of states in which the two bosons are localized in the same plaquette. Taking profit of this fact, we have mapped these two-boson states into single-particle states and derived non-interacting tight-binding models for describing each of the two subspaces. These two effective models, which can be interpreted respectively in terms of a SSH chain and a Creutz ladder, have a topological phase which can be obtained by tuning separately the strength of the interactions on the odd and even unit cells of the lattice. In principle, this could be done by means of a modulated electric or magnetic field that induces Feshbach resonances of the desired amplitude in each type of sites.

In order to check the analytical predictions, we have performed exact diagonalization calculations over the full Hamiltonian of the diamond chain and compared the low-energy sector of the spectrum with the results obtained by solving the effective models. We have found that, in the weakly-interacting regime, the effective models have an excellent agreement with the exact spectrum of the lattice filled with two bosons and predict correctly the presence of edge states in the topological phase. Finally, we have studied numerically how the properties of the system are modified in the presence of stronger attractive interactions and when the bands are not completely flat. In the former case, we have found that the effective models still provide a good qualitative description of the low-energy properties of the system and that the edge localization of the in-gap states is actually more pronounced for stronger interactions. In the latter case, we have observed that the topological edge states are preserved for values of the deviation from the flat-band limit that correspond to realistic values of the tunneling couplings.

As this is an initial analysis of the system, a number of further questions can be addressed. Analytical calculations in the flat-band limit incorporating higher-band states could be performed in order to explain the behaviour of the system in the presence of stronger interactions. The dynamics of the system and its interplay with topology could

be studied. Another interesting direction is to generalize the analytical and numerical studies of two-boson states to a lattice with a higher filling.

the

Second-order topological corner states with ultracold atoms carrying orbital angular momentum in optical lattices

In this Chapter, we study the topological properties of ultracold atoms loaded into Orbital Angular Momentum (OAM) states of a two-dimensional (2D) square optical lattice with unequal intra- and inter-cell spacings. We demonstrate that this system constitutes an example of a 2D higher-order topological insulator, displaying in its spectrum one-dimensional (1D) edge states and zero-dimensional corner states that are correlated with the topological properties of the bulk. We show that the topologically non-trivial regime can be explored in a wide range of experimentally feasible values of the parameters of the physical system. Furthermore, we propose an alternative way to characterize the second-order topological corner states based on the computation of the Zak's phases of the bands of first-order edge states.

The Chapter is organized as follows. In Sec. 7.1, we introduce the recently developed concept of higher-order topological insulators and give a brief overview on the main advances in this topic. In Sec. 7.2, we describe the physical system and derive the Hamiltonian that governs the tunneling dynamics of ultracold atoms carrying orbital angular momentum in the 2D optical lattice. We also introduce a basis rotation that decouples the full system with two orbitals per site into two independent and equivalent lattices with one orbital per site, and we analyse the band structure of these resulting subsystems. In Sec. 7.3, we perform the topological characterization of the model. First, we discuss the weak topological properties that give rise to the edge states, and we then move on to analyse the second-order effects, which are manifested through the

presence of zero-energy modes localized at the corners of the lattice. We also propose an alternative way to predict the presence of corner states by computing the Zak's phases of the bands of first-order edge states and we analyse the protecting symmetries of the corner states. Finally, in Sec. 7.4 we summarize the main conclusions of this work.

7.1   Introduction

Over the last decades, the study of topological insulators has become one of the most active fields in condensed matter physics [67, 310]. In these materials, the bulk-boundary correspondence establishes a relation between the topological properties of the insulating bulk and the presence of robust states at the boundaries of a finite system. Traditionally, this bulk-boundary correspondence has been considered in first-order D-dimensional topological insulators, where non-trivial bulk topological indices yield $(D-1)$-dimensional boundary states. In recent seminal works [82, 311], this concept has been extended to higher-order topological insulators (HOTIs), which display boundary modes localized in $D-n$ dimensions, with $n \geq 2$. Since their discovery, HOTIs have attracted a lot of theoretical interest [82, 311–328] and have been experimentally demonstrated in several physical platforms such as metamaterials [329, 330], microwave [331], topolectrical [332] and LC [333] circuits or solid state bismuth samples [334].

In this work, we propose a scheme to realize a 2D HOTI with zero-energy corner modes using ultracold atoms in optical lattices. These systems have proven to be a very versatile platform to create a variety of topological phases of matter [48, 83] in 1D [81, 100, 103, 212, 335] and 2D [46, 47, 94] settings. Our proposal is based on the use of OAM states, which are supported by any cylindrically symmetric potential. For concreteness, we focus our discussion on ultracold atoms trapped in arrays of ring potentials, which can be implemented by a variety of techniques [109–114, 116] and where OAM can be directly transferred to the atoms using focused light beams [120, 122]. Alternatively, OAM states can also be created in conventional optical lattices by exciting the atoms to the p-band [57, 58, 135, 221] or periodically modulating the lattice amplitude [136]. The distinctive advantage of OAM states is that they give rise to complex tunneling amplitudes in a natural way [137, 234], constituting an alternative to artificially engineered gauge fields [84, 85, 89, 233]. The relative phase between these complex tunneling amplitudes can be tuned by modifying the geometry of the system. Taking advantage of this fact, we consider a lattice in which the arrangement of the relative phases allows one to decouple the full model with two OAM states per site into two independent lattices with only one orbital per site. These lattices are just rotated versions of each other and thus share the same topological phases, giving rise to non-trivial topology in the global system. The latter is signalled by the presence of both

edge states, related to weak topological properties, and zero-energy corner states, which are due to second-order topological effects.

7.2 Physical system

The physical system that we consider consists of a gas of non-interacting ultracold atoms of mass m trapped in a 2D lattice with a unit cell formed by four sites, which we denote $\{A, B, C, D\}$, as depicted in Fig. 7.1. Each of the sites is the center of a ring-shaped optical trap of radius R, and the intra- and inter-cell separations between the outermost parts of the rings are s and s', respectively. Each of these ring traps creates a potential $V(r) = \frac{1}{2}m\omega^2(r-R)^2$, which defines a radial length scale $\sigma = \sqrt{\frac{\hbar}{m\omega}}$, where ω is the radial frequency and $\hbar$ the reduced Planck's constant. These potentials support modes with an integer OAM l.
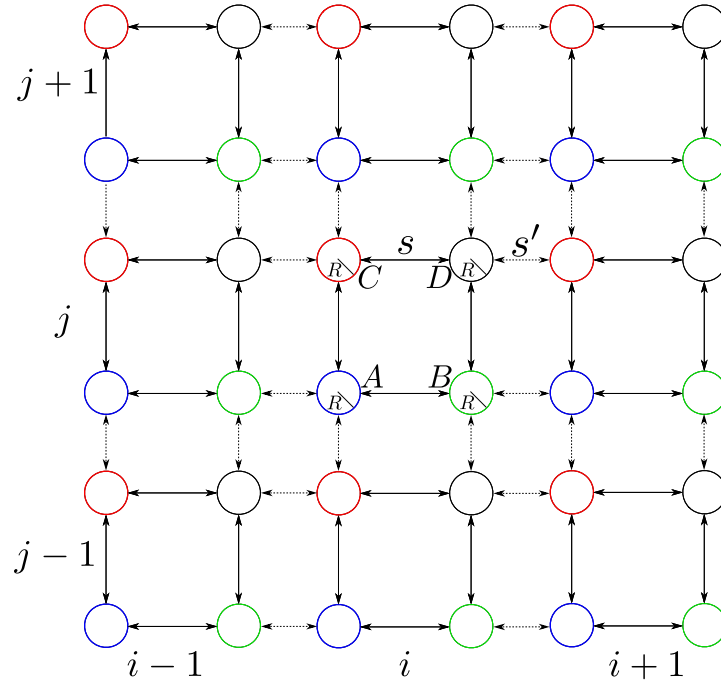
Figure 7.1: Sketch of the 2D lattice of rings of radius R considered in this work. The unit cells are formed by 4 rings, named $\{A, B, C, D\}$, with intra- and inter-cell separations between their outermost parts given by s and s', respectively.

For concreteness, in this work we focus on the particular case in which the atoms may occupy the two degenerate OAM $l = 1$ states with positive or negative circulation of each ring potential of the lattice, but all our considerations could be generalized to higher OAM states in a straightforward manner. We denote the OAM $l = 1$ states with

positive and negative circulations as $|O_{i,j}, \pm\rangle$, where i, j are indices that indicate the horizontal and vertical positions of the unit cell and $O = \{A, B, C, D\}$ labels the site. The wave functions of these states are given by

$$\phi_{\pm}^{O_{i,j}}(r_{O_{i,j}}, \varphi_{O_{i,j}}) = \langle \vec{r} | O_{i,j}, \pm \rangle = \psi(r_{O_{i,j}}) e^{\pm i(\varphi_{O_{i,j}} - \varphi_0)}, \qquad (7.1)$$

where $(r_{O_{i,j}}, \varphi_{O_{i,j}})$ are the polar coordinates with origin at the site $O_{i,j}$ and φ_0 is an absolute phase origin, which can be chosen arbitrarily. The tunneling dynamics of the OAM states has been reviewed in Sec. 2.4 of Chapter 2, where we showed that there are only three independent tunneling amplitudes whose absolute and relative values depend on the radius of the rings R and the distance between them s [see Fig. 2.4]. We denote these amplitudes as: i) $J_1(R, s)$, which corresponds to the self-coupling at each site between the two OAM states with opposite circulations, and ii) $J_2(R, s)$ and $J_3(R, s)$, which correspond to the cross coupling between OAM states in different sites with equal or different circulations, respectively. Note that we have dropped the OAM manifold index $l = 1$ from the tunneling amplitudes for simplicity. The origin of phases φ_0 plays the role of inducing complex factors $e^{\pm 2i\varphi_0}$ in the tunneling amplitudes which correspond to processes involving exchange of the OAM circulation, i.e., $J_1(R, s)$ and $J_3(R, s)$. In the lattice depicted in Fig. 7.1, destructive interference between neighbouring sites with different phases in the tunneling amplitudes causes the self-coupling terms J_1 to vanish [137]. Choosing φ_0 along the line that unites the sites $A_{i,j} \leftrightarrow B_{i,j}$, the couplings along the perpendicular direction $A_{i,j} \leftrightarrow C_{i,j}$ acquire a relative π phase and the Hamiltonian of the non-interacting system reads

$$
\begin{aligned}
\hat{H} = {} & J_2 \sum_{i,j} \sum_{\alpha=\pm} \hat{a}_\alpha^{i,j\dagger}(\hat{b}_\alpha^{i,j} + \hat{c}_\alpha^{i,j}) + \hat{d}_\alpha^{i,j\dagger}(\hat{b}_\alpha^{i,j} + \hat{c}_\alpha^{i,j}) \\
& + J_2' \sum_{i,j} \sum_{\alpha=\pm} \hat{a}_\alpha^{i,j\dagger}(\hat{b}_\alpha^{i-1,j} + \hat{c}_\alpha^{i,j-1}) + \hat{d}_\alpha^{i,j\dagger}(\hat{b}_\alpha^{i,j+1} + \hat{c}_\alpha^{i+1,j}) \\
& + J_3 \sum_{i,j} \sum_{\alpha=\pm} \hat{a}_\alpha^{i,j\dagger}(\hat{b}_{-\alpha}^{i,j} - \hat{c}_{-\alpha}^{i,j}) + \hat{d}_\alpha^{i,j\dagger}(-\hat{b}_{-\alpha}^{i,j} + \hat{c}_{-\alpha}^{i,j}) \\
& + J_3' \sum_{i,j} \sum_{\alpha=\pm} \hat{a}_\alpha^{i,j\dagger}(\hat{b}_{-\alpha}^{i-1,j} - \hat{c}_{-\alpha}^{i,j-1}) + \hat{d}_\alpha^{i,j\dagger}(-\hat{b}_{-\alpha}^{i,j+1} + \hat{c}_\alpha^{i+1,j}) \\
& + \text{H.c.}, \qquad\qquad\qquad\qquad\qquad\qquad\qquad\qquad\qquad\qquad\qquad (7.2)
\end{aligned}
$$

where we have defined $J_2 \equiv J_2(R, s)$, $J_3 \equiv J_3(R, s)$, $J_2' \equiv J_2(R, s')$, $J_3' \equiv J_3(R, s')$ and the annihilation operators $\hat{o}_{\pm}^{i,j}$, with $o = \{a, b, c, d\}$, associated with the states $|O_{i,j}, \pm\rangle$. The single-particle properties derived from the Hamiltonian (7.2) are independent of the quantum statistics. However, in some cases we will compute quantities that involve occupation by a single atom of consecutive quantum levels. In those instances, we will assume a spinless fermionic species, because non-interacting bosons would accumulate into the lowest-energy state.

7.2.1 Decoupling into two independent and equivalent lattices

In order to simplify the treatment of the model, we consider a new basis formed by the symmetric and anti-symmetric combinations of OAM states with opposite circulation at each site

$$|O_{i,j}, S\rangle = \frac{1}{\sqrt{2}}(|O_{i,j}, +\rangle + |O_{i,j}, -\rangle), \tag{7.3}$$

$$|O_{i,j}, A\rangle = \frac{1}{\sqrt{2}}(|O_{i,j}, +\rangle - |O_{i,j}, -\rangle). \tag{7.4}$$

The density profiles of the symmetric and anti-symmetric combinations resemble those of p_x and p_y orbitals, respectively. In this rotated basis, the non-vanishing matrix elements of the Hamiltonian (7.2) are

$$\left\langle A_{i,j}, S \left| \hat{H} \right| B_{i,j}, S \right\rangle = \left\langle C_{i,j}, S \left| \hat{H} \right| D_{i,j}, S \right\rangle = J_2 + J_3, \tag{7.5a}$$

$$\left\langle A_{i,j}, S \left| \hat{H} \right| C_{i,j}, S \right\rangle = \left\langle B_{i,j}, S \left| \hat{H} \right| D_{i,j}, S \right\rangle = J_2 - J_3, \tag{7.5b}$$

$$\left\langle B_{i,j}, S \left| \hat{H} \right| A_{i+1,j}, S \right\rangle = \left\langle D_{i,j}, S \left| \hat{H} \right| C_{i+1,j}, S \right\rangle = J_2' + J_3', \tag{7.5c}$$

$$\left\langle C_{i,j}, S \left| \hat{H} \right| A_{i,j+1}, S \right\rangle = \left\langle D_{i,j}, S \left| \hat{H} \right| B_{i,j+1}, S \right\rangle = J_2' - J_3', \tag{7.5d}$$

$$\left\langle A_{i,j}, A \left| \hat{H} \right| C_{i,j}, A \right\rangle = \left\langle B_{i,j}, A \left| \hat{H} \right| D_{i,j}, A \right\rangle = J_2 + J_3, \tag{7.5e}$$

$$\left\langle A_{i,j}, A \left| \hat{H} \right| B_{i,j}, A \right\rangle = \left\langle C_{i,j}, A \left| \hat{H} \right| D_{i,j}, A \right\rangle = J_2 - J_3, \tag{7.5f}$$

$$\left\langle C_{i,j}, A \left| \hat{H} \right| A_{i,j+1}, A \right\rangle = \left\langle D_{i,j}, A \left| \hat{H} \right| B_{i,j+1}, A \right\rangle = J_2' + J_3', \tag{7.5g}$$

$$\left\langle B_{i,j}, A \left| \hat{H} \right| A_{i+1,j}, A \right\rangle = \left\langle D_{i,j}, A \left| \hat{H} \right| C_{i+1,j}, A \right\rangle = J_2' - J_3'. \tag{7.5h}$$

Therefore, the basis rotation decouples the lattice with two OAM orbitals per site described by the Hamiltonian (7.2) into two independent lattices with only one symmetric or anti-symmetric orbital per site

$$\hat{H} = \hat{H}_S + \hat{H}_A, \tag{7.6}$$

$$\hat{H}_S = \sum_{i,j} t_1(\hat{a}_S^{i,j\dagger}\hat{b}_S^{i,j} + \hat{c}_S^{i,j\dagger}\hat{d}_S^{i,j}) + t_1'(\hat{b}_S^{i,j\dagger}\hat{a}_S^{i+1,j} + \hat{d}_S^{i,j\dagger}\hat{c}_S^{i+1,j})$$

$$+ \sum_{i,j} t_2(\hat{a}_S^{i,j\dagger}\hat{c}_S^{i,j} + \hat{b}_S^{i,j\dagger}\hat{d}_S^{i,j}) + t_2'(\hat{c}_S^{i,j\dagger}\hat{a}_S^{i,j+1} + \hat{d}_S^{i,j\dagger}\hat{b}_S^{i,j+1})$$

$$+ \text{H.c.}, \tag{7.7}$$

$$\hat{H}_A = \sum_{i,j} t_2(\hat{a}_A^{i,j\dagger}\hat{b}_A^{i,j} + \hat{c}_A^{i,j\dagger}\hat{d}_A^{i,j}) + t_2'(\hat{b}_A^{i,j\dagger}\hat{a}_A^{i+1,j} + \hat{d}_A^{i,j\dagger}\hat{c}_A^{i+1,j})$$

$$+ \sum_{i,j} t_1(\hat{a}_A^{i,j\dagger}\hat{c}_A^{i,j} + \hat{b}_A^{i,j\dagger}\hat{d}_A^{i,j}) + t_1'(\hat{c}_A^{i,j\dagger}\hat{a}_A^{i,j+1} + \hat{d}_A^{i,j\dagger}\hat{b}_A^{i,j+1})$$

$$+ \text{H.c.}, \tag{7.8}$$

where we have defined the new coupling constants $t_1 \equiv J_2 + J_3, t_1' \equiv J_2' + J_3', t_2 \equiv J_2 - J_3, t_2' \equiv J_2' - J_3'$. The lattices of symmetric and anti-symmetric orbitals described by the Hamiltonians (7.7) and (7.8) are represented in Figs. 7.2 (a) and (b), respectively. Both models possess chiral and x and y reflection symmetries, and one can be obtained from the other by applying a C_4 rotation.

Doing the same procedure of Fourier-transforming the annihilation and creation operators as described in Sec. 2.2 of Chapter 2, we obtain the following k-space bulk Hamiltonians for the symmetric and anti-symmetric lattices

$$H_S = \begin{pmatrix} 0 & 0 & t_1 + t_1'e^{-ik_x} & t_2 + t_2'e^{-ik_y} \\ 0 & 0 & t_2 + t_2'e^{ik_y} & t_1 + t_1'e^{ik_x} \\ t_1 + t_1'e^{ik_x} & t_2 + t_2'e^{-ik_y} & 0 & 0 \\ t_2 + t_2'e^{ik_y} & t_1 + t_1'e^{-ik_x} & 0 & 0 \end{pmatrix}, \tag{7.9}$$

and

$$H_A = \begin{pmatrix} 0 & 0 & t_2 + t_2'e^{-ik_x} & t_1 + t_1'e^{-ik_y} \\ 0 & 0 & t_1 + t_1'e^{ik_y} & t_2 + t_2'e^{ik_x} \\ t_2 + t_2'e^{ik_x} & t_1 + t_1'e^{-ik_y} & 0 & 0 \\ t_1 + t_1'e^{ik_y} & t_2 + t_2'e^{-ik_x} & 0 & 0 \end{pmatrix}, \tag{7.10}$$

where we have used the basis ordering $\{A, D, B, C\}$ in order to make manifest the chiral symmetry of the models.
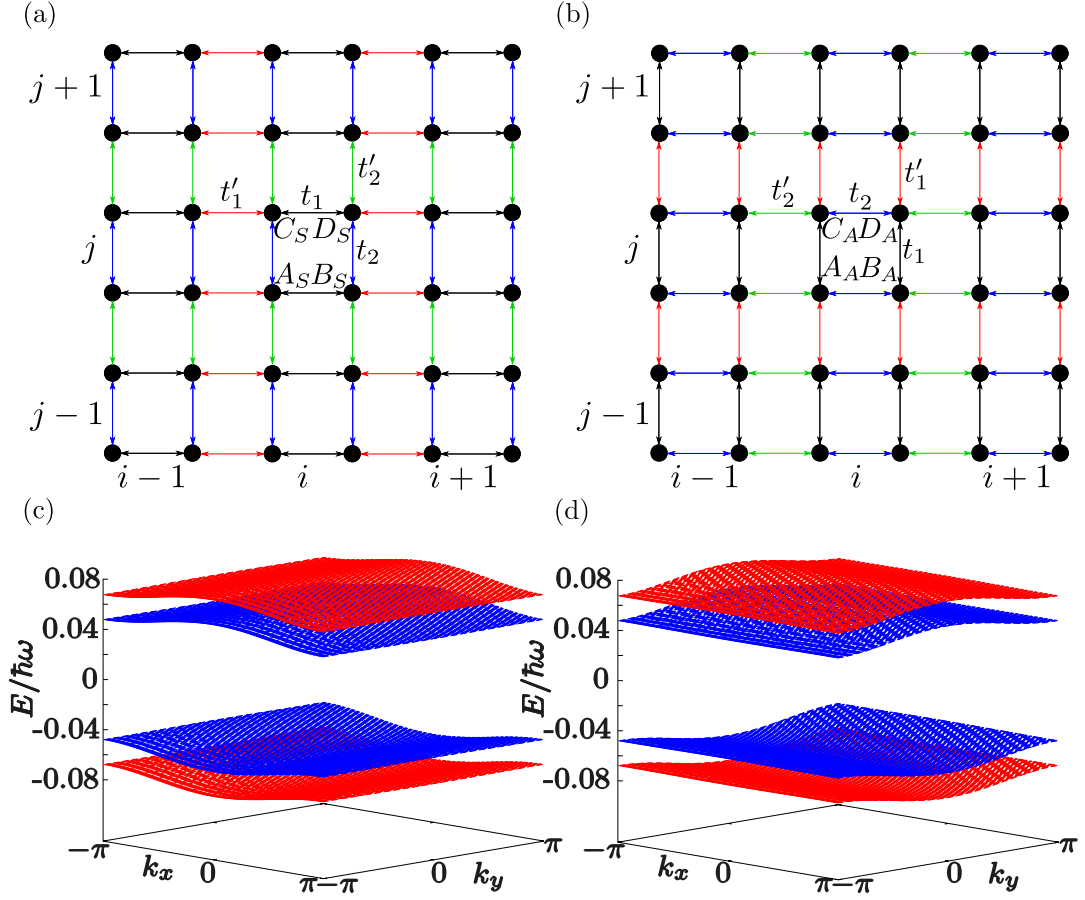
Figure 7.2: Sketches of the 2D lattices of (a) symmetric and (b) anti-symmetric combinations of OAM orbitals, which are described respectively by the Hamiltonians (7.7) and (7.8). Band structures of the (c) symmetric and (d) anti-symmetric lattices. The parameters of the physical lattice are $R = 2.5\sigma$, $s = 4\sigma$ and $s' = 2\sigma$, for which the coupling parameters of the symmetric and anti-symmetric lattices are $t_1/t_1' = 0.09$, $t_2/t_2' = 0.03$, $t_2'/t_1' = -0.16$.

The corresponding energy bands are given by

$$E_S^1 = -E_S^4 = -\sqrt{t_1^2 + t_1'^2 + 2t_1 t_1' \cos(k_x)} - \sqrt{t_2^2 + t_2'^2 + 2t_2 t_2' \cos(k_y)}, \qquad (7.11a)$$

$$E_S^2 = -E_S^3 = -\sqrt{t_1^2 + t_1'^2 + 2t_1 t_1' \cos(k_x)} + \sqrt{t_2^2 + t_2'^2 + 2t_2 t_2' \cos(k_y)}, \qquad (7.11b)$$

and

$$E_A^1 = -E_A^4 = -\sqrt{t_2^2 + t_2'^2 + 2t_2 t_2' \cos(k_x)} - \sqrt{t_1^2 + t_1'^2 + 2t_1 t_1' \cos(k_y)}, \qquad (7.12a)$$

$$E_A^2 = -E_A^3 = -\sqrt{t_2^2 + t_2'^2 + 2t_2 t_2' \cos(k_x)} + \sqrt{t_1^2 + t_1'^2 + 2t_1 t_1' \cos(k_y)}. \qquad (7.12b)$$

The band structures (7.11) and (7.12) are gapped at zero energy if the couplings fulfill either the relation $|t_1 - t'_1| > |t_2 + t'_2|$ or $|t_2 - t'_2| > |t_1 + t'_1|$. Owing to the dependence of the tunneling couplings $J_{2(3)}$ on the radius of the rings and their separation [see Fig. 2.4], these conditions are fulfilled for a wide range of experimentally reasonable values of R, s and s'. This is exemplified in Fig. 7.2 (c) and (d), where the gapped band structures of the symmetric and anti-symmetric lattices that are obtained for the coupling parameters corresponding to rings of radius $R = 2.5\sigma$ with intra- and inter-cell separations $s = 4\sigma$ and $s' = 2\sigma$ are shown.

The Hamiltonians (7.7) and (7.8) differ from the minimal model of a topological quadrupole insulator proposed in [311] by the fact that the cells of the lattices are not threaded by a net flux and have distinct staggering patterns for the coupling parameters along the x and y directions ($t_1 \leftrightarrow t'_1$ and $t_2 \leftrightarrow t'_2$). In a sense, this mimics the effect of a finite magnetic flux, in what concerns the opening of the energy gap around zero energy. As such, this system can also display second-order topological corner states and quadrupole moment. In Sec. 7.3, we discuss the topological properties of the model and show how they manifest themselves through the presence of edge and corner states in finite systems. Since the lattices of symmetric and anti-symmetric orbitals are equivalent, it is enough to analyse only one of them in order to characterize the full model with two OAM orbitals per site. In the following, we will focus the discussion on the lattice of symmetric orbitals. Although it is not necessary to experimentally distinguish between symmetric and anti-symmetric orbitals in order to observe the properties of the system that we shall discuss, we note that in other physical platforms supporting p_x and p_y orbitals it is possible to manipulate separately the lattices described by the models (7.7) and (7.8). In the p-band of a conventional optical lattice [58], this could be done by using lasers with different intensities along x and y, in such a way that the gaps between the s and p bands would be different along each direction and the energies of the p_x and p_y orbitals would be shifted. Energy shifting and separate manipulation of the p_x and p_y orbitals has also been demonstrated in an artificial electronic lattice [336], which is another physical platform where the model studied in this work could be implemented.

7.3   Topological properties

Let us consider a lattice of symmetric orbitals as the one depicted in Fig. 7.2 (a) formed by N_x and N_y unit cells along the x and y directions, respectively. In the limit of zero intra-cell couplings, $t_1 = t_2 = 0$, corner and edge states appear naturally in this lattice. The four corner sites are completely decoupled from the rest of the system, and therefore they arise as zero-energy states in the spectrum. Moreover, the horizontal edges
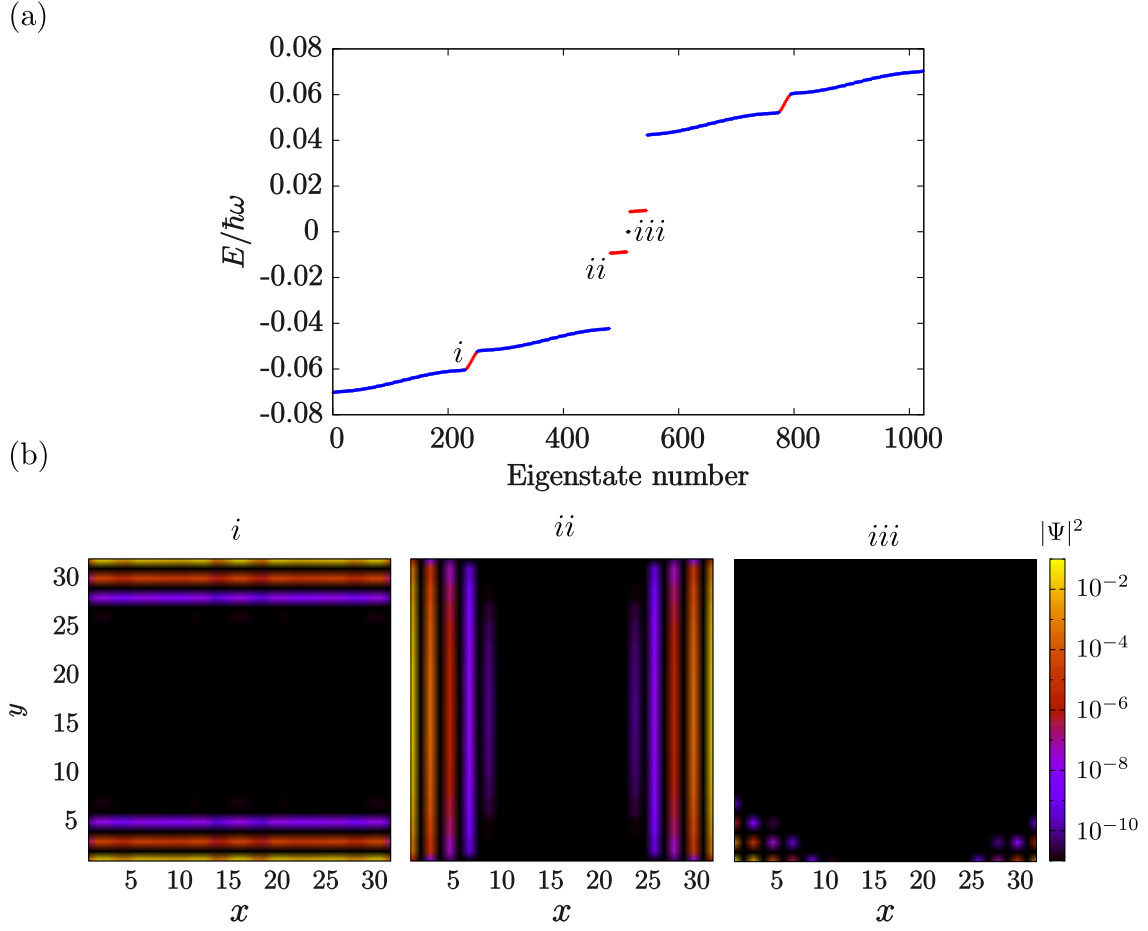
(a)

(b)

Figure 7.3: (a) Full energy spectrum of a symmetric lattice of $N_x \times N_y = 16 \times 16$ unit cells, with its corresponding bulk states (blue dots), horizontal and vertical edge states (red dots), and zero-energy corner states (black dots). (b) Density profiles of a vertical edge state (left plot), a horizontal edge state (middle plot) and a corner state (right plot). The A, B and C labels mark the position of the states in the spectrum. The parameters of the physical lattice are $R = 2.5\sigma$, $s = 4\sigma$ and $s' = 2\sigma$, for which the coupling parameters of the symmetric lattice are $t_1/t'_1 = 0.09$, $t_2/t'_2 = 0.03$, $t'_2/t'_1 = -0.16$.

are composed of $N_x - 2$ isolated dimers with internal coupling t'_1. Thus, the spectrum also has $2N_x - 4$ vertical edge states, of which one half have energy t'_1 and the other half $-t'_1$. Similarly, the y edges host $2N_y - 4$ horizontal edge states, of which one half have energy t'_2 and the other half $-t'_2$. All of these states have a topological origin, and are therefore present in the energy spectrum beyond the limit of null intra-cell couplings. This is illustrated in Fig. 7.3 (a), which shows the spectrum of a lattice of 16×16 unit cells formed by rings of radius $R = 2.5\sigma$ and inter- and intra-cell separations $s = 4\sigma$ and $s' = 2\sigma$, for which the coupling parameters fulfill the relations $|t'_1| > |t_1|, |t'_2| > |t_2|$ and

are such that all the gaps are open. While the corner states remain at zero energy, the horizontal and vertical edge states (labeled according to the direction over which they decay) change their energies with respect to the $t_1 = t_2 = 0$ limit and form dispersive bands. Examples of the density profiles of the corner modes and vertical and horizontal edge states are shown in Fig. 7.3 (b), where it can be appreciated that the three different types of states are exponentially localized.

The topological mechanisms that give rise to the edge and the corner states are different. On the one hand, the former are weak topological states, i.e., they can be regarded as a juxtaposition of 1D topological states, and are therefore characterized by the 2D generalization of the Zak's phase [337]. On the other hand, the latter are due to second-order topological effects [311]. Thus, in the next subsections we discuss separately these two different mechanisms, and we then combine all the results to fully characterize the topological phase diagram of the model.

7.3.1   Weak topology and edge states

The model under consideration does not constitute a Chern insulator [67, 310], since it has a vanishing Chern number. This is a consequence of the fact that the model is invariant under both time-reversal and inversion symmetry. The former implies that the Berry curvature of each band is an odd function of $\vec{k}$, $\Omega_n(\vec{k}) = -\Omega_n(-\vec{k})$, while the latter imposes that it must be an even function of $\vec{k}$, $\Omega_n(\vec{k}) = \Omega_n(-\vec{k})$. In order to satisfy both constraints simultaneously the Berry curvatures must vanish everywhere in quasimomentum space, implying that the Chern number is 0 for all energy bands [153]. Therefore, the presence of edge states in the energy spectrum must be explained in terms of another topological index.

According to the modern theory of polarization [159], the edge states are related to the polarization properties of the bulk. In turn, these properties are directly related to the topology of the model, which can be characterized using the Wilson-loop approach. This formalism, which was developed in the context of solid state physics, can be directly adapted to systems of ultracold atoms in optical lattices by identifying the negative/positive charges with bright/dark peaks in the atomic density distributions.

Let us consider the Bloch functions $|u_S^i(\mathbf{k})\rangle$, which are the eigenvectors associated with the energy bands E_S^i defined in Eqs. (7.11). From them, we define the Wilson-loop operators along the x and y directions $\mathcal{W}_x(k_y)$ and $\mathcal{W}_y(k_x)$, the matrix elements of which are given by

$$\mathcal{W}_x^{i,j}(k_y) = \prod_{n=0}^{N-1} \left\langle u_S^i(k_x + n\Delta k, k_y) \left| u_S^j(k_x + (n+1)\Delta k, k_y) \right\rangle \right., \tag{7.13}$$

$$\mathcal{W}_y^{i,j}(k_x) = \prod_{n=0}^{N-1} \left\langle u_S^i(k_x, k_y + n\Delta k) \left| u_S^j(k_x, k_y + (n+1)\Delta k) \right\rangle \right., \tag{7.14}$$

where N is the number of discrete points along each of the directions in $k-$space and $\Delta k = \frac{2\pi}{N}$. The indices of the matrix elements run in the range $i, j = 1, ..., N_{\text{occ}}$, where N_{occ} is the number of occupied bands. The symmetric lattice described by the Hamiltonian (7.7) has two bands below the gap centered around zero energy. Therefore, for a non-interacting spinless fermionic gas $N_{\text{occ}} = 2$ at half filling. Since the Wilson-loop operators are unitary in the thermodynamic limit (where $N \to \infty$ and $\Delta k \to 0$), their eigenvalues are complex numbers of modulus 1. From the Wilson-loop operators, we define the Wannier Hamiltonians [311]

$$H_{\mathcal{W}_x}(k_y) = -\frac{i}{2\pi} \ln \mathcal{W}_x(k_y), \tag{7.15}$$

$$H_{\mathcal{W}_y}(k_x) = -\frac{i}{2\pi} \ln \mathcal{W}_y(k_x), \tag{7.16}$$

whose eigenvalues and eigenvectors are denoted as $\nu_x^j(k_y), \nu_y^j(k_x)$ and $\left| \nu_x^j(k_y) \right\rangle, \left| \nu_y^j(k_x) \right\rangle$ $(j = 1, ..., N_{\text{occ}})$, respectively. The eigenvalues at each point in $k-$space are known as the Wannier centers, and the set of all the Wannier centers form the so-called Wannier bands [311]. Finally, the x and y bulk polarizations can be computed from the Wannier bands as

$$P_x = \frac{1}{2\pi} \sum_{j=1}^{N_{\text{occ}}} \int_0^{2\pi} dk_y \nu_x^j(k_y) \equiv \sum_{j=1}^{N_{\text{occ}}} P_x^j \pmod 1, \tag{7.17}$$

$$P_y = \frac{1}{2\pi} \sum_{j=1}^{N_{\text{occ}}} \int_0^{2\pi} dk_x \nu_y^j(k_x) \equiv \sum_{j=1}^{N_{\text{occ}}} P_y^j \pmod 1. \tag{7.18}$$

In the $N \to \infty$ limit, the polarizations can also be computed as $P_x^j = \frac{1}{2\pi}\gamma_x^j$, $P_y^j = \frac{1}{2\pi}\gamma_y^j$, where γ_x^j and γ_y^j are the 2D generalizations of the Zak's phase of the band j,

$$\gamma_x^j = \frac{i}{2\pi} \int_{\text{BZ}} d\mathbf{k} \left\langle u_S^j(\mathbf{k}) \left| \partial_{k_x} \right| u_S^j(\mathbf{k}) \right\rangle, \tag{7.19}$$

$$\gamma_y^j = \frac{i}{2\pi} \int_{\text{BZ}} d\mathbf{k} \left\langle u_S^j(\mathbf{k}) \left| \partial_{k_y} \right| u_S^j(\mathbf{k}) \right\rangle. \tag{7.20}$$

Our model has reflection symmetry in the x and y directions. In this situation, the 2D Zak's phases are quantized to 0 or π, and therefore the total polarizations can only be 0 or 1/2 for both directions.

For the lattice of symmetric orbitals all the bands have the same values of the 2D Zak's phases. Provided that all the gaps are open, these are

$$
(\gamma_x^j, \gamma_y^j) = \begin{cases} (0,0) & \text{if } t_1 > t'_1, t_2 > t'_2 \\ (\pi,0) & \text{if } t_1 < t'_1, t_2 > t'_2 \\ (0,\pi) & \text{if } t_1 > t'_1, t_2 < t'_2 \\ (\pi,\pi) & \text{if } t_1 < t'_1, t_2 < t'_2. \end{cases} \tag{7.21}
$$

Regardless of the values of the coupling parameters, the total polarizations of a non-interacting spinless fermionic system vanish both at half filling (two lower bands occupied) and unit filling (all bands occupied). However, if the $x(y)$ 2D Zak's phases of each band are non-trivial, horizontal (vertical) edge states appear in the energy spectrum of an open lattice. In Fig. 7.4 we plot the energy spectrum of a lattice of $N_x \times N_y = 10 \times 10$ unit cells formed by rings of radius $R = 2.5\sigma$ as a function of the inter- and intra-cell separations, keeping their sum constant at the value $s + s' = 6\sigma$. For $s < s'$, the couplings fulfill the relations $t_1 > t'_1, t_2 > t'_2$. Thus, the system is in the $(\gamma_x^j, \gamma_y^j) = (0,0)$ phase and no edge or corner states appear in the spectrum. At $s' = s$, the intra- and inter- cell couplings have equal strength and the middle gap closes at zero energy. For $s > s'$, the relations between the couplings are inverted with respect to the case $s < s'$. Therefore, the system enters the $(\gamma_x^j, \gamma_y^j) = (\pi, \pi)$ phase and horizontal and vertical edge states (red lines) as well as zero-energy corner state (black lines) appear in the spectrum. The horizontal edge states lie within the gap centered around zero energy and are always detached from the bulk. In contrast, the vertical edge states appear within bulk bands for $3\sigma < s \lesssim 3.8\sigma$. For inter-ring separations larger than $s \simeq 3.8\sigma$, the lower and upper gaps become larger and most of the vertical edge states lie within these gaps [as can also be seen in the energy spectrum for $s = 4\sigma$ in Fig. 7.3(a)].
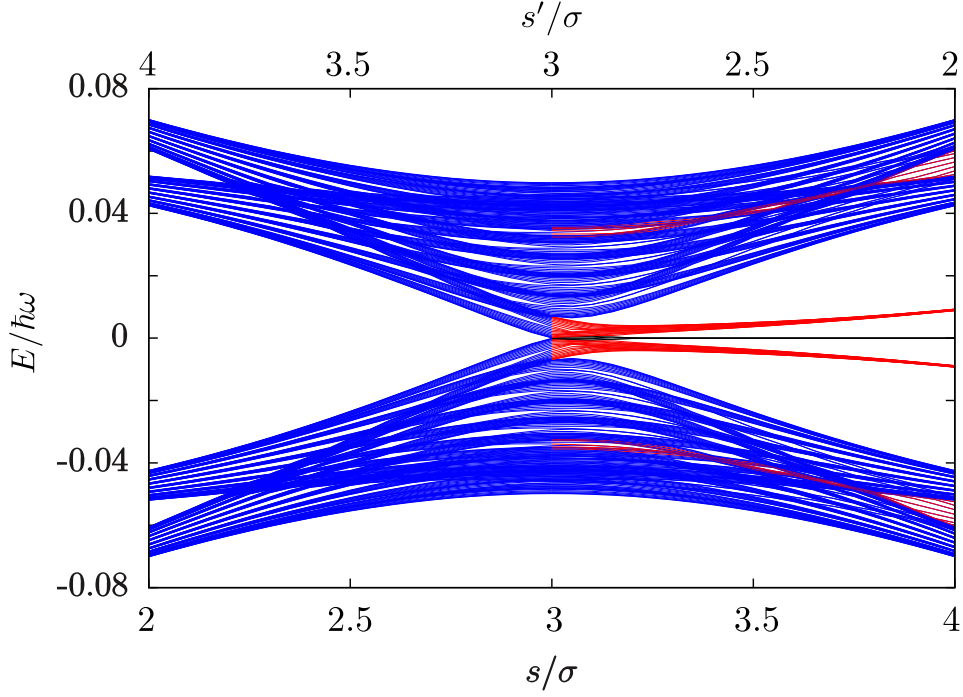
Figure 7.4: Energy spectrum of an open symmetric lattice of 10×10 unit cells formed by rings of radius $R = 2.5\sigma$ as a function of the inter-ring separation. Blue, red and black curves correspond to bulk, edge and corner states, respectively.

One-dimensional reduced models

The edge states can also be understood from a different perspective. By Fourier-transforming the Hamiltonian of the lattice of symmetric orbitals (7.7) along only the x (y) direction, quasi-one dimensional vertical (horizontal) models with coupling parameters that depend on k_x (k_y) are obtained. The Hamiltonians of these models read

$$\hat{H}_S^{\text{ver}}(k_x) = \sum_j \left\{ \left(t_1 + t_1' e^{-ik_x} \right) \left[\hat{a}_S^{j\dagger} \hat{b}_S^j + \hat{c}_S^{j\dagger} \hat{d}_S^j \right] + t_2 \left[\hat{a}_S^{j\dagger} \hat{c}_S^j + \hat{b}_S^{j\dagger} \hat{d}_S^j \right] \right.$$

$$\left. + t_2' \left[\hat{c}_S^{j\dagger} \hat{a}_S^{j+1} + \hat{d}_S^{j\dagger} \hat{b}_S^{j+1} \right] \right\} + \text{H.c.}, \tag{7.22}$$

$$\hat{H}_S^{\text{hor}}(k_y) = \sum_i \left\{ t_1 \left[\hat{a}_S^{i\dagger} \hat{b}_S^i + \hat{c}_S^{i\dagger} \hat{d}_S^i \right] + t_1' \left[\hat{b}_S^{i\dagger} \hat{a}_S^{i+1} + \hat{d}_S^{i\dagger} \hat{c}_S^{i+1} \right] \right.$$

$$\left. + \left(t_2 + t_2' e^{-ik_y} \right) \left[\hat{a}_S^{i\dagger} \hat{c}_S^i + \hat{b}_S^{i\dagger} \hat{d}_S^i \right] \right\} + \text{H.c.}, \tag{7.23}$$

where the $\hat{o}_S^i$ and $\hat{o}_S^j$ operators are respectively the y and x Fourier transforms of $\hat{o}_S^{i,j}$. Sketches of the vertical and horizontal 1D models are shown in Fig. 7.5 (a) and (b),

respectively. At $k_x, k_y = 0, \pm\pi$, all the couplings in both 1D models become real. At these points, one can define the basis rotations

$$\left|G_S^j, \pm\right\rangle = \frac{1}{\sqrt{2}}\left(\left|A_S^j\right\rangle \pm \left|C_S^j\right\rangle\right), \tag{7.24a}$$

$$\left|F_S^j, \pm\right\rangle = \frac{1}{\sqrt{2}}\left(\left|B_S^j\right\rangle \pm \left|D_S^j\right\rangle\right), \tag{7.24b}$$

and

$$\left|G_S^i, \pm\right\rangle = \frac{1}{\sqrt{2}}\left(\left|A_S^i\right\rangle \pm \left|B_S^i\right\rangle\right), \tag{7.25a}$$

$$\left|F_S^i, \pm\right\rangle = \frac{1}{\sqrt{2}}\left(\left|C_S^i\right\rangle \pm \left|D_S^i\right\rangle\right). \tag{7.25b}$$

After these basis rotations, the non-vanishing matrix elements of the vertical and horizontal Hamiltonians are

$$\left\langle G_S^j, \pm \left| \hat{H}_S^{\mathrm{ver}}(k_x = 0) \right| G_S^j, \pm \right\rangle = \pm(t_1 + t_1'), \tag{7.26a}$$

$$\left\langle F_S^j, \pm \left| \hat{H}_S^{\mathrm{ver}}(k_x = 0) \right| F_S^j, \pm \right\rangle = \pm(t_1 + t_1'), \tag{7.26b}$$

$$\left\langle G_S^j, \pm \left| \hat{H}_S^{\mathrm{ver}}(k_x = 0) \right| F_S^j, \pm \right\rangle = t_2, \tag{7.26c}$$

$$\left\langle G_S^j, \pm \left| \hat{H}_S^{\mathrm{ver}}(k_x = 0) \right| F_S^{j\pm1}, \pm \right\rangle = t_2', \tag{7.26d}$$

and

$$\left\langle G_S^i, \pm \left| \hat{H}_S^{\mathrm{hor}}(k_y = 0) \right| G_S^i, \pm \right\rangle = \pm(t_2 + t_2'), \tag{7.27a}$$

$$\left\langle F_S^i, \pm \left| \hat{H}_S^{\mathrm{hor}}(k_y = 0) \right| F_S^i, \pm \right\rangle = \pm(t_2 + t_2'), \tag{7.27b}$$

$$\left\langle G_S^i, \pm \left| \hat{H}_S^{\mathrm{hor}}(k_y = 0) \right| F_S^i, \pm \right\rangle = t_1, \tag{7.27c}$$

$$\left\langle G_S^i, \pm \left| \hat{H}_S^{\mathrm{hor}}(k_y = 0) \right| F_S^{i\pm1}, \pm \right\rangle = t_1'. \tag{7.27d}$$

At $k_x, k_y = \pm\pi$, the matrix elements are the same except for the diagonal ones, which become $\pm(t_1 - t_1'), \pm(t_2 - t_2')$. As illustrated in Fig. 7.5, the fact that only these couplings are present allows to re-express each of the 1D models as two decoupled Su-Schrieffer-Heeger (SSH) chains [161] with different on-site potentials, which are described by the Hamiltonians

$$\hat{H}_S^{\mathrm{ver}}(k_x = 0) = \sum_j V_+^1 \left[\hat{g}_{S,+}^{j\dagger}\hat{g}_{S,+}^j + \hat{f}_{S,+}^{j\dagger}\hat{f}_{S,+}^j\right] + \left\{t_2\hat{g}_{S,+}^{j\dagger}\hat{f}_{S,+}^j + t_2'\hat{g}_{S,+}^{j\dagger}\hat{f}_{S,+}^{j+1} + \mathrm{H.c.}\right\}$$

$$+ \sum_j V_-^1 \left[\hat{g}_{S,-}^{j\dagger}\hat{g}_{S,-}^j + \hat{f}_{S,-}^{j\dagger}\hat{f}_{S,-}^j\right] + \left\{t_2\hat{g}_{S,-}^{j\dagger}\hat{f}_{S,-}^j + t_2'\hat{g}_{S,-}^{j\dagger}\hat{f}_{S,-}^{j+1} + \mathrm{H.c.}\right\},$$

$$\tag{7.28}$$

and

$$\hat{H}_S^{\text{hor}}(k_x = 0) = \sum_j V_+^2 \left[\hat{g}_{S,+}^{i\dagger} \hat{g}_{S,+}^i + \hat{f}_{S,+}^{i\dagger} \hat{f}_{S,+}^i \right] + \left\{ t_1 \hat{g}_{S,+}^{i\dagger} \hat{f}_{S,+}^i + t_1' \hat{g}_{S,+}^{i\dagger} \hat{f}_{S,+}^{i+1} + \text{H.c.} \right\}$$

$$+ \sum_i V_-^2 \left[\hat{g}_{S,-}^{i\dagger} \hat{g}_{S,-}^i + \hat{f}_{S,-}^{i\dagger} \hat{f}_{S,-}^i \right] + \left\{ t_1 \hat{g}_{S,-}^{i\dagger} \hat{f}_{S,-}^i + t_1' \hat{g}_{S,-}^{i\dagger} \hat{f}_{S,-}^{i+1} + \text{H.c.} \right\},$$

$$(7.29)$$

where we have defined the on-site potentials $V_\pm^1 \equiv \pm(t_1 + t_1')$ and $V_\pm^2 \equiv \pm(t_2 + t_2')$.
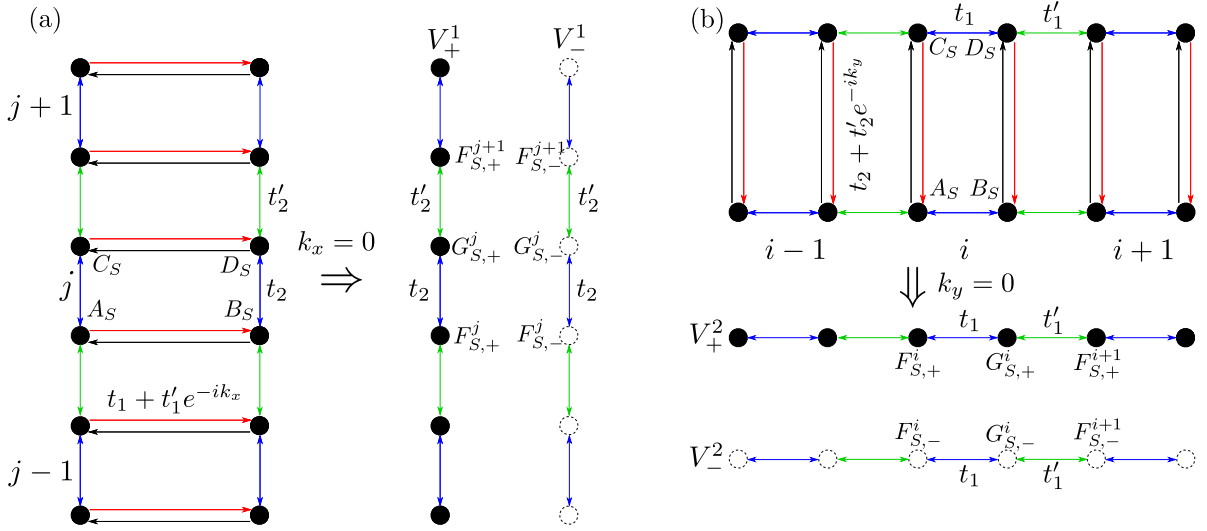

Figure 7.5: (a) Sketch of the vertical 1D model obtained by Fourier-transforming the symmetric lattice Hamiltonian (7.7) along the x direction (a) and along the y direction (b). The hopping amplitudes in the directions indicated by black arrows are the complex conjugates of those corresponding to the directions indicated by red arrows. The decoupled SSH chains that are obtained for $k_x, k_y = 0$ are also depicted.

When $t_2 < t_2'$ (i.e., when $\gamma_y^j = \pi$), the vertical SSH chains are in the topological phase and in-gap edge states with energies $V_\pm^1$ appear in their spectrum. Similarly, when $t_1 < t_1'$ (i.e., when $\gamma_x^j = \pi$) the horizontal SSH chains display edge states with energies $V_\pm^2$. Although the mappings to two decoupled SSH models can only be made for $k_x, k_y = 0, \pm\pi$, in the topological phase these edge states also appear for intermediate values of the quasi-momenta. This is illustrated in Fig. 7.6 (a) and (b), which show respectively the spectra of the vertical and horizontal 1D reduced models as a function of the k_x and k_y quasi-momenta, and where the edge states are marked with red lines. All the red lines of the spectra of Fig. 7.6 are two-fold degenerate, meaning that each of the 1D models has four edge states in the topological phase. Since the 1D vertical

(horizontal) model has been obtained from assuming periodic boundary conditions in the $x(y)$ direction of the original lattice, its edge states correspond to vertical (horizontal) edge states in the original 2D model. Therefore, the analysis of the reduced 1D models serves as a way to characterize the weak topological properties of the full 2D lattice. In the following section, we will discuss how the analysis of the bands that the edge states of the 1D models form as function of k_x and k_y can be used as a way to characterize the second-order topological properties of the model.
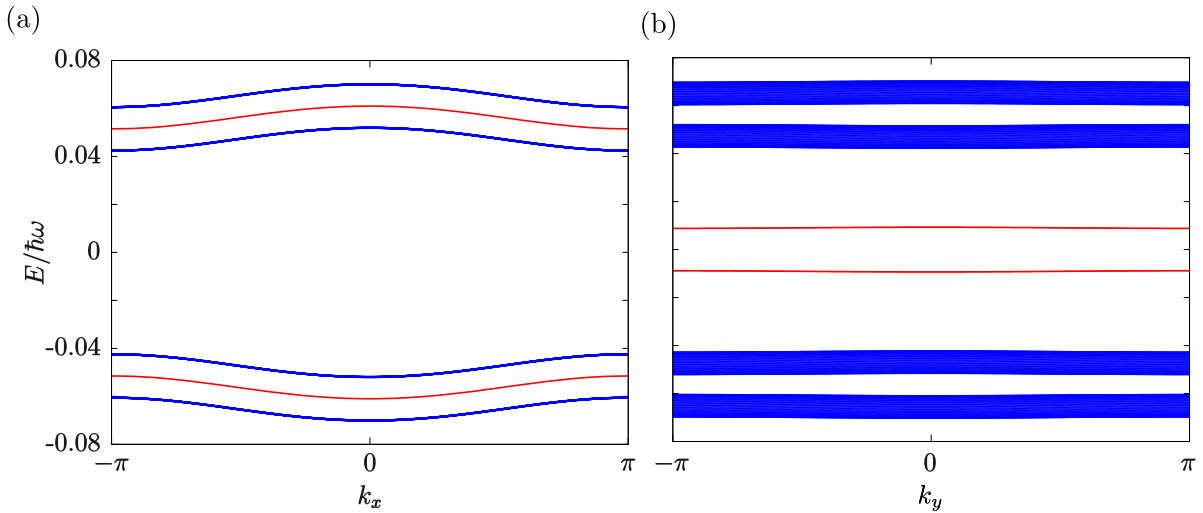

Figure 7.6: Energy spectra of (a) a vertical chain obtained by Fourier-transforming the Hamiltonian of the 2D symmetric lattice (7.7) along the x direction and (b) a horizontal chain obtained by Fourier-transforming the Hamiltonian of the 2D symmetric lattice (7.7) along the y direction. In both cases the chains have 50 unit cells and blue (red) curves correspond to bulk (edge) states. Each curve of edge states is doubly degenerate. Note that the bulk continua in (b) are much broader than in (a), where bulk states are nearly degenerate at each k_x. The parameters of the physical lattice are $R = 2.5\sigma$, $s = 4\sigma$ and $s' = 2\sigma$, for which the coupling parameters of the symmetric lattice are $t_1/t_1' = 0.09$, $t_2/t_2' = 0.03$.

7.3.2   Second-order topological effects and corner states

In the $(\gamma_x^j, \gamma_y^j) = (\pi, \pi)$ phase, a finite lattice has four zero-energy corner states. By introducing a small perturbation that breaks the chiral symmetry, this degeneracy is lifted and the states become localized at specific corners. In this situation, at half filling of the symmetric lattice (which, due to the degeneracy between the symmetric and anti-symmetric orbitals, corresponds to unit filling of the physical sites of the original model
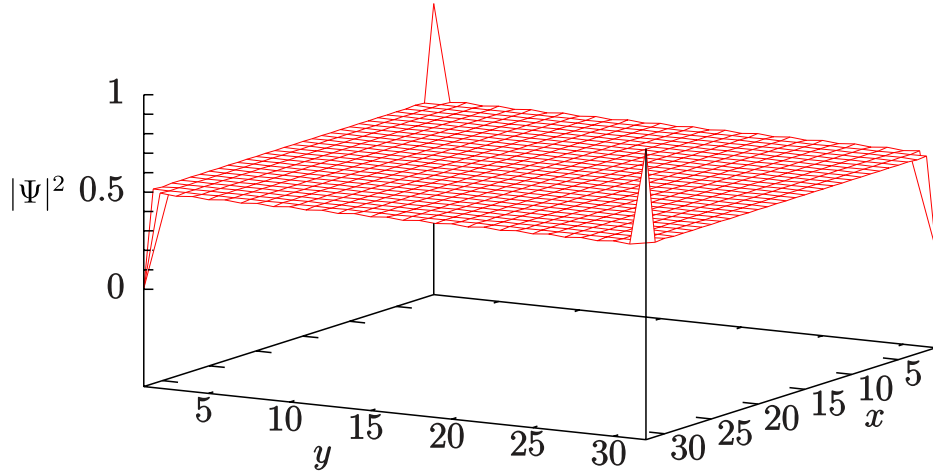
Figure 7.7: Atomic density distribution of a symmetric lattice of $N_x \times N_y = 16 \times 16$ unit cells for a non-interacting spinless fermionic gas at half filling. The parameters of the physical lattice are $R = 2.5\sigma$, $s = 4\sigma$ and $s' = 2\sigma$, for which the coupling parameters of the symmetric lattice are $t_1/t_1' = 0.09$, $t_2/t_2' = 0.03$, $t_2'/t_1' = -0.16$. A small perturbation that breaks the chiral symmetry has been introduced in the numerical calculations.

with two OAM states per ring), only two of the corner states are populated and the total density distribution has bright and dark peaks at the corners. This is exemplified in Fig. 7.7, where we plot the total density distribution of a half-filled lattice, defined as the square modulus of the state

$$|\Psi\rangle = \sum_{j=1}^{D/2} |\alpha_j, S\rangle \,, \tag{7.30}$$

where $D = 4N_x N_y$ is the total number of sites of the lattice and $|\alpha_j, S\rangle$ are the eigenstates of the Hamiltonian of the lattice of symmetric orbitals, Eq. (7.7), ordered from lower to higher energy. These density peaks are analogous to charge concentrations in an electronic system, and thus give rise to the atomic analogues of the edge polarizations and quadrupole moment.

Recently, a successful method to characterize the topological quadrupole moment has been proposed [311]. In order for a finite topological quadrupole moment to arise, at least two bands have to be occupied at half filling, as is the case in our model. Nevertheless, a necessary condition for the procedure to work is that the x and y mirror symmetries do not commute. In the minimal model for a bulk quadrupole insulator studied in [311], this non-commutativity between the reflection symmetries is achieved by introducing a π flux in each plaquette through alternating signs in the vertical couplings. In our model, however, the inversion symmetries commute and the quadrupole moment can not be characterized following the recipe presented in [311]. One way to circumvent this

(γ_x^j, γ_y^j)	Horizontal edge states	Vertical edge states	Corner states	q_{xy}
$(0,0)$	No	No	No	0
$(\pi,0)$	Yes, $\gamma_{\text{edge}}^x = 0$	No	No	0
$(0,\pi)$	No	Yes, $\gamma_{\text{edge}}^y = 0$	No	0
(π,π)	Yes, $\gamma_{\text{edge}}^x = \pi$	Yes, $\gamma_{\text{edge}}^y = \pi$	Yes	$\frac{1}{2}$

Table 7.1: Possible combinations of values of the 2D Zak's phases of the bulk and the Zak's phases of the bands of edge states of the 1D horizontal and vertical models. The last two columns indicate the presence of corner states in the 2D lattice under open boundary conditions in both the x and y directions and the values of the quadrupole moment defined in (7.31).

difficulty is to redefine the quadrupole moment per unit area as

$$q_{xy} \;=\; \frac{1}{2}\tilde{P}_x \tilde{P}_y, \tag{7.31}$$

$$\tilde{P}_{x(y)} \;=\; \sum_{j \in O} P_{x(y)}^j, \tag{7.32}$$

where O defines the set of occupied bands ($O = \{1,2\}$ in our case) and $\tilde{P}_x (\tilde{P}_y)$ is the direct sum of the polarizations along the $x(y)$ direction. Eq. (7.31) implies that the bulk quadrupole moment is $q_{xy} = \frac{1}{2}$ in the $(\gamma_x^j, \gamma_y^j) = (\pi,\pi)$ phase, that is, when both vertical and horizontal edge states are present, and $q_{xy} = 0$ otherwise. This is in accordance with our numerical calculations and allows to regard q_{xy} as the topological index associated with the appearance of corner states. The polarization $P_{x(y)}$ at half filling is related to $\tilde{P}_{x(y)}$ as $P_{x(y)} = \tilde{P}_{x(y)} \mod 1$. In our model we have $P_{x(y)} = 0$ for both $\tilde{P}_{x(y)} = 0$ (trivial phases) and $\tilde{P}_{x(y)} = 1$ (non-trivial phase), that is, the system is not polarized at half filling in either direction, which is why $P_{x(y)}$ cannot be used in the definition of q_{xy}, since it is insensitive to transitions between different second-order topological regimes.

Alternatively, the presence of edge polarizations and a finite quadrupole moment can also be tested by analysing the 1D models that are obtained by Fourier-transforming the 2D lattice along the x or y direction, Eqs. (7.22) and (7.23), respectively. As we discussed in Sec. 7.3.1, the horizontal and vertical edge states of the 2D lattice can also be seen as edge states of these 1D models. If one considers chains with finite sizes in the y (x) direction and periodic boundaries in the x (y) direction and diagonalizes them as a function of k_x (k_y), four bands of edge states (coming in two-fold degenerate pairs, see Fig. 7.6) are obtained if the original 2D lattice has bands with non-trivial 2D Zak's phases in the x (y) axis. The degeneracy of the edge bands can be lifted by introducing a small perturbation that breaks the chiral symmetry, allowing to compute their Zak's phases, γ_{edge}^x and γ_{edge}^y. A non-trivial Zak's phase in the edge states indicates the presence of "edge of edge" states (i.e., corner states) and a finite quadrupole moment

at half filling for a non-interacting spinless fermionic gas. The topological behavior of our model as a function of the values of the 2D Zak's phases in (7.19) and (7.20) is summarized in Table 7.1. The only topological phase of the bulk in which the edge bands have non-trivial Zak's phases is $(\gamma_x^j, \gamma_y^j) = (\pi, \pi)$. Thus, the simultaneous non-triviality of the Zak's phases of edge bands of the 1D models $\gamma_{\text{edge}}^x, \gamma_{\text{edge}}^y$ is in one to one correspondence with the appearance of corner states and a finite quadrupole moment in an open 2D lattice. More specifically, each pair of symmetric edge bands with a non-trivial 1D Zak's phase has two zero-energy corner-states associated with it. Each of these states is shared by a vertical and a horizontal edge band. Therefore, the four corner states that appear at zero energy are associated with the four occupied bands of edge states at half filling, of which two correspond to the 1D horizontal model and two to the 1D vertical model.

Symmetry protection of the corner states

Before concluding, let us briefly discuss the symmetries that are responsible for the topological protection of the corner states. While the quantization of the bulk polarizations P_x, P_y and the quadrupole moment q_{xy} is ensured by the x and y mirror symmetries, it is the chiral symmetry of $\hat{H}_S$ that protects the corner states. This can be justified by taking into account the fact that the spectrum of a Hamiltonian is symmetric around zero energy in the presence of chiral symmetry, implying that the zero-energy corner modes are eigenstates of the chiral operator [160]. Therefore, the corner states are not affected by perturbations that preserve the chiral symmetry.

In Fig. 7.8 (a) we illustrate two different kinds of perturbations. On the one hand, we consider an on-site potential V acting only on the corners of the lattice, which preserves the x and y reflection symmetries but breaks the chiral symmetry. On the other hand, we substitute in two of the corners the couplings of the model by a different one named t_3. This perturbation has an opposite effect to V, i.e., it breaks the reflection symmetries but preserves the chiral one. In Fig. 7.8 (b) we plot the spectrum of a finite lattice as a function of V leaving the corner couplings unchanged. As V increases, the energy of the corner modes (black line) increases until they merge into the bulk. Fig. 7.8 (c) shows the spectrum of the same lattice as in Fig. 7.8 (b) but for $V = 0$ and increasing t_3 until it reaches the value $t_3 = t_1'$, which is the largest coupling of the symmetric lattice. Since this perturbation preserves the chiral symmetry, all corner states, including the two localized around the corners with perturbed edge couplings t_3, remain locked at zero energy regardless of the value of t_3.
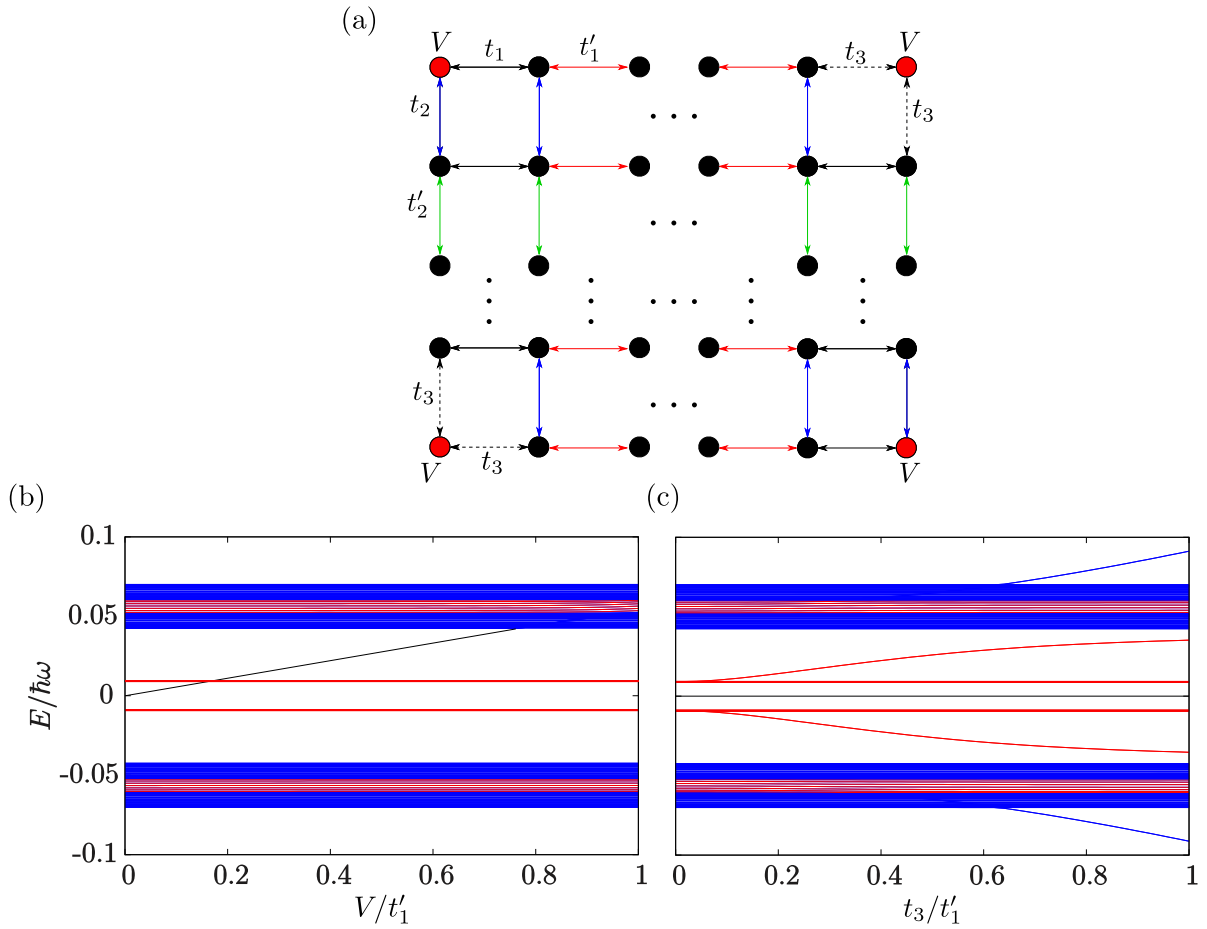
Figure 7.8: (a) Sketch of the different types of perturbations described in the main text: on-site potential V at the corners, which preserves the reflection symmetries but not the chiral one, and modified t_3 coupling in two of the corners, which has an effect opposite to V. (b) Spectrum of a lattice of 10×10 unit cells as a function of V leaving the corner couplings unchanged. (c) Spectrum of the same lattice as in (b) as a function of t_3 keeping $V = 0$. The parameters of the physical lattice are $R = 2.5\sigma$, $s = 4\sigma$ and $s' = 2\sigma$, for which the coupling parameters of the symmetric lattice are $t_1/t_1' = 0.09$, $t_2/t_2' = 0.03$, $t_2'/t_1' = -0.16$.

7.4   Conclusions

In this Chapter, we have shown that ultracold atoms carrying OAM in arrays of cylindrically symmetric potentials can be used to implement a second-order topological insulator. Specifically, we have considered a 2D square lattice with unequal intra- and inter-cell spacing between nearest-neighbour traps. This system displays both weak and

second-order topological properties. Owing to the bulk-boundary correspondence, the former manifest themselves in a finite system through the appearance of horizontal and vertical edge states, while the latter are signalled by the presence of zero-energy corner modes and a quantized quadrupole moment.

The topological properties of the system can be more directly analysed by performing a change of basis that decouples the original model with two states per site into two independent lattices with one p_x- or p_y-like orbital per site, formed respectively by symmetric and anti-symmetric combinations of the OAM states. In each of these subsystems, the presence of 1D edge states in the spectrum of an open lattice is correlated with the value of the 2D Zak's phase, which is computed in the bulk. Alternatively, these edge states can be understood in terms of the topological properties of the two 1D reduced models that are obtained by imposing periodic boundary conditions along one of the directions while keeping the other open.

We have shown that for experimentally realistic parameters the system can display zero-energy corner modes associated with the non-trivial second-order topological phase. An expression for the quantized quadrupole moment, involving a quantity defined as the direct sum of the polarizations of the occupied bands, has been identified as the relevant second-order topological index. A complementary approach to the topological characterization of the corner states, related to an analysis of the Zak's phases of the bands of edge states that appear in the 1D reduced models as a function of the quasimomentum, has been shown to be consistent with the former.

In an experimental implementation, the edge and corner states could be prepared by first populating only the corresponding sites of the lattice in the limit of zero intra-cell couplings and then adiabatically turning them on, as done in [100] to obtain the edge states of the SSH model in a system of ultracold atoms. The half-filled state, in which the quantized quadrupole moment is manifested through the density distribution, could be realized using a gas of spin-polarized fermions formed by as many atoms as sites has the lattice, in such a way that the states with energy below the Fermi level would be consecutively occupied. In order to image these states, a quantum gas microscope, which provides real-space images with single-site resolution [50–53], could be employed. We note that the topological edge states of the SSH model have been imaged in systems of ultracold atoms in optical lattices both in momentum [100] and real [212] space.

CHAPTER 8

Conclusions and outlook

The aim of this Chapter is to summarize the most important conclusions of the work presented in this dissertation and to provide an outlook of future lines of research.

This thesis has revolved around the investigation of different systems with the common characteristic of being formed by ultracold atoms carrying Orbital Angular Momentum (OAM) in cylindrically symmetric potentials. Our interest has been mainly focused on three different aspects of OAM states: their potential use for sensing purposes, their applications as quantum simulators of models of quantum magnetism, and the possibilities that they offer for realizing topological phases of matter.

Before entering into the details of our research, in Chapter 2 we have introduced the main models and tools that we have used throughout the next Chapters. We have started by reviewing the mean-field description of Bose–Einstein condensates (BECs) provided by the Gross–Pitaevskii equation (GPE) and the full quantum treatment of ultracold atoms in optical lattices through the Hubbard model. Then, we have discussed basic concepts related to the characterization of topological phases of matter. Finally, we have analysed the physics of a single ultracold atom carrying OAM in a single trap and in multiple side-coupled potentials. In this last part, we have shown that the tunneling dynamics of ultracold atoms in OAM states is governed by hopping amplitudes which are accompanied by complex phase factors that can be adjusted by modifying the geometrical arrangement of the traps.

Prior to delving into the applications that these complex tunnellings have, in Chapter 3 we have considered a BEC trapped in a single ring potential. The system, which

we have described in the context of the two-dimensional GPE, is initially prepared in a superposition of counter-rotating OAM $l = 1$ modes with unequal populations. By directly integrating the GPE, we have found that the density profile of this state exhibits a rotating minimal line. We have derived a simple expression that relates the frequency of this rotation to the strength of the atom-atom interactions, showing an excellent agreement with the GPE results in the weakly-interacting limit. Taking profit of this relation, we have proposed protocols to use the system as a device for sensing two-body interactions, magnetic fields and rotations. Finally, we have provided a method to prepare the initial imbalanced superposition of OAM modes based on the adiabatic deformation of the ring trap and we have checked its feasibility by means of numerical simulations. This work could be continued in several different directions. On the one hand, the performance of the sensing device could be further analysed in terms of the Fisher information [132]. It would also be interesting to study the dynamics of the OAM modes when the system is prepared in a superposition of higher OAM modes, in a regime of stronger atom-atom interactions, and for the case of a two-component BEC trapped in a ring potential [338, 339]. Another possibility is to investigate the non-linear tunneling dynamics [340] of BECs carrying OAM in configurations of side-coupled traps [341].

In the following Chapters, we have focused our attention on different configurations of side-coupled cylindrically symmetric traps where ultracold atoms are loaded in OAM states. In such scenarios, the complex amplitudes involved in the tunneling dynamics may give rise to topological effects and open up interesting possibilities for the simulation of relevant spin$-1/2$ models.

First, we have studied in Chapter 4 a quasi-one dimensional lattice with a diamond-chain shape in the non-interacting limit. Making use of consecutive analytical mappings, we have shown that the complex nature of the hopping amplitudes yields an effective π flux through the plaquettes of the chain. As a consequence of this, the energy bands have a topologically non-trivial structure that persists everywhere in parameter space, as evidenced by the presence of robust edge states that do not vanish after crossing the gap closing points. The topological characterization has been carried out with techniques specially adapted to lattices where the inversion axis is not at the center of the unit cell. Alternatively, the Wilczek-Zee formulation can be employed to describe the model as a square-root topological insulator. We have also made use of the mappings to reveal the shape of the different types of eigenstates of the system. Furthermore, we have demonstrated that a proper tuning of the tunneling parameters may lead to an energy spectrum composed entirely of flat bands. In this limit, the system exhibits Aharonov-Bohm caging, a destructive interference effect that prevents the propagation of wave packets through the lattice. In future studies, the fate of the Aharonov-Bohm caging effect with OAM states could be investigated both in the context of mean-field

interactions described by the GPE and of a full quantum treatment with the Bose-Hubbard model in a many-body scenario [307, 308]. Other possible continuations of this work include examining the topological properties of ultracold atoms carrying OAM in different geometries, considering interacting systems with higher fillings, or studying non-equilibrium situations involving time-dependent calculations.

The effect of interactions in a full quantum treatment of atoms carrying OAM has been introduced in Chapter 5, where we have employed a Bose-Hubbard model to analyse a family of systems consisting of arrays of cylindrically symmetric potentials with a flexible geometry filled with strongly correlated bosons. We have focused on the Mott insulator regime at unit filling, for which one can establish a correspondence between OAM and spin$-1/2$ states. By means of second-order perturbation theory, we have computed explicitly the dependence of the effective spin$-1/2$ couplings on the shape of the lattice. This dependence is rooted in the variation of the phases accompanying the tunneling amplitudes that occurs when the geometry of the system is changed. We have then demonstrated that by properly arranging the traps, the system can realize different spin models of interest in condensed matter physics related to a general XYZ Heisenberg with or without external fields. We have also shown how by tuning the geometry of the lattice one can adjust the relative strength of the effective couplings and explore different quantum phases. Finally, we have discussed techniques to retrieve the state of each individual spin and we have analysed the collisional stability of the system, reaching the conclusion that the use of ring potentials extends the lifetime of the Mott state. A direct extension of this work would be the derivation of an effective model for the case of fermionic atoms. Moreover, different scenarios leading to models describing different physics could be investigated. For instance, one could consider a strongly interacting system with a filling slightly below unity, where additional first-order terms would be needed to be taken into account, or a commensurable Mott insulator state with more atoms per site.

In Chapter 6 we have revisited the diamond chain of Chapter 4 adding the effect of attractive interactions. In particular, we have considered a lattice filled with two weakly interacting bosons in the limit where all the bands are flat. In this situation the single-particle spectrum is formed by highly degenerate localized states and the two-body physics is solely determined by the interactions. We have focused on the lowest-energy sector of the spectrum, which is formed by two-body configurations in which the two bosons occupy states belonging to the two lowest degenerate flat bands. Considering that the interaction strength can be tuned separately in the different sites of the lattice, we have derived effective single-particle models that describe the two subspaces of states with lowest self-energy. These effective models have a topological phase for which edge states appear in the middle of the energy gaps. These two-boson edge states are in turn composed of confined single-particle modes, and thus exhibit two simultaneous

localization effects. By means of exact diagonalization calculations, we have checked the accuracy of our analytical predictions and we have shown that the edge states are robust against deviations from the flat band and weakly interacting limits.

Differently from the preceding Chapters, in Chapter 7 we have investigated a genuinely two-dimensional setup consisting of a square lattice with unequal intra- and inter-cell separations filled with non-interacting ultracold atoms carrying OAM. We have shown that this system constitutes an example of a higher-order topological insulator, displaying both first- and second-order topological phases. The former are signalled in the spectrum by the presence of one-dimensional states exponentially localized at the edges of the lattice, whereas the second-order topology is correlated with the appearance of zero-energy states strongly confined in the corners. By means of numerical calculations with realistic coupling parameters, we have demonstrated that the second-order topological effects can be observed in a wide range of experimentally feasible conditions. In addition, we have analysed the symmetry protection of the corner states and we have proposed an alternative way to predict their presence based on the computation of the Zak's phases of the bands of first-order edge states. As a final remark, we note that the models describing both this system and the diamond chain without interactions of Chapter 4 could be realized with other platforms supporting non-interacting OAM states or p orbitals, such as artificial electronic lattices [336], photonic waveguides [204, 342] or polariton resonators, where the edge states of the Su-Schrieffer-Heeger model have already been observed [208].

Bibliography

[1] S. N. Bose, Zeitschrift für Physik A Hadrons and Nuclei **26**, 178 (1924).

[2] A. Einstein, Sitzber. Kgl. Preuss. Akad. Wiss. **261** (1924).

[3] A. Einstein, Sitzber. Kgl. Preuss. Akad. Wiss. **3** (1925).

[4] P. Kapitza, Nature **141**, 74 (1938).

[5] J. F. Allen and A. D. Misener, Nature **142**, 643 (1938).

[6] C. Cohen-Tannoudji, Physics Reports **219**, 153 (1992).

[7] W. Ketterle and N. J. Van Druten, Advances In Atomic, Molecular, and Optical Physics, **37**, 181 (1996).

[8] M. H. Anderson, J. R. Ensher, M. R. Matthews, C. E. Wieman, and E. A. Cornell, Science **269**, 198 (1995).

[9] K. Davis, M. Mewes, M. Andrews, N. van Druten, D. Durfee, D. Kurn, and W. Ketterle, Physical Review Letters **75**, 3969 (1995).

[10] C. C. Bradley, C. A. Sackett, J. J. Tollett, and R. G. Hulet, Physical Review Letters **75**, 1687 (1995).

[11] B. DeMarco and D. S. Jin, Science **285**, 1703 (1999).

[12] B. DeMarco, S. B. Papp, and D. S. Jin, Physical Review Letters **86**, 5409 (2001).

[13] A. G. Truscott, K. E. Strecker, W. I. McAlexander, G. B. Partridge, and R. G. Hulet, Science **291**, 2570 (2001).

[14] M. Zwierlein, Nature Physics **11**, 706 (2015).

[15] P. O. Fedichev, Y. Kagan, G. V. Shlyapnikov, and J. T. M. Walraven, Physical Review Letters **77**, 2913 (1996).

[16] M. Theis, G. Thalhammer, K. Winkler, M. Hellwig, G. Ruff, R. Grimm, and J. H. Denschlag, Physical Review Letters **93**, 123001 (2004).

[17] O. Thomas, C. Lippe, T. Eichert, and H. Ott, Nature Communications **9**, 2238 (2018).

[18] S. L. Cornish, N. R. Claussen, J. L. Roberts, E. A. Cornell, and C. E. Wieman, Physical Review Letters **85**, 1795 (2000).

[19] S. E. Pollack, D. Dries, M. Junker, Y. P. Chen, T. A. Corcovilos, and R. G. Hulet, Physical Review Letters **102**, 90402 (2009).

[20] C. Chin, R. Grimm, P. Julienne, and E. Tiesinga, Reviews of Modern Physics **82**, 1225 (2010).

[21] T. Weber, J. Herbig, M. Mark, H.-C. Nägerl, and R. Grimm, Science **299**, 232 (2003).

[22] C. A. Regal, M. Greiner, and D. S. Jin, Physical Review Letters **92**, 040403 (2004).

[23] M. W. Zwierlein, C. A. Stan, C. H. Schunck, S. M. F. Raupach, A. J. Kerman, and W. Ketterle, Physical Review Letters **92**, 120403 (2004).

[24] T. Bourdel, L. Khaykovich, J. Cubizolles, J. Zhang, F. Chevy, M. Teichmann, L. Tarruell, S. J. J. M. F. Kokkelmans, and C. Salomon, Physical Review Letters **93**, 050401 (2004).

[25] D. Budker and D. F. J. Kimball, *Optical Magnetometry* (Cambridge University Press, 2013).

[26] I. Dutta, D. Savoie, B. Fang, B. Venon, C. L. Garrido Alzar, R. Geiger, and A. Landragin, Physical Review Letters **116**, 183003 (2016).

[27] G. Rosi, F. Sorrentino, L. Cacciapuoti, M. Prevedelli, and G. M. Tino, Nature **510**, 518 (2014).

[28] G. E. Marti, R. B. Hutson, A. Goban, S. L. Campbell, N. Poli, and J. Ye, Physical Review Letters **120**, 103201 (2018).

[29] R. Grimm, M. Weidemüller, and Y. B. Ovchinnikov, Advances In Atomic, Molecular, and Optical Physics **42**, 95 (2000).

[30] M. Lewenstein, A. Sanpera, and V. Ahufinger, *Ultracold Atoms in Optical Lattices: Simulating quantum many-body systems* (OUP Oxford, 2012).

[31] I. Bloch, J. Dalibard, and W. Zwerger, Reviews of Modern Physics **80**, 885 (2008).

[32] M. Greiner, O. Mandel, T. Esslinger, T. W. Hänsch, and I. Bloch, Nature **415**, 39 (2002).

[33] M. P. A. Fisher, P. B. Weichman, G. Grinstein, and D. S. Fisher, Physical Review B **40**, 546 (1989).

[34] D. Jaksch, C. Bruder, J. I. Cirac, C. W. Gardiner, and P. Zoller, Physical Review Letters **81**, 3108 (1998).

[35] L. Pezzè, L. Pitaevskii, A. Smerzi, S. Stringari, G. Modugno, E. de Mirandes, F. Ferlaino, H. Ott, G. Roati, and M. Inguscio, Physical Review Letters **93**, 120401 (2004).

[36] M. Köhl, H. Moritz, T. Stöferle, K. Günter, and T. Esslinger, Physical Review Letters **94**, 080403 (2005).

[37] T. Stöferle, H. Moritz, K. Günter, M. Köhl, and T. Esslinger, Physical Review Letters **96**, 030401 (2006).

[38] R. Jördens, N. Strohmaier, K. Günter, H. Moritz, and T. Esslinger, Nature **455**, 204 (2008).

[39] C. Ospelkaus, S. Ospelkaus, L. Humbert, P. Ernst, K. Sengstock, and K. Bongs, Physical Review Letters **97**, 120402 (2006).

[40] G. Thalhammer, K. Winkler, F. Lang, S. Schmid, R. Grimm, and J. H. Denschlag, Physical Review Letters **96**, 050402 (2006).

[41] J. Struck, C. Olschlager, R. Le Targat, P. Soltan-Panahi, A. Eckardt, M. Lewenstein, P. Windpassinger, and K. Sengstock, Science **333**, 996 (2011).

[42] G.-B. Jo, J. Guzman, C. K. Thomas, P. Hosur, A. Vishwanath, and D. M. Stamper-Kurn, Physical Review Letters **108**, 045305 (2012).

[43] L. Tarruell, D. Greif, T. Uehlinger, G. Jotzu, and T. Esslinger, Nature **483**, 302 (2012).

[44] M. Lohse, C. Schweizer, O. Zilberberg, M. Aidelsburger, and I. Bloch, Nature Physics **12**, 350 (2016).

[45] K. Viebahn, M. Sbroscia, E. Carter, J.-C. Yu, and U. Schneider, Physical Review Letters **122**, 110404 (2019).

[46] H. Miyake, G. A. Siviloglou, C. J. Kennedy, W. C. Burton, and W. Ketterle, Physical Review Letters **111**, 185302 (2013).

[47] M. Aidelsburger, M. Atala, M. Lohse, J. T. Barreiro, B. Paredes, and I. Bloch, Physical Review Letters **111**, 185301 (2013).

[48] N. Cooper, J. Dalibard, and I. Spielman, Reviews of Modern Physics **91**, 015005 (2019).

[49] Y.-J. Lin, K. Jiménez-García, and I. B. Spielman, Nature **471**, 83 (2011).

[50] W. S. Bakr, J. I. Gillen, A. Peng, S. Fölling, and M. Greiner, Nature **462**, 74 (2009).

[51] J. F. Sherson, C. Weitenberg, M. Endres, M. Cheneau, I. Bloch, and S. Kuhr, Nature **467**, 68 (2010).

[52] L. W. Cheuk, M. A. Nichols, M. Okan, T. Gersdorf, V. V. Ramasesh, W. S. Bakr, T. Lompe, and M. W. Zwierlein, Physical Review Letters **114**, 193001 (2015).

[53] E. Haller, J. Hudson, A. Kelly, D. A. Cotta, B. Peaudecerf, G. D. Bruce, and S. Kuhr, Nature Physics **11**, 738–742 (2015).

[54] M. F. Parsons, F. Huber, A. Mazurenko, C. S. Chiu, W. Setiawan, K. Wooley-Brown, S. Blatt, and M. Greiner, Physical Review Letters **114**, 213002 (2015).

[55] A. Omran, M. Boll, T. A. Hilker, K. Kleinlein, G. Salomon, I. Bloch, and C. Gross, Physical Review Letters **115**, 263001 (2015).

[56] T. Müller, S. Fölling, A. Widera, and I. Bloch, Physical Review Letters **99**, 200405 (2007).

[57] G. Wirth, M. Ölschläger, and A. Hemmerich, Nature Physics **7**, 147 (2010).

[58] X. Li and W. V. Liu, Reports on Progress in Physics **79**, 116401 (2016).

[59] S. Baier, M. J. Mark, D. Petter, K. Aikawa, L. Chomaz, Z. Cai, M. Baranov, P. Zoller, and F. Ferlaino, Science **352**, 201 (2016).

[60] J. G. Danzl, E. Haller, M. Gustavsson, M. J. Mark, R. Hart, N. Bouloufa, O. Dulieu, H. Ritsch, and H.-C. Nagerl, Science **321**, 1062 (2008).

[61] P. Schauß, M. Cheneau, M. Endres, T. Fukuhara, S. Hild, A. Omran, T. Pohl, C. Gross, S. Kuhr, and I. Bloch, Nature **491**, 87 (2012).

[62] C. Gross and I. Bloch, Science **357**, 995 (2017).

[63] R. P. Feynman, International Journal of Theoretical Physics **21**, 467 (1982).

[64] L. Landau, Nature **138**, 840 (1936).

[65] L. Pitaevskii and S. Stringari, *Bose-Einstein Condensation and Superfluidity* (OUP Oxford, 2016).

[66] E. D. Bloch, *A First Course in Geometric Topology and Differential Geometry* (Birkhäuser, Boston, 1997).

[67] M. Hasan and C. Kane, Reviews of Modern Physics **82**, 3045 (2010).

[68] K. Klitzing, G. Dorda, and M. Pepper, Physical Review Letters **45**, 494 (1980).

[69] R. Laughlin, Physical Review B **23**, 5632 (1981).

[70] D. Thouless, M. Kohmoto, M. Nightingale, and M. den Nijs, Physical Review Letters **49**, 405 (1982).

[71] F. D. M. Haldane, Physical Review Letters **61**, 2015 (1988).

[72] C. L. Kane and E. J. Mele, Physical Review Letters **95**, 146802 (2005).

[73] B. A. Bernevig, T. L. Hughes, and S.-C. Zhang, Science **314**, 1757 (2006).

[74] M. Konig, S. Wiedmann, C. Brune, A. Roth, H. Buhmann, L. W. Molenkamp, X.-L. Qi, and S.-C. Zhang, Science **318**, 766 (2007).

[75] L. Fu and C. Kane, Physical Review B **76**, 45302 (2007).

[76] D. Hsieh, D. Qian, L. Wray, Y. Xia, Y. S. Hor, R. J. Cava, and M. Z. Hasan, Nature **452**, 970 (2008).

[77] R. Roy, Physical Review B **79**, 195322 (2009).

[78] Y. Xia, D. Qian, D. Hsieh, L. Wray, A. Pal, H. Lin, A. Bansil, D. Grauer, Y. S. Hor, and R. J. Cava, Nature Physics **5**, 398 (2009).

[79] C.-K. Chiu, J. C. Teo, A. P. Schnyder, and S. Ryu, Reviews of Modern Physics **88**, 035005 (2016).

[80] S.-Y. Xu, I. Belopolski, D. S. Sanchez, C. Zhang, G. Chang, C. Guo, G. Bian, Z. Yuan, H. Lu, T.-R. Chang, P. P. Shibayev, M. L. Prokopovych, N. Alidoust, H. Zheng, C.-C. Lee, S.-M. Huang, R. Sankar, F. Chou, C.-H. Hsu, H.-T. Jeng, A. Bansil, T. Neupert, V. N. Strocov, H. Lin, S. Jia, and M. Z. Hasan, Science Advances **1**, 1501092 (2015).

[81] E. J. Meier, F. A. An, A. Dauphin, M. Maffei, P. Massignan, T. L. Hughes, and B. Gadway, Science , 3406 (2018).

[82] W. A. Benalcazar, B. A. Bernevig, and T. L. Hughes, Science **357**, 61 (2017).

[83] N. Goldman, J. C. Budich, and P. Zoller, Nature Physics **12**, 639 (2016).

[84] N. Goldman, G. Juzeliūnas, P. Öhberg, and I. B. Spielman, Reports on Progress in Physics **77**, 126401 (2014).

[85] N. Goldman and J. Dalibard, Physical Review X **4**, 031027 (2014).

[86] M. Aidelsburger, S. Nascimbene, and N. Goldman, Comptes Rendus Physique **19**, 394 (2018).

[87] M. Aidelsburger, M. Atala, S. Nascimbène, S. Trotzky, Y.-A. Chen, and I. Bloch, Physical Review Letters **107**, 255301 (2011).

[88] Y.-J. Lin, R. L. Compton, K. Jiménez-García, J. V. Porto, and I. B. Spielman, Nature **462**, 628 (2009).

[89] K. Jiménez-García, L. J. LeBlanc, R. A. Williams, M. C. Beeler, A. R. Perry, and I. B. Spielman, Physical Review Letters **108**, 225303 (2012).

[90] A. Eckardt, Review of Modern Physics **89**, 011004 (2017).

[91] T. Kitagawa, E. Berg, M. Rudner, and E. Demler, Physical Review B **82**, 235114 (2010).

[92] M. S. Rudner, N. H. Lindner, E. Berg, and M. Levin, Physical Review X **3**, 031005 (2013).

[93] M. Aidelsburger, M. Lohse, C. Schweizer, M. Atala, J. T. Barreiro, S. Nascimbène, N. Cooper, I. Bloch, and N. Goldman, Nature Physics **11**, 162 (2015).

[94] G. Jotzu, M. Messer, R. Desbuquois, M. Lebrat, T. Uehlinger, D. Greif, and T. Esslinger, Nature **515**, 237 (2014).

[95] M. C. Beeler, R. A. Williams, K. Jiménez-García, L. J. LeBlanc, A. R. Perry, and I. B. Spielman, Nature **498**, 201 (2013).

[96] A. Celi, P. Massignan, J. Ruseckas, N. Goldman, I. B. Spielman, G. Juzeliūnas, and M. Lewenstein, Physical Review Letters **112**, 043001 (2014).

[97] T. Ozawa and H. M. Price, Nature Reviews Physics **1**, 349–357 (2019).

[98] B. K. Stuhl, H.-I. Lu, L. M. Aycock, D. Genkina, and I. B. Spielman, Science **349**, 1514 (2015).

[99] M. Mancini, G. Pagano, G. Cappellini, L. Livi, M. Rider, J. Catani, C. Sias, P. Zoller, M. Inguscio, M. Dalmonte, and L. Fallani, Science **349**, 1510 (2015).

[100] E. J. Meier, F. A. An, and B. Gadway, Nature Communications **7**, 13986 (2016).

[101] S. Diehl, E. Rico, M. A. Baranov, and P. Zoller, Nature Physics **7**, 971 (2011).

[102] J. C. Budich, P. Zoller, and S. Diehl, Physical Review A **91**, 042117 (2015).

[103] M. Atala, M. Aidelsburger, J. T. Barreiro, D. Abanin, T. Kitagawa, E. Demler, and I. Bloch, Nature Physics **9**, 795 (2013).

[104] A. Dauphin and N. Goldman, Physical Review Letters **111**, 135302 (2013).

[105] D. T. Tran, A. Dauphin, A. G. Grushin, P. Zoller, and N. Goldman, Science Advances **3**, 1701207 (2017).

[106] D. C. Tsui, H. L. Stormer, and A. C. Gossard, Physical Review Letters **48**, 1559 (1982).

[107] S. de Léséleuc, V. Lienhard, P. Scholl, D. Barredo, S. Weber, N. Lang, H. P. Büchler, T. Lahaye, and A. Browaeys, Science **365**, 775 (2019).

[108] L. Amico, G. Birkl, M. Boshier, and L.-C. Kwek, New Journal of Physics **19**, 020201 (2017).

[109] C. Ryu, M. Andersen, P. Cladé, V. Natarajan, K. Helmerson, and W. Phillips, Physical Review Letters **99**, 260401 (2007).

[110] E. M. Wright, J. Arlt, and K. Dholakia, Physical Review A **63**, 013608 (2000).

[111] S. K. Schnelle, E. D. van Ooijen, M. J. Davis, N. R. Heckenberg, and H. Rubinsztein-Dunlop, Optics Express **16**, 1405 (2008).

[112] K. Henderson, C. Ryu, C. MacCormick, and M. G. Boshier, New Journal of Physics **11**, 043030 (2009).

[113] B. E. Sherlock, M. Gildemeister, E. Owen, E. Nugent, and C. J. Foot, Physical Review A **83**, 043408 (2011).

[114] A. S. Arnold, Optics Letters **37**, 2505 (2012).

[115] T. A. Bell, J. A. P. Glidden, L. Humbert, M. W. J. Bromley, S. A. Haine, M. J. Davis, T. W. Neely, M. A. Baker, and H. Rubinsztein-Dunlop, New Journal of Physics **18**, 035003 (2016).

[116] A. Turpin, J. Polo, Y. V. Loiko, J. Küber, F. Schmaltz, T. K. Kalkandjiev, V. Ahufinger, G. Birkl, and J. Mompart, Optics Express **23**, 1638 (2015).

[117] A. Kumar, R. Dubessy, T. Badr, C. De Rossi, M. de Goër de Herve, L. Longchambon, and H. Perrin, Physical Review A **97**, 043615 (2018).

[118] J. Polo, R. Dubessy, P. Pedri, H. Perrin, and A. Minguzzi, Physical Review Letters **123**, 195301 (2019).

[119] S. Beattie, S. Moulder, R. J. Fletcher, and Z. Hadzibabic, Physical Review Letters **110**, 025301 (2013).

[120] M. Andersen, C. Ryu, P. Cladé, A. Natarajan, Vasantand Vaziri, K. Helmerson, and W. Phillips, Physical Review Letters **97**, 170406 (2006).

[121] A. Ramanathan, K. C. Wright, S. R. Muniz, M. Zelan, W. T. Hill, C. J. Lobb, K. Helmerson, W. D. Phillips, and G. K. Campbell, Physical Review Letters **106**, 130401 (2011).

[122] S. Franke-Arnold, Philosophical Transactions Mathematical Physical & Engineering Sciences **375**, 20150435 (2017).

[123] L. Corman, L. Chomaz, T. Bienaimé, R. Desbuquois, C. Weitenberg, S. Nascimbène, J. Dalibard, and J. Beugnon, Physical Review Letters **113**, 135302 (2014).

[124] K. C. Wright, R. B. Blakestad, C. J. Lobb, W. D. Phillips, and G. K. Campbell, Physical Review Letters **110**, 025302 (2013).

[125] S. Eckel, J. G. Lee, F. Jendrzejewski, N. Murray, C. W. Clark, C. J. Lobb, W. D. Phillips, M. Edwards, and G. K. Campbell, Nature **506**, 200 (2014).

[126] S. Eckel, F. Jendrzejewski, A. Kumar, C. Lobb, and G. Campbell, Physical Review X **4**, 031052 (2014).

[127] C. Ryu, P. W. Blackburn, A. A. Blinova, and M. G. Boshier, Physical Review Letters **111**, 205301 (2013).

[128] F. Jendrzejewski, S. Eckel, N. Murray, C. Lanier, M. Edwards, C. Lobb, and G. Campbell, Physical Review Letters **113**, 045305 (2014).

[129] A. Kumar, N. Anderson, W. D. Phillips, S. Eckel, G. K. Campbell, and S. Stringari, New Journal of Physics **18**, 025001 (2016).

[130] J. Helm, S. Cornish, and S. Gardiner, Physical Review Letters **114**, 134101 (2015).

[131] P. Navez, S. Pandey, H. Mas, K. Poulios, T. Fernholz, and W. von Klitzing, New Journal of Physics **18**, 075014 (2016).

[132] S. A. Haine, Physical Review Letters **116**, 230404 (2016).

[133] S. Safaei, L.-C. Kwek, R. Dumke, and L. Amico, Phys. Rev. A **100**, 013621 (2019).

[134] G. Pelegrí, J. Mompart, and V. Ahufinger, New Journal of Physics **20**, 103001 (2018).

[135] A. Kiely, A. Benseny, T. Busch, and A. Ruschhaupt, Journal of Physics B: Atomic Molecular and Optical Physics **49**, 215003 (2016).

[136] A. Kiely, J. G. Muga, and A. Ruschhaupt, Physical Review A **98**, 053616 (2018).

[137] J. Polo, J. Mompart, and V. Ahufinger, Physical Review A **93**, 033613 (2016).

[138] G. Pelegrí, A. M. Marques, R. G. Dias, A. J. Daley, V. Ahufinger, and J. Mompart, Physical Review A **99**, 023612 (2019).

[139] G. Pelegrí, A. M. Marques, R. G. Dias, A. J. Daley, J. Mompart, and V. Ahufinger, Physical Review A **99**, 023613 (2019).

[140] G. Pelegrí, A. M. Marques, V. Ahufinger, J. Mompart, and R. G. Dias, Physical Review B **100**, 205109 (2019).

[141] G. Pelegrí, J. Mompart, V. Ahufinger, and A. J. Daley, Physical Review A **100**, 023615 (2019).

[142] J. J. Sakurai, *Modern Quantum Mechanics* (Addison Wesley, 1985).

[143] E. P. Gross, Il Nuovo Cimento Series 10 **20**, 454 (1961).

[144] L. P. Pitaevskii, Sov. Phys. JETP **13**, 451 (1961).

[145] D. Aghamalyan, M. Cominotti, M. Rizzi, D. Rossini, F. Hekking, A. Minguzzi, L.-C. Kwek, and L. Amico, New Journal of Physics **17**, 045023 (2015).

[146] A. L. Fetter, Reviews of Modern Physics **81**, 647 (2009).

[147] D. S. Petrov, G. V. Shlyapnikov, and J. T. M. Walraven, Physical Review Letters **85**, 3745 (2000).

[148] D. S. Petrov, M. Holzmann, and G. V. Shlyapnikov, Physical Review Letters **84**, 2551 (2000).

[149] N. W. Ashcroft and N. D. Mermin, *Solid State Physics* (Holt, Rinehart, and Winston, 1976).

[150] D. Raventós, T. Grass, M. Lewenstein, and B. Juliá-Díaz, Journal of Physics B: Atomic Molecular and Optical Physics **50**, 113001 (2017).

[151] U. Schollwöck, Annals of Physics **326**, 96 (2011).

[152] M. V. Berry, Proceedings Mathematical Physical & Engineering Sciences **392**, 45 (1984).

[153] D. Xiao, M.-C. Chang, and Q. Niu, Reviews of Modern Physics **82**, 1959 (2010).

[154] Y. Aharonov and D. Bohm, Physical Review **115**, 485 (1959).

[155] P. G. Harper, Proceedings of the Physical Society Section A **68**, 874 (1955).

[156] D. Hofstadter, Physical Review B **14**, 2239 (1976).

[157] J. Zak, Physical Review Letters **62**, 2747 (1989).

[158] R. D. King-Smith and D. Vanderbilt, Physical Review B **47**, 1651 (1993).

[159] R. Resta, Reviews of Modern Physics **66**, 899 (1994).

[160] J. K. Asbóth, L. Oroszlány, and A. Pályi, *A Short Course on Topological Insulators: Band Structure and Edge States in One and Two Dimensions* (Springer International Publishing, Switzerland, 2016).

[161] W. P. Su, J. R. Schrieffer, and A. J. Heeger, Physical Review Letters **42**, 1698 (1979).

[162] F. Pinheiro, *Multi-species Systems in Optical Lattices (PhD thesis)* (Springer, 2016).

[163] I. Lesanovsky and W. von Klitzing, Physical Review Letters **99**, 083001 (2007).

[164] J. Polo, A. Benseny, T. Busch, V. Ahufinger, and J. Mompart, New Journal of Physics **18**, 015010 (2016).

[165] G. Gauthier, I. Lenton, N. McKay Parry, M. Baker, M. J. Davis, H. Rubinsztein-Dunlop, and T. W. Neely, Optica **3**, 1136 (2016).

[166] A. Lizana, A. Vargas, A. Turpin, C. Ramirez, I. Estevez, and J. Campos, Journal of Optics (IOPscience) **18**, 105605 (2016).

[167] D. Robbes, Sensors and Actuators A: Physical **129**, 86 (2006).

[168] R. L. Fagaly, Review of Scientific Instruments **77**, 1 (2006).

[169] H. Weinstock (Ed.), *SQUID Sensors: Fundamentals, Fabrication and Applications* (Springer Science & Business Media, 2012).

[170] I. K. Kominis, T. W. Kornack, J. C. Allred, and M. V. Romalis, Nature **422**, 596 (2003).

[171] D. Sheng, S. Li, N. Dural, and M. V. Romalis, Physical Review Letters **110**, 160802 (2013).

[172] I. Baumgart, J.-M. Cai, A. Retzker, M. Plenio, and C. Wunderlich, Physical Review Letters **116**, 240801 (2016).

[173] M. Koschorreck, M. Napolitano, B. Dubost, and M. W. Mitchell, Applied Physics Letters **98**, 074101 (2011).

[174] F. Wolfgramm, A. Cerè, F. A. Beduini, A. Predojević, M. Koschorreck, and M. W. Mitchell, Physical Review Letters **105**, 053601 (2010).

[175] V. Shah, S. Knappe, P. D. D. Schwindt, and J. Kitching, Nature Photonics **1**, 649 (2007).

[176] W. Wasilewski, K. Jensen, H. Krauter, J. J. Renema, M. V. Balabas, and E. S. Polzik, Physical Review Letters **104**, 133601 (2010).

[177] L. Rondin, J.-P. Tetienne, T. Hingant, J.-F. Roch, P. Maletinsky, and V. Jacques, Reports on Progress in Physics **77**, 056503 (2014).

[178] T. Wolf, P. Neumann, K. Nakamura, H. Sumiya, T. Ohshima, J. Isoya, and J. Wrachtrup, Physical Review X **5**, 041001 (2015).

[179] X. Zhang and J. Ye, National Science Review **3**, 189 (2016).

[180] M. L. Terraciano, M. Bashkansky, and F. K. Fatemi, Optics Express **16**, 13062 (2008).

[181] K. Hardman, P. Everitt, G. McDonald, P. Manju, P. Wigley, M. Sooriyabandara, C. Kuhn, J. Debs, J. Close, and N. Robins, Physical Review Letters **117**, 138501 (2016).

[182] T. Isayama, Y. Takahashi, N. Tanaka, K. Toyoda, K. Ishikawa, and T. Yabuzaki, Physical Review A **59**, 4836 (1999).

[183] M. Vengalattore, J. M. Higbie, S. R. Leslie, J. Guzman, L. E. Sadler, and D. M. Stamper-Kurn, Physical Review Letters **98**, 200801 (2007).

[184] F. K. Fatemi and M. Bashkansky, Optics Express **18**, 2190 (2010).

[185] Y. Eto, H. Ikeda, H. Suzuki, S. Hasegawa, Y. Tomiyama, S. Sekine, M. Sadgrove, and T. Hirano, Physical Review A **88**, 031602 (2013).

[186] Y. Eto, S. Sekine, S. Hasegawa, M. Sadgrove, H. Saito, and T. Hirano, Applied Physics Express **6**, 052801 (2013).

[187] W. Muessel, H. Strobel, D. Linnemann, D. Hume, and M. Oberthaler, Physical Review Letters **113**, 103004 (2014).

[188] S. Tojo, Y. Taguchi, Y. Masuyama, T. Hayashi, H. Saito, and T. Hirano, Physical Review A **82**, 33609 (2010).

[189] S. Wildermuth, S. Hofferberth, I. Lesanovsky, E. Haller, L. M. Andersson, S. Groth, I. Bar-Joseph, P. Krüger, and J. Schmiedmayer, Nature **435**, 440 (2005).

[190] S. Wildermuth, S. Hofferberth, I. Lesanovsky, S. Groth, P. Krüger, J. Schmiedmayer, and I. Bar-Joseph, Applied Physics Letters **88**, 264103 (2006).

[191] F. Yang, A. J. Kollár, S. F. Taylor, R. W. Turner, and B. L. Lev, Physical Review Applied **7**, 034026 (2017).

[192] B. T. Seaman, M. Krämer, D. Z. Anderson, and M. J. Holland, Physical Review A **75**, 023615 (2007).

[193] R. A. Pepino, J. Cooper, D. Z. Anderson, and M. J. Holland, Physical Review Letters **103**, 140405 (2009).

[194] Y.-H. Wang, A. Kumar, F. Jendrzejewski, R. M. Wilson, M. Edwards, S. Eckel, G. K. Campbell, and C. W. Clark, New Journal of Physics **17**, 125012 (2015).

[195] L. Amico, D. Aghamalyan, F. Auksztol, H. Crepaz, R. Dumke, and L. C. Kwek, Scientific Reports **4**, 4298 (2014).

[196] Y. Sato and R. E. Packard, Reports on Progress in Physics **75**, 16401 (2012).

[197] B. Barrett, R. Geiger, I. Dutta, M. Meunier, B. Canuel, A. Gauguet, P. Bouyer, and A. Landragin, Comptes Rendus Physique **15**, 875 (2014).

[198] F. I. Moxley, J. P. Dowling, W. Dai, and T. Byrnes, Physical Review A **93**, 053603 (2016).

[199] G. Watanabe and C. J. Pethick, Physical Review A **76**, 021605 (2007).

[200] K. A. Bagrinovskii and S. K. Godunov, Dokl. Akad. Nauk SSSR **115**, 431 (1957).

[201] C. J. Pethick and H. Smith, *Bose-Einstein Condensation and Superfluidity* (Cambridge University Press, 2011).

[202] G. Roati, M. Zaccanti, C. D'Errico, J. Catani, M. Modugno, A. Simoni, M. Inguscio, and G. Modugno, Physical Review Letters **99**, 010403 (2007).

[203] D. Guéry-Odelin, A. Ruschhaupt, A. Kiely, E. Torrontegui, S. Martínez-Garaot, and J. Muga, Review of Modern Physics **91**, 045001 (2019).

[204] T. Ozawa, H. M. Price, A. Amo, N. Goldman, M. Hafezi, L. Lu, M. C. Rechtsman, D. Schuster, J. Simon, O. Zilberberg, and I. Carusotto, Reviews of Modern Physics **91**, 015006 (2019).

[205] Y. E. Kraus, Y. Lahini, Z. Ringel, M. Verbin, and O. Zilberberg, Physical Review Letters **109**, 106402 (2012).

[206] M. Verbin, O. Zilberberg, Y. E. Kraus, Y. Lahini, and Y. Silberberg, Physical Review Letters **110**, 076403 (2013).

[207] M. Hafezi, S. Mittal, J. Fan, A. Migdall, and J. M. Taylor, Nature Photonics **7**, 1001 (2013).

[208] P. St-Jean, V. Goblot, E. Galopin, A. Lemaître, T. Ozawa, L. Le Gratiet, I. Sagnes, J. Bloch, and A. Amo, Nature Photonics **11**, 651 (2017).

[209] S. Weimann, M. Kremer, Y. Plotnik, Y. Lumer, S. Nolte, K. G. Makris, M. Segev, M. C. Rechtsman, and A. Szameit, Nature Materials **16**, 433 (2016).

[210] T. Kitagawa, M. A. Broome, A. Fedrizzi, M. S. Rudner, E. Berg, I. Kassal, A. Aspuru-Guzik, E. Demler, and A. G. White, Nature Communications **3**, 882 (2012).

[211] F. Cardano, A. D'Errico, A. Dauphin, M. Maffei, B. Piccirillo, C. de Lisio, G. De Filippis, V. Cataudella, E. Santamato, L. Marrucci, M. Lewenstein, and P. Massignan, Nature Communications **8**, 15516 (2017).

[212] M. Leder, C. Grossert, L. Sitta, M. Genske, A. Rosch, and M. Weitz, Nature Communications **7**, 13112 (2016).

[213] M. Metcalf, C.-Y. Lai, K. Wright, and C.-C. Chien, Europhysics Letters **118**, 56004 (2017).

[214] S. Mugel, A. Celi, P. Massignan, J. K. Asbóth, M. Lewenstein, and C. Lobo, Physical Review A **94**, 023631 (2016).

[215] H. Nonne, M. Moliner, S. Capponi, P. Lecheminant, and K. Totsuka, Europhysics Letters **102**, 37008 (2013).

[216] X.-J. Liu, Z.-X. Liu, and M. Cheng, Physical Review Letters **110**, 076401 (2013).

[217] M. Nakagawa and N. Kawakami, Physical Review B **96**, 155133 (2017).

[218] F. Matsuda, M. Tezuka, and N. Kawakami, Journal of the Physical Society of Japan **83**, 083707 (2014).

[219] X. Deng and L. Santos, Physical Review A **89**, 033632 (2014).

[220] D. Jaksch and P. Zoller, New Journal of Physics **5**, 56 (2003).

[221] T. Kock, C. Hippler, A. Ewerbeck, and A. Hemmerich, Journal of Physics B: Atomic Molecular and Optical Physics **49**, 042001 (2016).

[222] X. Li, E. Zhao, and W. Vincent Liu, Nature Communications **4**, 1523 (2013).

[223] A. M. Marques and R. G. Dias, Physical Review B **100**, 041104 (2019).

[224] J. Arkinstall, M. H. Teimourpour, L. Feng, R. El-Ganainy, and H. Schomerus, Physical Review B **95**, 165109 (2017).

[225] M. Kremer, I. Petrides, E. Meyer, M. Heinrich, O. Zilberberg, and A. Szameit, arXiv: 1805.05209 [cond-mat.mes-hall] .

[226] K. Sun, W. V. Liu, A. Hemmerich, and S. Das Sarma, Nature Physics **8**, 67 (2011).

[227] Z.-F. Xu, L. You, A. Hemmerich, and W. V. Liu, Physical Review Letters **117**, 085301 (2016).

[228] J. Vidal, R. Mosseri, and B. Douçot, Physical Review Letters **81**, 5888 (1998).

[229] B. Douçot and J. Vidal, Physical Review Letters **88**, 227005 (2002).

[230] S. Longhi, Optics Letters **39**, 5892 (2014).

[231] S. Mukherjee, M. Di Liberto, P. Öhberg, R. R. Thomson, and N. Goldman, Physical Review Letters **121**, 075502 (2018).

[232] J. Jünemann, A. Piga, S.-J. Ran, M. Lewenstein, M. Rizzi, and A. Bermudez, Physical Review X **7**, 031057 (2017).

[233] J. Dalibard, F. Gerbier, G. Juzeliūnas, and P. Öhberg, Reviews of Modern Physics **83**, 1523 (2011).

[234] G. Pelegrí, J. Polo, A. Turpin, M. Lewenstein, J. Mompart, and V. Ahufinger, Physical Review A **95**, 013614 (2017).

[235] A. A. Lopes and R. G. Dias, Physical Review B **84**, 085124 (2011).

[236] A. M. Marques and R. G. Dias, Journal of Physics Condensed Matter **30**, 305601 (2018).

[237] F. Wilczek and A. Zee, Physical Review Letters **52**, 2111 (1984).

[238] J. Struck, M. Weinberg, C. ölschläger, P. Windpassinger, J. Simonet, K. Sengstock, R. Höppner, P. Hauke, A. Eckardt, M. Lewenstein, and L. Mathey, Nature Physics **9**, 738 (2013).

[239] D. Greif, T. Uehlinger, G. Jotzu, L. Tarruell, and T. Esslinger, Science **340**, 1307 (2013).

[240] D. Greif, G. Jotzu, M. Messer, R. Desbuquois, and T. Esslinger, Physical Review Letters **115**, 260401 (2015).

[241] M. F. Parsons, A. Mazurenko, C. S. Chiu, G. Ji, D. Greif, and M. Greiner, Science **353**, 1253 (2016).

[242] L. W. Cheuk, M. A. Nichols, K. R. Lawrence, M. Okan, H. Zhang, E. Khatami, N. Trivedi, T. Paiva, M. Rigol, and M. W. Zwierlein, Science **353**, 1260 (2016).

[243] R. A. Hart, P. M. Duarte, T.-L. Yang, X. Liu, T. Paiva, E. Khatami, R. T. Scalettar, N. Trivedi, D. A. Huse, and R. G. Hulet, Nature **519**, 211 (2015).

[244] J. Drewes, L. Miller, E. Cocchi, C. Chan, N. Wurz, M. Gall, D. Pertot, F. Brennecke, and M. Köhl, Physical Review Letters **118**, 170401 (2017).

[245] P. T. Brown, D. Mitra, E. Guardado-Sanchez, P. Schauß, S. S. Kondov, E. Khatami, T. Paiva, N. Trivedi, D. A. Huse, and W. S. Bakr, Science **357**, 1385 (2017).

[246] A. Mazurenko, C. S. Chiu, G. Ji, M. F. Parsons, M. Kanász-Nagy, R. Schmidt, F. Grusdt, E. Demler, D. Greif, and M. Greiner, Nature **545**, 462 (2017).

[247] J. Simon, W. S. Bakr, R. Ma, M. E. Tai, P. M. Preiss, and M. Greiner, Nature **472**, 307 (2011).

[248] T. Fukuhara, P. Schauß, M. Endres, S. Hild, M. Cheneau, I. Bloch, and C. Gross, Nature **502**, 76 (2013).

[249] T. Fukuhara, A. Kantian, M. Endres, M. Cheneau, P. Schauß, S. Hild, D. Bellem, U. Schollwöck, T. Giamarchi, C. Gross, I. Bloch, and S. Kuhr, Nature Physics **9**, 235 (2013).

[250] T. Fukuhara, S. Hild, J. Zeiher, P. Schauß, I. Bloch, M. Endres, and C. Gross, Physical Review Letters **115**, 035302 (2015).

[251] S. Hild, T. Fukuhara, P. Schauß, J. Zeiher, M. Knap, E. Demler, I. Bloch, and C. Gross, Physical Review Letters **113**, 147205 (2014).

[252] F. Pinheiro, G. M. Bruun, J.-P. Martikainen, and J. Larson, Physical Review Letters **111**, 205302 (2013).

[253] S. Sachdev, K. Sengupta, and S. M. Girvin, Physical Review B **66**, 075128 (2002).

[254] A. S. Buyskikh, L. Tagliacozzo, D. Schuricht, C. A. Hooley, D. Pekker, and A. J. Daley, Physical Review Letters **123**, 090401 (2019).

[255] F. Meinert, M. J. Mark, E. Kirilov, K. Lauber, P. Weinmann, A. J. Daley, and H.-C. Nägerl, Physical Review Letters **111**, 053003 (2013).

[256] F. Meinert, M. J. Mark, E. Kirilov, K. Lauber, P. Weinmann, M. Grobner, A. J. Daley, and H.-C. Nagerl, Science **344**, 1259 (2014).

[257] R. Baxter, *Exactly Solvable Models in Statistical Mechanics* (Academic London, 1982).

[258] E. Ercolessi, S. Evangelisti, F. Franchini, and F. Ravanini, Physical Review B **88**, 104418 (2013).

[259] A. Isacsson and S. M. Girvin, Physical Review A **72**, 053604 (2005).

[260] K. Winkler, G. Thalhammer, F. Lang, R. Grimm, J. Hecker Denschlag, A. J. Daley, A. Kantian, H. P. Büchler, and P. Zoller, Nature **441**, 853 (2006).

[261] N. Strohmaier, D. Greif, R. Jördens, L. Tarruell, H. Moritz, T. Esslinger, R. Sensarma, D. Pekker, E. Altman, and E. Demler, Physical Review Letters **104**, 080401 (2010).

[262] P. M. Preiss, R. Ma, M. E. Tai, A. Lukin, M. Rispoli, P. Zupancic, Y. Lahini, R. Islam, and M. Greiner, Science **347**, 1229 (2015).

[263] M. E. Tai, A. Lukin, M. Rispoli, R. Schittko, T. Menke, D. Borgnia, P. M. Preiss, F. Grusdt, A. M. Kaufman, and M. Greiner, Nature **546**, 519 (2017).

[264] D. Petrosyan, B. Schmidt, J. R. Anglin, and M. Fleischhauer, Physical Review A **76**, 033606 (2007).

[265] M. Valiente and D. Petrosyan, Journal of Physics B: Atomic Molecular and Optical Physics **41**, 161002 (2008).

[266] M. Valiente and D. Petrosyan, Journal of Physics B: Atomic Molecular and Optical Physics **42**, 121001 (2009).

[267] R. A. Pinto, M. Haque, and S. Flach, Physical Review A **79**, 052118 (2009).

[268] R. A. Pinto, J. P. Nguenang, and S. Flach, Physica D: Nonlinear Phenomena **238**, 581 (2009).

[269] Y.-M. Wang and J.-Q. Liang, Physical Review A **81**, 045601 (2010).

[270] J. Javanainen, O. Odong, and J. C. Sanders, Physical Review A **81**, 043609 (2010).

[271] J.-P. Nguenang, S. Flach, and R. Khomeriki, Physics Letters A **376**, 472 (2012).

[272] J. M. Zhang, D. Braak, and M. Kollar, Physical Review Letters **109**, 116405 (2012).

184

[273] S. Longhi and G. Della Valle, Journal of Physics: Condensed Matter **25**, 235601 (2013).

[274] X. Qin, Y. Ke, X. Guan, Z. Li, N. Andrei, and C. Lee, Physical Review A **90**, 062301 (2014).

[275] C. Menotti, F. Minganti, and A. Recati, Physical Review A **93**, 033602 (2016).

[276] Y. Lahini, M. Verbin, S. D. Huber, Y. Bromberg, R. Pugatch, and Y. Silberberg, Physical Review A **86**, 011603 (2012).

[277] S. Mukherjee, M. Valiente, N. Goldman, A. Spracklen, E. Andersson, P. Öhberg, and R. R. Thomson, Physical Review A **94**, 053853 (2016).

[278] X. Qin, F. Mei, Y. Ke, L. Zhang, and C. Lee, New Journal of Physics **20**, 013003 (2017).

[279] M. Di Liberto, A. Recati, I. Carusotto, and C. Menotti, Physical Review A **94**, 062704 (2016).

[280] M. Di Liberto, A. Recati, I. Carusotto, and C. Menotti, The European Physical Journal Special Topics **226**, 2751 (2017).

[281] H. Guo and S.-Q. Shen, Physical Review B **84**, 195107 (2011).

[282] A. M. Marques and R. G. Dias, Physical Review B **95**, 115443 (2017).

[283] M. A. Gorlach, M. Di Liberto, A. Recati, I. Carusotto, A. N. Poddubny, and C. Menotti, Physical Review A **98**, 063625 (2018).

[284] G. Salerno, M. Di Liberto, C. Menotti, and I. Carusotto, Physical Review A **97**, 013637 (2018).

[285] M. A. Gorlach and A. N. Poddubny, Physical Review A **95**, 053866 (2017).

[286] M. A. Gorlach and A. N. Poddubny, Physical Review A **95**, 033831 (2017).

[287] M. Bello, C. E. Creffield, and G. Platero, Scientific Reports **6**, 22562 (2016).

[288] M. Bello, C. E. Creffield, and G. Platero, Physical Review B **95**, 094303 (2017).

[289] Q. Niu and D. J. Thouless, Journal of Physics A: Mathematical and General **17**, 2453 (1984).

[290] C. Cartwright, G. De Chiara, and M. Rizzi, Physical Review B **98**, 184508 (2018).

[291] D. Leykam, A. Andreanov, and S. Flach, Advances in Physics: X **3**, 1473052 (2018).

[292] S. D. Huber and E. Altman, Physical Review B **82**, 184502 (2010).

[293] G. Möller and N. R. Cooper, Physical Review Letters **108**, 045306 (2012).

[294] S. Takayoshi, H. Katsura, N. Watanabe, and H. Aoki, Physical Review A **88**, 063613 (2013).

[295] M. Tovmasyan, E. P. L. van Nieuwenburg, and S. D. Huber, Physical Review B **88**, 220510 (2013).

[296] S. Greschner, L. Santos, and T. Vekua, Physical Review A **87**, 033609 (2013).

[297] P. Pudleiner and A. Mielke, The European Physical Journal B / Condensed Matter and Complex Systems **88**, 207 (2015).

[298] L. G. Phillips, G. De Chiara, P. Öhberg, and M. Valiente, Physical Review B **91**, 054103 (2015).

[299] M. Tovmasyan, S. Peotta, P. Törmä, and S. D. Huber, Physical Review B **94**, 245149 (2016).

[300] B. Grémaud and G. G. Batrouni, Physical Review B **95**, 165131 (2017).

[301] R. Mondaini, G. G. Batrouni, and B. Grémaud, Physical Review B **98**, 155142 (2018).

[302] M. Tovmasyan, S. Peotta, L. Liang, P. Törmä, and S. D. Huber, Physical Review B **98**, 134513 (2018).

[303] T. Neupert, L. Santos, C. Chamon, and C. Mudry, Physical Review Letters **106**, 236804 (2011).

[304] H. Guo, S.-Q. Shen, and S. Feng, Physical Review B **86**, 085124 (2012).

[305] J. C. Budich and E. Ardonne, Physical Review B **88**, 035139 (2013).

[306] F. Baboux, L. Ge, T. Jacqmin, M. Biondi, E. Galopin, A. Lemaître, L. Le Gratiet, I. Sagnes, S. Schmidt, H. Türeci, A. Amo, and J. Bloch, Physical Review Letters **116**, 066402 (2016).

[307] G. Gligorić, P. P. Beličev, D. Leykam, and A. Maluckov, Physical Review A **99**, 013826 (2019).

[308] M. Di Liberto, S. Mukherjee, and N. Goldman, Physical Review A **100**, 043829 (2019).

[309] M. Creutz, Physical Review Letters **83**, 2636 (1999).

[310] X.-L. Qi and S.-C. Zhang, Reviews of Modern Physics **83**, 1057 (2011).

[311] W. A. Benalcazar, B. A. Bernevig, and T. L. Hughes, Physical Review B **96**, 245115 (2017).

[312] J. Langbehn, Y. Peng, L. Trifunovic, F. von Oppen, and P. W. Brouwer, Physical Review Letters **119**, 246401 (2017).

[313] Z. Song, Z. Fang, and C. Fang, Physical Review Letters **119**, 246402 (2017).

[314] B.-Y. Xie, H.-F. Wang, H.-X. Wang, X.-Y. Zhu, J.-H. Jiang, M.-H. Lu, and Y.-F. Chen, Physical Review B **98**, 205147 (2018).

[315] L. Li, M. Umer, and J. Gong, Physical Review B **98**, 205422 (2018).

[316] S. Hayashi, Communications in Mathematical Physics **364**, 343 (2018).

[317] L. Trifunovic and P. W. Brouwer, Physical Review X **9**, 011012 (2019).

[318] S. Franca, J. van den Brink, and I. C. Fulga, Physical Review B **98**, 201114 (2018).

[319] F. Schindler, A. M. Cook, M. G. Vergniory, Z. Wang, S. S. P. Parkin, B. A. Bernevig, and T. Neupert, Science Advances **4**, eaat0346 (2018).

[320] M. Ezawa, Physical Review Letters **120**, 026801 (2018).

[321] F. K. Kunst, G. van Miert, and E. J. Bergholtz, Physical Review B **97**, 241405 (2018).

[322] E. Khalaf, Physical Review B **97**, 205136 (2018).

[323] T. Fukui and Y. Hatsugai, Physical Review B **98**, 035147 (2018).

[324] M. Lin and T. L. Hughes, Physical Review B **98**, 241103 (2018).

[325] Q. Wang, C.-C. Liu, Y.-M. Lu, and F. Zhang, Physical Review Letters **121**, 186801 (2018).

[326] R.-J. Slager, L. Rademaker, J. Zaanen, and L. Balents, Physical Review B **92**, 085126 (2015).

[327] C. Zeng, T. D. Stanescu, C. Zhang, V. W. Scarola, and S. Tewari, Physical Review Letters **123**, 060402 (2019).

[328] B. J. Wieder, Z. Wang, J. Cano, X. Dai, L. M. Schoop, B. B. Bradlyn, and B. A. Bernevig, arXiv:1908.00016 [cond-mat.mes-hall] .

[329] M. Serra-Garcia, V. Peri, R. Süsstrunk, O. R. Bilal, T. Larsen, L. G. Villanueva, and S. D. Huber, Nature **555**, 342–345 (2018).

[330] H. Xue, Y. Yang, F. Gao, Y. Chong, and B. Zhang, Nature Materials **18**, 108–112 (2018).

[331] C. W. Peterson, W. A. Benalcazar, T. L. Hughes, and G. Bahl, Nature **555**, 346 (2018).

[332] S. Imhof, C. Berger, F. Bayer, J. Brehm, L. W. Molenkamp, T. Kiessling, F. Schindler, C. H. Lee, M. Greiter, T. Neupert, and R. Thomale, Nature Physics **14**, 925 (2018).

[333] M. Serra-Garcia, R. Süsstrunk, and S. D. Huber, Physical Review B **99**, 020304 (2019).

[334] F. Schindler, Z. Wang, M. G. Vergniory, A. M. Cook, A. Murani, S. Sengupta, A. Y. Kasumov, R. Deblock, S. Jeon, I. Drozdov, H. Bouchiat, S. Guéron, A. Yazdani, B. A. Bernevig, and T. Neupert, Nature Physics **14**, 918 (2018).

[335] B. Song, L. Zhang, C. He, T. F. J. Poon, E. Hajiyev, S. Zhang, X.-J. Liu, and G.-B. Jo, Science Advances **4**, 4748 (2018).

[336] M. Slot, S. Kempkes, E. Knol, W. van Weerdenburg, J. van den Broeke, D. Wegner, D. Vanmaekelbergh, A. Khajetoorians, C. Morais Smith, and I. Swart, Physical Review X **9**, 011009 (2019).

[337] F. Liu and K. Wakabayashi, Physical Review Letters **118**, 076803 (2017).

[338] T. B. T. White, Angela; Hennessy, Physical Review A **93**, 033601 (2016).

[339] Y. B. T. White, Angela C.; Zhang, Physical Review A **95**, 041604 (2017).

[340] A. Smerzi, S. Fantoni, S. Giovanazzi, and S. R. Shenoy, Physical Review Letters **79**, 4950 (1997).

[341] T. Bland, Q. Marolleau, P. Comaron, B. Malomed, and N. Proukakis, arXiv:1911.12802 [cond-mat.quant-gas] .

[342] A. Turpin, G. Pelegrí, J. Polo, J. Mompart, and V. Ahufinger, Scientific Reports **7**, 44057 (2017).